

Molecular Wire Based Bio-Electrochemical Sensing
Systems

Lee Ian Partington, MChem

PhD

The University of Hull and
the University of York

Hull York Medical School

June 2016

Abstract

This thesis aims to develop rapid, quantitative point of care sensing systems that exploit molecular wire platforms to enable the electrochemical detection of multiple target biomarkers, thereby empowering new technologies for the diagnosis of various medical conditions. Accordingly, the first chapter provides an overview of clinically important biomarkers for pregnancy and cardiovascular disease. The second chapter of this thesis details the electrochemical concepts underpinning subsequent chapters, with the third chapter providing an experimental overview.

The first two research chapters develop a nano-structured, molecular wire platform based on diazonium salt electrochemistry coupled with immobilisation of antibodies conjugated to a suitable electroactive label. Here, the abundance of amine functionalities present at the antibody paratope enable the statistically large number of redox tags to be present at the antibody-antigen binding site, empowering the exquisitely selective and strong affinity of the antibody for a suitable antigen to be monitored quantitatively, through assessing the extent with which the redox labels are partially blocked in the presence of the antigen. In Chapter 4, experiments are contrasted with bespoke theory developed in order to unravel the thermodynamic and kinetic factors that empower this methodology to be singularly sensitive for the pregnancy biomarker human chorionic gonadotropin (hCG). It is demonstrated that quantitative analysis of hCG detection in artificial urine does not suffer interference. Chapter 5 adapts this approach to survey other biomarkers including β -hCG and brain natriuretic peptide. Combinatorial immunoassays are also investigated through the use of two types of antibodies, each tagged with a different redox label.

Chapter 6 exploits the electroactive spin-trapping molecule TEMPO for the detection of biomolecules that have been damaged through oxidative stress.

Last, Chapter 7 presents an overall conclusion to the work presented in this thesis.

Contents

Chapter 1 Clinical Biomarkers: A Brief Overview	21
1.1 Introduction to Biomarkers of Interest	21
1.2 Cardiovascular Disease	21
1.2.1 Biomarkers of Cardiac Injury	23
1.2.1.1 Brain Natriuretic Peptides	23
1.2.1.2 Methods for Sensing BNP	25
1.2.1.3 Troponin T	26
1.2.1.4 Methods for cTnT sensing	28
1.3 Pregnancy	28
1.3.1 Biomarkers of Pregnancy	29
1.3.1.1 Human Chorionic Gonadotropin	29
1.3.1.2 Methods for hCG Sensing	35
1.4 Biosensing Methods for Biomarkers	38
1.4.1 Biosensors	38
1.4.2 Immunoassays	38
1.4.2.1 Antibodies	38
1.4.2.2 Radioimmunoassays	43
1.4.2.3 Enzyme Immunoassay	45
1.4.2.4 Fluoroimmunoassay	46
1.4.2.5 Chemiluminescent Immunoassay	48
1.4.2.6 Colorimetric Immunoassay	52
1.4.2.7 Electrochemical Immunoassay	53
1.5 Kinetics of Binding	58
1.6 Biological Matrices	61
1.6.1 Urine	62
1.6.2 Blood	64
1.7 Aims and Objectives of this Thesis	65

Chapter 2 Dynamic Electrochemistry	78
2.1 Basic Electrochemistry	78
2.1.1 Electrodes and the Electrochemical Cell	86
2.1.1.1 The Role of Supporting Electrolyte	87
2.2 Interfacial Region and the Electric Double Layer	89
2.3 Mass Transport Controlled Reactions	92
2.3.1 Convection	94
2.3.2 Migration	94
2.3.3 Diffusion	95
2.4 Electrode Kinetics and Processes	96
2.4.1 Butler-Volmer Kinetics	97
2.5 Marcus Theory of Electron Transfer	101
2.6 Electrochemical Detection Methods	108
2.6.1 Voltammetry	108
2.6.2 Cyclic Voltammetry	108
2.7 Electrochemical Reversibility	109
2.7.1 Reversible Systems	109
2.7.2 Quasi-Reversible Systems	110
2.7.3 Irreversible Systems	111
2.8 Square Wave Voltammetry	112
2.9 Cyclic Voltammetry of Adsorbed Species	113
2.10 Modifying the Electrode Surface	119
2.10.1 Molecular Wires	120
Chapter 3 Experimental	123
3.1 Instrumentation	123
3.1.1 Potentiostat	123
3.1.2 Electrodes	123
3.2 Materials	124
3.2.1 Chemicals	124
3.2.2 Solvents and Gases	127
3.3 Experimental Preparations	128
3.4 Electrode Characterisation	128

3.4.1	Preparation of Ferrocene-labelled Antibody Modified ITO Electrode Surface	129
3.4.1.1	Surface Deposition of 4-nitrobenzene Diazonium Salt	129
3.4.1.2	Molecular Wire Functionalisation	130
3.4.1.3	Synthesis of Antibody Bio-conjugates	130
3.4.1.4	Immobilisation of Ferrocene Labelled Antibody onto the ITO Surface	131
3.4.1.5	Finalising Electrode Preparation	133
3.5	Detection of hCG and Kinetic Investigation	134
3.5.1	Detection of hCG in PBS	134
3.5.2	Kinetic Investigation of hCG in PBS	134
3.5.3	Quantitative Detection of hCG in Artificial Urine and Laked Horse Blood	134
3.5.4	Interference Studies	135
3.5.4.1	Glucose	135
3.5.4.2	Haemoglobin	135
3.6	Cardiovascular Disease Detection at the Point of Care	136
3.6.1	Detection of BNP in PBS	136
3.7	Pregnancy Detection at the Point of Care	136
3.7.1	Detection of β -hCG in PBS	136
3.7.2	Kinetic Investigation of β -hCG in PBS	137
3.8	Multiplex studies: Chlorpromazine and Ruthenium N-3 Dye as Alternative Redox Tags	137
3.8.1	Preparation of Chlorpromazine-labelled Antibody	137
3.8.2	Detection of BNP with Chlorpromazine Modified Surface	138
3.8.3	Preparation of N-3 Dye labelled Antibody	139
3.8.4	Detection of BNP with N-3 Dye Modified Surface	139
3.8.5	Determination of the Number of Antibody Bound Redox Tags	139
3.8.5.1	Method One: UV-VIS	139
3.8.5.2	Method Two: Cyclic Voltammetry	140
3.9	TEMPO Immunoassay	140
3.9.1	Electrochemical Characterisation	140
3.9.2	Antibody Surface Attachment	140
3.9.3	Calibration of Sensor Response	141

Chapter 4 **143**

Electrochemical Measurement of Antibody-Antigen Recognition Biophysics: Thermodynamics, Kinetics and Analytical Detection of Human Chorionic Gonadotropin (hCG) Binding to Redox-Tagged Antibodies in Artificial Urine

4.1	Introduction	143
4.2	Theory	149
4.2.1	Development of a Global Antigen Coverage Parameter	149
4.2.2	Thermodynamics of Antigen-Antibody Recognition	152
4.2.3	Rate Laws for the Formation of the Antibody-Antigen Complex from Freely Diffusible Antigen and Surface-Confined Antibody	154
4.2.4	Specific Experimental Conditions	159
4.2.4.1	Fitting of Experimental Data to Determine the Global Antigen Coverage Parameter	159
4.3	Results and Discussion	160
4.4	Conclusions	169

Chapter 5 **173**

Voltammetric Investigation of Electrochemical Immunoassays: Towards Combinatorial Sensing of Biomarker Analytes

5.1	Introduction	173
5.2	Results and Discussion	174
5.2.1	Electrode Characterisation	174
5.2.2	Ferrocene Labelled Anti-BNP Antibody Characterisation	180
5.2.3	Voltammetric Investigation of Fc-Ab-BNP Modified ITO	183
5.2.4	Preliminary Electrochemical Immunoassay Viability Investigation	186
5.3	Voltammetric Determination of the Pregnancy Biomarker β -hCG	195
5.4	Investigation into Immunoassay Multiplexing	203
5.4.1	Chlorpromazine as an Alternative Redox Tag	204
5.4.2	Ruthenium Dye as an Alternative Redox Tag	211
5.5	Conclusions	219

Chapter 6	222
Electroimmunoassay of TEMPO for Biomarker Detection <i>via</i> Spin Trap Adducts	
6.1 Introduction	222
6.2 Route 1 - TEMPO Specific	223
6.3 Route 2 - Biomarker Specific	224
6.4 Special Experimental Conditions	225
6.5 Experimental Results and Discussion	225
6.5.1 Calibration of the Sensor Response	230
6.6 Conclusions	231
Chapter 7 Overall Conclusions	232
Definitions	234

List of Tables

Table 1 Different types of CVD, adapted from ref. ⁴	22
Table 2 Symbols for the common proteinogenic amino acids, adapted from Jones, 1997 ref. ⁷	24
Table 3 Concentration of total hCG in serum samples from women with term pregnancies measured using the Siemens Immulite 1000 total hCG assay. Adapted from Cole, 2010 ref. ³⁵	30
Table 4 Concentration of total hCG in urine samples from women with term pregnancies measured using the Siemens Immulite 1000 total hCG assay. Adapted from Cole, 2010 ref. ³⁵	31
Table 5 Evaluation of 15 home pregnancy tests with regular hCG and H-hCG standards. Adapted with permission from ref. ⁶	37
Table 6 Typical daily urine excretions for a normal healthy individual, reproduced from reference ¹⁹⁴	63
Table 7 Chemical reagents	125
Table 8 Biochemical reagents	126
Table 9 Solvents	127
Table 10 Gases	127
Table 11 Resistance measurements for each individual defined electrode area of the ITO electrode.	175

List of Figures

Fig. 1 Schematic drawing of proBNP showing enzymatic cleavage into biologically active BNP and NT-proBNP. ¹³	25
Fig. 2 Cardiac troponin consisting troponin C (cTnC), troponin I (cTnI) and troponin T (cTnT), of which cTnT is highlighted in blue. ²¹	27
Fig. 3 Illustration of the degradation of hCG from initial secretion to leaving the body. Reproduced with permission from ref. ³⁹	33
Fig. 4 Illustration of the IgG structure detailing the areas of variability and constancy divided into domains. There is a variable (V) and constant (C) domain for each light chain (VL and CL) and one V and three C domains for each heavy chain (VH and VL). The paratope contains the antigen binding clefts. Reproduced with permission from ref ⁶⁸	39
Fig. 5 The three-dimensional structure of IgG can be depicted as a Y-shaped molecule. Each sphere represents an amino acid residue. The two light chains are shades of blue and the two heavy chains are shades of grey. Reproduced with permission from ref. ⁶⁸	40
Fig. 6 Possible orientations of IgG molecules on the surface. Light blue and light brown denote the two heavy chains, and royal blue and green denote the two light chains. Reprinted with permission from ref. ⁶⁹ Copyright (2006) American Chemical Society.....	40
Fig. 7 Schematic representation of Ab orientation attached via a molecular wire to show the effects of steric hindrance with variation in Ab orientation. (i) Randomly biotinylated Ab- β -hCG and (ii) Fab-hCG fragment monobiotinylated in the hinge region to control orientation of binding. (a) glass substrate, (b) gold deposition layer, (c) molecular wire/self assembled monolayer, (d) linker, (e ₁) randomly biotinylated Ab- β -hCG, (e ₂) controlled biotinylated Fab-hCG fragment, (f) hCG and (g) labelled Ab for detection. Reprinted with permission from ref. ⁷⁴ Copyright (2005) American Chemical Society.	41
Fig. 8 Example of a standard curves used to determine unknown TA-0910 (stable thyrotropin releasing hormone analogue) concentration in RIA. ⁸²	44
Fig. 9 Jablonski diagram describing the electronic levels of common organic molecules and possible transitions between different singlet and triplet states. Adapted with permission from ref. ⁴⁶	47

Fig. 10 Reaction mechanism for the chemiluminescent reaction of luminol.....	49
Fig. 11 Reaction coordinate diagrams for chemical excitation processes: $A + B =$ reactants; $C + D =$ products formed in ground states; $C^* + D =$ products formed with C in an excited state and D in the ground state; $\Delta H =$ energy available from the reaction according to the usual thermodynamic criteria; $\Delta H^* =$ activation energy for formation of products in the ground state; $\Delta H^{**} =$ activation energy for formation of one product in an excited state; $h\nu =$ energy necessary for the excitation $C \rightarrow C^*$. Reprinted with permission from Hercules (1969) Copyright (1969) American Chemical Society.	51
Fig. 12 Use of enzymes in various methods of colorimetric immunoassays. The enzyme is depicted as the orange circle attached to the antibody and always performs the same function, to convert a substrate to a coloured product. ¹⁴²	52
Fig. 13 The analytical response as a function of concentration, where a series of decreasing concentrations by one order of magnitude show a dramatic slowing of the analytical response with time.	60
Fig. 14 The analytical response as a function of Ab affinity at constant Ag concentration, where a slower rate of association, K_{on} by two orders of magnitude show a dramatic slowing of the analytical response with time.....	61
Fig. 15 Representation of (a) reduction and (b) oxidation process of species A in solution. Molecular orbitals of species A shown are the HOMO and the LUMO. The arrows illustrate the change energy of the electrons in the electrode where it is increasing and decreasing in (a) and (b) as a result of the application of a negative and positive potential respectively.	80
Fig. 16 Schematic example of three electrode set up for electrochemical experiments	87
Fig. 17 Simple Schematic of a Randles circuit involving the double layer capacitance, C_{dl} . R_c , R_s , R_{ct} and R_t are the resistances for counter electrode, solution, charge transfer processes and transport processes respectively, where R_{ct} and R_t amount to the faradaic discharge processes. The terms i_c and i_f are the currents produced by the non-faradaic capacitance charging of the double layer and the faradaic redox process respectively.	88
Fig. 18 Basic illustration of the potentiostat design. The current flows between the working and counter electrode where this current is converted to voltage by operational amplifier B, such that $U_{out} = -iR$. Operational amplifier A ensures no	

current flows through the reference electrode where the CE passes sufficient current to keep the reference potential constant. R_f is a feedback resistor.	89
Fig. 19 Proposed model of the double-layer region under conditions where anions are specifically adsorbed.	90
Fig. 20 Schematic illustration of the variation of the potential across the electrical double layer. ⁴	91
Fig. 21 Description of the transport and electron transfer processes that occur in our simple case.	92
Fig. 22 Pathway of a general electrode reaction involving adsorption of reactants. .	93
Fig. 23 Concentration profiles for species A (–) and B (–) during a potential-step experiment demonstrating the increase in diffusion layer at increasing time, t , where C_{bulk} and C_0 are the concentrations of electroactive species in the bulk solution and at the electrode surface respectively.	96
Fig. 24 Reaction profile for an electrode process showing the influence of potential. At potentials E_1 and E_2 ; reduction and oxidation are favoured respectively. At the equilibrium potential, E^0 , no net reaction takes place. ‡ denotes the transition state.	98
Fig. 25 (a) Effects of a positive potential change on the standard free energies of activation for oxidation and reduction. (b) Magnification of the boxed area in (a) mathematically illustrating the energy difference. Adapted from Bard, 1980, ref ²¹	100
Fig. 26 Born-Oppenheimer approximation for the electron transfer process.	101
Fig. 27 Schematic difference between adiabatic and non-adiabatic ET mechanisms.	102
Fig. 28 Marcus Theory of Electron Transfer for reaction of A and B . ΔG^\ddagger is the Gibbs activation energy to reach the transition state, λ is the reorganisation energy and ΔG^0 is the Gibbs energy change. In the solid line case, $\Delta G^0 = 0$, the dotted line case demonstrates the normal region where a change in the ΔG^0 is observed upon formation of B	104
Fig. 29 Schematic illustration of the two electron reduction of cyclooctatetraene demonstrating a slow reorganisation of the initial structure from tub shaped to planar.	104
Fig. 30 Dependence of the electron transfer rates on ΔG^0 . It is clear that the maximum rate of electron transfer occurs when the driving force is equal to the	

reorganization energy (activationless case). When the driving force becomes greater than the reorganization energy, we enter the Marcus inverted region.	106
Fig. 31 Plots of the potential energies of the reactant and product as a function of the nuclear (reaction) coordinate in the zeroth-order approximation depicting electron transfer in the normal (left) and inverted (right) Marcus regions. The activationless case where $\Delta G^\ddagger = 0$ is shown in the middle illustration. Adapted with permission from ref. ²⁶	107
Fig. 32 Potential–time excursion signal in a cyclic voltammetric experiment over three scans.	109
Fig. 33 Example of a cyclic voltammogram for a reversible process	109
Fig. 34 Cyclic voltammogram illustrating the peak shift beginning to occur, this will be amplified at higher scan rates.	111
Fig. 35 Plot showing the peak shifts and less refined peak shapes associated with an irreversible system.	112
Fig. 36 A typical square wave voltammogram carried out with a microdisk electrode. ³²	113
Fig. 37 Simulated CV data for an adsorbed species.....	115
Fig. 38 The variation of peak potential with scan rate demonstrates the dependency of Λ_s on scan rate where as $\Lambda_s \rightarrow 0$, the electrochemical system tends towards irreversibility with increasing scan rate.	118
Fig. 39 Principle of the silylation chemical linkage method.....	119
Fig. 40 Schematic illustration of (a) a glassy carbon/gold working electrode, ² (b) a gold microdisk electrode ³ and (c) Ag AgCl reference electrode. ⁴ Images reproduced with permission from Bioanalytical Systems Inc. Instrumentation Catalogues.	124
Fig. 41 A diagram of the ITO electrode prepared for these studies. Three electrode areas of 6 mm diameter were prepared with Fisherclark WS5002 self adhesive paper reinforcement rings (0.28 cm^2 determined using a travelling microscope and $\text{area} = \pi r^2$). One end of the ITO was used for electrical connection <i>via</i> application of copper tape.	128
Fig. 42 Illustration of the 4-nitrophenyl surface modification <i>via</i> (a) the one electron reduction process which leads to the formation of aryl radicals followed by (b) the reaction between the radicals and electrode to yield a modified surface.	129

Fig. 43 Illustration of the surface functionalisation consisting the 6 electron, 6 proton reduction process to afford the conversion of the nitro- group to the amine-functionality.	130
Fig. 44 Illustration depicting the synthesis of the ferrocene tagged antibodies, where step (a) describes the initial attachment of the ferrocene moiety and imine formation; (b) shows the conditions required for the subsequent conversion of the imine to the secondary amine to form the final stable tagged product. This representation shows depicts the attachment of only one ferrocene, in reality this reaction occurs at any available -NH ₂ functional group.	131
Fig. 45 Illustration of the ferrocene functionalised antibody modified electrode surface procedure, where the carboxy terminal of the antibody is first activated using sulfo-NHS and EDC before application to the electrode surface for subsequent coupling at 4°c over 18 hours.	132
Fig. 46 Mechanism for EDC/Sulfo-NHS activation step and subsequent attachment to the surface bound amine.	133
Fig. 47 Conversion of the terminal dimethyl amine to the carboxylic acid functionality required for the labelling procedure.	138
Fig. 48 Schematic breakdown of surface attachment procedure for the CPZ modified antibodies.	138
Fig. 49 (a) Cyclic voltammograms of Au/Ab-CK-Fc at scan rates 0.02, 0.05 V s ⁻¹ and with increments of 0.025 V s ⁻¹ thereafter up to 0.5 Vs ⁻¹ . Inset a: Variation of CV peak oxidation current with experimental timescale. (b) Cyclic voltammograms on Au/Ab-CD14-FITC-Fc (I) and Au/Ab-IL10-FITC-Fc (II) immunosensors. $\nu = 0.1 \text{ V s}^{-1}$. The concentrations of the antibodies for modification were <i>ca.</i> 100 mg mL ⁻¹ in (a) and 15 mg mL ⁻¹ in (b). Scans were all in 10 mM PBS-0.1 M NaCl solutions, pH 7.4. Reproduced with permission from Dou <i>et al.</i> , 2012.	146
Fig. 50 Cyclic voltammograms of Au/Ab-CK-Fc sensor in biological buffer. After incubation in 0 (solid line), 0.5 (dash-dot) and 2 ng mL ⁻¹ CK (dash line) for 15 min. Scan rate, 0.1 Vs ⁻¹ . Inset: square wave voltammograms corresponding to CV. All potentials are <i>vs.</i> Ag AgCl (3 M NaCl). Reproduced with permission from Dou <i>et al.</i> , 2012.	147
Fig. 51 (a) Peak current variances with test temperature on Au/Ab-CK-Fc (●, i_{pAb}), Au/Ab-CK-Fc-AG (○, i_{pAg}) electrodes and the peak current drop Δi_p (▪). (b) Creatine kinase sensor with incubation time. Error bars represent electrode-to-electrode	

standard deviation (*SD*) ($n = 3$). In (a), the incubation time with 2 ng mL^{-1} antigen was 15 min and 1, 2, 5, 10, and up to 45 minutes in (b), respectively. SWV experiments were carried out in pH 7.4, 10 mM PBS-0.1 M NaCl solutions. Reproduced with permission from Dou *et al.*, 2012. 148

Fig. 52 CK sensor in biological PBS (a) and in MKH perfusion solution (b). Incubation was 15 min at room temperature. Concentration of conjugated Ab-CK-Fc was $\sim 100 \text{ mg mL}^{-1}$ in (a) and $\sim 230 \text{ mg mL}^{-1}$ in (b). The solid line in (a) is drawn to show the linear range. (b) The CK concentrations for the incubation in the SWV were: 0.001, 0.005, 0.01, 0.05, 0.1, 0.2, 0.5, 1, 2, 4, 6 ng mL^{-1} . Inset b: Linear range, 0.005 to 6 ng mL^{-1} . Error bars represent electrode-to-electrode standard deviation ($n=3$) from different batches in (a) and the same batch in (b). Test temperature, 25°C . Note that in both (a) and the Inset b, the abscissa refers to the CK concentration (on a logarithmic scale). Reproduced with permission from Dou *et al.*, 2012. 149

Fig. 53 3D space filling models of immunoglobulin G (IgG) protein structure revealing lysine residues. The lysine (Lys) residues are highlighted in green.²⁹ 150

Fig. 54 Schematic illustration of the electroimmunoassay considered 151

Fig. 55 Cyclic voltammograms of ferrocene derivatives (1 mM in phosphate buffer) using a freshly polished gold electrode. $\nu = 0.1 \text{ V s}^{-1}$.³⁸ 161

Fig. 56 Voltammograms of the ferrocene-tagged antibody immobilised on an ITO electrode immersed in PBS over 10 scan cycles. See text for details. 162

Fig. 57 The simulation fitting profile where peak potential for the oxidation (E_p^{ox}) is plotted against scan rate, ν . Insert shows variable scan rate data for ITO bound Fc-Ab-hCG in 10 mM PBS, pH 7.4. 163

Fig. 58 Fractional surface blocking vs. incubation time for incubations of 15, 30 and 60 minutes with varying concentrations of hCG (100 pg mL^{-1} to $1 \text{ }\mu\text{g mL}^{-1}$) in 10 mM PBS buffer at pH 7. 164

Fig. 59 Frumkin isotherm analysis of the antigen-antibody interaction. 164

Fig. 60 Comparison of experiment with numerical theory (see text). 166

Fig. 61 Calibration chart for the sensor response (fractional antigen coverage, θ) to hCG incubation (100 pg mL^{-1} to $10/100 \text{ ng mL}^{-1}$) at 15, 30 and 60 minute periods in 10 mM PBS at pH 7. 167

Fig. 62 Interference tests carried out for 15 minute incubations of 1 ng mL^{-1} hCG with 20 mg mL^{-1} glucose (\bullet) ($n=2$). 168

Fig. 63 Interference tests carried out for 15 minute incubations of 1 mg mL ⁻¹ hCG with 1 mg mL ⁻¹ haemoglobin (×) (n=4).	169
Fig. 64 Cyclic voltammograms obtained for the one electron reduction of nitrobenzene onto the surface of an ITO electrode, $\nu = 0.1 \text{ V s}^{-1}$	177
Fig. 65 Schematic illustration of the electro-deposition process where (a) shows the monolayer formation of nitrobenzene as per scan 1 and (b), multilayer formation <i>via</i> attachment through the <i>ortho</i> position (scan 2).	178
Fig. 66 Cyclic voltammograms obtained for the electrochemical reduction of the nitrophenyl group to the nitro-aniline, $\nu = 0.1 \text{ V s}^{-1}$	178
Fig. 67 Possible differences in attachment site and end result functional groups....	179
Fig. 68 UV-vis spectrum for ferrocenecarboxaldehyde in DMF.	181
Fig. 69 Calibration of the ferrocenecarboxaldehyde over the concentration range 0.01 - 1 mg mL ⁻¹ in DMF.	181
Fig. 70 UV-vis spectra of ferrocene tagged anti-BNP antibodies.	182
Fig. 71 Calibration of the ferrocene labelled anti-BNP antibodies over the concentration range $2.83 \times 10^{-2} - 3.53 \times 10^{-3} \text{ mg mL}^{-1}$	183
Fig. 72 Cyclic voltammograms of Fc-Ab-BNP modified ITO electrode showing five consecutive scans, $\nu = 0.1 \text{ V s}^{-1}$	184
Fig. 73 Square wave voltammograms of Fc-Ab-BNP modified ITO electrode showing four consecutive scans, frequency = 25 Hz, amplitude = 1 mV.	185
Fig. 74 Baseline corrected square wave voltammograms for the scans shown above in Fig. 73.	186
Fig. 75 Cyclic voltammograms for the blank and subsequent 15 minute incubations of increasing concentration of BNP (10 pg mL ⁻¹ – 1 mg mL ⁻¹) to the Fc-Ab-BNP modified ITO.	187
Fig. 76 Calibration obtained for change in baseline corrected peak current with increasing concentration of BNP antigen for the ferrocene labelled anti-BNP modified ITO under cyclic voltammetry investigation. Linear response ranges 100 pg mL ⁻¹ to 1 mg mL ⁻¹ BNP (n=3).	188
Fig. 77 Square wave voltammograms for the blank (highest current) and subsequent 15 minute incubations of increasing concentration of BNP (10 pg mL ⁻¹ – 1 mg mL ⁻¹) to the Fc-Ab-BNP modified ITO.	189
Fig. 78 Calibration obtained for change in peak current with increasing concentration of BNP antigen for the ferrocene labelled anti-BNP modified ITO under square wave	

voltammetry investigation. Linear response ranges 10 pg mL^{-1} to 1 mg mL^{-1} BNP (n=3).....	190
Fig. 79 Baseline corrected square wave voltammograms for the blank (highest current) and subsequent 15 minute incubations of increasing concentration of BNP (10 pg mL^{-1} – 1 mg mL^{-1}) to the Fc-Ab-BNP modified ITO.	191
Fig. 80 Calibration obtained for the baseline corrected square wave data shown above. Linear response ranges 10 pg mL^{-1} to 1 mg mL^{-1} BNP (n=3).....	192
Fig. 81 Calibration of oxidative peak potential shift with increasing antigen concentration during cyclic voltammetry.....	193
Fig. 82 Calibration of oxidative peak potential shift with increasing antigen concentration during square wave voltammetry.	193
Fig. 83 Calibration of oxidative peak potential shift with increasing antigen concentration for the baseline corrected square wave voltammetry data.	194
Fig. 84 (a) Cyclic voltammetry of the Fc-Ab β -hCG modified ITO electrode over ten scan cycles. (b) Variable scan rate of the system where $\nu = 0.02 - 1 \text{ V s}^{-1}$ from bottom to top.	196
Fig. 85 Plot of E_p vs. $\log(\nu)$ illustrating the peak splitting with increasing scan rate. (O) denotes E_p^{ox} and (●) denotes E_p^{red}	197
Fig. 86 Plots of peak current versus scan rate and square root scan rate for variable scan rate investigations of the Fc-Ab- β -hCG modified ITO electrode (n=3) where (a) illustrates a plot of peak current data versus the scan rate as for surface confined systems and (b) shows plot of peak current data versus square root of the scan rate as for mass transport controlled systems. Here (O) and (●) denote i_p^{ox} and i_p^{red} respectively.	198
Fig. 87 Voltammograms for CV response of the Fc-Ab- β -hCG modified ITO to increasing concentration of β -hCG at 15 minute incubation time.	199
Fig. 88 Calibration plot of CV oxidative current response to β -hCG incubation. ...	200
Fig. 89 Calibration plot of CV oxidative peak potential response to β -hCG incubation.....	201
Fig. 90 Baseline corrected SWV response of a Fc-Ab- β -hCG modified ITO electrode to β -hCG incubations (100 pg mL^{-1} to $10 \text{ } \mu\text{g mL}^{-1}$) of 15 minutes.....	201
Fig. 91 Calibration plot of SWV oxidative peak potential response to β -hCG incubation.....	202

Fig. 92 Calibration plot of SWV oxidative current response to β -hCG incubation (100 pg mL ⁻¹ to 1 μ g mL ⁻¹).....	203
Fig. 93 Structure of chlorpromazine.	204
Fig. 94 Converted CPZ used for the labelling procedure.....	205
Fig. 95 Schematic breakdown of surface attachment procedure for the CPZ modified antibodies.	205
Fig. 96 Cyclic voltammetry of CPZ in 0.1 M KCl at scan rates 0.02 V s ⁻¹ to 1 V s ⁻¹ . ¹⁴	206
Fig. 97 Cyclic voltammograms for CPZ-Ab-BNP modified glassy carbon surface over a four scan cycle.....	207
Fig. 98 CV data for incubations of increasing concentration of BNP (1 pg mL ⁻¹ to 10 ng mL ⁻¹) to a CPZ-Ab-BNP modified glassy carbon electrode surface in 10 mM PBS.....	207
Fig. 99 Calibration for the baseline corrected cyclic voltammetry data. Data averaged over 3 sequential scans following incubation. Linear response ranges 1 pg mL ⁻¹ to 10 ng mL ⁻¹ BNP.	208
Fig. 100 SWV for CPZ-Ab-BNP modified glassy carbon surface in 10 mM PBS, scan 1 only.	209
Fig. 101 SWV data for incubations of increasing concentration of BNP (1 pg mL ⁻¹ to 10 ng mL ⁻¹) to a CPZ-Ab-BNP modified glassy carbon electrode surface in 10 mM PBS.....	209
Fig. 102 Baseline corrected SWV data for incubations of increasing concentration of BNP to a CPZ-Ab-BNP modified glassy carbon electrode surface.	210
Fig. 103 Calibration for the baseline corrected square wave voltammetry data. Data averaged over 3 sequential scans following incubation.	211
Fig. 104 Structure of N-3 dye	212
Fig. 105 Baseline cyclic voltammogram for electrode #1 in PBS with 0 [BNP] antigen added.	212
Fig. 106 Cyclic voltammograms of electrode response to BNP additions (1 fg mL ⁻¹ to 1 mg mL ⁻¹) for electrode 1. For clarity these are split into three charts to more clearly define the differences between each incubation scan. (a) illustrates the sensor response 1 fg mL ⁻¹ to 1 pg mL ⁻¹ incubation concentrations, (b) shows 10 pg mL ⁻¹ to 100 ng mL ⁻¹ , (c) 1 μ g mL ⁻¹ to 1 mg mL ⁻¹ and (d) all scans overlaid.....	214

Fig. 107 Calibration of the CV response across 1 fg mL ⁻¹ to 1 mg mL ⁻¹ BNP incubations (n=3).	215
Fig. 108 Calibration of the peak potential shift in response to incubation of BNP over the range 1 fg mL ⁻¹ to 1 mg mL ⁻¹ BNP incubations (n=3).....	216
Fig. 109 Baseline corrected square wave voltammograms for electrode 1 for (a) the concentration range of antigen incubation: 1 fg mL ⁻¹ to 1 ng mL ⁻¹ and (b) 1 ng mL ⁻¹ to 1 mg mL ⁻¹	217
Fig. 110 Calibration of the baseline corrected SWV response across 1 fg mL ⁻¹ to 1 mg mL ⁻¹ BNP incubations (n=3).....	218
Fig. 111 Calibration plot for the shift in SWV peak potential with increasing antigen concentration (n=3).	219
Fig. 112 Schematic illustration of the proposed routes for the detection of TEMPO. (a) demonstrates the case for route (1) wherein antibodies specific to the spin trap molecule TEMPO are immobilised to the surface and (b) antibodies specific to the target biomarker are immobilised to the surface.....	223
Fig. 113 Structures of DMPO, TEMPO and the TEMPO-biomolecule adduct.....	223
Fig. 114 Voltammetric comparison of 1 mM TEMPO in 10 mM PBS (-) and 0.1 M TBAP in MeCN (- -) at scan rates 0.02, 0.05, 0.075, 0.1, 0.2, 0.4, 0.75 and 1 V s ⁻¹	225
Fig. 115 Randles-Sevcik plot showing i_p vs. $\sqrt{v} / V s^{-1}$ for the oxidation and reduction processes of 1 mM TEMPO in MeCN (O) and PBS (□).	226
Fig. 116 Graph showing E_p vs $\log(v / V s^{-1})$ to assess the electrochemical reversibility of TEMPO (O) denotes MeCN and (□) denotes PBS.....	227
Fig. 117 Variable scan rate scans via cyclic voltammetry for an anti-DMPO modified ITO surface incubated with 1 mM TEMPO in PBS for one hour, $v = 0.02 - 1 V s^{-1}$	228
Fig. 118 Square wave voltammetry following 1 hour incubation with 1 mM TEMPO in PBS over three scans.....	228
Fig. 119 Randles-Sevcik and peak potential shift plots for the anti-DMPO modified surface response to 1h incubation with 1 mM TEMPO in PBS.....	229
Fig. 120 Average baseline corrected SWV response for 1, 10 and 100 μ M TEMPO 1h incubation to Ab-DMPO modified ITO, (n=2).....	230

Acknowledgements

I would like to thank Professor Stephen Atkin, Professor Eric Kilpatrick, Dr. Grahame Mackenzie, Dr. Thozkuhat Sathyapayan and Dr. Jay Wadhawan for all their helpful advice and support in developing the research that is reported herein.

I am grateful to BBSRC, Boots, HYMS and the Department of Chemistry at the University of Hull for enabling me to pursue postgraduate doctoral training.

The work presented in this thesis has greatly benefited from input from Kevin Wright, Laurence Bolder, Mark Piper, Sam Morris, and Dan Love. I am gratified to have had the opportunity to discuss and develop my research with these colleagues.

Most of all I am thankful to my partner Rachel, my family and my friends for their love and support throughout this entire experience, I really couldn't have done this without them.

Authors Declaration

I confirm that this work is original and that if any passage(s) or diagram(s) have been copied from academic papers, books, the internet or any other sources these are clearly identified by the use of quotation marks and the reference(s) is fully cited. I certify that, other than where indicated, this is my own work and does not breach the regulations of HYMS, the University of Hull or the University of York regarding plagiarism or academic conduct in examinations. I have read the HYMS Code of Practice on Academic Misconduct, and that this piece of work is my own and does not contain any unacknowledged work from any other sources.

Chapter 1

Clinical Biomarkers: A Brief Overview

1.1 Introduction to Biomarkers of Interest

This study is aimed at the detection of clinical biomarkers associated with cardiovascular and pregnancy. In these medical fields, biomarkers are considered of paramount importance in the detection, diagnosis, risk stratification or monitoring of various conditions and situations of clinical significance. The biomarkers of interest, their functions, and clinical implications in each case are respectively discussed below.

Biomarkers are described as a broad subcategory of medical signs. Classically these can range from changes in pulse and blood pressure to more complex laboratory tests of blood and other tissues. In collaboration with the United Nations and the International Labour Organization, the World Health Organisation (WHO) defined the term biomarker as “any substance, structure, or process that can be measured in the body or its products and influence or predict the incidence of outcome or disease”. When applied to clinical environments, biomarkers are by definition objective, quantifiable characteristics of biological processes wherein almost any measurement (functional, physiological, biochemical at the cellular level, or a molecular interaction) reflects an interaction between a biological system and a potential hazard (chemical, physical, or biological).¹ Typically, they are analytes only detectable in biological samples during or as a direct result of a particular physiological event or condition. They should also be thoroughly characterized and repeatedly shown to correctly predict relevant clinical outcomes across a variety of treatments and populations.

1.2 Cardiovascular Disease

Cardiovascular disease (CVD) is a collection of several conditions that act on the cardiovascular system, affecting an extraordinary number of people worldwide. In the present day, CVDs account for the greatest single cause of adult mortality globally.² Despite the vast efforts and important achievements in the prevention and treatment of such conditions in recent decades, approximately 17.3 million people

die from CVDs every year, representing 31% of all global deaths, a number that is expected to grow as high as 23.6 million by 2030.^{3,4}

In the United Kingdom alone, National Health Services (NHS) expenditure exceeded more than £6.8 billion on treating CVD in 2012/13. Extending this to include six European economies (France, Germany, Italy, Spain, Sweden and the UK): the estimated total costs to the economies attributed to CVD was €102.1 billion in 2014.⁵ With global populations ever rising, these costs will continue to rise.

There are several conditions that make up CVD, these are detailed in Table 1. These conditions may lead to more severe, potentially fatal cardiac conditions such as acute myocardial infarction (AMI), heart failure (HF), acute coronary syndromes (ACS) and thromboembolic events (TE).

Table 1 Different types of CVD, adapted from ref. ⁴

CVDs: due to atherosclerosis	Other CVDs
ischaemic heart disease or coronary artery disease (e.g. heart attack)	congenital heart disease
cerebrovascular disease (e.g. stroke)	rheumatic heart disease
diseases of the aorta and arteries, including hypertension and peripheral vascular disease.	cardiomyopathies
	cardiac arrhythmias.

There are two common routes to determine the presence of CVDs, an abnormal electrocardiogram (ECG) or elevated cardiac biomarkers. The association of specific cardiac biomarkers to certain conditions or cardiac event, invites the potential to rapidly, accurately and specifically define the type of CVD or cardiac event in a patient, offering early detection and subsequent correct treatment, thus improving survival rates of these devastating conditions and reducing the costs incurred to our economies and healthcare infrastructures. Consequently, there has been intense research efforts over recent decades focused on achieving this, with significant advancements already made (see section 1.2.1.2).

1.2.1 Biomarkers of Cardiac Injury

Further to the earlier definition of biomarkers, cardiac biomarkers may be defined as biological analytes that are detectable in the bloodstream at elevated levels during the incidence of CVD or in the immediate outcome of myocardial damage. Characteristically, the ideal cardiac biomarkers should be highly specific for cardiac tissue, absent from other non-myocardial tissues and easily accessible to achieve high diagnostic sensitivity. The biomarkers of interest in this thesis are discussed below.

1.2.1.1 Brain Natriuretic Peptides

Brain natriuretic peptide (BNP) and N-terminal pro-B-type natriuretic peptide are well known markers for congestive heart failure (CHF) in serum and are routinely used in the clinical environment to both diagnose and monitor the severity of heart failure.²

BNP and NT-proBNP have gained significant interest in the last 20 years (BNP was originally identified in extracts of pig brain in 1988). It is present in the human brain, but there is considerably more in the cardiac tissue, particularly the ventricles where the protein is secreted in response to excessive constriction of the heart muscles, lending BNP clinical utility as a cardiovascular biomarker.⁶

Human pro-brain natriuretic peptide (ProBNP) contains 108 amino acids and is the polypeptide precursor to BNP. The amino acid sequence may be shortened by two conventions: the three-letter and one-letter symbol forms. Each respective amino acid has its own three letter symbol derived from its formal name and begin with the initial letter. The one letter convention is most commonly used for the presentation of sequence data, Table 2 below lists the standard symbols for the coded amino acids.⁷ The amino acid sequence code of BNP, NT-proBNP and proBNP by one-letter symbol convention is shown in Fig. 1.

ProBNP is stored in secretory granules in both ventricles and, to a lesser extent, in the atria. It is secreted into the circulatory system by the ventricular myocytes in response to pressure overload, volume expansion, and increase in myocardial wall stress that may result in myocardial stretch.⁸ ProBNP is then cleaved to the 76-

peptide, biologically inert N-terminal fragment (NT-proBNP, 8.457 kDa) and the 32-peptide, biologically active hormone BNP (3.456 kDa) in equimolar amounts.⁹ Both of these markers and have been clinically evaluated for use in the diagnosis and management of CHF.⁸

Table 2 Symbols for the common proteinogenic amino acids, adapted from Jones, 1997 ref. ⁷

Three-letter Symbol	Amino Acid	One-letter symbol
Ala	Alanine	A
Arg	Arginine	R
Asn	Asparagine	N
Asp	Aspartic acid	D
Cys	Cysteine	C
Gln	Glutamine	Q
Glu	Glutamic acid	E
Gly	Glycine	G
His	Histidine	H
Ile	Isoleucine	I
Leu	Leucine	L
Lys	Lysine	K
Met	Methionine	M
Phe	Phenylalanine	F
Pro	Proline	P
Ser	Serine	S
Thr	Threonine	T
Trp	Tryptophan	W
Tyr	Tyrosine	Y
Val	Valine	V

NT-proBNP and BNP circulate in the plasma, and concentrations are high in patients diagnosed with left ventricular dysfunction and heart failure.¹⁰ Once in the circulation, BNP has natriuretic, diuretic, and vasodilatory effects on the internal

climate.¹⁰ Both markers show a comparable clinical utility for assessing cardiac impairment and are well-established markers of heart failure in the general population.^{11, 12, 38}

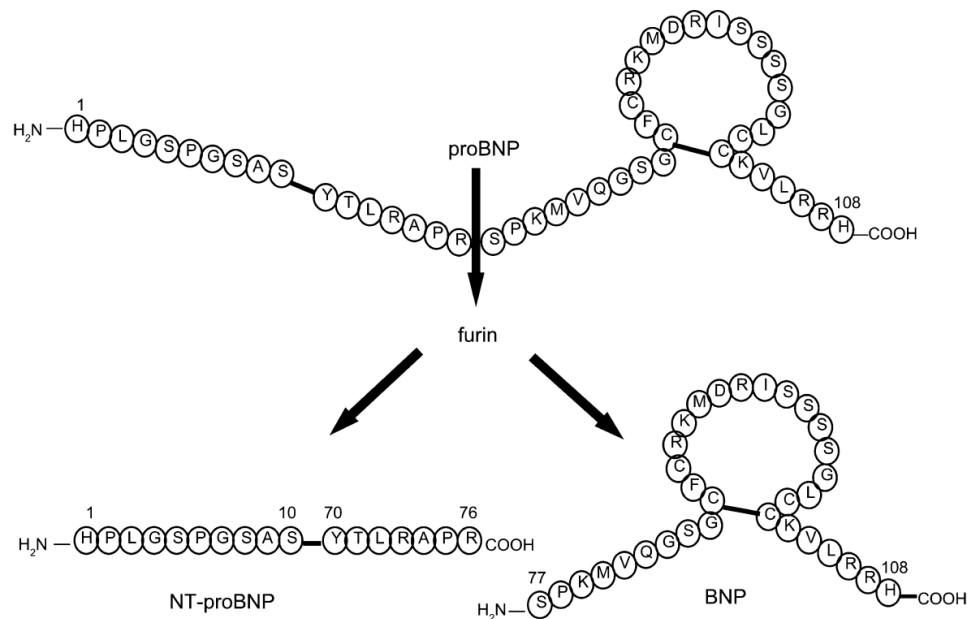


Fig. 1 Schematic drawing of proBNP showing enzymatic cleavage into biologically active BNP and NT-proBNP.¹³

Heart failure and acute myocardial infarction are classified as a major worldwide health issue with more than 15 million patients suffering heart failure in North America and Europe alone, with approximately 1.5 million new cases arising every year.¹⁴⁻¹⁶ Therefore, the development of fast, portable and highly sensitive measuring systems specific to B-type natriuretic peptide is greatly desired in clinical laboratories for the determination of BNP in clinical samples. The blood BNP levels are extremely low in normal healthy conditions, *ca.* 20 pg mL⁻¹, however they may elevate to >2 ng mL⁻¹ for patients diagnosed with severe congestive heart failure.^{11, 17}

1.2.1.2 Methods for Sensing BNP

In 1993, Shionogi (Osaka, Japan) introduced the first commercial assay for BNP. First-generation assays for BNP were competitive radioimmunoassays that required extraction and purification of the plasma sample but were not widely used in the clinical environment due to radiation issues. Second-generation assays were based on monoclonal antibodies with radioisotope labels that provided improved sensitivity and precision over that of first generation assays. Commercial versions of the

monoclonal antibody assay first appeared in 1994 and initially required 12-36 hours to complete.⁸

Third-generation assays, which provided results in as little as 15 minutes, became available in 2000. All of the assays for BNP and NT-proBNP that are currently commercially available for clinical use in the United States at least, are rapid immunoassays. The assay used in the Breathing Not Properly study⁸, which first suggested clinically useful BNP cut-off values for diagnosing acute CHF, was the point-of-care Triage BNP Test (Biosite Diagnostics Inc; San Diego, CA) approved by the US Food and Drug Administration (FDA) in 2001. This test is a fluorescence immunoassay for the quantitative determination of BNP in EDTA-anticoagulated whole blood and plasma specimens. The method requires at least 2 mL of sample and has a turnaround time of less than 60 minutes with a linear detection range between 20 and 1300 pg mL⁻¹, and a LOD of 20 pg mL⁻¹.¹⁸ Other manufacturers also market rapid-turnaround BNP assays, including the ADVIA Centaur BNP assay (Bayer HealthCare Diagnostics; Tarrytown, NY) with LOD = 2 pg mL⁻¹ and the AxSYM BNP assay (Abbott Diagnostics; Abbott Park, IL) with LOD = 15 pg mL⁻¹.¹⁹

Assays for the NT-proBNP fragment became available in late 2002. The EI70 NT-proBNP assay (Roche Diagnostics; Indianapolis, IN) with LOD = 5 pg mL⁻¹ was evaluated in the ProBNP Investigation of Dyspnea in the Emergency Department (PRIDE) study. Other NT-proBNP assays include the Dimension test and the Stratus CS Acute Care NT-proBNP assays (Dade Behring Inc; Deerfield, IL).

The limitation of these systems, though vastly improved over previous generation sensors, is the turnaround time. In the cases of patients exhibiting symptoms of chest pain or heart issues upon admission to A&E and those whom are unresponsive after being brought into hospital with suspected heart problems, diagnosis is required quickly and accurately for the correct decisions to be made with regards to treatment of heart failure, one hour is simply too long to wait.

1.2.1.3 Troponin T

Similar to BNP, troponin T (TnT) is a highly sensitive biomarker of myocardial injury. It is commonly used to diagnose and predict the near-, mid- and even long-term outcomes of patients with acute coronary syndrome (ACS), most frequently

non–ST–segment–elevation myocardial infarction (NSTEMI). The detection and regular monitoring of TnT concentration is useful for risk stratification and aiding of decisions over coronary interventions in patients suffering acute coronary symptoms.²⁰

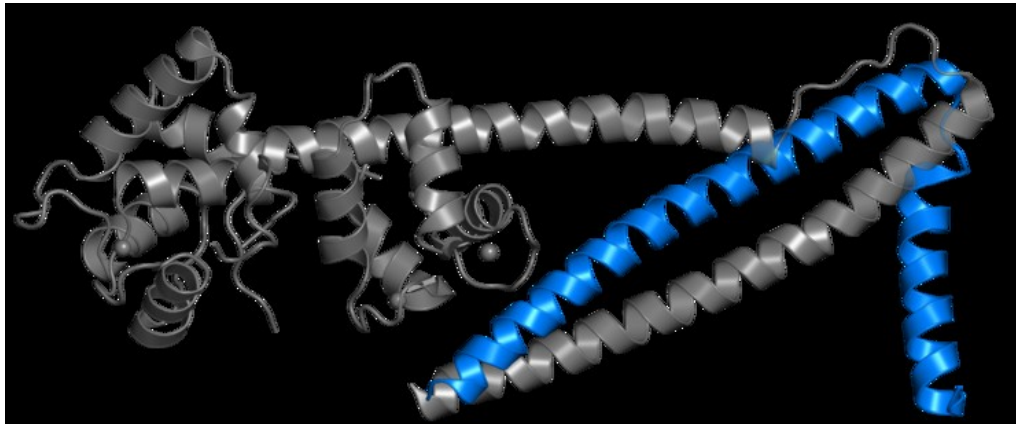


Fig. 2 Cardiac troponin consisting troponin C (cTnC), troponin I (cTnI) and troponin T (cTnT), of which cTnT is highlighted in blue.²¹

TnT is a contractile function component present in all striated muscle. Cardiac troponin (cTnT, molecular weight 39.7 kDa) however originates exclusively from the myocardium, differing from skeletal muscle TnT. Consequently, due to the very high tissue-specificity cTnT is a highly sensitive marker for myocardial damage.²² Following the onset of acute myocardial infarction (AMI), the blood concentration of cTnT increases over approximately 3-4 hours and may persist up for up to 2 weeks thereafter.^{23, 24}

On the other hand, low concentrations of cTnT can be detected in clinically stable patients, offering diagnostic value in patients such as those with ischemic or non-ischemic heart failure,²⁵ patients with different forms of cardiomyopathy, renal failure, sepsis and diabetes.^{26, 27} Furthermore, elevated levels of cTnT correlate with the severity of coronary artery disease.²⁸

According to the most recent universal definition of myocardial infarction, MI is diagnosed when the blood concentration of cTnT are above the 99th percentile of the reference limit (of a healthy population) together with evidence of myocardial ischemia (symptoms, ECG changes or imaging results).

1.2.1.4 Methods for cTnT sensing

Immunosensors with potential for point-of-care testing for cTnT are highly desirable, since these devices can be applied to cardiology emergencies, allowing a rapid screen of the patients and consequently the best clinical management. The quantitative clinical detection of cTnT requires that the assay used possesses an imprecision (coefficient of variation) at the 99th percentile less than or equal to²⁵ 10%.

There are numerous routes currently available for the clinical detection of cTnT, where the recent introduction of high-sensitivity cardiac troponin T (hs-cTnT) assay from Roche Diagnostics has lowered the diagnostic threshold to the 99th cTnT percentile of 0.014 ng mL^{-1} at turnaround times as low as 20 minutes.²² The introduction of these assays has made a tremendous impact on the screening of patients presenting cardiac-related symptoms, significantly reducing turnaround times when compared to previous technologies such as ELISA (4-6 hours).

Despite the significant advantages of these new high sensitivity assays, they are still lab based, hence requiring trained staff and involve the complex steps implicated in sandwich immunoassays. The need for a truly point of care device, that could potentially be intricately linked to cardiology equipment or as a handheld device for rapid (<20 mins) bed-side assessment has not yet been achieved and is still highly desired.

1.3 Pregnancy

The early determination of pregnancy and approximate gestational age is extremely important for female patients in various clinical settings such as Accident and Emergency and wards. The accurate exclusion of pregnancy is compulsory preceding medical interventions, for instance surgery, chemotherapy and abdominal X-ray in order to minimise or avoid health risks to the unborn child and/or patient.²⁹ The detection of biomarkers in easily accessible fluids such as urine and blood may facilitate the rapid, accurate determination of pregnancy. Furthermore, the detection of biomarkers in pregnancy may allow regular monitoring of hormone levels in order to identify the progression of the pregnancy and indicate any potential issues that may arise, such as ectopic pregnancies, spontaneous abortion and even the

occurrence of conditions such as Down's or Edwards syndromes, all at the point of care.

The current healthcare system is deficient of reliable, portable and quantitatively validated point of care (POC) routes for the rapid diagnosis of pregnancy in urine,^{29, 30} relying on qualitative, poor accuracy urine 'wand' testing or complicated, labour intensive and lengthy (4 - 6 hour) lab based assay methods unsuitable for point of care testing methodologies, where rapid quantitative data is commonly required.^{31, 32}

1.3.1 Biomarkers of Pregnancy

1.3.1.1 Human Chorionic Gonadotropin

Human chorionic gonadotropin (hCG) and its beta subunit beta hCG (β -hCG) have been used commercially as biomarkers for the confirmation of pregnancy since 1977, where the first home urine test became available (Crane, 1968). With abortion made legal in the USA in 1973 (Roe v. Wade, 1973), this market quickly expanded where the first "one step" test, Clearblue Easy, (Unilever, 1988) was released. This product revolutionised pregnancy testing into the "Wand Era" that became the most common way to test for pregnancy in the modern world today, where there are numerous tests available.

The one letter sequence of hCG is as follows:

(NH₂-)APDVQDCPECTLQENPFFSQPGAPILQCMGCCFSRAYPTPLRSKKTML
VQKNVTSESTCCVAKSYNRVTVMGGFKVENHTACHCSTCYHKSKEPLRP
RCRPINATLAVEKEGCPVCITVNTTICAGYCPTMTRVLQGVLPALPQVVCNY
RDVRFESIRLPGCPRGVNPVVSYAVALSCQCALCRRSTTDCGGPKDHPLTCD
DPRFQDSSSSKAPPPSLPSPRLPGPSDTPILPQ(-COOH)).³³ It is a 36.7 kDa glycoprotein hormone that is produced primarily by trophoblast tissue, a group of specialized cells of the placenta that play an important role in embryo implantation and interaction with the decidualised maternal uterus in pregnancy. There are many physiological functions of hCG during pregnancy including promoting the growth of the uterus in line with the growth of the fetus, stimulating progesterone production and many others roles.³⁴ hCG is the primary marker used to confirm pregnancy currently employed in serum and urine pregnancy tests. The typical levels of this

marker range significantly with gestational age in both serum and urine, as shown in Table 3 and Table 4.

Table 3 Concentration of total hCG in serum samples from women with term pregnancies measured using the Siemens Immulite 1000 total hCG assay. Adapted from Cole, 2010 ref. ³⁵

Gestational Age (weeks since start of menstrual period)	N	Median Total hCG / ng mL ⁻¹
3 weeks - 3 weeks 6 days	42	0.26 (16 of 42 <0.1)
4 weeks - 4 weeks 6 days	42	3.4
5 weeks - 5 weeks 6 days	67	65
6 weeks - 6 weeks 6 days	33	252
7 weeks - 7 weeks 6 days	30	3,278
8 weeks - 8 weeks 6 days	33	4,331
9 weeks - 9 weeks 6 days	24	5,832
10 weeks - 10 weeks 6 days	20	10,352
11 weeks - 13 weeks 6 days	41	5,953
14 weeks - 17 weeks 6 days	57	2,934
18 weeks - 26 weeks 6 days	62	1,931
27 weeks - 40 weeks 6 days	49	1,911

Clinically, the hCG concentration in serum or urine is referred to in milli-international units per millilitre (mIU mL⁻¹). **The unit conversion for hCG concentration ng mL⁻¹ to mIU mL⁻¹ is 1 ng mL⁻¹ to 9.3 mIU mL⁻¹, as described by the WHO First International Reference Preparation standards.**³⁶ These two unit terms may be used interchangeably throughout this thesis.

Intact hCG is composed of two dissimilar subunits, α and β , joined non-covalently. The α -subunit of hCG (14.5 kDa, one letter sequence:

(N-)APDVQDCPECTLQENPFFSQPGAPILQCMGCCFSRAYPTPLRSKKTMLVQ
KNVTSESTCCVAKSYNRVTVMGGFKVENHTACHCSTCYHKS(-COOH))³³

is similar to that of the pituitary glycoprotein hormones, composed of 92 amino acids

linked by five disulfide bridges with two N-linked oligosaccharide side chains, attached at amino acid residues 52 and 78.³⁷ The β -subunit (22.2 kDa, one letter code:

(NH₂-)SKEPLRPRCRPINATLAVEKEGCPVCITVNTTICAGYCPTMTRVLQGVL
PALPQVVCNYRDVRFESIRLPGCPRGVNPVVSYAVALSCQCALCRRSTTDCG
GPKDHPLTCDDPRFQDSSSSKAPPPSLPSPSRLPGPSDTPILPQ(-COOH)).³³

Table 4 Concentration of total hCG in urine samples from women with term pregnancies measured using the Siemens Immulite 1000 total hCG assay. Adapted from Cole, 2010 ref. ³⁵

Gestational Age (weeks since start of menstrual period)	N	Median Total hCG / ng mL ⁻¹
3 weeks - 3 weeks 6 days	574	0.24 (255 of 574 <0.1)
4 weeks - 4 weeks 6 days	574	21.7 (20 of 574 <0.1)
5 weeks - 5 weeks 6 days	574	301.2
6 weeks - 6 weeks 6 days	574	1,472
7 weeks - 7 weeks 6 days	574	4,795
8 weeks - 8 weeks 6 days	574	6,813
9 weeks - 9 weeks 6 days	65	8,869
10 weeks - 10 weeks 6 days	45	9,864
11 weeks - 13 weeks 6 days	74	1,984
14 weeks - 17 weeks 6 days	494	768.8
18 weeks - 26 weeks 6 days	74	506.3
27 weeks - 40 weeks 6 days	50	522.4

This fragment is unique and distinguishes hCG from the other glycoprotein hormones. It closely resembles the β -subunit of luteinizing hormone (LH), the two being identical in 97 of 121 amino acids, however β -hCG differs in its unique serine- and proline-rich, extended carboxyl-terminal (C-terminal) peptide (24 amino acids). It is composed of 145 amino acids linked by six disulphide bridges and contains two

N-linked oligosaccharide side chains attached to residues 13 and 30. It also has four O-linked oligosaccharide units, located in the C-terminal extension (residues 122 to 145). Since LH is so similar to hCG it is important to define the differences in physiological roles. LH is responsible for triggering ovulation and initiating the conversion of the residual follicle into a corpus luteum. This initiates production of progesterone and estradiol to prepare the endometrium (inner mucous membrane of the uterus) for possible embryo implantation. LH is necessary to maintain luteal function (preparation of the lining) for the first two weeks of the menstrual cycle. If pregnancy occurs, LH levels will decrease and luteal function will instead be maintained by the action of hCG however, if no pregnancy occurs the lining is shed at menstruation.³⁸

A hyperglycosylated form of hCG (hCG-H) also exists that has the same polypeptide structure as hCG, though with much larger N- and O-linked oligosaccharides. The oligosaccharides increase the molecular weight of hCG from 36-37 kDa up to 40-41 kDa, depending on the extent of hyperglycosylation. The molecule is independent to hCG with separate biological functions such as the growth of cytotrophoblast cells for placental implantation in pregnancy as well as promotion of trophoblast invasion during choriocarcinoma cancers.³⁴

All of the forms of hCG discussed above are present at various stages following secretion, as the whole hCG protein is degraded in circulation. A two-dimensional representation of the structure of hCG, its degraded counterparts and their excretion pathways is illustrated in Fig. 3.

The serum and urine concentration of biologically active hCG rise exponentially in the first trimester of pregnancy to a peak at about tenth weeks of gestation. Concentrations decrease from the tenth to the sixteenth week of gestation.^{37, 39} The clinical utility of hCG includes the determination of early pregnancy, ectopic pregnancies (in combination with progesterone), miscarriages, threatened abortions, preeclampsia, detection of premature rupture of the membranes (measurement in vaginal fluid) and risk calculations for trisomy-21 (Down's Syndrome) and trisomy-18 (Edward's syndrome). Cole³⁹ highlights the importance of measuring multiple forms of hCG and β subunit depending on the clinical context.

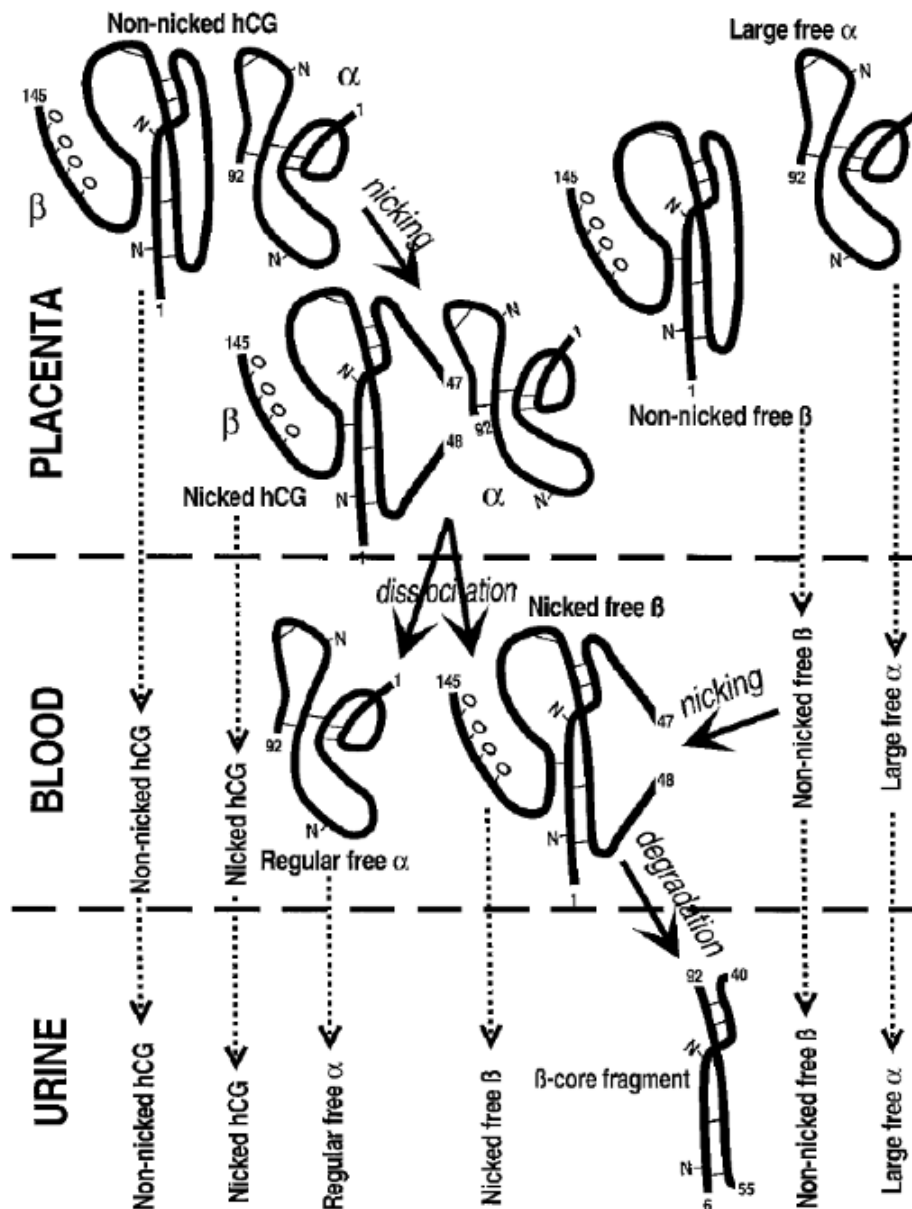


Fig. 3 Illustration of the degradation of hCG from initial secretion to leaving the body. Reproduced with permission from ref.³⁹

Recent studies have showed a significant increase in the level of free β -hCG subunit in trisomy 21 cases as compared with controls. It was found the combination of maternal serum α -fetoprotein and the human free β -hCG is useful in the prenatal detection of trisomy 21.⁴⁰ Free β -hCG measurements have also proved to be useful in the diagnosis and management of trophoblast diseases such as choriocarcinoma,⁴¹ in an indication as a tumour marker for testicular cancer⁴² and possibly other malignancies.^{43, 44}

The diagnosis of ectopic pregnancies is currently of great interest in the clinical environment. An ectopic pregnancy is the implantation of the fertilized ovum outside of the uterine cavity, most commonly into the fallopian tubes. There is a 1-2% incidence of ectopic implantation occurring in all pregnancies in the developed world, resulting in 10-13% of all pregnancy-related deaths.^{45, 46} In the UK, around 10 000 ectopic pregnancies are diagnosed annually with an incidence rate of 11.1/1000 pregnancies.⁴⁷ The diagnosis of an ectopic pregnancy is usually made by ultrasound scan alone however this is not always effective; it is complemented with serum β -hCG analysis.⁴⁸

In 1975, the WHO released three hCG preparations, the First International Reference Preparation (First IRP) 75/735, prepared by Professor Canfield and Professor Birken from Columbia University, USA, contained intact and nicked hCG in a 9:1 ratio. In 1986, the First IRP changed status to become the Third International Standard (Third IS) for hCG. The Third IS (WHO code: 75/537) and Fourth IS (WHO code: 75/589) have been widely used throughout the world for calibrating and testing all laboratory hCG tests and point of care hCG assays for more than 20 years. As stated for whole hCG, clinical results are expressed in biological units; international units per litre (IU L⁻¹ or mIU mL⁻¹). **The equivalence of 1 mIU mL⁻¹ of free β -hCG = 1 ng mL⁻¹ in terms of the WHO First IRP of chorionic gonadotropin beta subunit human, code: 75/551.**⁴⁹

The WHO has now established a new standard to include six of the most clinically useful hCG forms calibrated on a molar basis so that measurement of hCG and degradation products is completely compatible and comparable.⁵⁰ The six preparations of the new First Reference Reagents and have the following codes: hCG 99/688, hCGbeta 99/650, hCGalpha 99/720, hCGn 99/642 (nicked), hCGbetan 99/692 (nicked), and hCGbeta_{cf} 99/708 (fragment) and now serve as the current standard for immunoassays. However many laboratories and manufacturers have refrained from adopting these new standards because they are calibrated on a molar basis, not mIU mL⁻¹.

1.3.1.2 Methods for hCG Sensing

The measurement of hCG is most widely used to detect and monitor early pregnancy through one of seven common antibody combinations designed to detect specific full, free or degraded fragmented molecules related to hCG,⁵¹ and only few methods are specific for free β -hCG.³⁹ Most qualitative assays are designed to detect the intact hCG heterodimer.⁵²

These assays are most commonly chromatogenic sandwich type immunoassays. operating *via* the immobilisation of a capture antibody specific to distinct epitopes on the alpha or beta subunits in a translucent line in the result window; the secondary “signal” antibody is specific the opposite subunit to the capture antibody and is labelled with a blue or red dye or gold matrix dye. Once mixing occurs with the serum or urine, hCG present in the sample is captured and the resulting hCG-dye antibody complex becomes immobilized by the action of the capture antibody upon reaching the results window. A positive result is indicated by a coloured line formed at this point by the immobilized antibody-hCG-dye antibody complex.⁵³ This yields a user friendly, rapid measurement, however this approach merely provides the user with a qualitative 'yes' or 'no' answer, dependent upon the sensitivity of the test. The severe disadvantages and inherent limitation with this detection method is the lack of quantitative data, when coupled with significant variances in sensitivity and selectivity entertains the possibility of false positive readings. Table 5 demonstrates the considerable variances in home pregnancy testing systems.

Further to these findings, other commercially available urine pregnancy tests including the Siemens Clinitest, Inverness Accreava hCG Basic II and both the Mainline Maxie and Confirm hCG tests have been reported to have poorly detected hyperglycosylated hCG relative to regular hCG. Only the Quidel QuickVue and the Beckman Coulter Icon 25 tests equally detect regular and hyperglycosylated hCG. In addition, it was found that no POC tests were sensitive for detecting free β -hCG or β -core fragment, and no over-the-counter test detects β -core fragment.⁵³

On the whole, these qualitative tests are subject to several erroneous issues including false-negative results due to dilute urine, operator error, high dose hook effect, and hCG variant effects.^{54, 55} In 2012, Cole⁵⁶ voiced the opinion that out of all hCG tests commercially available, only one POC test, the Beckman-Coulter Icon 25, and one

brand of over-the-counter device, First Response, are suitable for early pregnancy detection. This further expresses the need for reliable, quantitative detection of hCG.

On the other hand, automated lab assays are available which offer quantitative detection of hCG in serum or urine though this comes at the cost of significantly longer assay times, the requirement for skilled personnel and increased experimental and equipment running costs. The turnaround times for these lab assays averages 4-6 hours though can take longer in hospital settings where several steps are involved; sample acquisition, labelling, transport, analysis and determination of results. Cole's view was that just one automated assay, the Siemens Immulite was suitable for early pregnancy detection in serum,⁵⁶ which operates at a minimum 42 minute analysis time,⁵⁷ not including sample preparation to obtain the serum.

The disadvantage of these systems is clear when in a scenario such as the arrival of an unconscious female patient into A&E who requires immediate abdominal X-ray or surgery; the hospital practice must ensure the presence or absence of a pregnancy before medical intervention. Quantitative information in this setting is invaluable to the determination of pregnancy, where a much more informed decision can be made as to the treatment route to pursue in the case of a confirmed pregnancy. This is imperative to better protect the best interests of the patient and the unborn child.

A discussion of biosensors follows, including a more in-depth study of immunological bio-recognition interactions and how common sensing methodologies utilise this natural phenomenon for biosensing applications.

Table 5 Evaluation of 15 home pregnancy tests with regular hCG and H-hCG standards. Adapted with permission from ref.⁶

Device	Read taken / min	Regular hCG / mIU mL ⁻¹				H-hCG / mIU mL ⁻¹				Manufacturer hCG limit / mIU mL ⁻¹
		6.3	13	25	50	6.3	13	25	50	
Clear Blue Easy	1	+	+	++	++	-	-	+	+	50
Target Early Pregnancy Test	5	±	+	+	++	-	-	-	-	50
American Fare Easy to Read	3	-	+	++	++	-	+	+	+	100
First Response Early Result	3	-	+	+	++	-	-	+	++	~50
E.P.T.	3	-	-	+	++	-	+	++	++	40
Answer	2	-	-	+	++	-	-	±	+	100
Fact Plus Pro	3	-	-	±	±	-	-	+	+	100
Fact Plus Select	3	-	-	+	+	-	-	+	+	100
Equate	1	-	-	+	+	-	-	-	+	25
Walgreens E.P.T.	5	-	-	±	++	-	-	-	±	100
Walgreens One Step	3	-	-	+	++	-	-	-	+	50
Inverness Medical E.P.T.	3	-	-	+	++	-	-	-	-	100
Longs Pregnancy Test	3	-	-	+	+	-	-	-	-	100
Rite Aid One Step	3	-	-	+	++	-	-	-	-	50
Confirm	2	-	-	-	+	-	+	+	+	25

1.4 Biosensing Methods for Biomarkers

1.4.1 Biosensors

Biosensors are analytical devices that integrate a biological recognition component within or connected to a suitable transducer capable of converting the biological event into an observable, measurable signal or readout. The common outcome of this is an electronic signal proportional to the concentration of a specific analyte. If the recognition component is an antibody, the biosensor is classified as an immunosensor. Further classification of immunosensors depends on the chosen transducer for example, optical,⁵⁸⁻⁶⁰ piezoelectric,⁶¹⁻⁶³ electrochemical,^{64, 65} and micromechanical.⁶⁶

It is clear that the immunoassay technique is the most common route for detection of the analytes described above, therefore this technique was chosen as the basis of the research carried out in this thesis. The fundamental theory and operation of immunoassays is described below.

1.4.2 Immunoassays

Immunoassays are fundamentally simple bioanalytical techniques for the quantitative or qualitative detection of an analyte that come in many different forms though the common operational feature between them is the use of antibodies (Ab) specific to a corresponding antigen (Ag) to form an immuno-complex.



1.4.2.1 Antibodies

Antibodies themselves are glycoprotein structures the most common of which are known as immunoglobulins (IgG) and are synthesised by mammals in response to a foreign entity, the antigen. IgG proteins have a four chain structure as their basic unit composed of two identical heavy chains and two identical light chains made up of ~450 polypeptide residues and the light chains with ~215 polypeptide residues respectively, linked by a disulphide bonds and non-covalent interactions.⁶⁷ Within these chains there are a further two main structural and functional regions; the Fab

region (fragment of antigen binding) consisting two fragments and the Fc region (fragment crystallisable) consisting one fragment.

The Fab region is situated at the paratope of the Ab and contains the variable domain responsible for Ag binding and specificity. The Fc region is involved in binding specific proteins to induce immune responses *via* interaction with certain Fc receptors and is a region of constant structure.

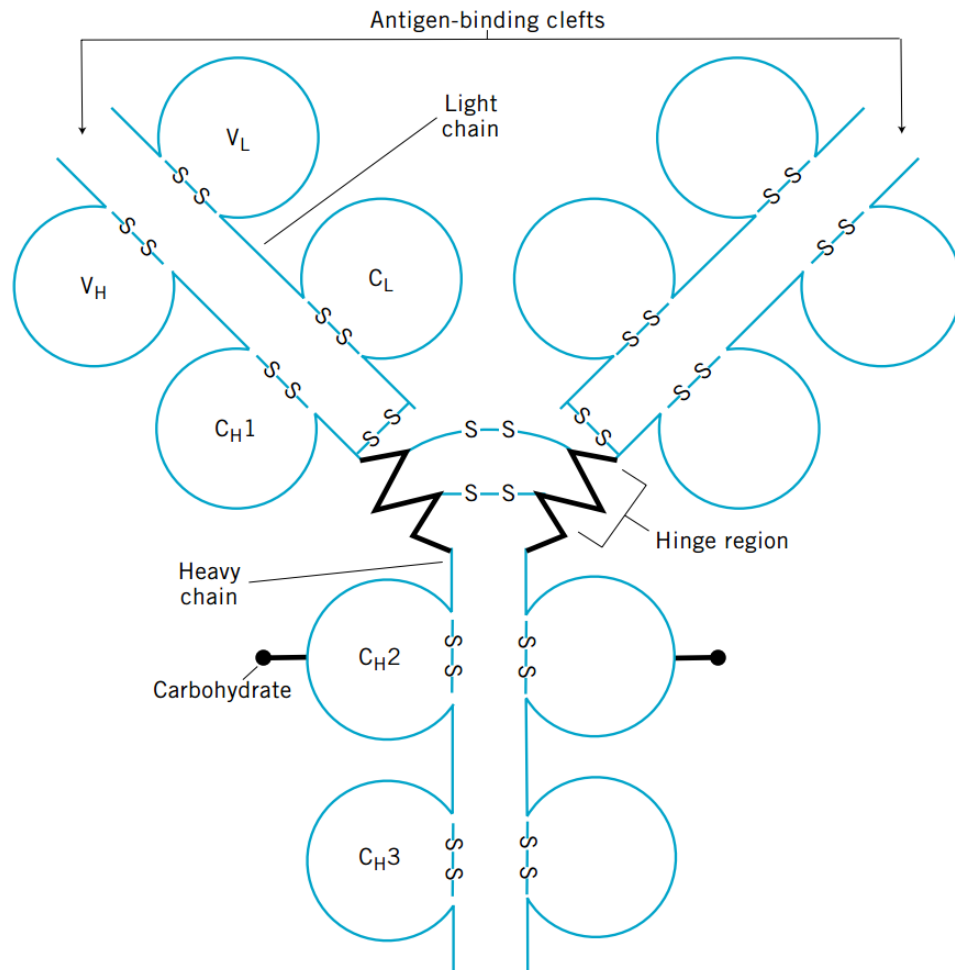


Fig. 4 Illustration of the IgG structure detailing the areas of variability and constancy divided into domains. There is a variable (V) and constant (C) domain for each light chain (V_L and C_L) and one V and three C domains for each heavy chain (V_H and C_H1, C_H2, and C_H3). The paratope contains the antigen binding clefts. Reproduced with permission from ref⁶⁸.

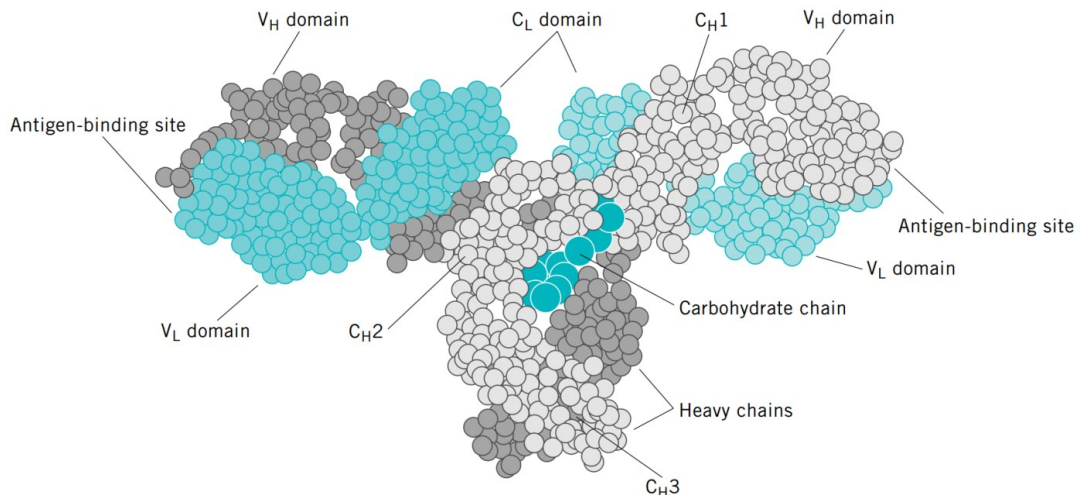


Fig. 5 The three-dimensional structure of IgG can be depicted as a Y-shaped molecule. Each sphere represents an amino acid residue. The two light chains are shades of blue and the two heavy chains are shades of grey. Reproduced with permission from ref. ⁶⁸

Since the paratopes of the Ab contain the Ag binding regions, it is of paramount importance that when Abs are coupled to surfaces, the orientation is controlled in order to retain sensitivity of the system. If the Abs are bound in an uncontrolled manner, such that the access of antigens to the binding sites on the surface of each Fab is obstructed, significant reductions or in some cases no signal will be detected. The most effective orientation is with the Fab regions expressed outwards from the surface (“end-on” orientation) they are bound to in order to maximise availability of the binding sites to the Ag.

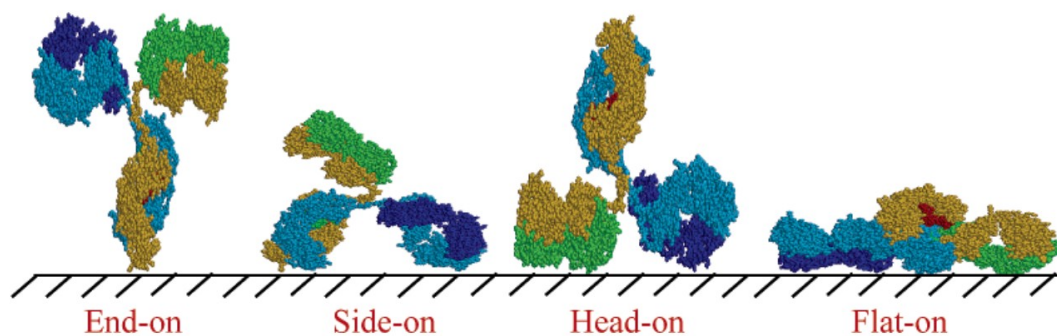


Fig. 6 Possible orientations of IgG molecules on the surface. Light blue and light brown denote the two heavy chains, and royal blue and green denote the two light chains. Reprinted with permission from ref. ⁶⁹ Copyright (2006) American Chemical Society.

There are several methods to bind antibodies to solid surfaces, though this is most commonly achieved through two methods: physical adsorption to the surface or attachment *via* covalent bonds, the differences are discussed:

Physical adsorption techniques immobilise the antibody to the solid surface through adsorption (van der Waals' forces) however the orientation cannot be controlled, difficult to predict and the bonds are relatively weak.⁷⁰ Covalent attachment methods offer more promise, where the Ab is bound to the surface through chemical bonds that are strong and orientation may be better controlled. There are several articles in the literature discussing the effects of the Ab immobilisation and the subsequent effects on sensitivity, binding capacities and kinetics of the Ag binding process.^{69, 71-76}

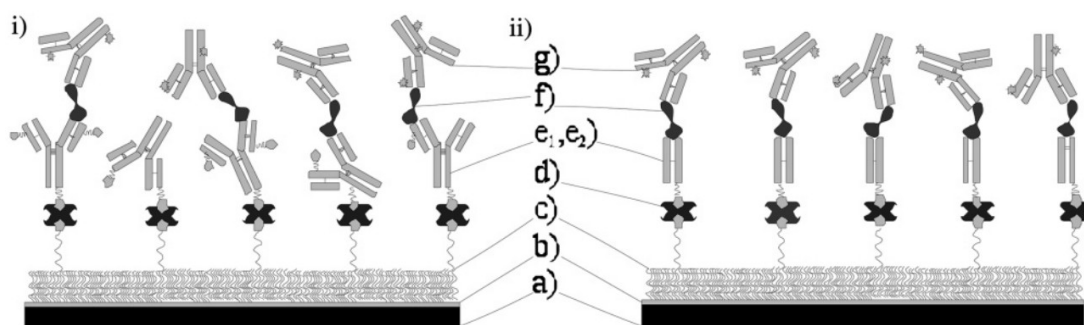


Fig. 7 Schematic representation of Ab orientation attached via a molecular wire to show the effects of steric hindrance with variation in Ab orientation. (i) Randomly biotinylated Ab-β-hCG and (ii) Fab-hCG fragment monobiotinylated in the hinge region to control orientation of binding. (a) glass substrate, (b) gold deposition layer, (c) molecular wire/self assembled monolayer, (d) linker, (e₁) randomly biotinylated Ab-β-hCG, (e₂) controlled biotinylated Fab-hCG fragment, (f) hCG and (g) labelled Ab for detection. Reprinted with permission from ref.⁷⁴ Copyright (2005) American Chemical Society.

The Fab regions of the Ab have a high affinity for specific sequences (epitopes) on the target analyte where binding to the specific Ag occurs, the strength of which is characterised by average affinity constants or the ratio between the rate constants for association and dissociation of the Ab and Ag, usually of the order 10^8 - 10^{10} M⁻¹.⁷⁷

At equilibrium, the affinity constant, K is defined as

$$K = \frac{[Ab-Ag]}{[Ab][Ag]} \quad (1.2)$$

hence at fixed concentration of Ab, the ratio of free to bound Ag at equilibrium is quantitatively related to the total amount of Ag. This forms the basis of all immunoassays.⁷⁰

Therefore the changes arising from the antibody-antigen interaction occurring on the immunologically reactive surface can be monitored and investigated to determine the presence of antigenic material. The use of such interactions was first reported in 1959 by Yalow and Berson who demonstrated that insulin could be detected by a method they called the radioimmunoassay (RIA).⁷⁸ This later led to Yalow receiving the Nobel Prize in 1977. In 1960, Ekins⁷⁹ reported a similar RIA for thyroxine and both contributions revolutionised detection methods for the accurate and specific measurements of low level species such as hormones, proteins, drugs, viruses, antigens and many others that were previously difficult or impossible to detect.⁷⁰ The immunoassay technique has undergone many important developments and improvements over the last six decades, primarily in clinical diagnosis and lately environmental analysis with expansion into pharmaceuticals, veterinary, forensic, military and food sciences.⁸⁰ Due to the inherently high selectivity of the antibody-antigen interaction, impressive sensitivity and low detection limits, the immunoassay technique has become one of the most popular and powerful routes for detection in the modern world where in theory, any analyte may be investigated so long as the respective antibody exists.⁷⁷

As mentioned previously, immunoassays are available in numerous formats and several classification criteria exist, however the major distinction is made between homogeneous (no separation steps required before detection) and heterogeneous (the separation of free and bound fractions is required before detection).⁷⁷ Homogeneous immunoassays profit from fast sample to answer speed, low cost, and procedural simplicity though their sensitivity is commonly affected by the challenge of distinguishing the signals detected for the free and bound fractions. Heterogeneous immunoassays require the separation step and in some cases, immobilisation steps.

Despite these extra steps, they are more commonly used because of the increased sensitivity and reduced interference that these systems display.

Homogeneous and heterogeneous immunoassays may be further divided into competitive which are reagent limited and non-competitive where reagent is in excess.⁷⁷ Further characterisations are based on whether or not a tag is required for detection and if so, what type of label is used and how is the label detected. The general classifications of immunoassays are:

- i. radioimmunoassay (RIA),
- ii. enzyme immunoassay (EIA),
- iii. fluoroimmunoassay (FIA),
- iv. chemiluminescent immunoassay (CLIA),
- v. colorimetric immunoassay, and
- vi. electrochemical immunoassay

These are next described in turn.

1.4.2.2 Radioimmunoassays

As discussed, radioimmunoassays were the first immunoassays to be developed of which there are two main techniques, competitive and non-competitive heterogeneous formats. The most common RIA is the competitive technique where the Ab is free or bound to a solid matrix and a known amount of both labelled (radioactive substance, usually ^{125}I gamma or ^3H beta) Ag and unlabelled (sample) Ag are introduced to contend for binding.⁸¹ At equilibrium, the radioactive complex (Ab-Ag*) is separated from the radioactive Ag (free), this is most commonly carried out by precipitation (though other methods exist; adsorption techniques including micro-plates, coated tubes and beads)⁸¹ of the Ab-Ag* complexes by adding a second Ab directed against the first. For example, if a rabbit IgG is used to bind the Ag, the complex can be precipitated by adding an anti-rabbit IgG antiserum (raised by immunising a goat with rabbit IgG). After centrifugation and washing (if required), the radioactivity of both the precipitate and free Ag is measured in counts per minute (CPM) using gamma or beta scintillation detection equipment, depending upon the tag used. If there is no Ag in the sample then there will be a high level of radiation since the radiolabelled Ag can bind to all available Ab sites. However if Ag is

present in the patient sample then the radioactivity will be decreased proportionally to the amount of Ag present. The concentration of Ag in unknown samples is determined by comparing the bound-free ratio to the bound-free ratios obtained by incubating varying amounts of known non-labelled Ag with the same amount of Ab as in the unknown sample under similar assay conditions. From this, the data are plotted as a "binding curve" where sample Ag concentrations can be determined directly from the inverse proportionality relationship between signal and concentration.⁸¹

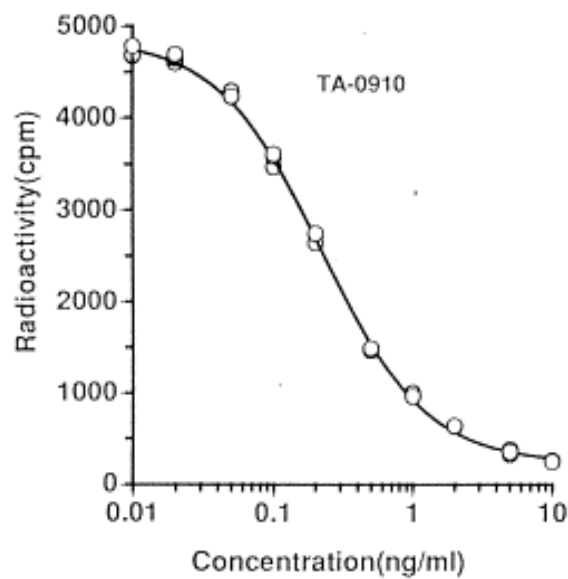


Fig. 8 Example of a standard curves used to determine unknown TA-0910 (stable thyrotropin releasing hormone analogue) concentration in RIA.⁸²

Sensitivity of the order of 10^{-12} M may be achieved through the use of a labelled Ag of high specific activity in conjunction with antisera (the serum of an animal or human containing antibodies against a specific target antigen) of appropriately high affinity. The degree of specificity is dependent upon the ability of the antiserum to recognize subtle structural features of the Ag molecule.

Non-competitive RIAs have also recently gained greater popularity following their original demonstration by Miles and Hales in 1968.⁸³ These non-competitive RIAs are similar to that of competitive techniques except it is a two Ab system, otherwise known as the "sandwich assay". The bound Ab is unlabelled and the patient sample incubated, this is followed by extraction where a second labelled antibody is added for detection.⁸¹

Since the initial description of competitive binding radio-assay techniques, there have been numerous contributions to its further development, refinement, and application. RIAs offer precision, high sensitivity and specificity and ease of isotope conjugation however they suffer from the requirement of expensive equipment and trained personnel, short shelf lives (imposed by half lives of isotopes, *e.g.* ^{125}I , $t_{1/2} = 60$ days), poses a health hazard and requires the disposal of radioactive waste.⁸¹ The greatest disadvantage of these systems is they are highly unsuitable for POC analysis, due to typical analysis times of 4-6, not including up to 28 hours for serum and reagent preparation procedures.⁸⁴

Despite this, RIA methods are still widely used for several applications including endocrinology studies (insulin, Millipore, Billerica, MA hCG, Demeditec Diagnostics, Germany), pharmacology (drug detection, Roche Diagnostics, UK “Abuscreen” for barbiturates and opiates), clinical immunology (Ab/Ag detection, Abbott, UK “AxSYM” assay for β -hCG), Oncology (cancer detection and diagnostics, Biomira Diagnostics Inc. “Truquant BR”). There exists a relatively fast RIA for the detection of intact hCG; the Siemens Coat-A-Count® IRMA hCG assay, which requires approximately two hours to complete analysis,⁸⁵ not including serum preparation, however this is still unsuitable for POC use.

1.4.2.3 Enzyme Immunoassay

Enzyme immunoassays are a development of the investigation into the use non-isotopic labels in immunoassay techniques, pioneered by Engvall & Perlmann^{86, 87} and Van Weemen & Schurs.^{88, 89} The use of enzymes has overcome some of the limitations of RIA, including improvements of relatively cheap equipment and reagents, comparably rapid detection, no radiation hazards and a large variety of enzymatic labels are available (alkaline phosphatase AP, horseradish peroxidase HRP, glucose oxidase GOx *etc.*).

Most EIAs are analogous of RIAs in that they involve at least one separation step in which the bound enzyme labelled reagent is separated from the unbound enzyme however they can be homogenous in nature. There are competitive and double Ab (sandwich) assay methods operating on exactly the same principle as that for RIA except that the detection method depends upon the conjugate used. The most common types of signal produced are chemiluminescence (luminescent peroxidation

of luminol by HRP tag in presence of peroxide)⁹⁰ and colour change (AP instigates a bright yellow colour upon hydrolysis that can be quantified using a spectrophotometer peak absorbance 400 nm or used qualitatively for screening,^{86, 87} peroxidase is also a good choice, producing a visible brown product on reaction with 5-aminosalicylic acid and hydrogen peroxide as substrates, peak absorbance 449 nm).⁹¹⁻⁹³

The most popular of all EIAs are the enzyme-linked immunosorbent assay (ELISA) (Engvall and Perlmann, 1971). ELISA tests can be competitive, non-competitive (sandwich assays) or indirect.⁹⁴ Competitive and non-competitive methods are similar to that of RIA except the change in enzyme activity is investigated by the addition of substrate. Indirect methods involve the adsorption of enzyme to a solid phase followed by the addition and incubation of an anti-IgG enzyme conjugate. This will attach to any Ab bound to the Ag. Further washing removes un-reacted material and the enzyme substrate is added. The colour change is a measure of the amount of the bound conjugate, which itself is proportional to the amount of Ab present.⁹⁵

Overall these systems are highly sensitive, accurate and capable of high throughput however ELISA performance is largely reliant on antibody and reagent qualities, in addition to operator skills and experience.⁹⁶ Moreover, enzymes are subject to risks of inhibition and denaturation. In addition, the enzymatic reactions are under temperature control, fluctuations to which will affect the enzyme activity and hence, the accuracy of the assay. The narrow dynamic range in the photometric detection measurement (at most three decades) also limits the dynamic range of ELISA,⁹⁷ where in high concentration cases, sample dilution is required to achieve concentration determination, substantially delaying turnaround times.

Typically in the clinical environment, quantitative ELISA detection methods incur a turnaround time of a day, however this can be reduced to approximately 3-6 hours for urgent requirements.^{94, 98}

1.4.2.4 Fluoroimmunoassay

Fluorescence is the emission of light from a molecule as a result of excitation to a higher energy state by exposure to an external light source.⁹⁹ The phenomenon occurs upon absorption of sufficient light energy, the molecule reaches one of the

higher vibrational levels of an excited state, where the molecule rapidly loses its excess of vibrational energy by vibrational relaxation and falls to the lowest vibrational level of the excited state. From this level, the molecule can return to any of the vibrational levels of the ground state, emitting its energy in the form of fluorescence at a rate of $10^{-9} - 10^{-6}$ seconds.^{99, 100}

Fig. 9 illustrates the excitation and relaxation processes and Fig. 11 describes this in the style of Marcus theory.

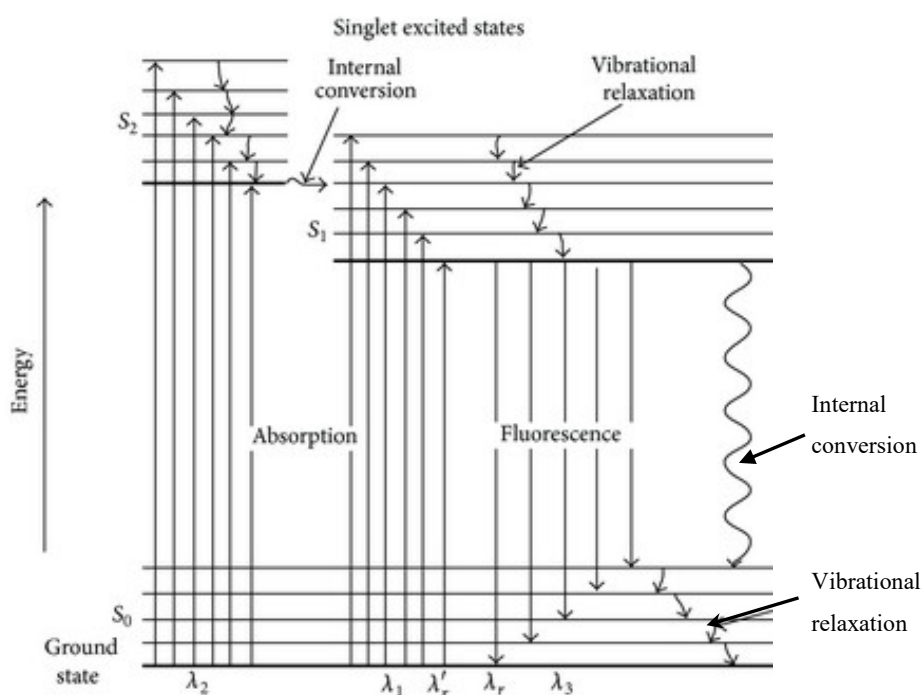


Fig. 9 Jablonski diagram describing the electronic levels of common organic molecules and possible transitions between different singlet and triplet states. Adapted with permission from ref.⁴⁶

It is only recently that fluorescence has been used for the quantitative detection of specific compounds such as various proteins (*e.g.* antibodies and enzymes), hormones and drugs. Compared with RIA methods, fluorometric labelling is relatively inexpensive, the lifetime of the kit is considerably longer and the fluorescence can be measured on relatively simple fluorescence spectrometers, without the disadvantage of handling and counting radioactive labelling agents.¹⁰¹

FIA's like the many other techniques require a label for detection and are available as homogenous or heterogeneous assays that disseminate into several applications:

fluorescence polarisation,¹⁰²⁻¹⁰⁵ fluorescence enhancement^{106, 107} and quenching,^{108, 109} fluorescence excitation transfer¹⁰⁸ and time-resolved fluorescence.¹¹⁰ Heterogeneous methods are most popular in order to reduce interference where similar methods of separation used in RIAs are implemented such as the single or double Ab precipitation techniques.¹¹¹ Common labels used in FIAs include fluorescein,¹¹²⁻¹¹⁴ various rhodamines,¹¹⁵⁻¹¹⁷ dansyl chloride,¹¹⁸ fluram,¹¹⁹ and recently, metal chelates.¹⁰¹

Turnaround times for some automated fluorescence based methods has been demonstrated to be impressively low at 20 minutes,¹²⁰ with one assay developed by Lode *et al.*¹²¹ demonstrating quantitative detection of total hCG at the POC in as little as 5 minutes using direct time-resolved fluorescence. However, The disadvantages of this particular example is the need for expensive rare earth lanthanide chelate labels such as europium that can suffer from quenching caused by blood constituents.¹²² Perhaps the major disadvantage is the difficulty in minimising this technology into to a handheld device more suitable for POC analysis, due to the need for a sizeable analyser machine. Other disadvantages of fluorescence based immunoassays includes the possibility damage biological samples containing proteins through the radiation heat from a light source, potentially reducing or totally destroying biological activity of the samples by heat deterioration.¹²³

1.4.2.5 Chemiluminescent Immunoassay

Unlike fluorescence, chemiluminescence (the process of emission of electromagnetic radiation, light), occurs when the excitation of a molecule or species to an excited state relaxes to the ground state occurs as a result of electron transfer stimulated by a chemical reaction, and not by the absorption of photons.¹²⁴ This process takes place *via* the Marcus inverted region of electron transfer.^{125, 126} The Marcus inverted region is a feature of Marcus electron transfer theory (discussed in section 2.5), which describes the energetics of electron transfer in terms of the obligatory reorganization of a solvent shell and bonding environment following an electron transfer.¹²⁶

The Marcus inverted region is described to occur in the event of a highly exergonic ET reaction, where the intersection of the potential energy surface of the reactants with that of the electronic ground-state products produces a large energetic barrier compared to the intersection with respect to one producing an excited state.

Normally, the formation of ground-state species in the high-energy electron-transfer reaction incurs the production of highly excited vibrational states and the reaction energy dissipates as excess heat. However an alternative route exists; the formation of an electronic excited state allows the later dissipation of the reaction energy in the form of an emitted photon, i.e. process of chemiluminescence.¹²⁷ This is phenomenon is illustrated in Fig. 11.

In the middle case of Fig. 11, the reactant and both product curves intersect such that that either excited state or ground-state formation is exothermic, hence it is feasible for the chemical reaction to be chemiluminescent depending upon the relative activation energies for production of both the ground and excited states. The right-hand case illustrates the formation of the excited-state production when it is slightly endothermic. In this case, thermal activation can provide small amounts of energy to a chemical reaction. Since chemiluminescence is observed as an absolute light intensity it is possible to detect low efficiency reactions, as a result the emission of light from endothermic reactions may be observed.¹²⁸

One of the most well known chemiluminescent compounds is Luminol, (5-amino-2,3 dihydro-1,4 phthalazinedione), for which the first insight into the mechanism of chemiluminescence properties were described by White *et al.* in 1961.¹²⁹ White *et al.*¹³⁰ later showed in 1964 a more complete mechanism wherein the chemiluminescence process involves the formation of a negative ion of luminol, (II in Fig. 10) which reacts with oxygen or an oxidizing agent to yield an excited singlet state of the amino phthalate ion, III and the resulting emission of light.

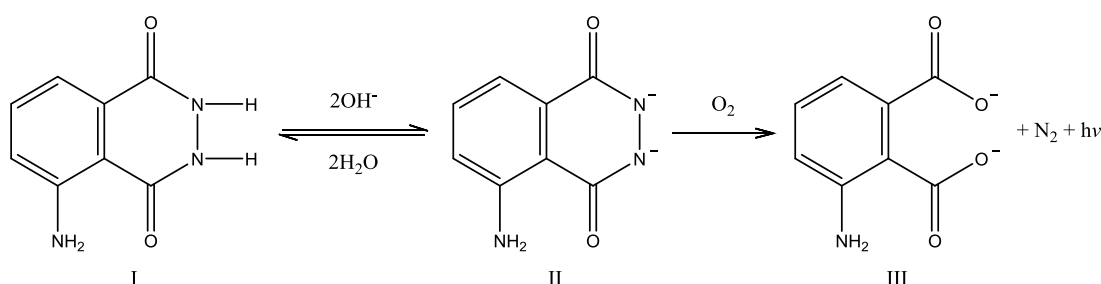


Fig. 10 Reaction mechanism for the chemiluminescent reaction of luminol

More recently, the process of chemiluminescence is generally catalysed by the use of enzyme labels, where the most popular route to chemiluminescence (CL) production

in CLIAs is *via* Ab or Ag bound enzymes such as HRP and AP used to catalyse the reaction between luminol and hydrogen peroxide. However CL does not have to be instigated by the use of enzymes. With the recent advances in nanotechnology, materials such as gold nanoparticles (AuNPs), carbon nanotubes (CNTs) and others were found to exhibit catalytic behaviour towards the luminol-peroxide system, acting as enzyme mimics to achieve signal amplification.¹³¹⁻¹³⁴ Other systems have been developed without the use of enzymatic labels: Chen *et al.* synthesised a new biacridine compound used in a sandwich assay method for the detection of carcino-embryonic Ag in human serum.¹³⁵ Scorilas *et al.* synthesised two novel biotinylated acridinium derivatives that produce CL in the presence of hydrogen peroxide.¹³⁶

Overall, CLIA methods are highly sensitive and are a rapid alternative to RIA techniques. They offer good specificity, large linear response ranges (up to six decades), high stability of several reagents and most of the conjugates (increased stability is often observed after conjugation), low consumption of expensive reagents and require only simple equipment,¹²⁴ with even Smartphone cameras recently demonstrated as suitable detectors.¹³⁷ For these reasons, CLIAs are being used increasingly in all manner of fields including clinical diagnosis, pharmaceutical and environmental analysis.¹³⁸ The turnaround times for automated quantitative systems of this design can be as high as six hours,¹³⁹ however this has been largely reduced in recent years with readings available in as little as 15 minutes,¹⁴⁰ and easily inside one hour.

The disadvantages of this methodology are its susceptibility to inaccuracies and false readings. These can occur through numerous pathways, such as the selectivity of the chemiluminescence causing reagent that may yield significant emission for more than one unique analyte. Furthermore, CL emission intensities are sensitive to a variety of environmental factors such as temperature, solvent, ionic strength, pH, and other species present in the sample. The difficulty lies in standardising the CL response to a wide range of sample constituents and characteristics where inaccuracies or contamination can be a real problem. Another issue is the emission intensity from a CL reaction varies with time (signal increase after reagent mixing, passing through a maximum, then decreasing back to the base-line), the CL emission versus time profile differs widely from one compound to another and could be altered by the sample constituents.¹⁴¹

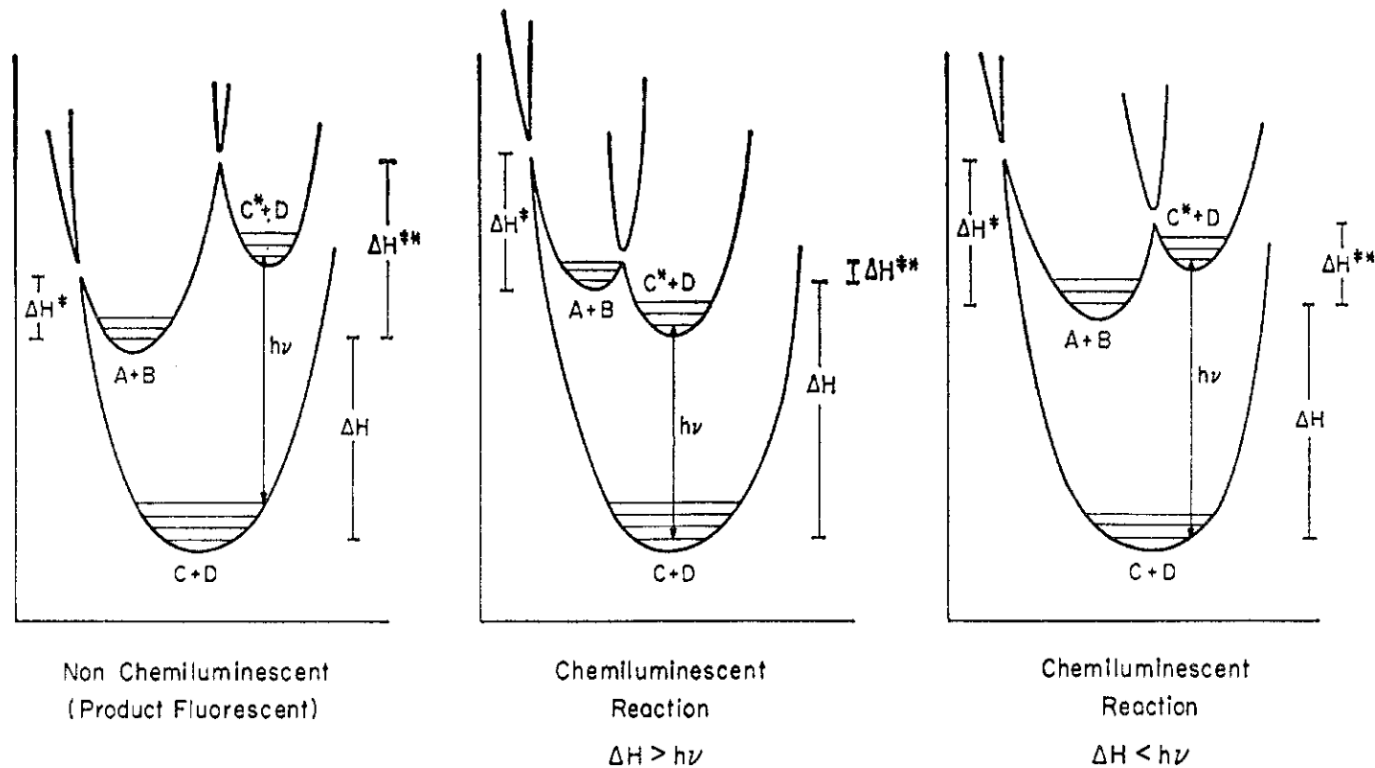


Fig. 11 Reaction coordinate diagrams for chemical excitation processes: $A + B =$ reactants; $C + D =$ products formed in ground states; $C^* + D =$ products formed with C in an excited state and D in the ground state; $\Delta H =$ energy available from the reaction according to the usual thermodynamic criteria; $\Delta H^* =$ activation energy for formation of products in the ground state; $\Delta H^{**} =$ activation energy for formation of one product in an excited state; $h\nu =$ energy necessary for the excitation $C \rightarrow C^*$. Reprinted with permission from Hercules (1969) Copyright (1969) American Chemical Society.

1.4.2.6 Colorimetric Immunoassay

Colorimetric immunoassays are mostly an extension of EIAs where an enzyme conjugate is used to form a coloured product in the presence of analyte. Like in other EIA techniques, the most popular enzymes are HRP and AP.

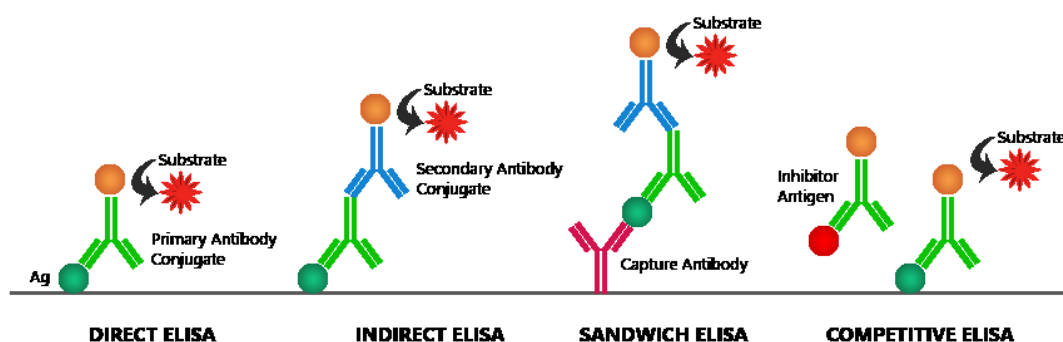


Fig. 12 Use of enzymes in various methods of colorimetric immunoassays. The enzyme is depicted as the orange circle attached to the antibody and always performs the same function, to convert a substrate to a coloured product.¹⁴²

Quantitative and qualitative measurement of antigenic materials present in blood serum or other biological fluids or cells is effected may be achieved. This process is mostly competitive and comprises the addition of enzyme labelled Ag and unlabelled Ag that compete for the Ab binding sites. After washing, a substrate is added that initiates the colour formation and the intensity is measured using a spectrophotometer at the characteristic absorbance spectrum in the visible light wavelength range. The colour formation step is highly dependent on the enzyme activity, though typically requires anywhere from 5 to 120 minutes to ensure sufficient colour formation occurs;¹⁴³ short incubation times significantly reduce the sensitivity of these assay methods however this may be suitable for qualitative screening methods. However in this methodology it is not the colorimetric detection strategy that prolongs the turnaround time, but the multiple incubation, washing and blocking steps that require hours to complete limit the application of the immunoassays for rapid clinical diagnosis and subsequent treatment applications.¹⁴⁴ Overall, this method provides a relatively fast, simple and direct measurement of the antigen concentration. An example of a commercially successful colorimetric immunoassay is the ESEQuant, Qiagen, Germany.

1.4.2.7 Electrochemical Immunoassay

Electrochemical immunoassays (ECIAs) are different to the previously mentioned techniques in that a biological recognition element is intimately coupled to an electrode transducer. The purpose of the transducer is to convert the biological recognition event into a useful electrical signal. This detection of changes in electrical activity caused by the Ab-Ag immunological binding process, has gained popularity and is widely recognised as one of the most sensitive detection methods used in immunoassays.

Recent advances in this area have led to various sensing strategies that involve the use of on-chip and off-chip methods, including though not limited to: magnetic beads,^{145,146} carbon nanotubes,^{147, 148} nanoparticles,¹⁴⁹ enzymes¹⁵⁰ and electrochemiluminescence.¹⁵¹⁻¹⁵³ A significant advantage ECIA have over other immunoassays is the ability to scale down sample volumes to very small dimensions (μL scale), owing to the nature of interfacial rather than bulk phenomenon. Furthermore, ECIA is particularly useful for coloured or opaque sample matrices that could pose problems for other optically reliant based sensing methods.¹⁵⁴

Turnaround times for these systems can be as little as minutes to over an hour, though typical timescales are around 25-60 minutes,¹⁵⁵⁻¹⁵⁷ a vast improvement on commercial ELISA based detection strategies of between 2.5 – 4 hours minimum, whilst retaining comparable sensitivity.¹⁵⁸

ECIAs consist of the same classifications as previously reported; heterogeneous, homogeneous, competitive and non-competitive, the principles of which are transferrable.

There are five distinguished electrochemical systems used in ECIA:

- i. voltammetric,
- ii. amperometric,
- iii. potentiometric,
- iv. capacitive,
- v. conductometric, and
- vi. impedimetric

The operational concepts, characteristics and differences between these electrochemical techniques are discussed below:

Voltammetric detection involves the application of a time dependent cathodic or anodic potential and analysis of the resulting current response as a function of the potential. Voltammetric detection is the primary detection method used across the vast majority of the literature for ECIA's. Voltammetric methods are classed as active techniques because of the imposed potential drives a change in concentration of an electroactive species at the electrode surface, due to a redox reaction.⁷⁷ There are a variety of methods within voltammetry that are classified according to the differences in how the potential is applied and how the resulting current is analysed, these include: linear sweep, cyclic, pulsed and stripping voltammetry.

Linear sweep voltammetry (LSV) is different in that the applied potential is varied linearly with time and the peak current is recorded as a function of the potential. The central limitation to LSV is the significant contribution of the capacitive current, often making it difficult to assign the current directly responsible for the redox process. The implications of the charging current may be reduced with the use of differential pulse voltammetry (DPV) where the potential waveform consists of small pulses superimposed upon a staircase waveform.¹⁵⁹ Cyclic voltammetry is a variation of linear sweep voltammetry and is discussed in greater detail in chapter two.

Anodic stripping (ASV) methods are primarily used for metalloimmunoassay applications where a negative potential is applied to the electrode for a specific period of time in order to deposit the metal ions from the solution onto the electrode surface. This is followed by a positive potential sweep where current responses are observed at the corresponding potentials for the oxidation (stripping) of each metal back into solution. This gives rise to sensitive quantification of trace metals (10^{-12} M) and opens up applications for use with metal-labelled analytes. Metal labels that are well documented in the literature include Au,¹⁶⁰ In(III),¹⁶¹ Co(II)¹⁶² and Pb¹⁶³ to name but a few. Since different metal will strip at different potentials, the system may be exploited for multianalyte detection, where two or more analytes are labelled with metals that are stripped at sufficiently separate potentials. This was demonstrated by Hayes *et al.* for the simultaneous detection of Bi²⁺ and In³⁺ labelled human serum albumin (HSA) and IgG.¹⁶⁴

Amperometric biosensors are similar to voltammetric techniques in that a potential is applied, however this is kept constant and the resulting current associated with the reduction or oxidation of an electroactive species involved in the recognition process is observed. An amperometric biosensor may be more attractive because of its high sensitivity and wide linear range, because of this amperometry is the most commonly used technique in ECIA methods. This commonly involves the incorporation of enzymatic labels such as HRP or AP however there are techniques that combine amperometric detection with flow analysis as an immunoassay system.^{165, 166} A common problem with amperometric detection is that the oxidation or reduction of other electroactive species in solution, for example uric and ascorbic acid in blood samples, may occur at the applied potential leading to interferences and sometimes, electrode fouling. To combat this, amperometric systems must impose as low a potential as possible to achieve only the desired reaction; this is usually accomplished by optimisation of the detection system.

Potentiometric detection for immunoassay techniques is effectively the opposite of voltammetric methods in that the analytical information is obtained by converting the bio-recognition process into a measurable potential or charge accumulation, measurable as a potential difference change between the working and reference electrodes, not current a change; this was first demonstrated by Jenata.^{167, 168} A profitable advantage of this potentiometric devices for immunoassay applications is that a label is not required for detection since proteins behave as polyelectrolytes in aqueous solution,¹⁶⁹ though the use of labels (HRP, laccase *etc.*) is still common in this technique. A further advantage is that there is no need for separation steps though the limitation is that the potential change caused by the Ab-Ag interactions is very small, therefore background effects can cause reliability and sensitivity issues.⁷⁷

Capacitance detection measures the changes in dielectric properties, charge distribution, and/or conductivity change in the thickness of the electric double layer at the electrode | electrolyte interface that is brought about by Ab-Ag complex formation on the surface of the electrodes.¹⁷⁰ The capacitive sensor comprises two plates, one the metal or semi-conductor substrate with immobilised Ab or Ag and the other, the counter electrode as represented by the electrolyte.⁷⁷ This makes possible the real time, label free monitoring of the immunological interactions,^{171, 172} hence capacitive immunoassays are promising alternatives to existing immunochemical

tests for the development of hand-held devices which can be used for point-of-care applications. The attraction of affinity-based capacitive sensors is that they are able to determine the analyte directly in a sample with no or very little sample preparation. For high-quality sensor operation, it is imperative that the coupling of the Ab or Ag to the electrode surface does not compromise the insulating properties of the immobilised bio-molecular layer once formed. Furthermore, this interaction also excludes water from the dielectric layer at the surface causing a change in the dielectric properties between the electrodes where a change in capacitance is incurred. This is caused by the difference in dielectric properties of the Ab or Ag in comparison with water. Typical sensitivities for use of this method in monitoring immunological binding are in the low ng mL^{-1} (mIU mL^{-1}) range however detection down to 0.5 pg mL^{-1} ($\mu\text{IU mL}^{-1}$) has been demonstrated for hCG.¹⁷³

Conductometric based measurements detect a measurable electrical conductivity change of a bulk or film material affected by an analyte, providing a measure of the ion mobility and concentration in a medium or cell solution. Most reactions involve a change in the composition of solution, thus conductometric biosensors can detect reactive changes occurring in a solution. In conductometric immunological sensors, the change in conductivity upon Ab-Ag binding is small and usually returns detection limits in the micromolar region, restricting the analytical worth of this method, however the introduction of enzyme labels has significantly improved this as demonstrated by Thomson *et al.* for detection of hCG at low ng mL^{-1} levels.¹⁷⁴

Finally impedimetric detection is based on the response of resistive and capacitive properties of materials when perturbed by a small amplitude sinusoidal excitation signal where at a fixed frequency. The resulting current sine wave differs in time (phase shift) with respect to the perturbing (voltage) wave, and the ratio $V(t)/I(t)$ is defined as the impedance (Z), and accounts for the combined opposition of all the components within the electrochemical cell (resistors, capacitors, inductors) to the flow of electrons.¹⁷⁵ Characteristic changes in impedance are directly proportional the concentration of the analyte.¹⁷⁶ In immunoassay systems, small differences in impedance are measured as a result of the Ab-Ag interaction process. For impedance based IAs to operate efficiently, it is of paramount importance that the possibility for non-specific binding is eliminated, this is usually achieved by adsorption or covalent attachment to the electrode surface and if required, the subsequent blocking of

unfilled sites. Though this can be a direct label free detection method, difficulties in data analysis and interpretation coupled with lowered sensitivities when compared to other ECIA techniques makes impedance detection less popular for IA applications.⁷⁷

Overall, amperometric and potentiometric transducers are most commonly used in conjunction with electrochemical biosensors. Several of these methods are capable of generating the analytical signal without the use of an electroactive label, where the immunological interaction may be probed directly; however the majority of ECIAs utilise a wide variety conjugates in order to register the signal as mentioned in the technique descriptions above.

A popular class of label used for ECIAs are enzymes. Due to their catalytic ability and capacity to produce electrochemically active products from adequate substrates, the sensitivity of such assays may be greatly enhanced with detection limits at zeptomolar or even attomolar concentrations reported.^{177, 178} The most established enzyme labels are AP, HRP and GOx though many more are frequently used, dependent upon the type of reaction involved. However, there are issues with enzyme labels in that their electron transfer efficiency can be poor as the redox centres are commonly buried deep in the protein shell. In many cases a mediator is required to transport electrons from the redox centre of the enzyme to the indicator electrode surface, adding further complexity to these systems. These mediators are generally small, low molecular weight compounds that are stable in both the oxidised and reduced forms, exhibit reversible heterogeneous kinetics (can undergo rapid charge transfer), have low formal potentials for the redox couple in order to avoid interferences and are ideally, non-toxic.⁷⁰ Commonly used electron mediators include ferrocene derivatives,¹⁷⁹⁻¹⁸² quinones,¹⁷⁹ and redox dyes.^{183, 184} Other diverse labels include liposomes,¹⁸⁵⁻¹⁸⁷ and polyelectrolytes.^{169, 188}

Other electrochemical techniques exist that do not directly register an electrical change upon the Ab-Ag binding process but rather apply the electric field in order to induce a response otherwise measured. Electrochemiluminescence is a prime example of this where the light emitting reaction is preceded by an electrochemical reaction offering greater experimental control of generic CL techniques. Recent advancements in the field have made quantitative turnaround times as little as 18 minutes possible, such as the Elecsys® Troponin T high sensitive (TnT-hs, Roche

Diagnostics).¹⁸⁹ While this is an impressive achievement, this turnaround time ideally needs to be reduced to be truly POC suitable.

In this thesis, the development of an electrochemical immunosensor is reported for the analytes described above. Molecular wire attachment to electrode surfaces and the subsequent functionalisation with redox active species is later described.

1.5 Kinetics of Binding

It is important to discuss and understand the Ab-Ag interactions from a kinetic standpoint and the theory that governs these immunological reactions. For kinetics of free Ab and Ag in homogeneous solution at equilibrium, the rate of dissociation can be determined as

$$K_{dissoc.} = \frac{1}{K_{assoc.}} \quad (1.3)$$

the rate of association and dissociation can therefore be derived

$$\text{rate of association} = k_a[Ab][Ag] \quad (1.4)$$

$$\text{rate of dissociation} = k_d[Ab-Ag] \quad (1.5)$$

therefore the association and dissociation constants are equal to

$$K_{assoc.} = \frac{k_a}{k_d} \quad (1.6)$$

$$K_{dissoc.} = \frac{k_d}{k_a} \quad (1.7)$$

The ratio of change in [Ab-Ag] concentration is

$$\frac{d[Ab-Ag]}{dt} \quad (1.8)$$

$$= \text{rate of formation of Ab-Ag} - \text{rate of destruction of Ab-Ag}$$

$$\Rightarrow k_a[Ab][Ag] - k_d[Ab-Ag] \quad (1.9)$$

substitute the [Ab] in equation (1.8) for the free to bind Ab fraction, [Ab]_{free}

$$[Ab]_{free} = [Ab]_{t=0} - [Ab-Ag] \quad (1.10)$$

where [Ab]_{t=0} is the initial concentration of Ab in solution.

$$\Rightarrow \frac{d[Ab-Ag]}{dt} = k_a[Ag]\{Ab_{t=0} - [Ab-Ag]\} - k_d[Ab-Ag] \quad (1.11)$$

we further assume that $[Ag] \gg [Ab]_{t=0}$, so that $[Ag]$ in solution does not change.

Now if the analytical response, R , is directly proportional to $[Ab-Ag]$ then

$$\frac{dR}{dt} = k_a[Ag]\{R_{\max} - R\} - k_dR \quad (1.12)$$

$$\frac{dR}{dt} = k_a[Ag]R_{\max} - k_a[Ag]R - k_dR \quad (1.13)$$

$$\frac{dR}{dt} = k_a[Ag]R_{\max} - R\{k_a[Ag] + k_d\} \quad (1.14)$$

where $k_a[Ag]R_{\max}$ and $R\{k_a[Ag] + k_d\}$ are constants, integration yields:

$$\Rightarrow -\frac{\ln\{k_a[Ag]R_{\max} - R(k_a[Ag] + k_d)\}}{k_a[Ag] + k_d} = t + C \quad (1.15)$$

where C is a constant of integration.

When $t = 0$, $R = 0$ because no binding occurs at zero time

$$\therefore C = -\frac{\ln\{k_a[Ag]R_{\max}\}}{k_a[Ag] + k_d} \quad (1.16)$$

$$\Rightarrow -\ln\{k_a[Ag]R_{\max} - R(k_a[Ag] + k_d)\} \quad (1.17)$$

||

$$t(k_a[Ag] + k_d) - \ln(k_a[Ag]R_{\max}) \quad (1.18)$$

where

$$A = (k_a[Ag]R_{\max}) \quad (1.19)$$

and

$$B = k_a[Ag]R_{\max} - R(k_a[Ag] + k_d) \quad (1.20)$$

applying a log function to equation (1.17) and (1.18) so that

$$\log A - \log B = \log\left(\frac{A}{B}\right) \quad (1.21)$$

$$\ln\left\{\frac{k_a[Ag]R_{\max}}{k_a[Ag]R_{\max} - R(k_a[Ag] + k_d)}\right\} = t(k_a[Ag] + k_d) \quad (1.22)$$

application of an exponential gives rise to

$$\frac{k_a[Ag]R_{\max} - R(k_a[Ag] + k_d)}{k_a[Ag]R_{\max}} = \exp[-t(k_a[Ag] + k_d)] \quad (1.23)$$

so that for a general case

$$\frac{1 - \exp[-t(k_a[Ag] + k_d)]}{k_a[Ag] + k_d} = R \quad (1.24)$$

a plot of this equation can give insight into the kinetics of an immunological reaction, where the effects of Ag concentration and Ab affinities can be significant

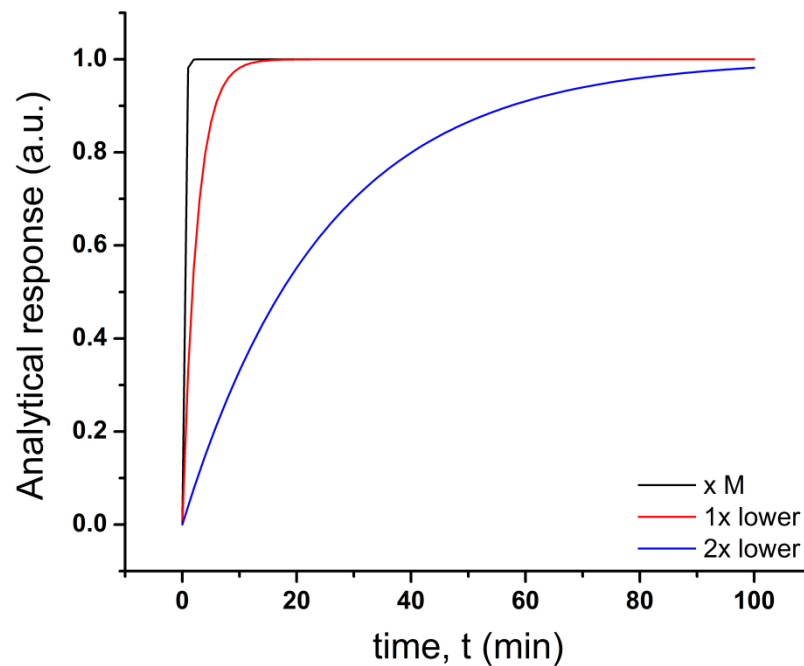


Fig. 13 The analytical response as a function of concentration, where a series of decreasing concentrations by one order of magnitude show a dramatic slowing of the analytical response with time.

The intricate nature of this equation therefore allows the perturbation of how changes in Ag concentration or Ab binding affinities can impact the intensity of the analytical signal with time. Here we see that in Fig. 13, the effect of Ag concentration on the analytical response with time becomes rather significant as the concentration decreases where a change as small as one order of magnitude incurs appreciable change in the response with time profile. This is expected as it will take longer to reach equilibrium with a lower amount of Ag available and thus the signal response requires considerably more time to reach a steady state. In Fig. 14, the effect of a change in affinity constant for the binding process is illustrated, where it is clear that

slower rate constants of binding affinity, K_{on} induces an increase in the time required to reach steady state, a similar response to reducing the concentration of Ag. From these simulations it is clear that the analytical response is dependent on this multi-factor relationship of affinity and concentration and therefore requires consideration when designing and optimising an immunoassay system.

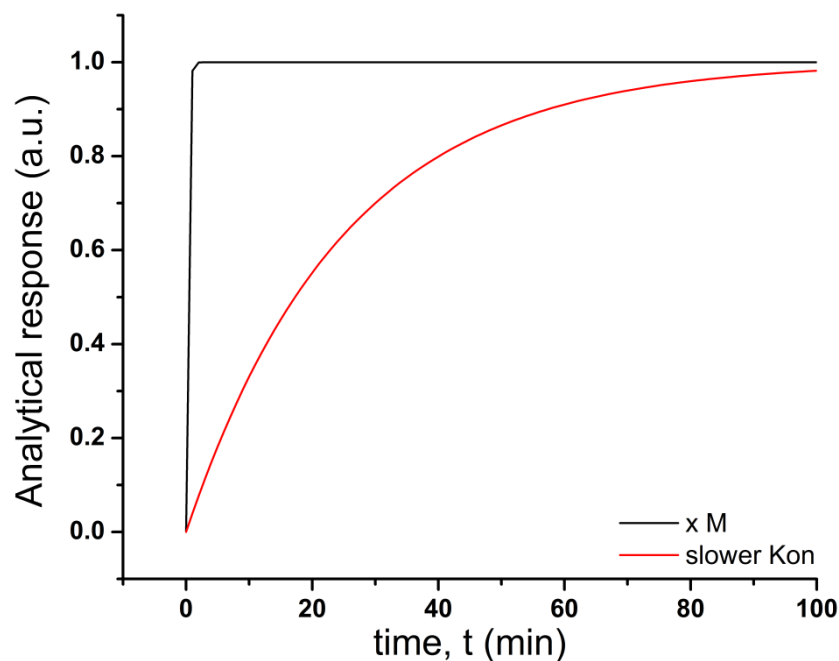


Fig. 14 The analytical response as a function of Ab affinity at constant Ag concentration, where a slower rate of association, K_{on} by two orders of magnitude show a dramatic slowing of the analytical response with time.

1.6 Biological Matrices

The human body offers numerous routes to obtain a physiological sample; typically this can be from sweat, tears, saliva, blood or urine. Urine and blood are the most common samples for POC testing; however in recent years there have been increased interests in fluids such as sweat, tears and saliva due their non-invasive nature. Blood and urine are both incredibly useful in the clinical setting where they are relatively simple and quick to obtain. Rapid analysis of these samples may provide real time concentrations of specific analytes linked to symptoms of a patient, offering prompt diagnostics and subsequent treatment. Each of these samples comes with their own benefits and drawbacks. For the purpose of this study, only urine and blood will be discussed as potential sample matrices.

1.6.1 Urine

Urine is a complex matrix that contains a vast amount of clinically indicative information and is easily accessible by non-invasive means, however varies widely in its composition. This can be affected by diet and many other factors including illnesses or ailments of the body that in turn may cause issues for its analysis. The composition of a typical daily urine excretion for a normal, healthy individual is detailed in Table 6.

There are many possible interferences within this composition, though very few are electrochemically active, or at a concentration where they may be an issue. The constituents that may pose issue with an electrochemical sensing system are uric acid, phenols and purine bases as they are easily oxidised. Others not included in this list but may still be present in real samples are ascorbic acid, folic acid and dopamine. The oxidation of ascorbic acid and dopamine occurs at relatively low potentials of 0.2 V and 0.22 V respectively,¹⁹⁰ with uric acid close to this at ~ 0.35 V;¹⁹¹ in general these interferences may oxidise anywhere from 0 V up to 0.4 V. Folic acid oxidises much higher at 0.7 V - 0.85 V depending on pH of the solution.¹⁹² Man made drugs such as paracetamol are also not without issue on interference of electrochemical sensing, oxidising at ~ 0.6 V.¹⁹³ As can be seen, there is large variation in the oxidation potentials of these possible interferences, therefore it is critical to take this into account when selecting an electrochemically active mediator or label such that the oxidation potential is as least affected by these as possible.

There are common health issues where the human body may add other potential interferences to urine; these are primarily glucose, bilirubin and haemoglobin.

Glucose may be present in urine in the case of Diabetes Mellitus, wherein the sugar is not reabsorbed in the proximal tubule of the kidney.¹⁹⁴ This occurs when the blood glucose level exceeds the renal threshold for glucose (RTG), an overwhelming of the proximal tubule that is commonly reported as 180 – 200 mg mL⁻¹ (10 - 11 mM).¹⁹⁵ A blood glucose concentration at or above this subsequently causes glucose excretion into the urine.¹⁹⁴

Table 6 Typical daily urine excretions for a normal healthy individual, reproduced from reference ¹⁹⁴.

Constituent	Mass / g
Water	1200.0
Solids	60.0
Urea	30.0
Uric acid	0.7
Hippuric acid	0.7
Creatinine	1.2
Indican	0.01
Oxalic acid	0.02
Allantoin	0.04
Amino acid nitrogen	0.2
Purine bases	0.01
Phenols	0.2
Chloride as NaCl	12.0
Sodium	4.0
Potassium	2.0
Calcium	0.2
Magnesium	0.15
Sulfur, total, as S	1.0
Inorganic sulphates as S	0.8
Neutral sulphur as S	0.12
Conjugated sulphur as S	0.08
Phosphate as P	1.1
Ammonia	0.7

Bilirubin is formed by the degradation of the haemoglobin heme in the extrahepatic reticuloendothelial system of the liver. This then conjugates to the protein albumin before transportation to the liver for processing. Here it is liberated of protein and further conjugated to glucuronic acid before excretion in the bile. Finally the conjugated form is transported to the intestine where it is further broken down into urobilinogen and other products that are reabsorbed or excreted.¹⁹⁶ Raised urinary

bilirubin (conjugated) with absent or reduced urobilinogen is suggestive of obstructive jaundice whereas normal or raised urinary bilirubin with elevated urobilinogen suggests hepatocellular failure or increased red cell breakdown (e.g. haemolytic jaundice). In these cases, a patient will present a urine sample with increased concentration of bilirubin that may cause inference to electrochemical sensing systems because bilirubin is known to be electroactive.¹⁹⁷

1.6.2 Blood

Like urine, blood is an extremely complex medium that contains a huge amount of clinically indicative information. Generally this is the most ideal biological sample as it can be collected easily and quickly, with little to no sample preparation conditions required depending on analysis technique, however it contains or may contain several interfering chemicals or molecules. Furthermore, access to blood is invasive and can be uncomfortable for patients to deal with. The general components of blood are red blood cells, white blood cells and plasma. By volume, they constitute approximately 45%, 0.7% and 54.3% of whole blood respectively.¹⁹⁸

The plasma is the blood's liquid medium, essentially an aqueous solution containing 92% water, 8% blood plasma proteins, and trace amounts of other materials. Plasma circulates dissolved nutrients, such as glucose, amino acids, fatty acids and hormones whilst facilitating the removal of waste products, such as carbon dioxide, urea, and lactic acid.¹⁹⁸

Many blood samples are treated as to remove many of these interferences and leave behind the analytes of interest; this is called serum. The term serum refers to plasma from which the clotting proteins have been removed. Most of the proteins remaining are albumin and immunoglobulins. This is common in clinical analysis of blood however requires laboratory treatment which significantly delays analysis time.

Because of its vast contents, whole blood can pose extreme difficulty with regards to its analysis with immunoassay techniques, especially electrochemical. Contents of blood may be electrochemically active or foul electrode surfaces, thus tarnishing their ability to make accurate or reproducible readings.

1.7 Aims and Objectives of this Thesis

The primary aim is to develop a robust combinatorial sensing platform for rapid quantitative detection of a plethora of biomarkers to aid analysis at the POC in emergency and clinical environments. These include markers specific to cardiovascular disease such as BNP and troponin T for the detection and monitoring of heart failure and pregnancy related marker hCG for the early detection of pregnancy. The assay development is projected for use in clinical samples including blood, urine and saliva, with preference to the latter two as these afford non-invasive measurements.

These systems are of significant diagnostic value in heart failure as it is classified as a major worldwide health issue with more than 15 million patients suffering heart failure in North America and Europe alone and approximately 1.5 million new cases arising every year.¹⁴⁻¹⁶ The blood BNP levels are extremely low in normal healthy conditions, *ca.* 20 pg mL⁻¹, however they may elevate to >2 ng mL⁻¹ for patients diagnosed with severe congestive heart failure.^{11, 17} The development of fast, portable, highly sensitive measuring systems specific to BNP are therefore greatly desired for point of care diagnostics in the clinical environment.

There is also great interest in the detection of hCG for the confirmation of pregnancy as well as the diagnosis of potentially life threatening ectopic pregnancies. Utilising the translational properties of the sensing platform developed in this report for BNP, the sensor may be adapted for detection of hCG in urine or blood matrices.

In this report, the development of an electrochemical immunosensor utilising molecular wire chemistry for direct attachment to a tin doped indium oxide (ITO) coated glass slide electrode surface and the subsequent functionalisation is described. The ITO surface is used for its flat dimensions where the sample may be dropped onto the surface, significantly reducing sample volume requirements (*ca.* 30 µL) for a measurement to be carried out.

The next chapter details the fundamental processes and basic theory relevant to this study.

References

1. WHO, *Biomarkers and Risk Assessment: Concepts and Principles*; ; [IPCS, International Programme on Chemical Safety], World Health Organisation, Geneva, 1993.
2. B. McDonnell, S. Hearty, P. Leonard and R. O'Kennedy, *Clinical Biochemistry*, 2009, **42**, 549-561.
3. S. C. Smith Jr, A. Collins, R. Ferrari, D. R. Holmes Jr, S. Logstrup, D. V. McGhie, J. Ralston, R. L. Sacco, H. Stam, K. Taubert, D. A. Wood and W. A. Zoghbi, *Journal of the American College of Cardiology*, 2012, **60**, 2343-2348.
4. S. Mendis, P. Puska and B. Norrving, *Journal*, 2011.
5. S. Bernick, *The Economic Cost of Cardiovascular Disease from 2014-2020 in Six European Economies*, London, 2014.
6. S. A. Butler, S. A. Khanlian and L. A. Cole, *Clinical chemistry*, 2001, **47**, 2131-2136.
7. J. Jones, *Amino acid and peptide synthesis*, Oxford University Press, Oxford, 1997.
8. A. S. Maisel, P. Clopton, P. Krishnaswamy, R. M. Nowak, J. McCord, J. E. Hollander, P. Duc, T. Omland, A. B. Storrow, W. T. Abraham, A. H. Wu, G. Steg, A. Westheim, C. W. Knudsen, A. Perez, R. Kazanegra, V. Bhalla, H. C. Herrmann, M. C. Aumont and P. A. McCullough, *Am Heart J*, 2004, **147**, 1078-1084.
9. J. L. Januzzi and A. S. Maisel, *Circulation*, 2004, **109**, e325-e326.
10. E. R. Levin, D. G. Gardner and W. K. Samson, *New England Journal of Medicine*, 1998, **339**, 321-328.
11. Q. Dao, P. Krishnaswamy, R. Kazanegra, A. Harrison, R. Amirnovin, L. Lenert, P. Clopton, J. Alberto, P. Hlavin and A. S. Maisel, *Journal of the American College of Cardiology*, 2001, **37**, 379-385.
12. K. T. Yeo, A. H. Wu, F. S. Apple, M. H. Kroll, R. H. Christenson, K. B. Lewandrowski, F. A. Sedor and A. W. Butch, *Clin Chim Acta*, 2003, **338**, 107-115.
13. C. Hall, *European Journal of Heart Failure*, 2004, **6**, 257-260.
14. M. M. Redfield, *New England Journal of Medicine*, 2002, **347**, 1442-1444.

15. S. A. Hunt, D. W. Baker, M. H. Chin, M. P. Cinquegrani, A. M. Feldman, G. S. Francis, T. G. Ganiats, S. Goldstein, G. Gregoratos, M. L. Jessup, R. J. Noble, M. Packer, M. A. Silver and L. W. Stevenson, *Circulation*, 2001, **104**, 2996-3007.
16. W. G. MEMBERS, D. Lloyd-Jones, R. Adams, M. Carnethon, G. De Simone, T. B. Ferguson, K. Flegal, E. Ford, K. Furie, A. Go, K. Greenlund, N. Haase, S. Hailpern, M. Ho, V. Howard, B. Kissela, S. Kittner, D. Lackland, L. Lisabeth, A. Marelli, M. McDermott, J. Meigs, D. Mozaffarian, G. Nichol, C. O'Donnell, V. Roger, W. Rosamond, R. Sacco, P. Sorlie, R. Stafford, J. Steinberger, T. Thom, S. Wasserthiel-Smoller, N. Wong, J. Wylie-Rosett, Y. Hong, f. t. A. H. A. S. Committee and S. S. Subcommittee, *Circulation*, 2009, **119**, e21-e181.
17. P. A. McCullough, E. F. Philbin, J. A. Spertus, S. Kaatz, K. R. Sandberg and W. D. Weaver, *Journal of the American College of Cardiology*, 2002, **39**, 60-69.
18. A. S. Maisel, J. Koon, P. Krishnaswamy, R. Kazenegra, P. Clopton, N. Gardetto, R. Morrissey, A. Garcia, A. Chiu and A. De Maria, *American heart journal*, 2001, **141**, 367-374.
19. M. L. Rawlins, W. E. Owen and W. L. Roberts, *American journal of clinical pathology*, 2005, **123**, 439-445.
20. C. Bjurman, M. Larsson, P. Johanson, M. Petzold, B. Lindahl, M. L. X. Fu and O. Hammarsten, *Journal of the American College of Cardiology*, 2013, **62**, 1231-1238.
21. S. Takeda, A. Yamashita, K. Maeda and Y. Maéda, *Nature*, 2003, **424**, 35-41.
22. 2013.
23. H. A. Katus, A. Remppis, S. Looser, K. Hallermeier, T. Scheffold and W. Kubler, in *J Mol Cell Cardiol*, England, 1989, vol. 21, pp. 1349-1353.
24. H. A. Katus, A. Remppis, T. Scheffold, K. W. Diederich and W. Kuebler, *American Journal of Cardiology*, 1991, **67**, 1360-1367.
25. J. S. Alpert, K. Thygesen, A. Jaffe and H. D. White, in *Heart*, England, 2008, vol. 94, pp. 1335-1341.
26. A. S. Jaffe, L. Babuin and F. S. Apple, *Journal of the American College of Cardiology*, 2006, **48**, 1-11.
27. J. K. French and H. D. White, *Heart*, 2004, **90**, 99-106.

28. R. Latini, S. Masson, I. S. Anand, E. Missov, M. Carlson, T. Vago, L. Angelici, S. Barlera, G. Parrinello, A. P. Maggioni, G. Tognoni, J. N. Cohn and F. T. I. for the Val-He, *Circulation*, 2007, **116**, 1242-1249.
29. P. Berger and C. Sturgeon, *Trends in Endocrinology & Metabolism*.
30. F. L. Cate, C. Moffett, A. M. Gronowski, D. G. Grenache, K. E. Hartmann and A. Woodworth, *Clinica Chimica Acta*, 2013, **421**, 104-108.
31. *Journal*, 2014, 1-2.
32. T. R. J. Holford, F. Davis and S. P. J. Higson, *Biosensors and Bioelectronics*, 2012, **34**, 12-24.
33. F. J. Morgan, S. Birken and R. E. Canfield, *J Biol Chem*, 1975, **250**, 5247-5258.
34. L. A. Cole, *Placenta*, 2010, **31**, 653-664.
35. L. A. Cole, *Reproductive Biology and Endocrinology : RB&E*, 2010, **8**, 102-102.
36. P. L. Storrington, R. E. Gaines-Das and D. R. Bangham, *The Journal of endocrinology*, 1980, **84**, 295-310.
37. S. Birken and R. Canfield, in *Chorionic Gonadotropin*, ed. S. Segal, Springer US, 1980, ch. 5, pp. 65-88.
38. P. Kumar and S. F. Sait, *Journal of Human Reproductive Sciences*, 2011, **4**, 2-7.
39. L. A. Cole, *Clinical chemistry*, 1997, **43**, 2233-2243.
40. J. N. Macri, R. V. Kasturi, D. A. Krantz, E. J. Cook, N. D. Moore, J. A. Young, K. Romero and J. W. Larsen, Jr., *Am J Obstet Gynecol*, 1990, **163**, 1248-1253.
41. R. Berkowitz, M. Ozturk, D. Goldstein, M. Bernstein, L. Hill and J. R. Wands, *Obstet Gynecol*, 1989, **74**, 212-216.
42. I. Marcillac, F. Troalen, J.-M. Bidart, P. Ghillani, V. Ribrag, B. Escudier, B. Malassagne, J.-P. Droz, C. Lhommé, P. Rougier, P. Duvillard, M. Prade, P.-M. Lugagne, F. Richard, T. Poynard, C. Bohuon, J. Wands and D. Bellet, *Cancer Research*, 1992, **52**, 3901-3907.
43. G. L. Perkins, E. D. Slater, G. K. Sanders and J. G. Prichard, *Am Fam Physician*, 2003, **68**, 1075-1082.
44. T. Malati, *Indian Journal of Clinical Biochemistry*, 2007, **22**, 17-31.

45. J. Coste, N. Job-Spira, H. Fernandez, E. Papiernik and A. Spira, *Am J Epidemiol*, 1991, **133**, 839-849.
46. T. E. Goldner, H. W. Lawson, Z. Xia and H. K. Atrash, *MMWR CDC Surveill Summ*, 1993, **42**, 73-85.
47. R. Varma and J. Gupta, *BMJ Clinical Evidence*, 2009, **2009**, 1406.
48. C. Chandrasekhar, *Clinical Imaging*, 2008, **32**, 468-473.
49. A. M. Fernandez-Alonso, C. J. Valdera-Simbron, G. Fiol-Ruiz, F. Rodriguez-Sanchez, P. Chedraui and F. R. Perez-Lopez, *Gynecol Endocrinol*, 2011, **27**, 1061-1064.
50. S. Birken, P. Berger, J.-M. Bidart, M. Weber, A. Bristow, R. Norman, C. Sturgeon and U.-H. Stenman, *Clinical chemistry*, 2003, **49**, 144-154.
51. C. M. Thomas, F. J. Reijnders, M. F. Segers, W. H. Doesburg and R. Rolland, *Clinical chemistry*, 1990, **36**, 651-655.
52. F. L. Cate, C. Moffett, A. M. Gronowski, D. G. Grenache, K. E. Hartmann and A. Woodworth, *Clinica chimica acta; international journal of clinical chemistry*, 2013, **421**, 10.1016/j.cca.2013.1002.1026.
53. L. A. Cole, *Expert Rev Mol Diagn*, 2009, **9**, 721-747.
54. D. N. Greene, R. L. Schmidt, S. M. Kamer, D. G. Grenache, C. Hoke and T. S. Lorey, *Clinica chimica acta; international journal of clinical chemistry*, 2013, **415**, 317-321.
55. A. M. Gronowski, M. Powers, U. H. Stenman, L. Ashby and M. G. Scott, *Clinical chemistry*, 2009, **55**, 1885-1886.
56. L. A. Cole, *Clinical chemistry and laboratory medicine : CCLM / FESCC*, 2012, **50**, 617-630.
57. Siemens, IMMULITE 1000 Immunoassay System, (accessed 10th June, 2015).
58. J. Švitel, A. Dzgoev, K. Ramanathan and B. Danielsson, *Biosensors and Bioelectronics*, 2000, **15**, 411-415.
59. R. G. Heideman, R. P. H. Kooyman and J. Greve, *Sensors and Actuators B: Chemical*, 1993, **10**, 209-217.
60. S. Rodriguez-Mozaz, M. L. de Alda and D. Barceló, *Water Research*, 2005, **39**, 5071-5079.
61. J. Zhou, N. Gan, T. Li, H. Zhou, X. Li, Y. Cao, L. Wang, W. Sang and F. Hu, *Sensors and Actuators B: Chemical*, 2013, **178**, 494-500.

62. R. Chauhan, P. R. Solanki, J. Singh, I. Mukherjee, T. Basu and B. D. Malhotra, *Food Control*, 2015, **52**, 60-70.
63. J. Ngeh-Ngwainbi, P. H. Foley, S. S. Kuan and G. G. Guilbault, *Journal of the American Chemical Society*, 1986, **108**, 5444-5447.
64. Y.-H. Dou, S. J. Haswell, J. Greenman and J. Wadhawan, *Electroanalysis*, 2012, **24**, 264-272.
65. M. Giannetto, L. Elviri, M. Careri, A. Mangia and G. Mori, *Biosensors and Bioelectronics*, 2011, **26**, 2232-2236.
66. R. Raiteri, M. Grattarola, H.-J. Butt and P. Skládal, *Sensors and Actuators B: Chemical*, 2001, **79**, 115-126.
67. J. P. Gosling, *Immunoassays: A Practical Approach*, Oxford University Press, Oxford, 2000.
68. K. D. Elgert, in *Immunology: Understanding the Immune System*, Wiley, New York, 1996, ch. 4, pp. 58-78.
69. D. E. Williams, H. Xu and J. R. Lu, *J Phys Chem B*, 2006, **110**, 1907-1914.
70. A. P. F. Turner, I. Karube and G. S. Wilson, *Biosensors – Fundamentals and Applications*, Oxford University Press, Oxford, New York, Tokyo, 1987.
71. A. P. Le Brun, S. A. Holt, D. S. Shah, C. F. Majkrzak and J. H. Lakey, *Biomaterials*, 2011, **32**, 3303-3311.
72. B. J. Cowsill, T. A. Waigh, S. Eapen, R. Davies and J. R. Lu, *Soft Matter*, 2012, **8**, 9847-9854.
73. H. Xu, X. Zhao, C. Grant, J. R. Lu, D. E. Williams and J. Penfold, *Langmuir*, 2006, **22**, 6313-6320.
74. M. M. L. M. Vareiro, J. Liu, W. Knoll, K. Zak, D. Williams and A. T. A. Jenkins, *Analytical Chemistry*, 2005, **77**, 2426-2431.
75. H. Xu, X. Zhao, J. R. Lu and D. E. Williams, *Biomacromolecules*, 2007, **8**, 2422-2428.
76. V. Gubala, C. Crean, R. Nooney, S. Hearty, B. McDonnell, K. Heydon, R. O'Kennedy, B. D. MacCraith and D. E. Williams, *Analyst*, 2011, **136**, 2533-2541.
77. J. Yakovleva and J. Emnéus, in *Bioelectrochemistry: Fundamentals, Experimental Techniques and Applications*, ed. P. N. Bartlett, John Wiley & Sons, Ltd, 2008, pp. 377-410.
78. R. S. Yalow and S. A. Berson, *Nature*, 1959, **184 (Suppl 21)**, 1648-1649.

79. R. P. Ekins, *Clinica Chimica Acta*, 1960, **5**, 453-459.
80. J. Reed and J. K. Gimzewski, in *The Immunoassay Handbook (Fourth Edition)*, ed. D. Wild, Elsevier, Oxford, 2013, pp. 203-207.
81. M. B. Ranke and P. E. Mullis, *Diagnostics of Endocrine Function in Children and Adolescents*, Karger, 2011.
82. S. Morikawa, T. Sakai, K. Murata, K. Banno, T. Sato, T. Takai and T. Suzuki, *Journal of Pharmaceutical and Biomedical Analysis*, 1998, **16**, 1267-1274.
83. L. E. Miles and C. N. Hales, *Nature*, 1968, **219**, 186-189.
84. K. L. Campbell, O. C. Schultheiss and D. C. McClelland, *Clin Biochem*, 1999, **32**, 83-85.
85. Siemens, *Journal*, 2010.
86. E. Engvall and P. Perlmann, *J Immunol*, 1972, **109**, 129-135.
87. E. Engvall and P. Perlmann, *Immunochemistry*, 1971, **8**, 871-874.
88. B. K. Van Weemen and A. H. Schuurs, *FEBS Lett*, 1972, **24**, 77-81.
89. B. K. Van Weemen and A. H. W. M. Schuurs, *FEBS Letters*, 1971, **15**, 232-236.
90. M. J. Cormier and P. M. Prichard, *Journal of Biological Chemistry*, 1968, **243**, 4706-4714.
91. S. Avrameas and J. Uriel, *C R Acad Sci Hebd Seances Acad Sci D*, 1966, **262**, 2543-2545.
92. P. K. Nakane and G. B. Pierce, Jr., *J Histochem Cytochem*, 1966, **14**, 929-931.
93. P. K. Nakane, *Annals of the New York Academy of Sciences*, 1975, **254**, 203-210.
94. G. B. Wisdom, *Clinical chemistry*, 1976, **22**, 1243-1255.
95. A. Voller, A. Bartlett and D. E. Bidwell, *Journal of Clinical Pathology*, 1978, **31**, 507-520.
96. S. X. Leng, J. E. McElhaney, J. D. Walston, D. Xie, N. S. Fedarko and G. A. Kuchel, *The journals of gerontology. Series A, Biological sciences and medical sciences*, 2008, **63**, 879-884.
97. I. Hemmila, *Clinical chemistry*, 1985, **31**, 359-370.
98. A. Voller, D. E. Bidwell and A. Bartlett, *Bulletin of the World Health Organization*, 1976, **53**, 55-65.

99. T. H. Fereja, A. Hymete and T. Gunasekaran, *ISRN Spectroscopy*, 2013, **2013**, 12.
100. A. T. R. Williams, *An Introduction to Fluorescence Spectroscopy*, Perkin-Elmer, 1981.
101. E. Soini and I. Hemmilä, *Clinical chemistry*, 1979, **25**, 353-361.
102. W. B. Dandliker, H. C. Schapiro, J. W. Meduski, R. Alonso, F. G. A. and J. R. Hamrick Jr., *Immunochemistry*, 1964, **1**, 324.
103. W. B. Dandliker and V. A. De Saussure, *Immunochemistry*, 1970, **7**, 799-828.
104. W. B. Dandliker and S. A. Levison, *Immunochemistry*, 1968, **5**, 171-183.
105. R. P. Tengerdy, *J Lab Clin Med*, 1967, **70**, 707-714.
106. E. F. Ullman, *Journal*, 1976.
107. D. S. Smith, *FEBS Letters*, 1977, **77**, 25-27.
108. E. F. Ullman, M. Schwarzberg and K. E. Rubenstein, *J Biol Chem*, 1976, **251**, 4172-4178.
109. E. J. Shaw, R. A. Watson, J. Landon and D. S. Smith, *Journal of Clinical Pathology*, 1977, **30**, 526-531.
110. K. Pettersson, H. Siitari, I. Hemmilä, E. Soini, T. Lövgren, V. Hänninen, P. Tanner and U. H. Stenman, *Clinical chemistry*, 1983, **29**, 60-64.
111. K. D. McClatchey, *Clinical Laboratory Medicine*, Lippincott Williams & Wilkins, 2002.
112. H. Rinderknecht, *Experientia*, 1960, **16**, 430-431.
113. F. Tietze, G. E. Mortimore and N. R. Lomax, *Biochimica et Biophysica Acta*, 1962, **59**, 336-346.
114. W. B. Dandliker and R. Alonso, *Immunochemistry*, 1967, **4**, 191-196.
115. P. Brandtzaeg, *Ann N Y Acad Sci*, 1975, **254**, 35-54.
116. L. Amante, A. Ancona and L. Forni, *J Immunol Methods*, 1972, **1**, 289-301.
117. , !!! INVALID CITATION !!! {}.
118. F. Yahioğlu, C. W. Pouton and M. D. Threadgill, *Bioconjug Chem*, 1997, **8**, 611-616.
119. S. Katsh, F. W. Leaver, J. S. Reynolds and G. F. Katsh, *Journal of Immunological Methods*, 1974, **5**, 179-187.
120. A. T. R. Williams, *Fluoroimmunoassay: A Review of Present Methods*, Perkin-Elmer, 1980.

121. P. von Lode, J. Rainaho and K. Pettersson, *Clinical chemistry*, 2004, **50**, 1026-1035.
122. G. Mathis, *Clinical chemistry*, 1993, **39**, 1953-1959.
123. *United States Pat.*, 4451149, 1984.
124. C. Dodeigne, L. Thunus and R. Lejeune, *Talanta*, 2000, **51**, 415-439.
125. R. Pyati and M. M. Richter, *Annual Reports Section "C" (Physical Chemistry)*, 2007, **103**, 12-78.
126. K. Andrzej, in *Electrogenerated Chemiluminescence*, CRC Press, 2004, pp. 163-211.
127. Y. Zu, F.-R. F. Fan and A. J. Bard, *The Journal of Physical Chemistry B*, 1999, **103**, 6272-6276.
128. D. M. Hercules, *Accounts of Chemical Research*, 1969, **2**, 301-307.
129. E. H. White, in *A Symposium on Light and Life*, eds. W. D. McElroy and B. Glass, Johns Hopkins Press, Baltimore, 1 edn., 1961, pp. 183-195.
130. E. H. White, O. Zafiriou, H. H. Kagi and J. H. M. Hill, *Journal of the American Chemical Society*, 1964, **86**, 940-941.
131. C.-F. Duan and H. Cui, *Chemical Communications*, 2009, 2574-2576.
132. Z.-F. Zhang, H. Cui and M.-J. Shi, *Physical Chemistry Chemical Physics*, 2006, **8**, 1017-1021.
133. Z. F. Zhang, H. Cui, C. Z. Lai and L. J. Liu, *Anal Chem*, 2005, **77**, 3324-3329.
134. Z. Wang, J. Hu, Y. Jin, X. Yao and J. Li, *Clinical chemistry*, 2006, **52**, 1958-1961.
135. H.-S. Zhuang, J.-L. Huang and G.-N. Chen, *Analytica Chimica Acta*, 2004, **512**, 347-353.
136. A. Scorilas, K. Agiamarnioti and K. Papadopoulos, *Clinica Chimica Acta*, 2005, **357**, 159-167.
137. A. Roda, E. Michelini, L. Cevenini, D. Calabria, M. M. Calabretta and P. Simoni, *Analytical Chemistry*, 2014, **86**, 7299-7304.
138. C. Wang, J. Wu, C. Zong, J. Xu and H.-X. Ju, *Chinese Journal of Analytical Chemistry*, 2012, **40**, 3-10.
139. N. Ismail, G. E. Fish and M. B. Smith, *Journal of Clinical Microbiology*, 2004, **42**, 610-617.
140. J. Lin and H. Ju, *Biosensors & bioelectronics*, 2005, **20**, 1461-1470.

141. W. R. G. Baeyens, S. G. Schulman, A. C. Calokerinos, Y. Zhao, A. M. García Campaña, K. Nakashima and D. De Keukeleire, *Journal of Pharmaceutical and Biomedical Analysis*, 1998, **17**, 941-953.
142. B. B. Technology, ELISA Kits , ELISA Principle - Immunoassays, <https://www.bosterbio.com/protocol-and-troubleshooting/elisa-principle>, (accessed 17th February, 2017).
143. S. Kerrigan and W. H. Phillips Jr, *Clinical chemistry*, 2001, **47**, 540-547.
144. C. Shao-Hsuan Chuag and Guan-Hua Chen and Hsin-Hao Chou and Shu-Wei Shen and Chien-Fu, *Science and Technology of Advanced Materials*, 2013, **14**, 044403.
145. V. Mani, B. V. Chikkaveeraiah and J. F. Rusling, *Expert opinion on medical diagnostics*, 2011, **5**, 381-391.
146. J. F. Rusling, C. V. Kumar, J. S. Gutkind and V. Patel, *The Analyst*, 2010, **135**, 2496-2511.
147. J. Wang, *Analyst*, 2005, **130**, 421-426.
148. S. N. Kim, J. F. Rusling and F. Papadimitrakopoulos, *Adv Mater*, 2007, **19**, 3214-3228.
149. J. Wang, *Electroanalysis*, 2007, **19**, 769-776.
150. M. Díaz-González, M. B. González-García and A. Costa-García, *Electroanalysis*, 2005, **17**, 1901-1918.
151. M. M. Richter, *Chemical Reviews*, 2004, **104**, 3003-3036.
152. K. Kadimisetty, S. Malla, N. Sardesai, A. A. Joshi, R. C. Faria, N. Lee and J. F. Rusling, *Analytical chemistry*, 2015, **87**, 4472-4478.
153. A. Ravalli, D. Voccia, I. Palchetti and G. Marrazza, *Biosensors*, 2016, **6**, 39.
154. A. Warsinke, A. Benkert and F. W. Scheller, *Fresenius J Anal Chem*, 2000, **366**, 622-634.
155. J. Do and C. H. Ahn, *Lab on a chip*, 2008, **8**, 542-549.
156. G. Proczek, A. L. Gassner, J. M. Busnel and H. H. Girault, *Analytical and bioanalytical chemistry*, 2012, **402**, 2645-2653.
157. D. M. Pearce, D. P. Shenton, J. Holden and C. A. Gaydos, *IEEE transactions on bio-medical engineering*, 2011, **58**, 755-758.
158. C. F. Woolley and M. A. Hayes, *Bioanalysis*, 2013, **5**, 245-264.
159. M. P. Kreuzer, R. McCarthy, M. Pravda and G. G. Guilbault, *Analytical Letters*, 2005, **37**, 943-956.

160. M. Dequaire, C. Degrand and B. Limoges, *Analytical Chemistry*, 2000, **72**, 5521-5528.
161. J. Qiu and J. Song, *Analytical Biochemistry*, 1996, **240**, 13-16.
162. Y. I. Dykhal, E. P. Medyantseva, N. R. Murtazina, G. R. Safina, G. K. Budnikov and N. V. Kalacheva, *Applied Biochemistry and Microbiology*, 2003, **39**, 553-558.
163. I. A. Alam and G. D. Christian, *Analytical Letters*, 1982, **15**, 1449-1456.
164. F. J. Hayes, H. B. Halsall and W. R. Heineman, *Analytical Chemistry*, 1994, **66**, 1860-1865.
165. W. O. Ho, D. Athey and C. J. McNeil, *Biosensors and Bioelectronics*, 1995, **10**, 683-691.
166. E. M. Abad-Villar, M. T. Fernández-Abedul and A. n. Costa-García, *Analytica Chimica Acta*, 2002, **453**, 63-69.
167. J. Janata and G. F. Blackburn, *Annals of the New York Academy of Sciences*, 1984, **428**, 286-292.
168. J. Janata, *Journal of the American Chemical Society*, 1975, **97**, 2914-2916.
169. M. E. Meyerhoff, B. Fu, E. Bakker, J. H. Yun and V. C. Yang, *Anal Chem*, 1996, **68**, 168A-175A.
170. A. Qureshi, J. H. Niazi, S. Kallempudi and Y. Gurbuz, *Biosensors and Bioelectronics*, 2010, **25**, 2318-2323.
171. P. Bataillard, F. Gardies, N. Jaffrezic-Renault, C. Martelet, B. Colin and B. Mandrand, *Analytical Chemistry*, 1988, **60**, 2374-2379.
172. A. Gebbert, M. Alvarez-Icaza, W. Stoecklein and R. D. Schmid, *Analytical Chemistry*, 1992, **64**, 997-1003.
173. C. Berggren and G. Johansson, *Analytical Chemistry*, 1997, **69**, 3651-3657.
174. J. C. Thompson, J. A. Mazoh, A. Hochberg, S. Y. Tseng and J. L. Seago, *Analytical Biochemistry*, 1991, **194**, 295-301.
175. M. I. Prodromidis, *Electrochimica Acta*, 2010, **55**, 4227-4233.
176. E. Katz and I. Willner, *Electroanalysis*, 2003, **15**, 913-947.
177. C. G. Bauer, A. V. Eremenko, E. Ehrentreich-Förster, F. F. Bier, A. Makower, H. B. Halsall, W. R. Heineman and F. W. Scheller, *Analytical Chemistry*, 1996, **68**, 2453-2458.
178. M. A. Cousino, T. B. Jarbawi, H. B. Halsall and W. R. Heineman, *Anal Chem*, 1997, **69**, 544A-549A.

179. A. Chaubey and B. D. Malhotra, *Biosensors & bioelectronics*, 2002, **17**, 441-456.
180. M. Del Carlo and M. Mascini, *Analytica Chimica Acta*, 1996, **336**, 167-174.
181. S. Laschi, M. Fránek and M. Mascini, *Electroanalysis*, 2000, **12**, 1293-1298.
182. J. Wang, A. Ibanez and M. P. Chatrathi, *Electrophoresis*, 2002, **23**, 3744-3749.
183. A. M. Bond, G. B. Deacon, J. Howitt, D. R. MacFarlane, L. Spiccia and G. Wolfbauer, *Journal of The Electrochemical Society*, 1999, **146**, 648-656.
184. M. Grätzel, *Journal of Photochemistry and Photobiology C: Photochemistry Reviews*, 2003, **4**, 145-153.
185. A. J. Edwards and R. A. Durst, *Electroanalysis*, 1995, **7**, 838-845.
186. A. J. Baumner and R. D. Schmid, *Biosensors & bioelectronics*, 1998, **13**, 519-529.
187. C.-H. Yoon, J.-H. Cho, H.-I. Oh, M.-J. Kim, C.-W. Lee, J.-W. Choi and S.-H. Paek, *Biosensors and Bioelectronics*, 2003, **19**, 289-296.
188. S. Dai and M. E. Meyerhoff, *Electroanalysis*, 2001, **13**, 276-283.
189. Z. Zhelev, C. Hyde, E. Youngman, M. Rogers, S. Fleming, T. Slade, H. Coelho, T. Jones-Hughes and V. Nikolaou, *BMJ*, 2015, **350**.
190. O. E. Fayemi, A. S. Adekunle and E. E. Ebenso, *Sensing and Bio-Sensing Research*, 2017, **13**, 17-27.
191. S. Thiagarajan, T.-H. Tsai and S.-M. Chen, *Biosensors and Bioelectronics*, 2009, **24**, 2712-2715.
192. B. E. K. S. H. J. C. C. V. K.V. Harisha, *Anal. Bioanal. Electrochem.*, 2015, **7**, 454-465.
193. M. Zidan, T. W. Tee, A. H. Abdullah, Z. Zainal and G. J. Kheng, *Int J Electrochem Sci*, 2011, **6**, 279-288.
194. P. B. Hawk, *Hawk's Physiological Chemistry*, McGraw-Hill Book Co., 14th edn., 1965.
195. K. Rave, L. Nosek, J. Posner, T. Heise, K. Roggen and E.-J. van Hoogdalem, *Nephrology Dialysis Transplantation*, 2006, **21**, 2166-2171.
196. *Textbook of Biochemistry and Human Biology*, Prentice-Hall of India Private Limited, New Delhi, 3rd edn., 2006.
197. F. Moussa, G. Kanoute, C. Herrenknecht, P. Levillain and F. Trivin, *Analytical Chemistry*, 1988, **60**, 1179-1185.

198. A. Kumar, S. Chandna, T. Bamrah and A. Kadian, *New York Science Journal*, 2012, **5**, 10-15.

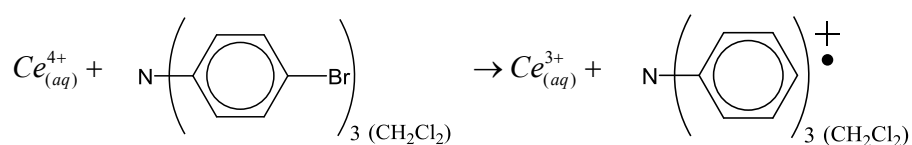
Chapter 2

Dynamic Electrochemistry

2.1 Basic Electrochemistry

Electrochemistry is the study of charge transfer processes. The process of electron transfer may occur homogeneously in solution or heterogeneously at (or on) the surface of an electrode. In homogeneous solution, electrons are transferred from one species to another *via* chemical reaction processes in a reaction known as an oxidation-reduction ("redox"). In heterogeneous systems, the interface is typically of solid | liquid variety consisting an electron conductor and an ionic conductor. These are typically an electrode; usually a metal or semiconductor and the supporting electrolyte, respectively.¹ The interface may also be of liquid | liquid nature, termed the interface between two immiscible electrolyte solutions (ITIES), an example of this is water | dichloromethane. Both of these situations involve reactions occurring by charge transfer processes (*via* electrons or ions) depending on the nature of the reaction, which may occur spontaneously or require an external driving force. When the reaction is driven by an externally applied potential difference across an interface, it is electrochemical in nature. In contrast, the process of redox reactions is chemical, where two or more species react in homogeneous solution or across an interface. The difference in these systems is illustrated by the following processes:

$Fe_{(aq)}^{2+} - e_{(metal)}^- \rightarrow Fe_{(aq)}^{3+}$ is an electrochemically-driven redox process;



is an heterogeneous chemical electron transfer process;

$Ag_{(aq)}^+ + \frac{1}{2}I_{2(aq)} \rightarrow AgI_{(s)}$ is a homogenous chemical redox process.

For electrochemical reactions to take place, at least two electrodes are required with a half-reaction taking place at each electrode. A reaction may be initiated by the application of a potential difference to an electrode in solution (supporting electrolyte) through which electron transfer may occur at the electrode | electrolyte interface,¹ or the reaction may occur spontaneously (galvanic cells). It is therefore

important to discuss the fundamental mechanisms by which these reactions occur. Consider the simple electrode process shown below:



where A and B symbolise the oxidised and reduced forms of the redox couple respectively and n is the number of electrons (e^-) transferred per mol of A and B and the rate constants k_f and k_b describe the reduction and oxidation or cathodic and anodic processes respectively.

The electron transfer process can be realised in terms of energy and the favourability or driving force for the reaction. The electrochemical potential of the electrons of a species or metal, j , in a phase, α ($\bar{\mu}_j^\alpha$) is called the *Fermi level* or *Fermi energy* and corresponds to an electron energy (not an electrical potential) and represents the average energy of available electrons in phase α , related to the chemical potential of electrons in that phase (μ_j^α), and the inner potential (or Galvani potential), (ϕ) of α itself.² The value of $\bar{\mu}_j^\alpha$ is therefore defined as a sum of its chemical potential and the local electrostatic potential:

$$\bar{\mu}_j^\alpha = \mu_j^\alpha + zF\phi^\alpha \quad (2.2)$$

where z is the charge of the species, F is Faraday constant ($96484.6 \text{ C mol}^{-1}$).

The basic representation of the electron transfer process in relation to Fermi levels is shown in Fig. 15; to form B , electrons are required to transfer from the electrode phase to species A in the solution phase. To achieve this, electrons in the electrode need to be of higher Fermi energy than those for the species A , as to make the electron transfer favourable, either kinetically or thermodynamically. This can be understood by molecular orbital theory. By driving the electrode to more negative potentials (e.g. by use of a potentiostat), the energy of the electrons in the electrode is raised where with sufficient energy they may transfer into the lowest un-occupied molecular orbital (LUMO) of a species in the electrolyte. In that case, a flow of electrons occurs from electrode to solution known as a reduction (Fig. 15a). Similarly, a more positive potential may be imposed resulting in a lowering of the energy of the electrons. At a critical point, electrons from the highest occupied

molecular orbital (HOMO) of the species in the electrolyte will find a more favourable energy on the electrode and will transfer there. This is termed an oxidation (Fig. 15b).

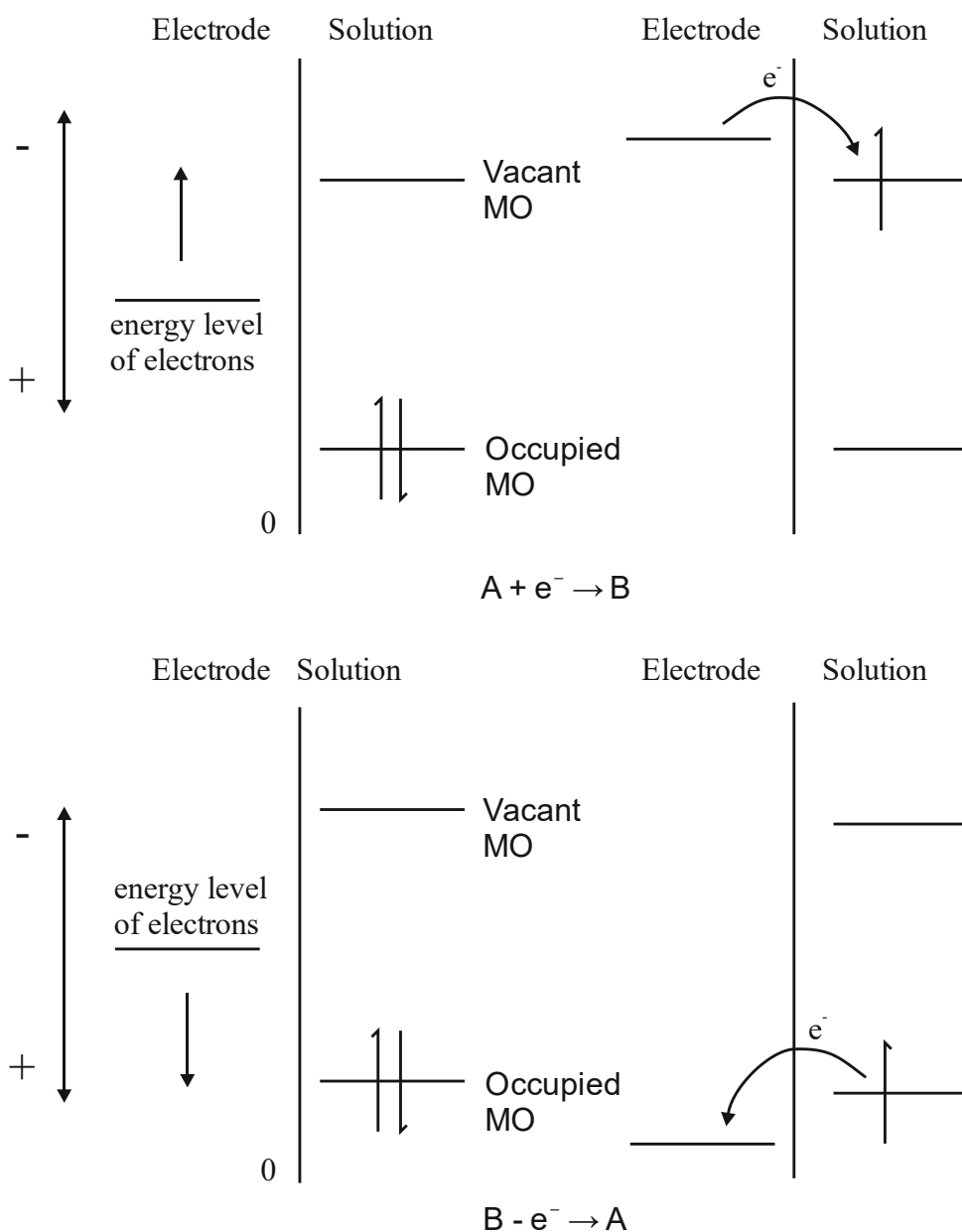
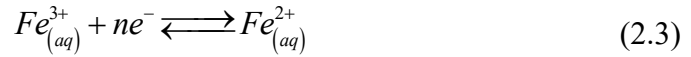


Fig. 15 Representation of (a) reduction and (b) oxidation process of species A in solution. Molecular orbitals of species A shown are the HOMO and the LUMO. The arrows illustrate the change energy of the electrons in the electrode where it is increasing and decreasing in (a) and (b) as a result of the application of a negative and positive potential respectively.

In the case of spontaneous reactions, the Fermi energy of one of the reactants may be sufficiently high or low enough to induce the electron transfer when connected to an

external circuit without the need for an external driving force. This phenomenon is widely used in the battery industry where electrical energy is produced from spontaneous reactions in a cell. Characteristically, the Fermi level of a metal or semiconductor depends on the work function of the material, for a solution phase, it is a function of the electrochemical potentials of the dissolved oxidised and reduced species.

For an example where A is Fe^{3+} and B is Fe^{2+} ;



this reaction is in equilibrium, therefore

$$\bar{\mu}_{\text{Fe}^{3+}}^{aq} = \bar{\mu}_{\text{Fe}^{2+}}^{aq} \quad (2.4)$$

For equilibrium to occur, the Fermi levels of the electrode and solution phases must be equal, where equality of electrochemical potentials is attained *via* the transfer of electrons from the phase of higher Fermi level to that of the lower Fermi level. The equality of the electrochemical potential can be written as in eq. (2.5)

$$\bar{\mu}_{\text{Fe}^{3+}}^{aq} + \bar{\mu}_{e^-} = \bar{\mu}_{\text{Fe}^{2+}}^{aq} \quad (2.5)$$

The Galvani potential difference of the system (*i.e.* the electric potential difference between two points in the bulk of two phases) can therefore be determined as follows:

$$\bar{\mu}_{\text{Fe}^{3+}}^{aq} + 3F\phi^{solution} + \bar{\mu}_{e^-} = \bar{\mu}_{\text{Fe}^{2+}}^{aq} + 2F\phi^{solution} \quad (2.6)$$

$$\mu_{\text{Fe}^{3+}}^0 + RT \ln \alpha_{\text{Fe}^{3+}} + 3F\phi^{solution} + \bar{\mu}_{e^-} - F\phi^{metal} = \mu_{\text{Fe}^{2+}}^0 + RT \ln \alpha_{\text{Fe}^{2+}} + 2F\phi^{solution} \quad (2.7)$$

$$F(\phi^{solution} - \phi^{metal}) = (-\mu_{\text{Fe}^{2+}}^0 + \mu_{e^-} + \mu_{\text{Fe}^{3+}}^0) + RT \ln \left(\frac{\alpha_{\text{Fe}^{3+}}}{\alpha_{\text{Fe}^{2+}}} \right) \quad (2.8)$$

$$\begin{aligned}\phi^{metal} - \phi^{solution} &= \left(\frac{\mu_{Fe^{3+}}^0 + \mu_{e^-} - \mu_{Fe^{2+}}^0}{F} \right) + \frac{RT}{F} \ln \left(\frac{\alpha_{Fe^{3+}}}{\alpha_{Fe^{2+}}} \right) \\ \Rightarrow E &= E^\theta + \frac{RT}{F} \ln \left(\begin{array}{c} \text{concentration} \\ \text{fraction} \end{array} \right)\end{aligned}\quad (2.9)$$

where $\bar{\mu}_{Fe^{2+/3+}}^{aq}$ is the electrochemical potential, $\mu_{Fe^{2+/3+}}^{aq}$ is the chemical potential and $\mu_{Fe^{2+/3+}}^0$ is the standard electrochemical potential for each of the species in solution.

$\alpha_{Fe^{2+/3+}}$ is the activity or *effective concentration* of the species, where $\alpha_j = \gamma_j C_j$; C_j is the concentration of species j , γ_j is the activity coefficient of unitless value greater than zero, where if $\gamma_j = 1$, the activity is the same as the concentration of the species of interest. The R term is the molar gas constant ($8.314 \text{ J mol}^{-1} \text{ K}^{-1}$) and T represents the absolute temperature (K). The difference on the left hand side of equation (2.9) is the Galvani potential. Typically, the potentials of electrodes (and half-cell electromotive forces) are referenced to the normal hydrogen electrode (NHE), or for the *absolute* or *single electrode potential*, referenced vs. the potential of a free electron in vacuum. The absolute potential of the NHE can be estimated as 4.6 V, thus the potential for the reduction of a proton,



is -4.6 eV . With this value, the standard potentials of other couples and reference electrodes can be expressed on the absolute scale.

Returning to eq. (2.9), this final derivation is similar to the Nernst equation, that describes a definitive relationship between the potential applied to the electrode and the concentration of redox species in solution at the interfacial region of the electrode, under conditions of thermodynamic control and equilibrium.

$$E = E^\theta + \frac{RT}{nF} \ln \frac{\gamma_A [A]}{\gamma_B [B]} \quad (2.11)$$

where the potential at equilibrium, E is related to the standard potential for the redox reaction, E^θ by the inclusion of activity coefficient effects from the oxidised and reduced species.^{3, 4} In reality it is difficult to determine activities, hence the formal

potential, $E^{\theta'}$ is used where the concentrations of species A and B are such that the ratio $[A]/[B]$ is unity, so that

$$E = E^{\theta'} + \frac{RT}{nF} \ln \frac{[A]}{[B]} \quad (2.12)$$

With respect to our simple case in eq. (2.1), if $E^{\theta'}$ is negative, the oxidised form is liable to be reduced, and the forward reaction (reduction) is more favourable.

The Nernst expression identifies two types of electrochemical experiments to undertake: the first is to fix the concentrations and the second is to fix the potential at the electrode | electrolyte interface. The former allows for a change in the potential difference across the electrode | electrolyte interface; the latter empowers the perturbation of concentration of the redox species; this is the realm of dynamic electrochemistry.

The rearrangement of equation (2.12) to calculate the concentration of oxidised and reduced species at the electrode surface is shown below:

$$\frac{[A]}{[B]} = \exp \left[\frac{nF}{RT} (E - E^{\theta'}) \right] \quad (2.13)$$

Since electron transfer between the electrode interface and redox species (and *vice versa*) occurs *via* quantum mechanical tunnelling, for any process of electron transfer, the species of interest must be located within a critical distance of the electrode surface (typically 10-30 Å).⁵⁻⁷ This is necessary as the electron tunnelling reduces rapidly at an exponential rate with increasing separation from the electrode surface. Hence the redox species must enter this critical area for subsequent passage of current to occur, where diffusion of the electroactive species from the bulk solution must first take place, this is discussed in section 2.3.

Once the above conditions are satisfied, electron transfer between the electrode and a redox-active solution-phase species is observed by the flow of current, often termed the Faradaic current, i , (ampere units) quantified *via* eq. 2.14. The current is directly related to the flux of reactant (number of moles of species passing through unit area in unit time at distance x from the electrode surface, J (mol cm⁻² s⁻¹)) undergoing oxidation or reduction at an electrode of area, S (cm²), as shown below:

$$i = nFSJ \quad (2.14)$$

The Nernst–Planck equation, given here for one dimensional transport, mathematically describes the flux

$$J_j(x,t) = -D_j \frac{\partial C_j(x,t)}{\partial x} - \frac{z_j F}{RT} D_j C_j \frac{\partial \phi(x,t)}{\partial x} + C_j v(x,t) \quad (2.15)$$

where D is the diffusion coefficient ($\text{cm}^2 \text{s}^{-1}$), $[\partial C_j(x,t)]/\partial x$ is the concentration gradient (at distance x and time t), $[\partial \phi(x,t)]/\partial x$ is the potential gradient, z_j is the charge of the electroactive species and $v(x,t)$ is the hydrodynamic velocity (in the x direction). The flux and mass transport effects are discussed later. Ultimately, the rate of reaction can be described as

$$\text{Rate (mol cm}^{-2} \text{ s}^{-1}) = \frac{i}{nFS} = \frac{J}{nF} \quad (2.16)$$

By IUPAC convention, currents due to reduction, i_{red} , are negative and those due to oxidation, i_{ox} , are positive. The extent of the charge passed between the electrode and solution is governed by Faraday's Laws, given as follows.

Faraday's first law of electrolysis: the amount of substance oxidised/reduced is proportional to the charge passed.

Faraday's second law of electrolysis: for a given charge, the amount of each particular substance that is converted is dependent upon the stoichiometry of the electrode reaction.

The charge carried by on one mole of electrons is defined by Faraday's constant, calculated from

$$F = q_0 N_A \quad (2.17)$$

where q_0 is the charge on one electron ($1.602 \times 10^{-19} \text{ C}$) and N_A is Avogadro's number ($6.023 \times 10^{23} \text{ mol}^{-1}$). The charge, Q measured in coulombs (C) is therefore defined by

$$Q = nNF \quad (2.18)$$

where N is the number of moles of reactant. The current is otherwise known as the rate at which charge is passed with time, where 1 A of current amounts to 1 C s⁻¹ charge passed every second:

$$i = \frac{dQ}{dt} \quad (2.19)$$

The total current observed resulting from an electrochemical process is the combination of both Faradaic and non-Faradaic processes:

$$i_t = i_f + i_{nf} \quad (2.20)$$

where i_t is the total current, i_f is the Faradaic current and i_{nf} is the sum of the current contributions from non-Faradaic processes. The Faradaic current results from a change of oxidation state of the electroactive species of interest under obedience of Faraday's law (*i.e.* the reaction of 1 mol of species involves a change of $n \times 96,487$ C). The magnitude of the Faradaic current is determined by the variables including the technique used, mass transport, electrode area, the applied potential and whether the charge transfer is limited by mass transport, electron transfer kinetics and chemical kinetics. Non-Faradaic currents are those that do not involve chemical reaction or electron transfer across the interface, only the accumulation of electrical charges on the electrode surface and in the electrolyte solution close to the interface. This arises from processes such as adsorption and desorption, changes in the structure of the electrode | electrolyte interface with varying potential or solution composition and as a result of the electric double layer that is present at the electrode | electrolyte interface. The latter gives rise to a capacitance at the electrode surface where the charging of the double layer occurs. This charging current is considered as a background (residual) process; a source of noise in the electrochemical system that gives rise to a limitation of the electrochemical system wherein the application of a voltage that is temporally dependant cannot be faster than the time constant (product of resistance, R and capacitance, C) for the capacitor charging. The second problem that arises from the non-Faradaic current is that it is intimately coupled with the Faradaic process through the Ohmic loss, where the solution resistance (R_s) acts as the major cause of this voltage drop. This parameter is related to both the cell geometry and the nature of the supporting electrolyte.⁸ This is problematic when seeking to subtract baseline currents from voltammograms.

If we consider the Cottrell equation that describes current as a function of time following a stepped potential perturbation in a diffusion limited case

$$i = \frac{SFC_j^{bulk}\sqrt{D}}{\sqrt{\pi t}} \quad (2.21)$$

where C_j^{bulk} is the concentration of species j in the bulk solution,⁵ we infer that for $t = 0$, $i \rightarrow \infty$. However in reality this does not occur, since the double layer imposes a capacitance, giving rise to a experimental and instrumental limitations for example mass transport, resistances and capacitance of the system and potentiostatic limitations, thus there is a need to consider Randles circuit that takes into account both resistance and capacitance in an electrochemical setup. We must first illustrate the arrangement and roles of the electrodes involved in the electrochemical investigation.

2.1.1 Electrodes and the Electrochemical Cell

Voltammetry requires a three electrode configuration as well as the highly conductive analyte/electrolyte solution. The three electrodes are the working electrode (WE), the reference electrode (RE) and the counter electrode (CE). The WE is where the half-reaction of interest occurs whose initiation is brought about by the application of a known potential (the potential difference - controlled by a potentiostat) between the working and reference electrodes. Ideally, the WE allows electron transfer to occur at its surface without participating in the reaction or reacting itself. The role of the RE is to maintain a constant potential with respect to the WE whilst current does not flow through it and should be thoroughly characterised. The CE allows the other half of the reaction to occur and should be sufficiently spaced from the working electrode to avoid interferences at the WE. Furthermore, the CE should be sufficiently sized with large surface area as to reduce the current density at its surface; this is necessary to avoid the processes occurring at this electrode from limiting or affecting the reaction process at the electrode of interest and hence the overall current observed. Typically a platinum wire or similar electrode is used. An example of a three electrode set up is shown in Fig. 16.

There are a variety of working electrodes to choose from ranging macro- to nano-sized surfaces, the choice of which depends on the type of experiment to be carried

out. Classically, most working electrodes were made of mercury due to excellent reproducibility and had easily renewable surfaces. However, the mercury electrode is not particularly useful for oxidation reactions since mercury itself is oxidised at very low positive potentials thus other working electrode materials must be used for performing oxidations.

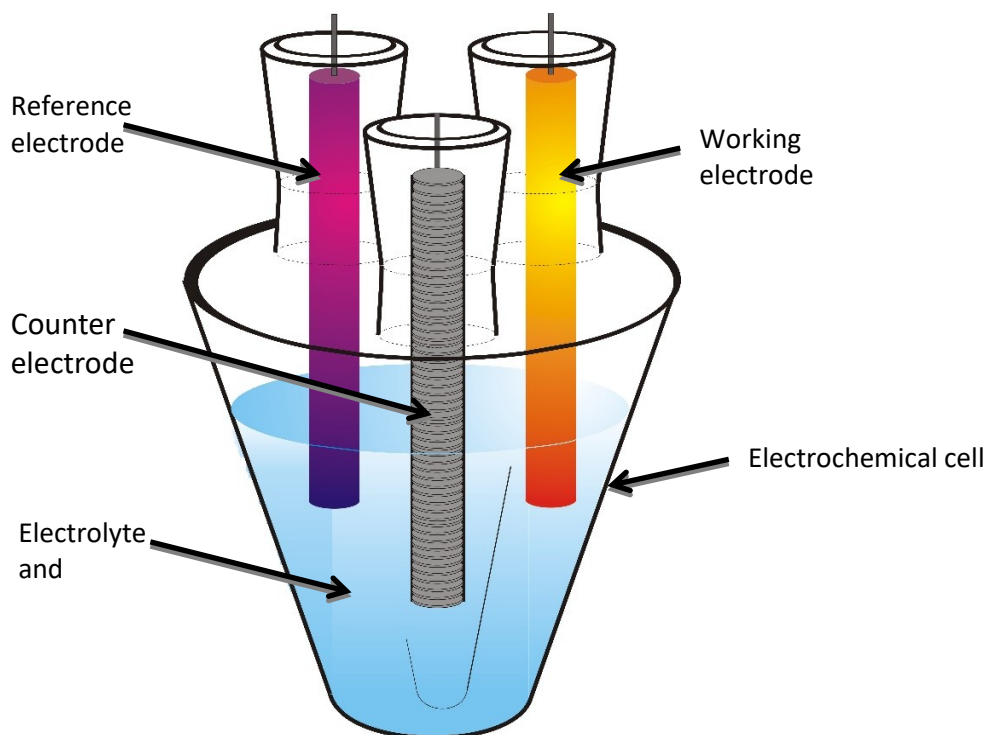


Fig. 16 Schematic example of three electrode set up for electrochemical experiments

Since biochemical reactions tend to occur at positive potentials, solid electrodes made of platinum, gold, carbon or other conductive/semi-conductive materials are used instead. These electrodes are relatively inexpensive, reusable and operate within a wide variety of potential windows though their major disadvantage is that the surface of these electrodes can interact irreversibly with the analyte or contaminants in the solution. This often changes the electrochemical behaviour, sometimes blocking the surface and impeding the electron transfer.

2.1.1.1 The Role of Supporting Electrolyte

The supporting electrolyte is employed to increase solution conductivity but must not affect the measurement *i.e.* electrochemically inert. This minimises Ohmic losses and consequently reduces the distortion effects on the current due to solution resistance.

The addition of electrolyte in high concentration (typically *ca.* 0.1 M compared to 1 mM of electroactive species) is also advantageous because most electrochemical measurements are dependent on activity as opposed to concentration; the high concentration of electrolyte maintains a constant ionic strength and therefore keeps the activity coefficients constant, even with variations in analyte concentration.

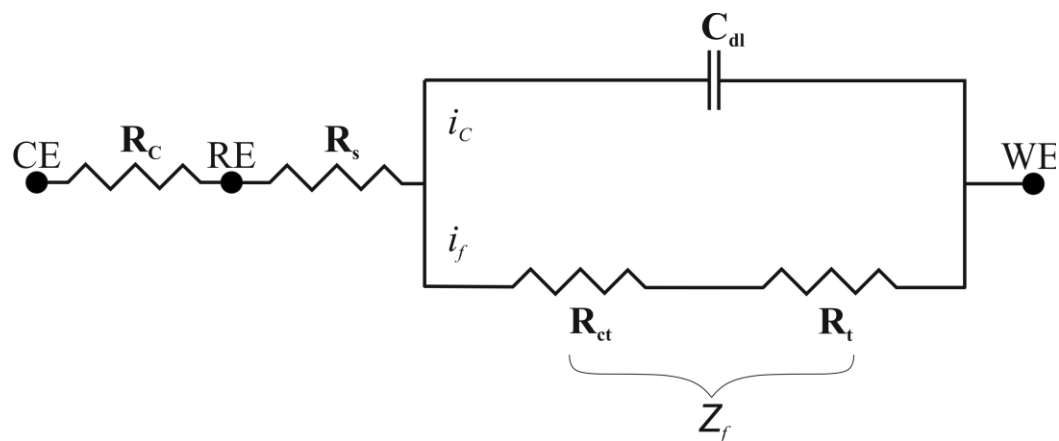


Fig. 17 Simple Schematic of a Randles circuit involving the double layer capacitance, C_{dl} . R_c , R_s , R_{ct} and R_t are the resistances for counter electrode, solution, charge transfer processes and transport processes respectively, where R_{ct} and R_t amount to the faradaic discharge processes. The terms i_c and i_f are the currents produced by the non-faradaic capacitance charging of the double layer and the faradaic redox process respectively.

The motion of charged ions from the electrolyte (rather than the redox analyte) is induced in or against the direction of the passing field (depending upon the ions charge *i.e.* positive or negative) as a means for conducting the current between the working and counter electrodes. This has the effect of suppressing migration of the electroactive species to within the double-layer region (section 2.2) at the electrode surface.^{1,9}

For a three electrode set-up for voltammetry of a solution containing an electroactive species, we must consider the transport, kinetic and solution resistances imposed on a system under current flow and the capacitance charging incurred at the electrode | electrolyte interface. This can be simply explained by the Randles circuit.

Electrochemical Cell

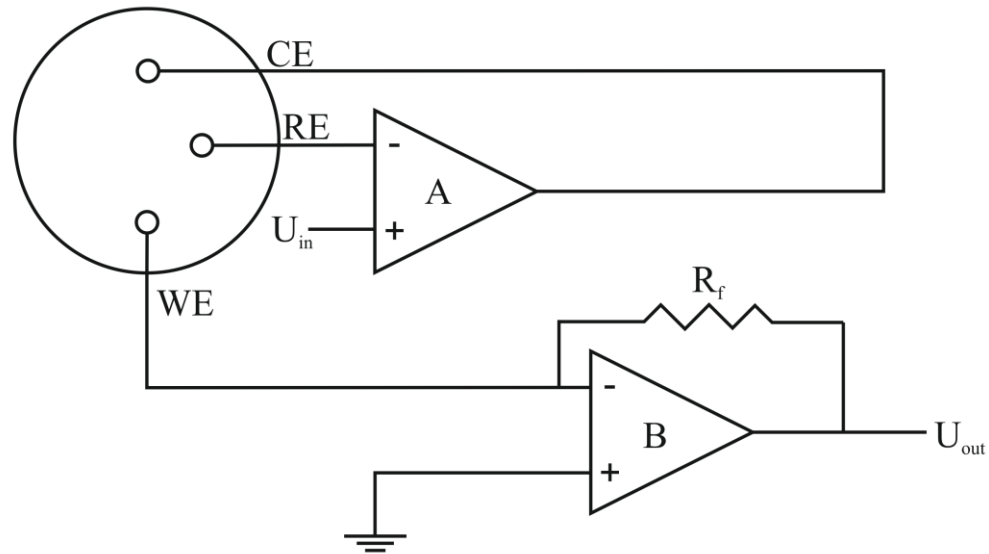


Fig. 18 Basic illustration of the potentiostat design. The current flows between the working and counter electrode where this current is converted to voltage by operational amplifier B, such that $U_{out} = -iR$. Operational amplifier A ensures no current flows through the reference electrode where the CE passes sufficient current to keep the reference potential constant. R_f is a feedback resistor.

The potential of the working electrode may be observed or controlled with respect to the constant potential established by the reference electrode the reference (eq. 2.22); this is equivalent to observing or controlling the energy of the electrons within the working electrode, hence

$$E = (\phi_M - \phi_S)_{working} - (\phi_M - \phi_S)_{reference} \quad (2.22)$$

2.2 Interfacial Region and the Electric Double Layer

As discussed, the interfacial region at the solid | liquid interface possesses a diffusion layer dependent upon concentration gradients and time. However there is another layer very close to the electrode surface, the electrical double layer. This layer consists of an array of charged particles and/or orientated dipoles formed to compensate for the excess charged imposed on the electrode (q_e). For example, a positively charged electrode attracts a layer of negative ions (and *vice versa*) to afford neutrality at the electrode surface, $q_e + q_s = 0$, where q_s represents the charge of the ions near to the electrode. The conception of this model dates back to the work of Helmholtz^{10, 11} in 1853 that proposed a compact monolayer of ions with opposite

charge to that of the interface thus neutralising the excess charge, with a linear potential. This model was a simple description of the double layer region, not taking into account specific adsorption of ions to the surface or the effects of random and thermal motion.^{3, 9} Another model proposed by Gouy¹² and Chapman¹³ introduced the concept of a diffuse double layer in which the accumulated ions, due to the Boltzmann distribution, extend to some distance from the solid surface. Stern¹⁴ later combined these theories in 1924 suggesting that the electrified solid | liquid interface includes both the rigid Helmholtz layer and the diffuse layer of Gouy and Chapman. In 1947 the specific adsorption of ions at the metal surface was pointed out by Grahame.¹⁵ In consecutive developments, the role of the solvent has been taken into account (Parsons 1954; Bockris 1963) where it was proposed that dipolar solvents, such as water, must also interact with the charged metal surface *via* their dipoles.

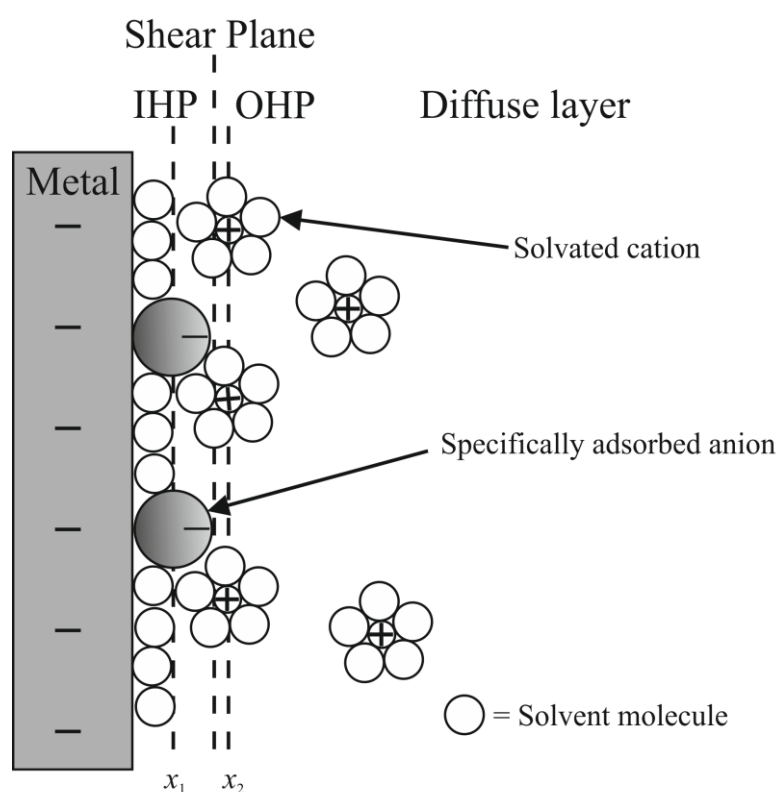


Fig. 19 Proposed model of the double-layer region under conditions where anions are specifically adsorbed.

The final double layer model then depicts two defined layers; the inner Helmholtz plane (IHP) and the outer Helmholtz plane (OHP) which precede the outer diffuse layer. As shown in Fig. 19, the IHP is composed of solvent molecules and

specifically adsorbed ions, extending distance x_1 from the electrode surface to form a "fixed" layer. At distance x_2 , the OHP reflects the imaginary "moveable" plane crossing the centre of the solvated ions at their closest approach to the electrode/interface surface.⁴ Between these two planes exists the Shear plane, a sharp cut-off point to distinguish the ions adhering to the surface and the extended mobile phase. The solvated ions are non-specifically adsorbed, attracted to the surface by long range coulombic forces. Overall, the IHP and OHP layers form a *compact layer* with thickness ≥ 10 nm. The outer layer represents the *diffuse layer* which due to thermal agitation in the solution, the non-specifically adsorbed ions are distributed in a three dimensional region that extends from the OHP into the bulk of the solution.

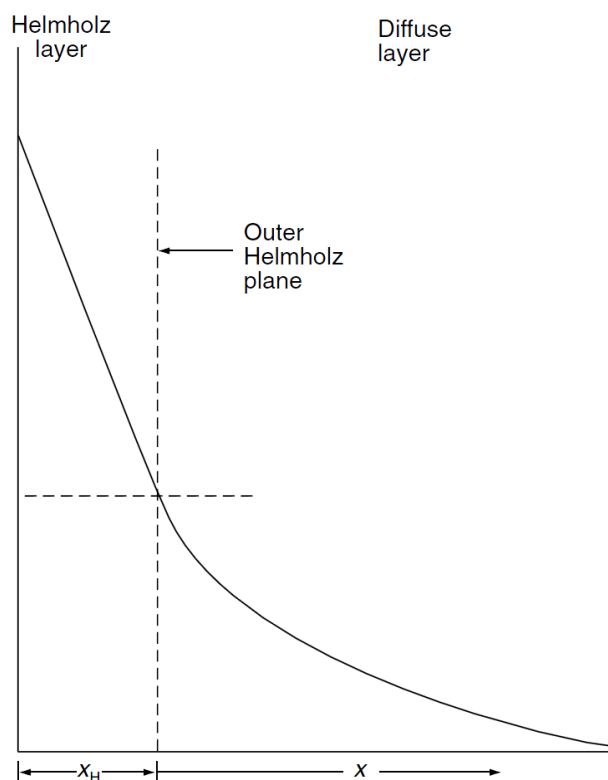


Fig. 20 Schematic illustration of the variation of the potential across the electrical double layer.⁴

Furthermore there is a potential drop over the double layer region proceeding into the bulk solution such that the potential experienced at edge of the double layer at distance x_H from the electrode surface is not the same as that imposed at the electrode. This is caused by the interactions of the charged adsorbed layer with the potential as it extends into solution.¹⁶ The effect of this potential drop across the diffuse layer can have undesirable effects on the kinetics of the electron transfer.

This may be due to defects in the double layer structure, blocking of the electrode surface by interactions with specifically adsorbed ions and counter ions therefore inhibiting electrode reactions or the rate constant for the heterogeneous electron transfer, k^0 may be a function of the supporting electrolyte concentration or of its ionic components. These instances are called *Frumkin effects*.

2.3 Mass Transport Controlled Reactions

Considering the same typical redox process (2.1)

The conversion of A to B involves at least the following steps:

- i. continual diffusive transport of A from the bulk solution to the electrode surface
- ii. heterogeneous electron transfer process at, or close to the electrode surface to form B , and
- iii. diffusion of species B from the electrode surface into the bulk solution.

This is further illustrated below in Fig. 21

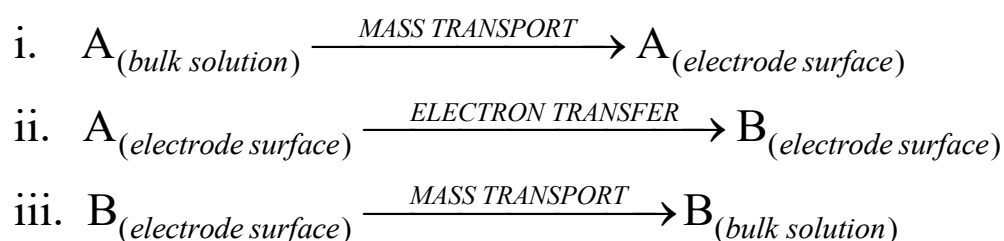


Fig. 21 Description of the transport and electron transfer processes that occur in our simple case.

Here, the rate of reduction of species A is dependent upon the slowest elementary step. This limitation may be associated with mass transport to and from the electrode surface or with the rate of heterogeneous electron transfer between electrode and reagent or *vice versa*. Other heterogeneous processes, such as adsorption or desorption of reactants, intermediates or products may govern in the initiation and rate of the electron transfer processes and may also cause fouling (poisoning) of the electrode surface, preventing further reaction. In addition, homogeneous chemical reactions such as the rearrangement of species in solution or their interaction with

other solution components, may precede or follow the heterogeneous electrode process *e.g.* decomposition of unstable products.¹⁷

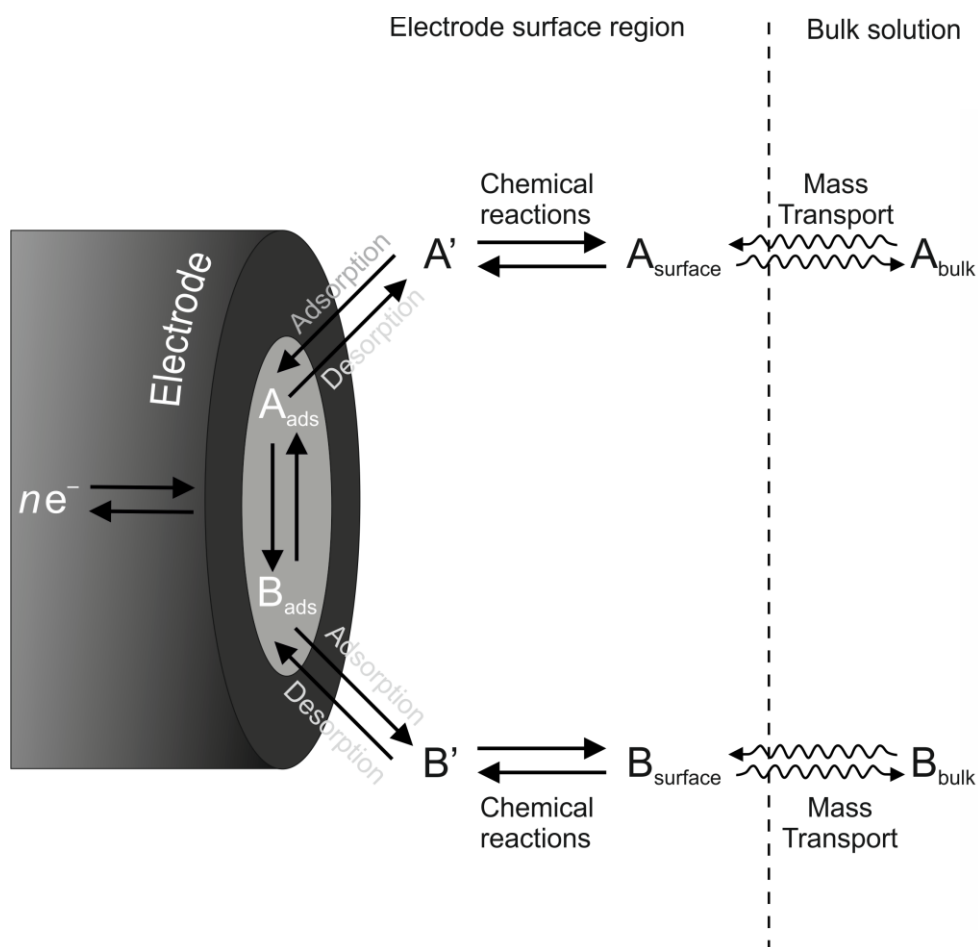


Fig. 22 Pathway of a general electrode reaction involving adsorption of reactants.

The heterogeneous electron transfer step may proceed through one of two methods; inner-sphere and outer-sphere mechanisms. The inner-sphere mechanisms are identified as those where the electron transfer process occurs *via* the direct contact of the electroactive species with the electrode surface. Outer-sphere mechanisms are defined as those where the electron transfer occurs a short distance away from the electrode surface (typically 10-20 Å) *via* electron tunnelling.¹⁷ As discussed previously, this occurs through the layer of solvent in direct contact with the electrode surface, such that the electroactive species and the electrode are separated sufficiently to imply the chemical interaction between them can be considered negligible, except for their electrostatic interaction.¹⁷

The transport of electroactive species from bulk to the solid | liquid interface and *vice versa* is a fundamental process in electrochemical dynamics and may occur *via*

several different mechanisms: convection, migration and diffusion. For a mass transport controlled reaction where electron transfer kinetics are fast, one or more of these processes may limit the rate of reaction.

2.3.1 Convection

Convective transport is concerned with movement of bulk species under the action of a mechanical force, this movement may be "natural" or "forced". Natural convection may result from temperature, density or pressure gradients which operate to randomly mix the solution in an unpredictable manner and is always present in any solution. Natural convection effects only begin to cause issues in electrochemical experiments when the measurement timescale extends to over periods of 10 - 20 seconds; adequate time for convective forces to take place, therefore natural convection can be excused if experimental timescales are shorter than this.^{5, 18, 19}

Forced convection is intentionally induced convection, usually by controlled stirring, bubbling, pumping or even *via* rotation of the electrode. Forced convection can be avoided by preventing stirring and vibrations in the electrochemical cell.² However, convective transport effects do not occur close to the electrode | solution interface as solid | liquid frictions and bouncing phenomena result in an immobile solution layer. This simplified splitting of the solution into two parts; the immobile stagnant layer and the remainder of the solution (homogeneous in nature due to agitations) introduces a convection-free layer *ca.* 30 - 50 μm thickness dependent upon fluid velocity, thermal and vibration induced agitations. The imposition of forced convection at maximum agitation reduces the convective-free layer to the order of *ca.* 10 - 20 μm .

2.3.2 Migration

Migration is the transport of ions under the influence of an electrical potential gradient for example; when a negative potential is imposed upon the working electrode, positive ions are attracted to the electrode surface and the negatively charged ions repelled. As mentioned previously, the addition of supporting electrolyte to the system has the effect of suppressing the significance of migration of the electroactive species to negligible levels, effectively shielding them from migratory effects.

2.3.3 Diffusion

Diffusion is an entropically driven, spontaneous process where the "random walk" movement of a species occurs under the influence of an electrochemical potential gradient.^{17, 20} This phenomenon may be better understood by the term "spreading". The diffusional properties of a particular species are determined by its hydrodynamic size, mobility and solution properties (*e.g.* viscosity). As previously discussed it is possible to restrict mass transfer of electroactive species to diffusion limitations only by the addition of supporting electrolyte and operating in a quiescent solution; most electrochemical methods are built on the assumption that such conditions are imposed, thus diffusion is a process of central importance. It is appropriate to take a closer look at the phenomenon of diffusion (in one-dimension) at a planar electrode and the mathematical models describing it.

Fick developed two laws describing diffusion relating the flux of a substance and its concentration as functions of time and position.⁵ Consider the case of linear (one-dimensional) diffusion where at any point from the electrode, x , there will be a diffusive flux quantified by Fick's first law:

$$J_j(x,t) = -D_j \frac{\partial C_j(x,t)}{\partial x} \quad (2.23)$$

where the proportional relationship to current is

$$J_j(x,t) = nFSD \frac{\partial C_j(x,t)}{\partial x} \quad (2.24)$$

Here ∂C_j is a partial derivative: $C = C(x,t)$. Fick's first law thereby states that the flux is proportional to the concentration gradient, where the negative sign implies the movement from high to low concentration.

Fick's second law derives how the concentration of species A changes with time.⁵ Both laws operate under the conditions of a concentration gradient that arises from the depletion or production of species at the electrode surface. This reaction at the electrode surface creates a "depletion layer" that becomes thicker (length δ) with increasing electrolysis time; this is known as the diffusion layer. Fig. 23 illustrates the concentration profiles of species A and B during the reduction of A to B where initially only species A is present in solution. In the beginning, the concentration of species A is that of the bulk concentration, though as the potential is applied, the

concentration of A at the surface becomes zero. At t_1 , the concentration gradient is steep and the diffusion layer is thin however. As time passes, the diffusion layer expands (to δ_2 and δ_3 at t_2 and t_3) as the region of depleted species A increases, and hence the concentration gradient decreases. On the other hand, as the reduction proceeds and species B is formed, the concentration of species B gradually increases from the surface towards the bulk.

$$\frac{\partial C_j(x,t)}{\partial t} = D_j \frac{\partial^2 C_j(x,t)}{\partial x^2} \quad (2.25)$$

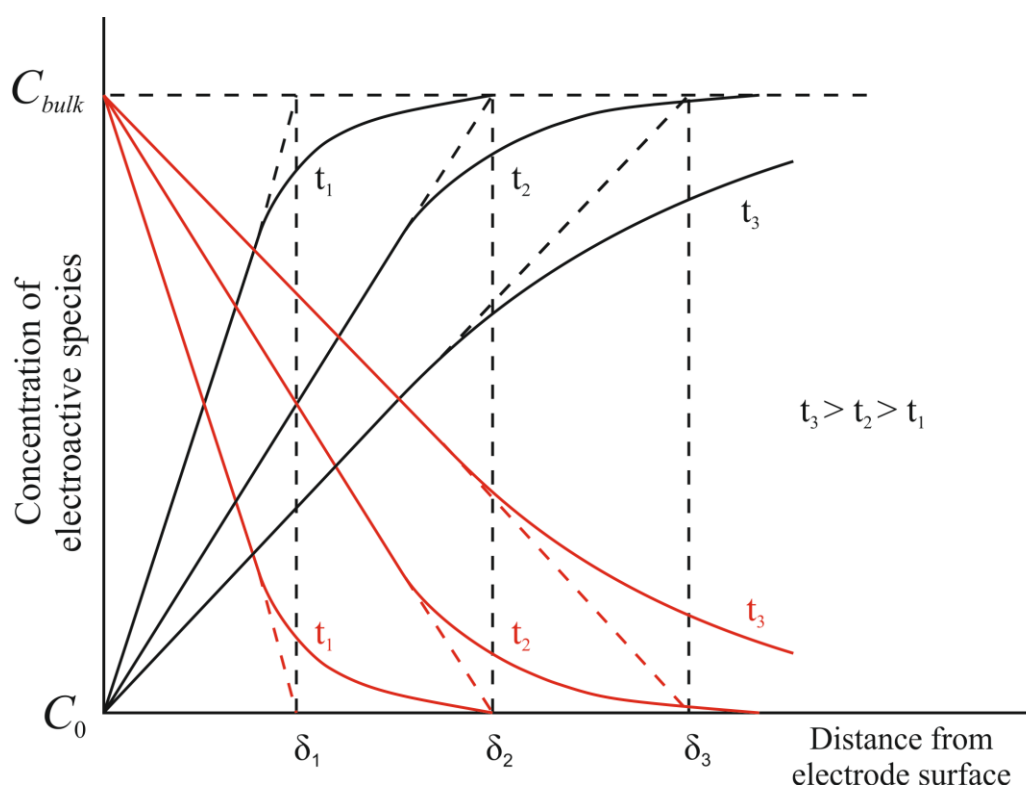


Fig. 23 Concentration profiles for species A (—) and B (—) during a potential-step experiment demonstrating the increase in diffusion layer at increasing time, t , where C_{bulk} and C_0 are the concentrations of electroactive species in the bulk solution and at the electrode surface respectively.

2.4 Electrode Kinetics and Processes

Considering our simple reaction in eq. (2.1), the rate at which this heterogeneous process occurs, V can be treated in much the same way as a homogeneous chemical process:

$$V_f = k_f [A]_0^n \quad (2.26)$$

$$V_b = k_b [B]_0^n \quad (2.27)$$

where n is the order of the reactant, k is a n th order rate constant and the subscript '0' on the concentration term denotes the surface concentration of reactant *i.e.* that inside the critical electron tunnelling distance.⁵ As shown in Fig. 23, it can be seen that at $t=0$, $[A]_0 = [A]_{bulk}$ leading to $[A]_0 \neq [A]_{bulk}$ during the reaction.

The overall rate of a heterogeneous electrochemical reaction is determined by either the rate of electron transfer or the transport of the electroactive species to the electrode.

2.4.1 Butler-Volmer Kinetics

The rate laws described in eq. 2.26 and 2.27 can be further developed into the Butler-Volmer kinetic model that despite relying on classical concepts elucidates the most current theory of electrode kinetics.²¹ Considering once more the simple reaction in eq. (2.1), it follows that the rate law for such a reaction can be written as

$$V_{net} = V_f - V_b = k_f [A]_0 - k_b [B]_0 \quad (2.28)$$

The potential applied to the electrode is known to strongly affect these kinetic constants, where typically the reduction will occur at more negative (positive energy) and oxidation at more positive (negative energy) potentials respectively. The effect of such changes in potential is illustrated in Fig. 24.

When the potential is changed, the relative energy of the electron local to the electrode is changed by $-F\Delta E = -F(E - E^0)$ hence a change in the energy barrier (Gibbs energy of activation) for oxidation or reduction (application of positive or negative potential respectively) is also observed as a fraction of the total energy change.

Assuming that the rate constants k_f and k_b are of Arrhenius form:

$$\left(\Delta G_f^{0(\ddagger)} = G^{0(\ddagger)} - G^0(A) \text{ and } (\Delta G_b^{0(\ddagger)} = G^{0(\ddagger)} - G^0(B)) \right)$$

coupling this with pre-exponential factors (A_f and A_b) we can derive that

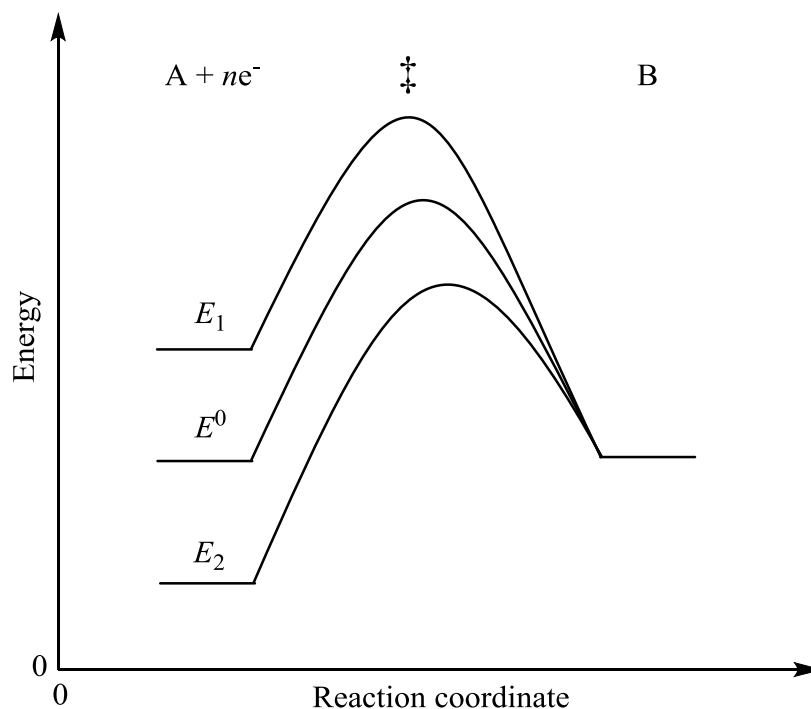


Fig. 24 Reaction profile for an electrode process showing the influence of potential. At potentials E_1 and E_2 ; reduction and oxidation are favoured respectively. At the equilibrium potential, E^0 , no net reaction takes place. ‡ denotes the transition state.

$$k_f = A_f \exp \frac{-\Delta G_f^{(\ddagger)}}{RT} \quad (2.29)$$

and

$$k_b = A_b \exp \frac{-\Delta G_b^{(\ddagger)}}{RT} \quad (2.30)$$

In the case of a positive change in potential (E_2) from the equilibrium potential E^0 , the energy barrier for oxidation, $\Delta G_b^{(\ddagger)}$ is reduced, hence becoming the more favourable process. The fractional difference between these two energies may be described by $1 - \alpha$, where α is a transfer coefficient ($\alpha = \frac{\partial \Delta G_0^\ddagger}{\Delta G^0}$), a measure of the symmetry of the energy barrier which reflects the position of the transition state in the reaction co-ordinate with a value ranging $0 \leq \alpha \leq 1$; a value of $\frac{1}{2}$ for this factor merely reflects that the slopes of the lines which intersect at the transition state are identical in magnitude since the transition state is located mid-way between the positions of species A and B on the reaction co-ordinate.^{5, 21} The fractional difference

for the reverse cathodic process (ΔG_f^{\ddagger}) may then be described by a . Applying this to the total change in energy ($-F(E - E^0)$), results in

$$\Delta G_f^{\ddagger} = \Delta G_{0f}^{\ddagger} - (1 - \alpha)F(E - E^0) \quad (2.31)$$

and

$$\Delta G_b^{\ddagger} = \Delta G_{0b}^{\ddagger} - \alpha F(E - E^0) \quad (2.32)$$

Another way to illustrate this is shown in Fig. 25

At equilibrium, typically

$$\alpha \sim 0.5, \quad (2.33)$$

inferring that the transition state lies mid-way between A and B , therefore E^0 represents the potential at which the forward and reverse reaction rate constants are equal.^{214,230} It follows that the rate constants can be expressed simply in terms of k^0 . Combining this with the Gibbs energy of activation for the anodic and cathodic reactions (2.31) and (2.32) returns

$$k_f = k^0 \exp \left[\frac{-\alpha F(E - E^0)}{RT} \right] \quad (2.34)$$

$$k_b = k^0 \exp \left[\frac{(1 - \alpha)F(E - E^0)}{RT} \right] \quad (2.35)$$

The relationship may also be applied to the formal potential of the redox couple, E^θ as opposed to the equilibrium potential. In this case $E - E^\theta$ replaces $E - E^0$, where $E - E^0$ is the measure of applied potential at the working electrode relative to that of the redox couple under investigation.

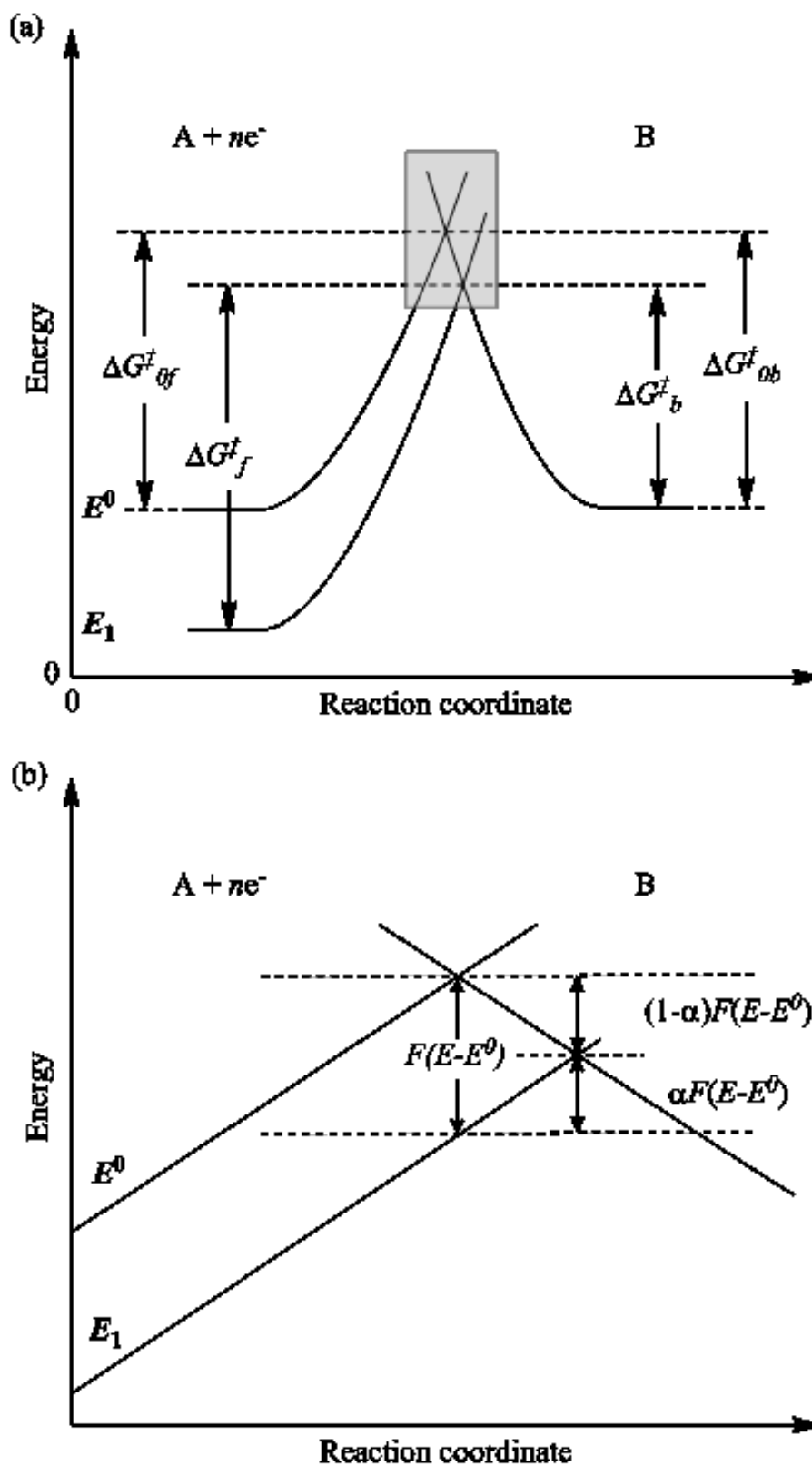


Fig. 25 (a) Effects of a positive potential change on the standard free energies of activation for oxidation and reduction. (b) Magnification of the boxed area in (a) mathematically illustrating the energy difference. Adapted from Bard, 1980, ref²¹.

2.5 Marcus Theory of Electron Transfer

Marcus theory is a development of the Butler-Volmer free energy-rate relation, in the context of modern electron-transfer theory, developed by Rudolph A. Marcus^{22, 23} following earlier work by Libby.²⁴ The theory can be summarised as a quantitative method of calculating the theory of electron transfer reactions through analysis of the free energy of reorganization of the solvent molecules about the reactants prior to the electron transfer process. In addition to changes in the solvation shell structure, the Marcus theory of electron transfer further states that in order to achieve the electron tunnelling process the reactant state must normally distort along the reaction coordinate from its equilibrium precursor position in curve A (lowest point of energy curve) to the crossing position between the two species, the transition state, which has the same nuclear configuration as the initially formed product state. The resulting product state then relaxes to its equilibrium successor position in curve B. This is illustrated in Fig. 26.

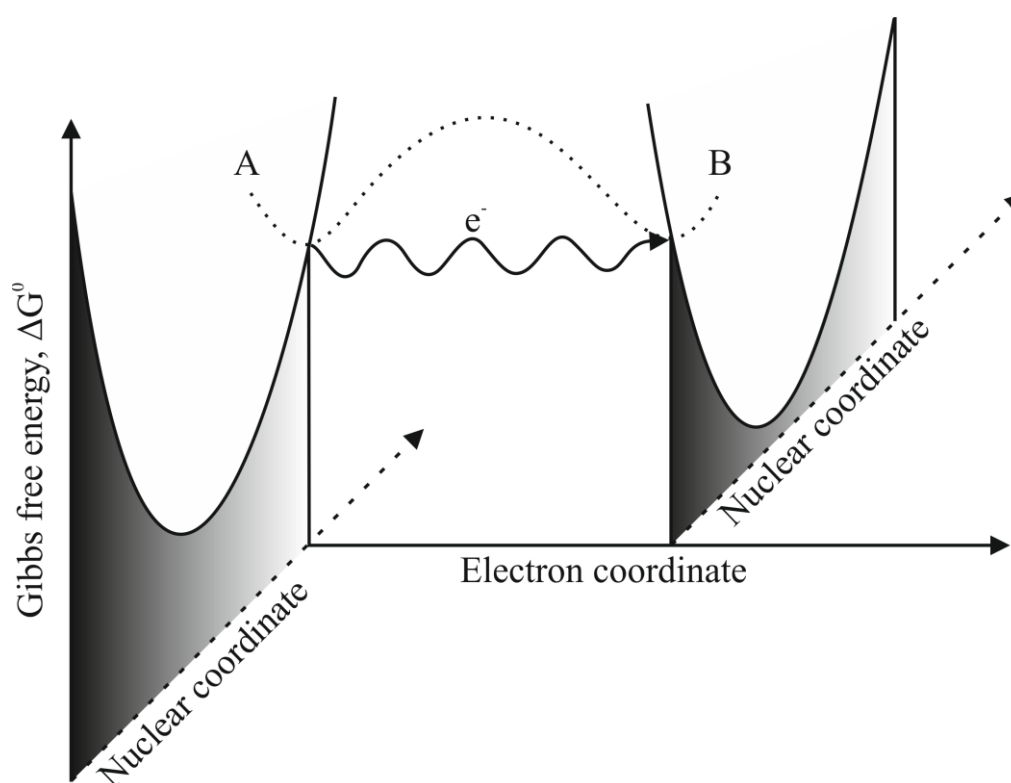


Fig. 26 Born-Oppenheimer approximation for the electron transfer process.

The activation barrier for reaction is low when reactant and product are close in molecular geometry and *vice versa*. This infers that the greater the change in reaction

coordinate, the higher the activation energy required to reach transition state, wherein the separation of reaction coordinates between reactant and product represents the resemblance of reactant and product molecular geometries. This theory was only applied to outer sphere ET between an electron donor and an electron acceptor, though variations for ET involving inner sphere mechanisms have since been developed by Hush,²⁵ known as Marcus-Hush Theory.

The electron transfer process may proceed through one of two mechanisms, either adiabatic or non-adiabatic as demonstrated in Fig. 27. Adiabatic processes occur when the extent of interaction is strong, causing splitting of the two surfaces at their intersection. Since the surfaces are separated in the intersection region, the reaction always remains on the lower surface as it proceeds through the transition state, and the transmission coefficient, $\kappa_{el} \sim 1$. On the other hand in the non-adiabatic process, when the interaction between two reactants is very weak, the split at the intersection of the two surfaces is negligible and the extent of the reaction will follow the continuous reactant surface (left) and remains on the reactant surface resulting in a reduced probability of electron transfer. In this case, only occasionally does the electron transfer occur at the transition state and $\kappa_{el} \ll 1$. This relationship between the strength of interactions between reactants and the subsequent probability of electron transfer is often described in terms of adiabaticity.

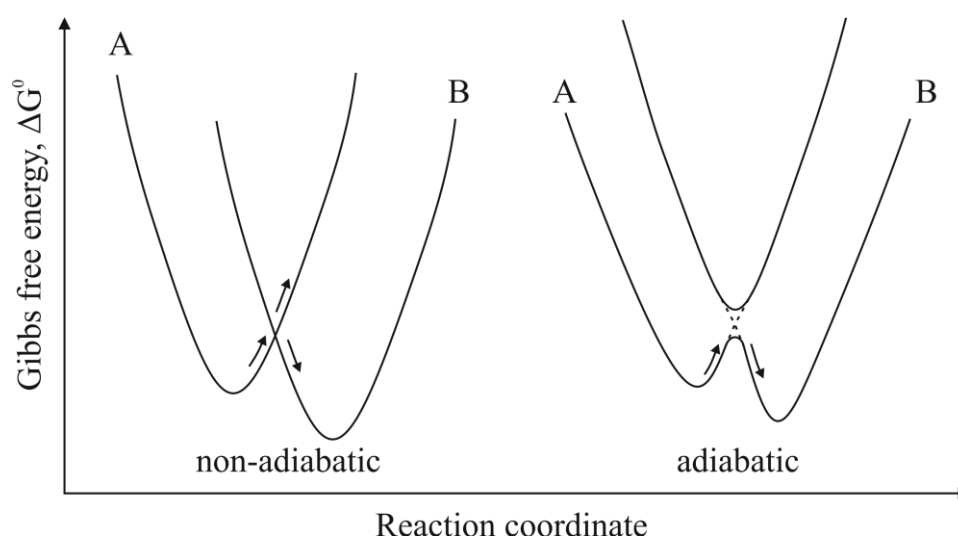


Fig. 27 Schematic difference between adiabatic and non-adiabatic ET mechanisms.

Let us take the case for a classical redox reaction, where reactants proceed *via* chemical reaction and electron transfer to form products. For ET to occur the reactant

state must distort from its equilibrium energy state to reach a transition state geometry ‡ which also exists as a distorted form of the product state. Electron transfer occurs at the point along the reaction coordinate where the transition state has a 50% probability of producing the *B* state (at least in this ideal symmetrical case with $\Delta G^0 = 0$). It is notable that this theory assumes that the *A* and *B* curves are of equal shape, neglecting external solvation effects. When solvation effects are included, a more accurate non-parabolic curve is obtained.

The expression for the rate constant of electron transfer, k_{ET} of the reaction is given by

$$k_{ET} = \kappa_{el} v_n \exp \left[\frac{-\Delta G^\ddagger}{k_B T} \right] \quad (2.36)$$

where v_n is the frequency of passage (nuclear motion) through the transition state ($\sim 10^{13} \text{ s}^{-1}$) and k_B is the Boltzmann constant.

Following the mathematical description of parabolic curves, where ΔG^\ddagger is given by

$$\Delta G^\ddagger = \frac{(\lambda + \Delta G^0)^2}{4\lambda} \quad (2.37)$$

The determination of λ is made through the summation of solvation (λ_s) and vibrational (λ_v) components.

$$\lambda = \lambda_s + \lambda_v \quad (2.38)$$

The electron transfer rate constant, k_{ET} can be determined classically *via* transition state theory as

$$k_{ET} = \kappa_{el} v_n \exp \left[\frac{(-\Delta G^\ddagger)^2}{k_B T} \right] \quad (2.39)$$

The application of Marcus theory then yields

$$k_{ET} = \kappa_{el} v_n \exp \left[\frac{-(\lambda + \Delta G^0)^2}{4\lambda k_B T} \right] \quad (2.40)$$

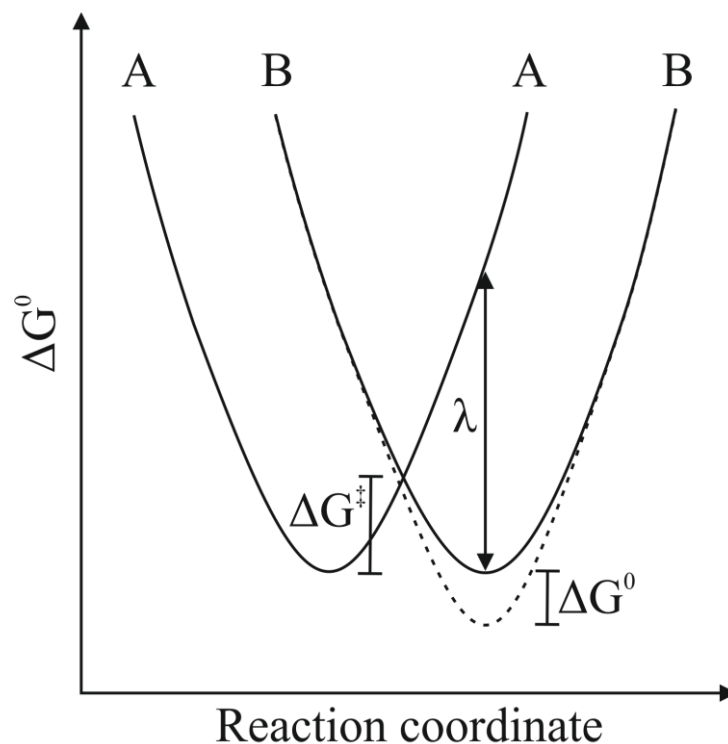


Fig. 28 Marcus Theory of Electron Transfer for reaction of *A* and *B*. ΔG^\ddagger is the Gibbs activation energy to reach the transition state, λ is the reorganisation energy and ΔG^0 is the Gibbs energy change. In the solid line case, $\Delta G^0 = 0$, the dotted line case demonstrates the normal region where a change in the ΔG^0 is observed upon formation of *B*.

Furthermore, this can be approached electrochemically. Following on from section 2.4.1, it follows that if species *A* and *B* are similar in molecular geometry then k^0 will be large; hence the activation barrier for such a reaction is low and favourable. The opposite is true if species *A* and *B* are dissimilar, where the value of k^0 is small incurs the need for a more significant input of energy in order for the consequential chemical transformation to proceed.

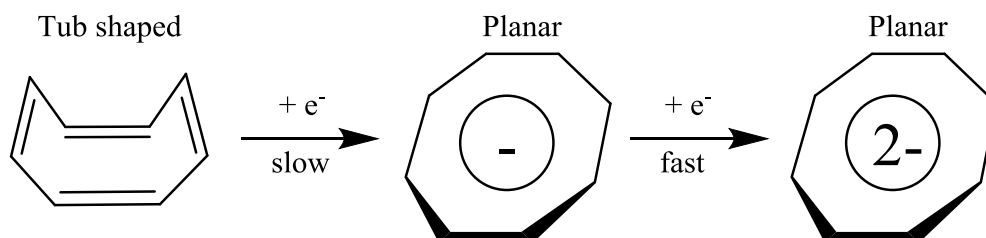


Fig. 29 Schematic illustration of the two electron reduction of cyclooctatetraene demonstrating a slow reorganisation of the initial structure from tub shaped to planar.

In this case, one assumes that the applied potential (free energy, overpotential, $\eta = E - E^{\theta'}$) is much smaller than the electrode reaction reorganizational energy barrier. The dependency of $k_{f,\eta}$ and $k_{b,\eta}$ (the forward and reverse η -dependent half reaction rate constants) on η as expressed by Butler-Volmer is

$$k_{f,\eta} = k^0 \exp\left(-\frac{\eta}{2k_B T}\right) \quad (2.41)$$

$$k_{b,\eta} = k^0 \exp\left(\frac{\eta}{2k_B T}\right) \quad (2.42)$$

the analogous Marcus relations are then

$$k_{f,\eta} = k^0 \exp\left(-\frac{\eta}{2k_B T} - \frac{\eta^2}{4\lambda k_B T}\right) \quad (2.43)$$

$$k_{b,\eta} = k^0 \exp\left(\frac{\eta}{2k_B T} - \frac{\eta^2}{4\lambda k_B T}\right) \quad (2.44)$$

In the case when $\eta / \lambda \ll 1$, equations 2.43 and 2.44 reduce to the Butler-Volmer equations. The Marcus relations predict that, as η approaches λ , the rate constants do not continue to increase exponentially with η (as is always the case in the Butler-Volmer formulation) but maximizes at $\eta = \pm\lambda$ and actually decreases at larger η (classical Marcus "inverted" region).

The Marcus inverted region occurs under conditions of when the free energy, ΔG^0 of a highly exergonic reaction is greater than the reorganization energy, the ET rate decreases with increasing ΔG^0 . Further investigation reveals that as the increasingly exergonic reaction approaches and surpasses the point where $\Delta G^\ddagger = 0$ and $-\Delta G^0 = 1$, k_{ET} will reach its maximum value of $\kappa_{el} v_\eta$. However, as $-\Delta G^0$ becomes more negative, the intersection point of A and B moves to the left causing ΔG^\ddagger to increase again and k_{ET} unexpectedly begins to decrease as the reaction becomes increasingly exergonic. This "ambiguous" observation is known as the Marcus inverted region. The various cases of Marcus Theory and their respective parabola are illustrated in Fig. 30 and Fig. 31.

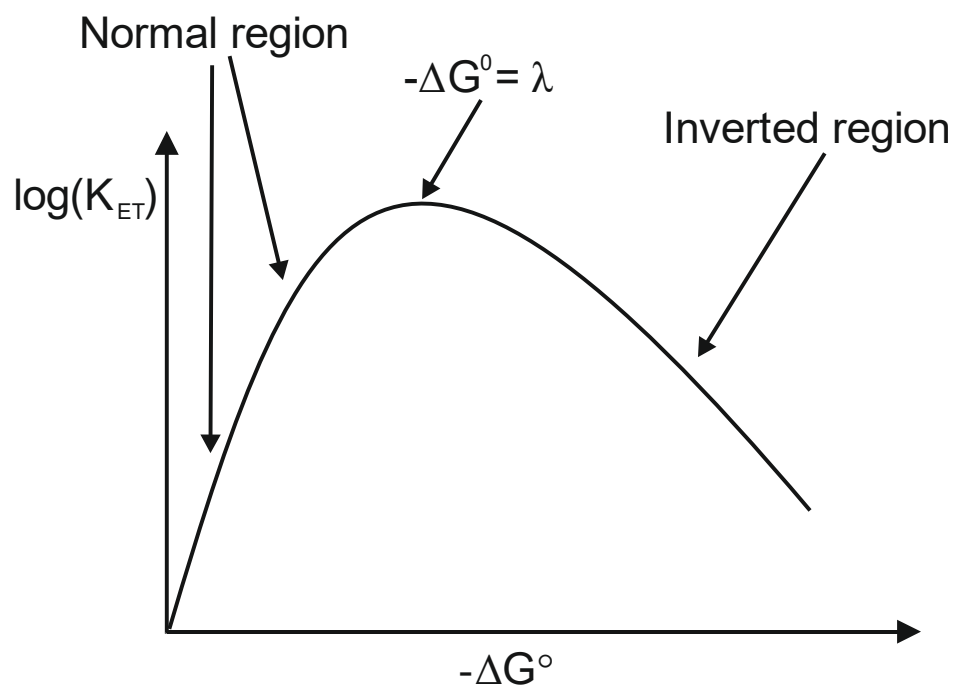


Fig. 30 Dependence of the electron transfer rates on ΔG° . It is clear that the maximum rate of electron transfer occurs when the driving force is equal to the reorganization energy (activationless case). When the driving force becomes greater than the reorganization energy, we enter the Marcus inverted region.

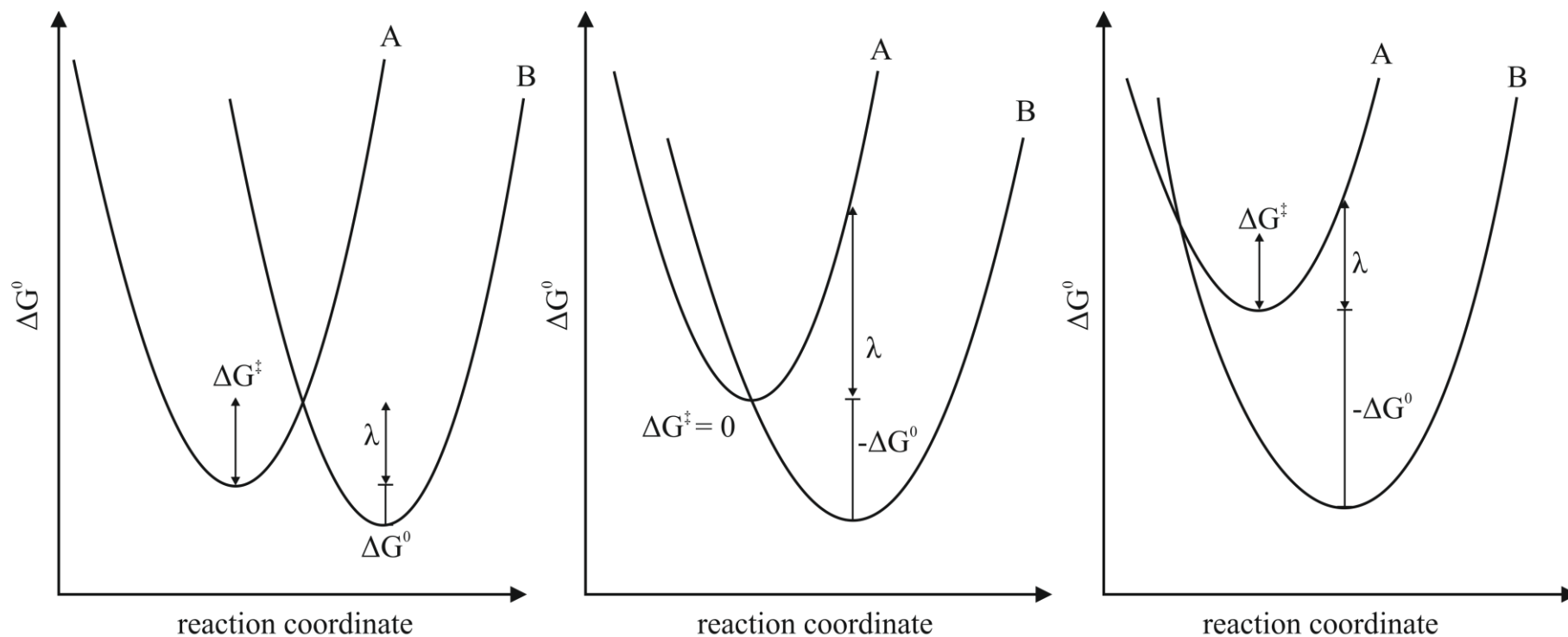


Fig. 31 Plots of the potential energies of the reactant and product as a function of the nuclear (reaction) coordinate in the zeroth-order approximation depicting electron transfer in the normal (left) and inverted (right) Marcus regions. The activationless case where $\Delta G^\ddagger = 0$ is shown in the middle illustration. Adapted with permission from ref.²⁶

2.6 Electrochemical Detection Methods

2.6.1 Voltammetry

Voltammetry is a series of techniques where potential is controlled and current is measured. In this technique, the current is due to a redox half-reaction induced by the applied potential. The graph of current versus potential, called a voltammogram, provides information about the chemical reaction. It is important that the voltammogram reflects the reaction of the analyte at the working electrode. Thus, it is important that the potentials measured be in a region where solvent, electrolyte and electrode are not reacting.

2.6.2 Cyclic Voltammetry

Exploration into cyclic voltammetry (CV) techniques began as early as 1935 with Kolthoff and Tomsicek²⁷ and was further contributed to post 1950s by Randles²⁸, Nicholson²⁹ and Shain³⁰. Over recent decades, potential sweep methods have been developed and applied to an ever increasing variety of systems and applications that constitutes CV to most certainly be the most versatile and useful techniques for the preliminary determination and characterisation of the redox properties of an electroactive species in solution.

CV is the most widely used technique for acquiring qualitative information about electrochemical reactions. It provides information on redox processes, heterogeneous electron-transfer reactions and adsorption processes as well as offering a rapid location of redox potential of the electroactive species. CV consists of scanning linearly the potential of a stationary working electrode using a triangular potential waveform, forward from an initial potential, E_0 to E_1 and then in reverse from E_1 to E_0 , as illustrated in Fig. 32.

The cyclic voltammogram is a current response as a function of the applied potential (measured by a potentiostat). When the electrochemical process is limited by diffusion the concentration gradients generated from the redox equation affect the current values. In general, as the applied potential approaches the characteristic formal potential for the redox process, a cathodic current begins to increase until a peak is reached and then decreases upon the semi-infinite linear diffusion conditions.

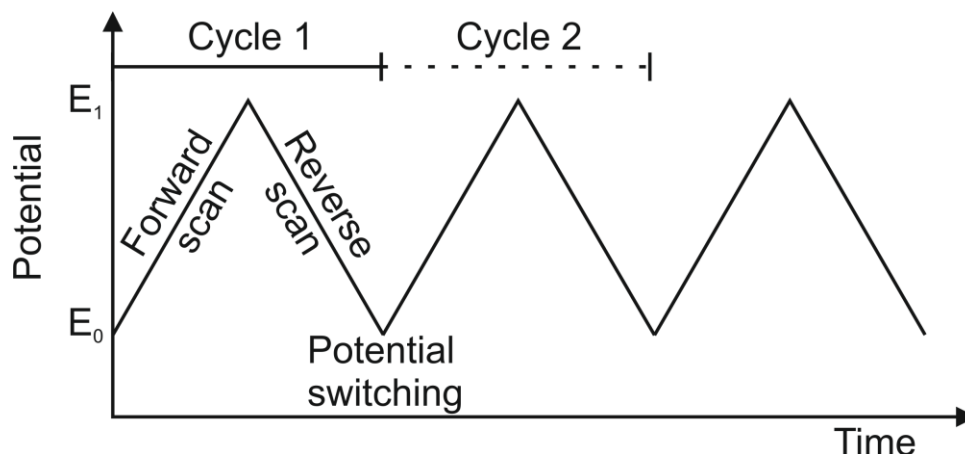


Fig. 32 Potential–time excursion signal in a cyclic voltammetric experiment over three scans.

2.7 Electrochemical Reversibility

The electrochemical response may be characterised to one of three groups; reversible, quasi-reversible and irreversible.

2.7.1 Reversible Systems

The heterogeneous electron transfer kinetics are said to be reversible, meaning fast compared with the experimental timescale when the concentrations of A and B at the electrode surface are given by the Nernst equation at all times.³

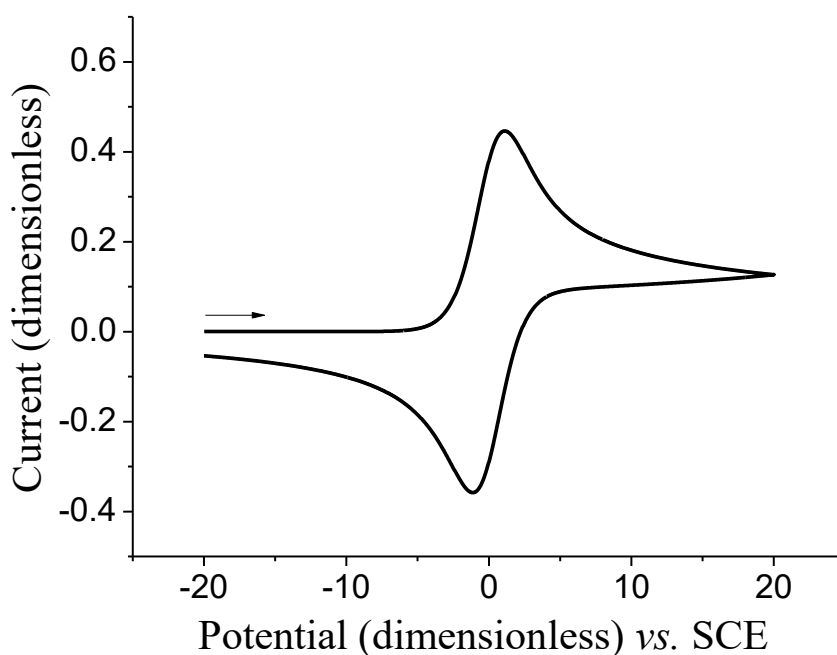


Fig. 33 Example of a cyclic voltammogram for a reversible process

The cyclic voltammogram is characterised by several important parameters. Four of these observables, the two peak currents and two peak potentials, provide the basis for the diagnostics developed by Nicholson and Shain³⁰ for analyzing the cyclic voltammetric response.

The peak current can be calculated *via* the Randles-Sevcik equation, valid at 298 K

$$i_p = (2.69 \times 10^5) n^{3/2} SCD^{1/2} \nu^{1/2} \quad (2.45)$$

when the temperature is not equal to 298 K, a variation of the equation is employed

$$i_p = (0.4463) nF \left(\frac{nF}{RT} \right)^{1/2} SCD^{1/2} \nu^{1/2} \quad (2.46)$$

where ν the potential scan rate (V s^{-1}).

Classic characteristics of a reversible process include: the cathodic and anodic peak current ratio is unity *i.e.* $\left(|i_{p_f}| = |i_{p_b}| \right)$, the peak currents are proportional to $\sqrt{\nu}$, the E_p values do not change as a function of ν and the difference (ΔE_p) between the cathodic peak potential (E_{p_f}) and anodic peak potential (E_{p_b}) is $56.4/n \text{ mV}$.^{2,4}

$$\Delta E_p = E_{p_f} - E_{p_b} = \frac{56.4 \text{ mV}}{n} \quad (2.47)$$

By decreasing the reversibility, the difference between the two peak potentials increases. Moreover, the half-wave potential, which is used to identify the formal redox potential, is obtained by

$$E_{1/2} = \frac{(E_{p_f} + E_{p_b})}{2} \quad (2.48)$$

2.7.2 Quasi-Reversible Systems

The quasi-reversible system is one where the current is controlled by both the charge transfer and mass transport.⁴ The electron transfer is not fully reversible showing considerably different behaviour from their reversible counterparts. As the rate constants for the oxidation and reduction processes decrease, the equilibrium at the surface is no longer establishing so rapidly. In these cases the peak separation is no

longer fixed but varies as a function of v , usually increasing with increasing v . Similarly the peak current no longer varies as a function of the \sqrt{v} . The nature of this increasing separation at high scan rates is due to the electrode kinetics at the surface of the electrode. The low scan rates practically demonstrate reversible kinetic characteristics as the electrode kinetics are fast enough to cope with the flux of the oxidative species. However at higher scan rates, the reverse is true; the electrode kinetics cannot be maintained with the increase in flux and consequently irreversible behaviour occurs due to the loss of the Nernstian equilibrium.

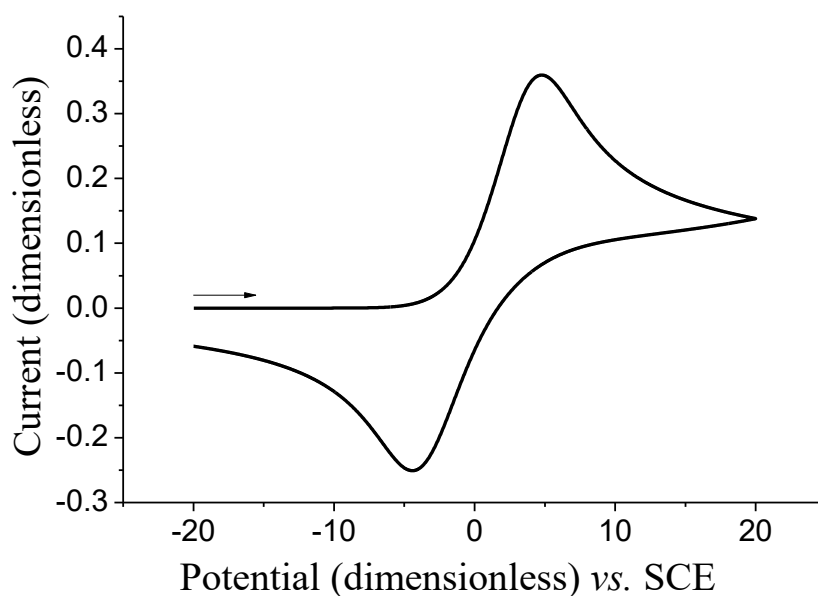


Fig. 34 Cyclic voltammogram illustrating the peak shift beginning to occur, this will be amplified at higher scan rates.

As can be seen in Fig. 34, the voltammograms of a quasi-reversible system are more drawn out and exhibit a larger separation in peak potentials compared to a reversible system.

2.7.3 Irreversible Systems

Irreversible systems therefore may be described as those with sluggish electron transfer kinetics that are slower than the mass transport leading to a marked change in the voltammograms appearance. As a result, there is a breakdown of the Nernstian equilibrium at the electrode surface that causes the peaks to become split much further apart and in many cases there is no reverse peak occurs at all, where the products are electrochemically unreactive or have decomposed.

The peak current for a reversible system may be determined *via* a variation of the Randles-Sevcik equation, correct at 298 K only

$$i_p = (2.99 \times 10^5) n(\alpha n_a)^{1/2} SCD^{1/2} n^{1/2} \quad (2.49)$$

where n_a is the number of electrons involved in the charge transfer step.

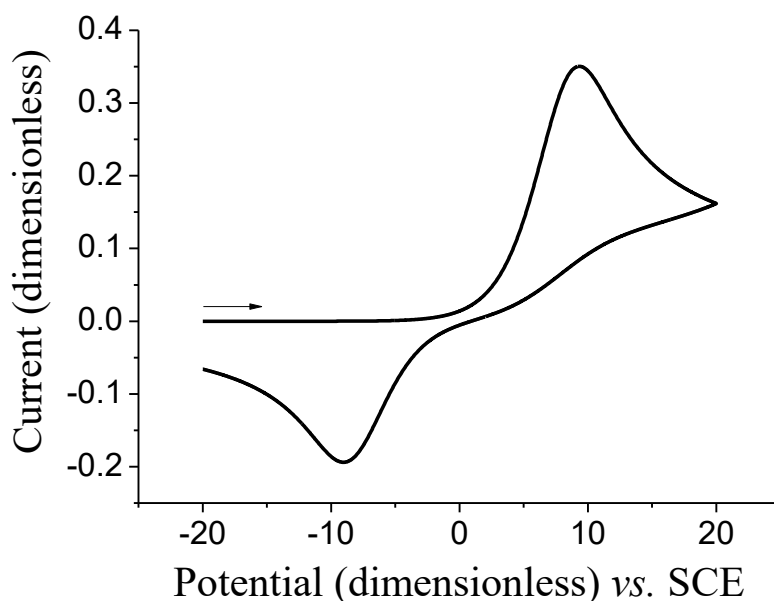


Fig. 35 Plot showing the peak shifts and less refined peak shapes associated with an irreversible system.

2.8 Square Wave Voltammetry

Square-wave voltammetry (SWV) is a large-amplitude differential technique in which a waveform composed of a symmetric square wave, superimposed on a base staircase potential, is applied to the working electrode.³¹ The resulting peak-shaped voltammogram is symmetric about the half-wave potential, and the peak current is proportional to the concentration. The advantage of square wave voltammetry is the analysis time is drastically reduced, leading to readouts in a few seconds with increased current outputs over other techniques such as differential-pulse voltammetry.⁴ Furthermore, square wave voltammetry offers increased sensitivity over other techniques since the current observed is a subtraction of the capacitance from the overall current measured, including the faradaic current from the redox reaction of interest. Finally, unlike cyclic voltammetry, SWV is unaffected by

oxygen due to the pulsing nature of the technique making it ideal for measurements in blood and other oxygenated media.

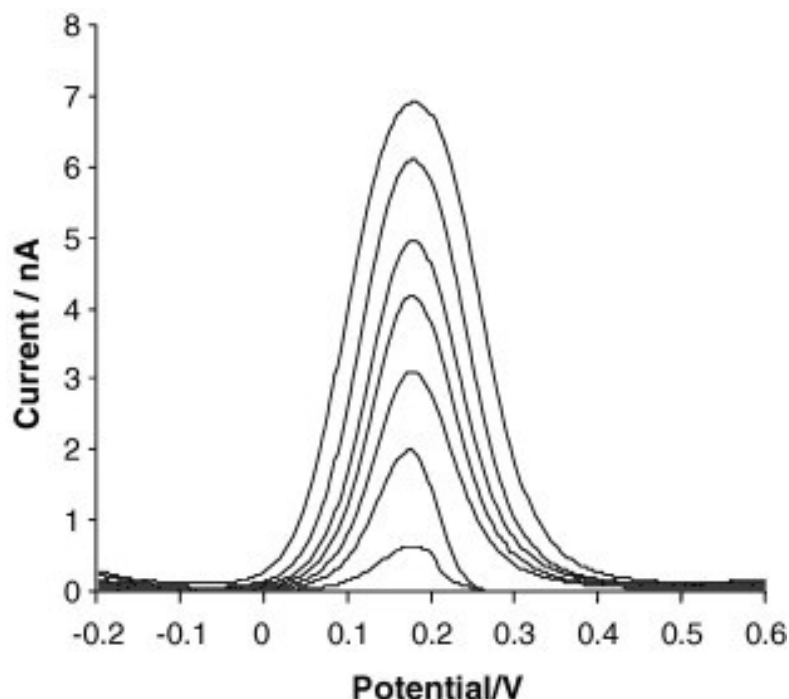


Fig. 36 A typical square wave voltammogram carried out with a microdisk electrode.³²

2.9 Cyclic Voltammetry of Adsorbed Species

As in equation (2.1), consider the one-electron reduction of a species, A , which is attached to the surface of an electrode, to furnish the reduced species B , which is likewise tethered to the electrode.

This is similar to the reduction, in aprotic solvents, of *para*-nitrobenzene attached to a carbon electrode. If we assume that the voltammetric timescale is sufficiently long compared with the heterogeneous electron transfer kinetics (this corresponds to the slow scan rate limit), then the ratio of the surface concentrations (expressed in terms of amount per unit electrode surface area of species A and B , Γ_A and Γ_B respectively, follow the Nernst equation under the assumption of non-interacting adsorbates)

$$\frac{\Gamma_A}{\Gamma_B} = e^{\frac{F}{RT}(E-E^{\theta'})} \quad (2.50)$$

Under the assumption that the application of a potential to the electrode does not change the surface coverage, and that the entire potential drop across the modified

electrode | electrolyte interface occurs between the electrode and the redox centre, the Faradaic current, i , is a function of the ratio of electrolytic consumption of species A:

$$\frac{i}{FS} = \frac{d\Gamma_A}{dt} = -\frac{d\Gamma_B}{dt} \quad (2.51)$$

Hence, assuming that a complete monolayer coverage of species A exists, and that both species A and B initially occupy the same area, normalising the surface concentrations with respect to the constant total coverage, Γ_0 , defined by

$$1 = \frac{\Gamma_A}{\Gamma_0} + \frac{\Gamma_B}{\Gamma_0} = a + b \quad (2.52)$$

The dimensionless concentration of species A and B may be deduced from equation (2.50).

$$a = \frac{1}{1 + e^{-\frac{F}{RT}(E-E^{\theta'})}}; b = \frac{1}{1 + e^{\frac{F}{RT}(E-E^{\theta'})}} \quad (2.53)$$

Noting that for linear sweeps; potential with time (t), viz. $E = u - vt$ for reductions, where u is the initial applied potential, $E = 2f - u - vt$ where f is the potential at which the direction of the potential ramp is reversed, the voltammetric scan rate, $v = \left| \frac{dE}{dt} \right|$, enables the Faradaic current flowing to be deduced *via* differentiation of the expression in equation (2.54):

$$\frac{i}{FS\Gamma_0} = \frac{da}{dt} = \frac{Fv}{RT} \cdot \frac{e^{\frac{F}{RT}(E-E^{\theta'})}}{\left\{ 1 + e^{\frac{F}{RT}(E-E^{\theta'})} \right\}^2} \quad (2.54)$$

The voltammogram is often, for convenience, described in terms of dimensionless parameters for current and potential, derived as follows:

$$\text{Potential} : \xi = -\frac{F}{RT}(E - E^{\theta'}) \quad (2.55)$$

$$\text{Current} : \Psi = \frac{i}{\frac{F^2}{RT}S\Gamma_0v} = \frac{e^{-\xi}}{(1 + e^{-\xi})^2} \quad (2.56)$$

Note that the current decays to zero with increasing driving force in both forward and reverse directions, owing to the fact that exhaustive electrolysis has occurred, all of species A has been converted into species B at the end of the reduction sweep; *mutatis mutandis* the converse is true for the oxidation scan. The area under the peak is related quantitatively to the number of electrons transferred through Faraday's Law; for the dimensionless plot, integration of each wave equals unity. The symmetrical voltammogram around the formal potential for the A/B redox couple indicates that the electrolytic product (species B) is chemically stable (the reaction is chemically reversible), and that the heterogeneous electron transfer kinetics are fast (electrochemically reversible).

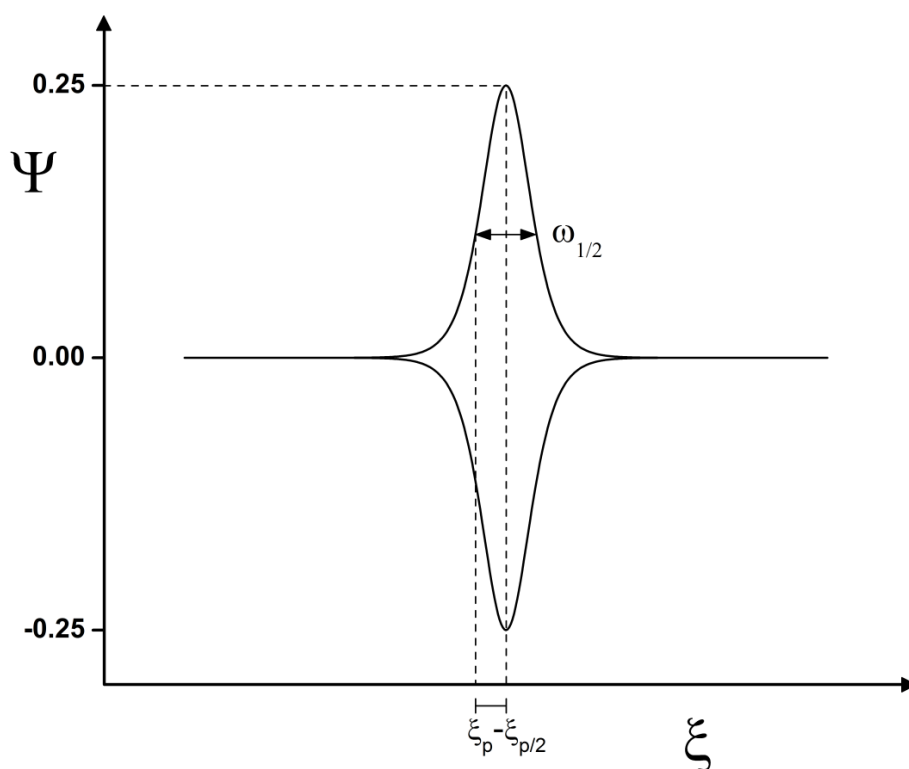


Fig. 37 Simulated CV data for an adsorbed species.

The peak currents for this system occur when the applied electrode potential equals the formal electrode potential for the A/B surface confined redox couple, and take a magnitude of $\Psi_p = 1/4$. The half-peak potential, defined as $\xi_p - \xi_{p/2} = -\ln(3-2\sqrt{2})$, and full width at half-maximum taken as a value of $\omega_{1/2} = \left(\frac{3+2\sqrt{2}}{3-2\sqrt{2}}\right)$, so that in real terms, the reversible cyclic voltammogram is described as being with a peak potential that is independent of scan rate, with a half-peak potential of $1.763 \frac{RT}{F}$, with full width at

half-maximum, $\omega_{1/2} = 3.525 \frac{RT}{F}$, with peak currents that are directly proportional to the voltage sweep rate and which furnish oxidation and reduction waves of equal heights.

In the event that the heterogeneous electron transfer is not fast compared with the electrochemical timescale, the cyclic voltammogram change in these quasi-reversible (“medium fast/slow”) and irreversible (“slow”) regimes. Qualitatively, the voltammetric peaks decrease in height, broaden to a limit and move away from each other, so that the reduction becomes more difficult, likewise for the oxidations – greater driving force (“overpotential”) is required to drive electrolysis. Understanding this behaviour quantitatively requires the assumption of a kinetic law for the heterogeneous electron transfer. Whilst it is important to employ theory that takes into consideration the molecular factors affecting the electron transfer process, we can approximate these for low overpotentials by the assumption of Butler-Volmer electrode kinetics; again, we consider the heterogeneous electron transfer process in eq (2.1).

In this phenomenological model, the electrode kinetics are assumed to obey the transition-state model (equations 2.29 and 2.30), in which ΔG_f^\ddagger or ΔG_b^\ddagger following a linear dependence on the driving force:

$$\Delta G_f^\ddagger = \Delta G_0^\ddagger + \alpha F(E - E^{\theta'}) ; \Delta G_b^\ddagger = \Delta G_0^\ddagger + (\alpha - 1)F(E - E^{\theta'}) \quad (2.57)$$

In equation (2.57), the intrinsic barrier (or standard activation free energy) is denoted by ΔG_0^\ddagger , it is important to note that in the Butler-Volmer formulation, these two parameters are considered to be independent of the electromotive driving force. Thus combining equations (2.29, 2.30 and 2.57) allows the development of the electrode kinetics:

$$k_f = k_s e^{-\alpha \frac{F}{RT}(E - E^{\theta'})} ; k_b = k_s e^{(1-\alpha) \frac{F}{RT}(E - E^{\theta'})} \quad (2.58)$$

In which the standard rate constant for the heterogeneous electron transfer, $k_s = A_n e^{-\Delta G_0^\ddagger/RT}$ is the value of the electron transfer kinetics when $E = E^{\theta'}$, viz. at zero driving force. It follows that the Faradaic current observed due to electrolytic depletion of species A is given by the following:

$$\frac{i}{F\Gamma_0} = -\frac{da}{dt} = k_s \eta^{-\alpha} (a - b\eta) \quad (2.59)$$

In which we have defined a new dimensionless potential: $\eta = e^{-\xi}$. Thus, re-writing equation (2.59) in terms of the normalised current introduced in expression (2.56) yields:

$$\Psi = -\frac{RT}{Fv} \cdot \frac{da}{dt} = \Lambda_s \eta^{-\alpha} (a - b\eta) \quad (2.60)$$

In which the adimensional rate constant is defined as $\Lambda_s = k_s \frac{RT}{Fv}$. Treating the scan rate as having no sign, *viz.*, $E = u + vt$, and changing the temporal variable to that corresponding to the dimensionless potential, allows the formulation of the following linear ordinary differential equations relating dimensionless current to the normalised potential from equations (2.59) and (2.60):

$$\begin{aligned} \frac{da}{d\eta} + \Lambda_s(1+\eta)\eta^{-(1+\alpha)}a &= \Lambda_s\eta^{-\alpha} \\ \frac{db}{d\eta} + \Lambda_s(1+\eta)\eta^{-(1+\alpha)}b &= \Lambda_s\eta^{-(1+\alpha)} \end{aligned} \quad (2.61)$$

Equations (2.61) are soluble using the integration factor method, to afford the variation of the normalised concentrations of species *A* and *B* with applied potential, noting that the integration constant is determinable *via* the irreversible (“slow”) electron transfer case: when $\Lambda_s \rightarrow 0$, only the reduction wave occurs when $\eta^{(1-\alpha)} \ll \eta^\alpha$ and $\eta \ll 1$, and only the oxidation peak occurs when $\eta^{-\alpha} \ll \eta^{1-\alpha}$ and $\eta \gg 1$. Accordingly; the voltammetric waveshapes are given by the following expressions, using *z* as a dummy index.

$$\begin{aligned} \text{Reduction } \Psi &= \Lambda_s \eta^{-\alpha} \left\{ 1 - \Lambda_s (1+\eta) e^{\frac{\Lambda_s \eta^{-\alpha}}{\alpha(1-\alpha)}} [1 - \alpha(1+\alpha)] \right\} \\ &\quad \downarrow \\ &= \int_{\infty}^{\eta} A_f^{-(1+\alpha)} e^{-\frac{\Lambda_s}{\alpha(1-\alpha)} A_f^{-\alpha[1-\alpha(1+Z)]}} dz \end{aligned} \quad (2.62)$$

$$\text{Oxidation } \Psi = -\Lambda_s \eta^{-\alpha} \left\{ \eta - \Lambda_s (1 + \eta) e^{\frac{\Lambda_s}{\alpha(1-\alpha)}} [1 - \alpha(1 + \eta)] \right\}$$

$$\downarrow$$

$$\int_{0a}^{\eta} A_b^{-\alpha} e^{-\frac{\Lambda_s}{\alpha(1-\alpha)} A_b^{-\alpha[1-\alpha(1+A_b)]}} dz$$
(2.63)

It is clear that the oxidation and reduction waves are symmetrical around the formal potential. This is only true for the case of $\alpha = 1/2$. The waveshapes and shifts in the position of the voltammograms are as described earlier; $\Lambda_s \rightarrow \infty$ reproduces the reversible CVs discussed earlier; $\Lambda_s \rightarrow 0$ causes the voltammograms to behave as though they are completely irreversible, *viz.* there is no oxidation current underneath the reduction wave, and *vice versa*. Accordingly, the waveshape is now best described by the following expressions.

$$\text{Reduction } \Psi = \Lambda_s \eta^{-\alpha} e^{\frac{\Lambda_s}{\alpha} \eta^{-\alpha}}$$

$$\text{Oxidation } \Psi = -\Lambda_s \eta^{-\alpha} e^{-\frac{\Lambda_s}{1-\alpha} \eta^{(1-\alpha)}}$$
(2.64)

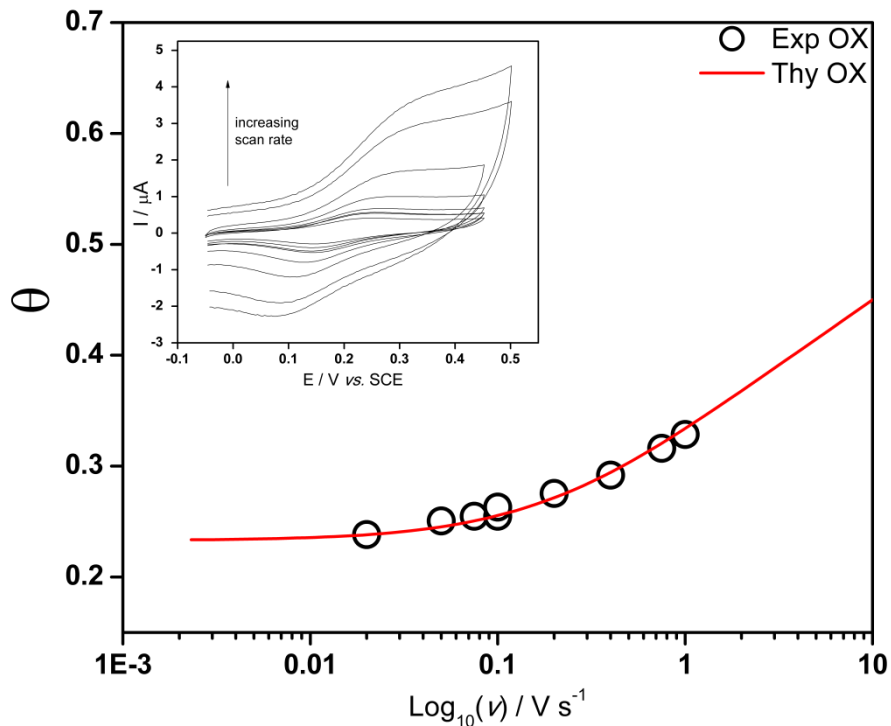


Fig. 38 The variation of peak potential with scan rate demonstrates the dependency of Λ_s on scan rate where as $\Lambda_s \rightarrow 0$, the electrochemical system tends towards irreversibility with increasing scan rate.

Fig. 38 describes rate constant dependency of the peak potential change with increasing scan rate, which in this case tends towards quasi-reversibility with increasing ν . However there are also resistance affects to take into account here, where the resistive characteristics of the electrode material may directly restrict the reversibility of a particular electrochemical system. In the case of fairly resistive materials such as the semi-conductor ITO, at high ν it is possible to observe such resistive phenomena, that may otherwise not occur on more conductive surfaces.

2.10 Modifying the Electrode Surface

The sensor surface can be modified in a multitude of ways to yield favourable characteristics and properties. This can range from creating anti-fouling surfaces that reduce or resist fouling of the electrode surface by substances present in the sample (improve sensor lifetime) through to enabling the direct contact and subsequent electrochemical communication with an analyte of choice. The latter is beneficial for immunoassay based electrochemical sensors since the possibility to intimately couple the sensing element and electronic transducer may improve sensitivity and robustness of the sensing system.

Direct chemical linkage (DCL) involves the attachment of molecules to the electrode material *via* covalent bond formation. This leads to a firmly bound layer or coat of the intended molecules however it is often difficult to control orientational arrangements and may require water sensitive reagents. One of the most common methods for DCL is silylation where a silicon atom is linked to the surface, commonly with a terminal $-NH_2$, $-Cl$ or $-COOH$ functionality to allow for further modification of the coating. This typically leads to the formation of a single monolayer coating.³³ Other methods for DCL exist though are not discussed in this thesis.

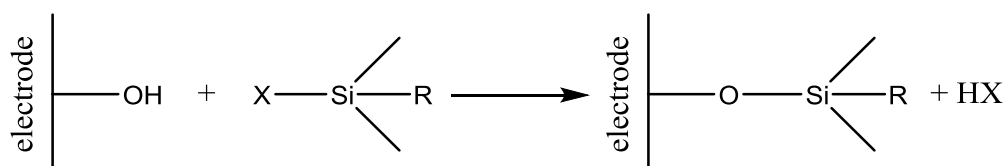


Fig. 39 Principle of the silylation chemical linkage method

Adsorption is the simplest method of surface modification since one only has to dip the electrode surface into a coating solution for a controlled period of time. It can be reversible wherein the adsorbed molecules are in dynamic equilibrium with molecules in the coating solution or irreversible, for example a polymer dissolved in organic solvent is 'painted' onto the surface and allowed to dry - the resulting coating is insoluble in aqueous phases thus coatings prepared by this method remain relatively stable. The issues faced with this method include a lack of control over the number of molecules bound to the electrode surface during the coating process and since there is no direct chemical bonding involved, the modified surface can be unstable giving rise to difficulties in reproducibility of the coating technique.³³

These issues can be addressed by the use of electrochemically controlled coatings. In this method the coating can be prepared in a more controlled manner with the possibility to grow individual layers sequentially in order to form superstructures of 20 layers or more which allows for application specific coatings to be prepared.³³ This preparation and operation of this technique does however require the use of specialised equipment (potentiostat, *etc.*) and a firm knowledge of electrochemistry.

Finally, plasma discharge can be used to grow polymeric coatings by initiating the more difficult polymerisation of radical intermediates onto the electrode surface. It may also allow for DCL to carbon surfaces wherein the plasma is exposed to the carbon surface, providing a 'clean' activated surface that when exposed to olefins, amines and functionalised molecules with these groups become bound to the electrode surface. These bound molecules may contain the desired electroactive groups, though if not they may be further functionalised to contain the preferred group.³³

2.10.1 Molecular Wires

The modification of surfaces can also include the attachment of conductive 'wire' systems that can be used for direct electrochemical connection to various molecules of interest. The concept of 'molecular wires' was first introduced by Hess *et al.*³⁴ whom demonstrated the use of molecular wires to directly conjugate an enzyme to a gold electrode surface. Since then, a multitude of molecular wires and conjugation routes to various electrode surfaces have been demonstrated, these include simple benzene ring structures to more elaborate carbon nanotube (CNT) arrays. These

'wires' are highly conductive to facilitate rapid electron transfer to and from a localised redox centre. This ability to create well-defined electrode surface structures with a wide variety of materials and functional molecules is highly valuable in biosensing chemistry. The molecular wires investigated in this thesis are described in Chapters 4 through 6.

References

1. D. R. Crow, *Principles and applications of electrochemistry*, Blackie Academic & Professional, London, 1994.
2. A. J. Bard and L. R. Faulkner, *Electrochemical methods : fundamentals and applications*, Wiley, New York, 2nd edn., 2001.
3. D. Pletcher, R. Greff, R. Peat, L. M. Peter and J. Robinson, *Instrumental Methods in Electrochemistry*, Ellis Horwood Ltd., Chichester, 1985.
4. J. Wang, *Analytical Electrochemistry*, Wiley-VCH, New Jersey, 3 edn., 2006.
5. R. G. Compton and C. E. Banks, *Understanding voltammetry*, Imperial College Press, London, 2nd edn., 2011.
6. J. T. Hupp and M. J. Weaver, *The Journal of Physical Chemistry*, 1984, **88**, 1463-1467.
7. J. Leddy, A. J. Bard, J. T. Maloy and J. M. Savéant, *Journal of Electroanalytical Chemistry and Interfacial Electrochemistry*, 1985, **187**, 205-227.
8. J. E. Halls, A. Hawthornthwaite, R. J. Hepworth, N. A. Roberts, K. J. Wright, Y. Zhou, S. J. Haswell, S. K. Haywood, S. M. Kelly, N. S. Lawrence and J. D. Wadhawan, *Energy & Environmental Science*, 2013, **6**, 1026-1041.
9. C. H. Hamann, A. Hamnett and W. Vielstich, *Electrochemistry*, Wiley, Weinheim, 2007.
10. H. Helmholtz, *Annalen der Physik*, 1853, **165**, 211-233.
11. H. Helmholtz, *Annalen der Physik*, 1879, **243**, 337-382.
12. M. Gouy, *J. Phys. Theor. Appl.*, 1910, **9**, 457-468.
13. D. L. Chapman, *Philosophical Magazine Series 6*, 1913, **25**, 475-481.
14. O. Stern, *Zeitschrift für Elektrochemie und angewandte physikalische Chemie*, 1924, **30**, 508-516.
15. D. C. Grahame, *Chemical Reviews*, 1947, **41**, 441-501.

16. R. F. Savinell, E. S. I. Electrolysis, E. E. Division, E. S. E. T. Division and E. S. B. Division, *Tutorials in Electrochemical Engineering--mathematical Modeling: Proceedings of the International Symposium*, Electrochemical Society, 1999.
17. P. Zanello, 2003.
18. C. W. Tobias, M. Eisenberg and C. R. Wilke, *Journal of The Electrochemical Society*, 1952, **99**, 359C-365C.
19. A. Tuteja, *Fundamentals of Physical Chemistry*, Discovery Publishing House, New Delhi, 2007.
20. C. M. A. Brett and A. M. O. Brett, *Electrochemistry: Principles, Methods, and Applications*, Oxford University Press, 1993.
21. A. J. Bard and L. R. Faulkner, *Electrochemical methods: fundamentals and applications*, John Wiley & Sons, New York, 1980.
22. R. A. Marcus, *The Journal of Chemical Physics*, 1956, **24**, 966.
23. R. A. Marcus, *The Journal of Chemical Physics*, 1965, **43**, 679.
24. W. F. Libby, *The Journal of Physical Chemistry*, 1952, **56**, 863-868.
25. N. S. Hush, in *Progress in Inorganic Chemistry*, John Wiley & Sons, Inc., 1967, pp. 391-444.
26. K. Andrzej, in *Electrogenerated Chemiluminescence*, CRC Press, 2004, pp. 163-211.
27. I. M. Kolthoff and W. J. Tomsicek, *The Journal of Physical Chemistry*, 1935, **39**, 945-954.
28. J. E. B. Randles, *Transactions of the Faraday Society*, 1952, **48**, 828-832.
29. R. S. Nicholson, *Analytical Chemistry*, 1965, **37**, 1351-1355.
30. R. S. Nicholson and I. Shain, *Analytical Chemistry*, 1964, **36**, 706-723.
31. J. G. Osteryoung and R. A. Osteryoung, *Analytical Chemistry*, 1985, **57**, 101A-110A.
32. P. Enright, J. Cassidy and A. Betts, *Journal of Electroanalytical Chemistry*, 2008, **619-620**, 206-208.
33. W. J. Albery and A. R. Hillman, *Annual Reports Section "C" (Physical Chemistry)*, 1981, **78**, 377-437.
34. C. R. Hess, G. A. Juda, D. M. Dooley, R. N. Amii, M. G. Hill, J. R. Winkler and H. B. Gray, *Journal of the American Chemical Society*, 2003, **125**, 7156-7157.

Chapter 3 Experimental

3.1 Instrumentation

3.1.1 Potentiostat

All electrochemical measurements were carried out using a Metrohm Autolab B.V. μ -AUTOLAB-type-III potentiostat, Netherlands, connected to and controlled by a Viglen Ltd Genie desktop PC powered by an Intel^(R) Core^(TM) 2 Quad CPU model Q8200 at 2.33 GHz clock speed. The operating system was Windows Vista^(TM) Home Basic 32-bit. General Purpose Electrochemical System (GPES, Metrohm) Software was installed for control of the potentiostat during any electrochemical investigations.

3.1.2 Electrodes

A standard three-electrode set-up as described previously, was used in all cases unless otherwise stated. These consisted of either a glassy carbon (GC) or gold (Au) disc macroelectrode (BASi, UK). The GC electrode area was 0.07 cm^2 , $d = 3 \text{ mm}$ and gold 0.02 cm^2 , $d = 1.6 \text{ mm}$. Before use, electrodes were polished using increasingly finer grades of abrasive paper (carburundum, grades P400, P1200, P2400, P4000, Presi, France) followed by final polishing on a wetted, napped polishing cloth with $0.3 \mu\text{m}$ alumina slurry (Presi, France). A modified three-electrode set-up was also used, consisting a flat tin-doped indium oxide (ITO) semi-conducting glass slide as the working electrode that did not require polishing procedures; this was instead carefully cleaned with isopropanol prior to first use. In one case, a gold microelectrode, of area $1.96 \times 10^{-5} \text{ cm}^2$, $d = 50 \mu\text{m}$ was used.

Platinum or nickel wire (Advent Research Materials Ltd, UK), coiled to increase surface area, or a carbon rod served as a counter electrode and either a saturated calomel electrode (SCE, Radiometer Analytical, France) or silver|silver chloride (Ag|AgCl, BASi, UK) reference electrode was used. At 25°C , the electrode potentials for the SCE and Ag|AgCl reference electrodes is $+0.244 \text{ V}$ and $+0.197 \text{ V}$ vs. the standard hydrogen electrode (SHE), respectively.¹ The potential of a reference electrode varies with temperature (typically $0.5 - 1.0 \text{ mV}/^\circ\text{C}$).

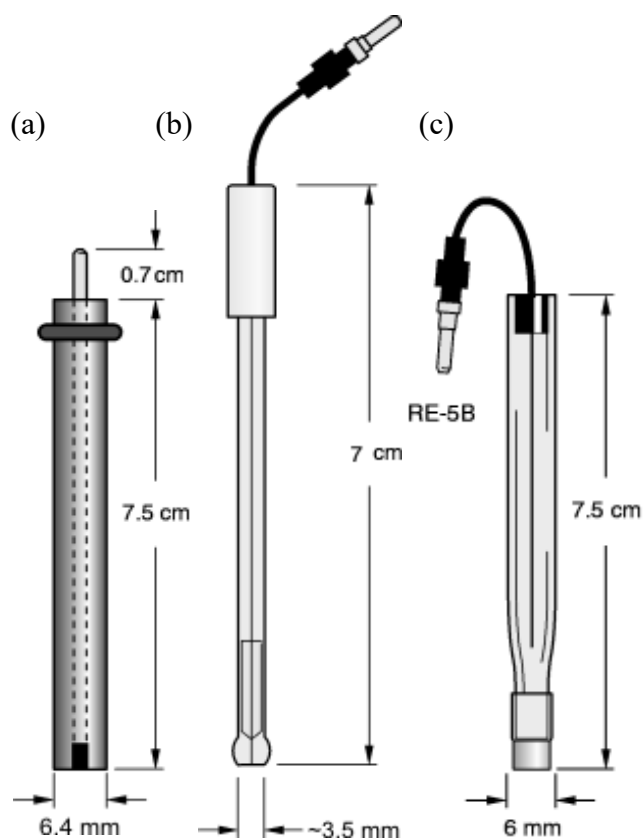


Fig. 40 Schematic illustration of (a) a glassy carbon/gold working electrode,² (b) a gold microdisk electrode³ and (c) Ag|AgCl reference electrode.⁴ Images reproduced with permission from Bioanalytical Systems Inc. Instrumentation Catalogues.

3.2 Materials

The chemicals, biochemical reagents, solvents and gases used throughout are tabulated in the following sections. Deionised and doubly filtered water (D.I. H₂O), of resistivity not less than 18.2 MΩ cm, was obtained from an UHQ PS water purifier (Elgastat, UK).

3.2.1 Chemicals

Tables 7 and 8 below detail the chemicals and reagents used throughout the experiments carried out in this thesis, listed alphabetically and grouped by supplier.

Table 7 Chemical reagents

Chemical	Purity / %	Supplier
ammonium chloride	>99	Fisher Scientific
calcium chloride.2H ₂ O	>99	Fisher Scientific
citric acid	99	Fisher Scientific
di-potassium hydrogen phosphate	>98	Fisher Scientific
iron(II) sulfate.7H ₂ O	>99.5	Fisher Scientific
magnesium sulfate.7H ₂ O	97	Fisher Scientific
potassium dihydrogen phosphate	>99	Fisher Scientific
sodium bicarbonate	>99	Fisher Scientific
sodium chloride	99.5	Fisher Scientific
sodium sulfate.10H ₂ O	99	Fisher Scientific
2,2,6,6-Tetramethyl-1-piperidinyloxy (TEMPO)	98	Sigma Aldrich
4-nitrobenzenediazonium tetrafluoroborate	97	Sigma Aldrich
chlorophyllin sodium copper salt	–	Sigma Aldrich
cis-bis(isothiocyanato)bis(2,2'-bipyridyl-4,4'- dicarboxylato)ruthenium(II) (N-3 Dye)	95	Sigma Aldrich
iron(III) chloride	97	Sigma Aldrich
nafion [®]	–	Sigma Aldrich
potassium carbonate	>99	Sigma Aldrich
potassium chloride	>99	Sigma Aldrich
sodium borohydride	>99	Sigma Aldrich
tetrabutylammonium perchlorate	>99	Sigma Aldrich
tetrabutylammonium tetrafluoroborate	>99	Sigma Aldrich
tween 20	–	Sigma Aldrich
variamine blue b	–	Sigma Aldrich
β-D-glucose	>99.5	Sigma Aldrich
ferrocene carboxaldehyde	98	Strem
ferrocene carboxylic acid	>97	Strem
ferrocene methanol	97	Strem
tert-Butylferrocene	>98	Strem

Table 8 Biochemical reagents

Biochemical reagent	Purity / %	Supplier
active human hCG full length protein hormone ab77874	>95	Abcam
anti-BNP antibody rabbit polyclonal: reactivity Human ab19645	–	Abcam
anti-hCG antibody [hCG1]: reactivity Human ab400	>99	Abcam
BNP hormone: reactivity Human ab123777	>98	Abcam
β -hCG hormone: reactivity Human ab126653	–	Abcam
laked horse blood	–	Oxoid Ltd.
anti-progesterone antibody: reactivity Human	–	Randox
progesterone hormone: reactivity Human	–	Randox
bovine serum albumin	>96	Sigma Aldrich
creatinine	>98	Sigma Aldrich
glucose oxidase lyophilized solid ~192 U/mg	–	Sigma Aldrich
haemoglobin Human	–	Sigma Aldrich
lactic acid	–	Sigma Aldrich
<i>N</i> -(3-Dimethylaminopropyl)- <i>N'</i> -ethylcarbodiimide hydrochloride (EDC)	>99	Sigma Aldrich
<i>N</i> -hydroxysulfosuccinimide sodium salt (Sulfo-NHS)	>98	Sigma Aldrich
phosphate buffered saline tablets, 10 mM	–	Sigma Aldrich
urea	–	Sigma Aldrich
uric acid	>99	Sigma Aldrich

The hormones BNP, β -hCG and hCG were each reconstituted to 1 mL with 10 mM PBS and 1 mL standards ranging 1 fg mL⁻¹ to 1 mg mL⁻¹ were prepared from this stock solution with dilution 10 mM PBS with several smaller 30 μ L aliquots and stored in the freezer at -18°C until use. The antibodies were also stored in the freezer as 10 μ L aliquots. A surface activation buffer was prepared by dissolving sulfo-NHS (2.2 mg, 5 mM) and EDC (0.8 mg, 2 mM) in 2 mL 10 mM PBS immediately prior to use.

3.2.2 Solvents and Gases

Tables 9 and 10 below detail the solvents and gases used.

Table 9 Solvents

Solvent	Purity / %	Supplier
acetonitrile (MeCN)	>99.9	Fisher Scientific
ethanol (EtOH)	>99.9	Fisher Scientific
hydrochloric acid (HCl)	–	Fisher Scientific
isopropanol	>99.5	Fisher Scientific
nitrobenzene	99	Fisher Scientific
methyl iodide (MeI)	99.5	Sigma Aldrich
<i>N,N</i> -dimethylformamide (DMF)	>99.8	Sigma Aldrich
<i>n</i> -butyllithium (<i>n</i> -BuLi)	–	Sigma Aldrich
perchloric acid (HClO ₄)	70	Sigma Aldrich

Table 10 Gases

Gas	Purity / %	Supplier
nitrogen (oxygen-free)	–	BOC
argon	>99.99	BOC

3.3 Experimental Preparations

A multitude of detection strategies have been explored and studied for medical markers involved in cardiovascular disease and pregnancy. The experimental approaches designed and carried out for each of these areas of clinical interest are discussed in the following sub-sections. Unless explicitly identified, all procedures and experiments were undertaken under ambient conditions (temperature = 293 ± 2 K).

3.4 Electrode Characterisation

Tin doped indium oxide (ITO) material was investigated for use as an electrode as the basis of the modification platform.

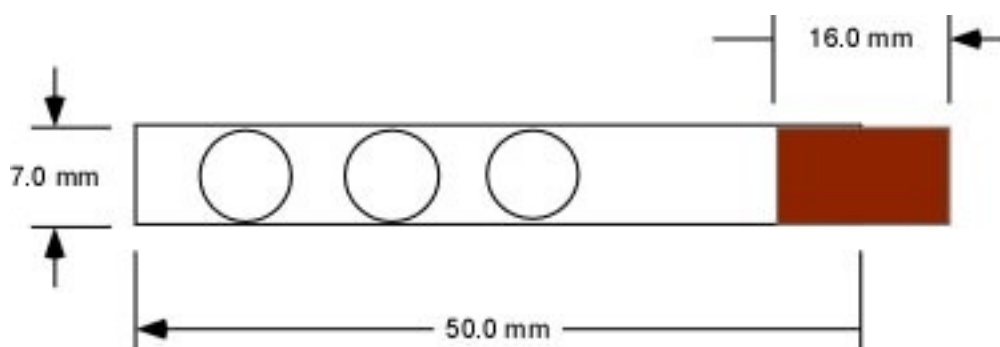


Fig. 41 A diagram of the ITO electrode prepared for these studies. Three electrode areas of 6 mm diameter were prepared with Fisherclark WS5002 self adhesive paper reinforcement rings (0.28 cm^2 determined using a travelling microscope and area = πr^2). One end of the ITO was used for electrical connection *via* application of copper tape.

The resistance of the prepared ITO electrode surface was investigated at three defined sites; 11.9 ± 0.4 , 23.7 ± 0.6 and 35.6 ± 0.4 mm from the connection site as to be evenly distributed along the electrode surface. To determine whether there was a significant change in resistance with increasing distance from the connection site, where one pin was gently pressed against the centre of each respective electrode area and the other on the electrode-facing edge of the connective copper tape.

3.4.1 Preparation of Ferrocene-labelled Antibody Modified ITO Electrode Surface

Electrochemical studies were performed in a modified three-electrode set-up with a tin-doped indium oxide (ITO) coated glass working electrode (CB-50IN-CUV, sheet resistance 5-15 Ω , dimensions 7x50x0.7 mm, Delta Technologies Ltd.).

Electrochemical measurements made in a 30 μ L sample droplet. Nichrome wire was used as the counter electrode and a silver chloride (Ag|AgCl; 3 M NaCl) reference electrode (BASi, UK). All potentials are reported against this reference unless otherwise stated.

The preparation of the surface and ferrocene tagged antibodies is described in the following sections.

3.4.1.1 Surface Deposition of 4-nitrobenzene Diazonium Salt

Electrodes were carefully cleaned prior to modification with isopropanol and dried under a stream of oxygen-free N_2 . The electrochemically controlled 1 electron reduction of 2 mM 4-nitrobenzenediazonium tetrafluoroborate prepared in 0.1 M tetrabutylammonium perchlorate in acetonitrile (TBAP-MeCN) for four reduction-oxidation cycles (+0.7 V – -0.4 V, $\nu = 0.1$ V s⁻¹) yields a nitrophenyl modified electrode.⁵ Fig. 42 describes the modification process.

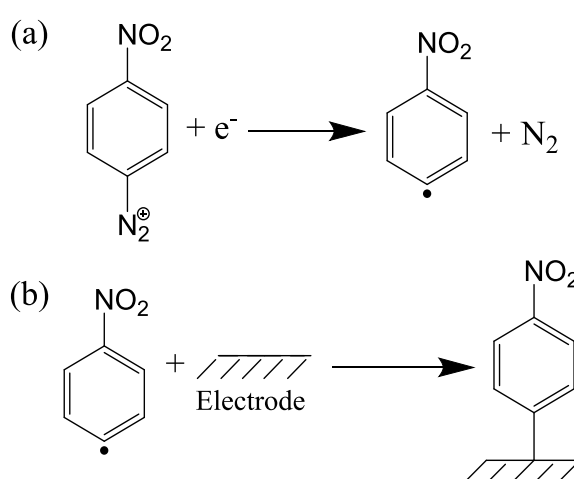


Fig. 42 Illustration of the 4-nitrophenyl surface modification *via* (a) the one electron reduction process which leads to the formation of aryl radicals followed by (b) the reaction between the radicals and electrode to yield a modified surface.

A monolayer deposition was assumed after the first cycle and with the possible formation of a multilayer during the second/subsequent scans.⁶ The electrode was removed from the electrolyte and rinsed thoroughly in MeCN followed by D.I. H₂O and drying under nitrogen.

3.4.1.2 Molecular Wire Functionalisation

Following the initial modification with the nitrobenzene layer, voltammetrically controlled reduction from +0.4 V – -1.2 V over four cycles was then carried out in a protic solution (90:10 EtOH into 0.1 M KCl). The observed cyclic voltammetric wave observed becomes irreversible and the peak height increases by a factor of *ca.* 6, suggesting that the classical reduction of NO₂ to NH₂ occurs within the grafted layer. The electroformation of a phenylamine modified electrode surface is required for binding with carboxyl groups in the bio-conjugation step (*q. v.* Fig. 45 & Fig. 46).

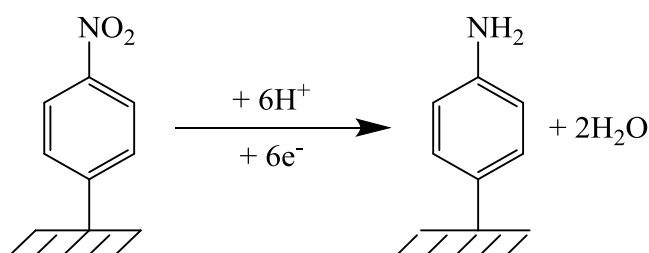


Fig. 43 Illustration of the surface functionalisation consisting the 6 electron, 6 proton reduction process to afford the conversion of the nitro- group to the amine-functionality.

3.4.1.3 Synthesis of Antibody Bio-conjugates

Antibodies were chemically labelled with ferrocene redox tags through a general coupling scheme developed by Matsunaga *et al.*,⁷ (Fig. 44). This method was used for the ferrocene tagging modifications of all antibodies disclosed in Table 8. Firstly, in suitably sized eppendorf, 10 μ L antibody IgG was dissolved in 190 μ L 10 mM PBS (pH 7.4) in order to total 200 μ L solution and the pH adjusted to \sim 9 with 5 wt.% potassium carbonate (\sim 15-25 μ L). This solution was subsequently diluted with a 100 mg mL⁻¹ solution of FcCHO in DMF, such that the FcCHO was in excess (\sim 200 μ L). Following incubation at ambient temperature for 30 min to form the imine, sodium borohydride (1.0 mg) was added and incubated at ambient temperature for 10 min in order to form the secondary amine, after which the

solution pH was adjusted to pH \sim 7.3 using 1.0 M HCl (\sim 40 μ L). After reaction, excess FcCHO and solvent were removed from products Ab-NH-CH₂-Fc by centrifugation and washed with PBS (12k rpm for 20 min, followed by 1st PBS wash (top up to \sim 200 μ L total volume) and 12k rpm for 5 mins, followed by 2nd PBS wash (top up to \sim 200 μ L) and final 12k rpm for 5 mins, Vivaspin 500 centrifuge tubes, GE Healthcare, Sweden). After the final centrifuge step, each tube is topped up such that the total volume is 200 μ L in each to yield the final purified Ab-Fc complex and stored at 4 $^{\circ}$ c when not in use.

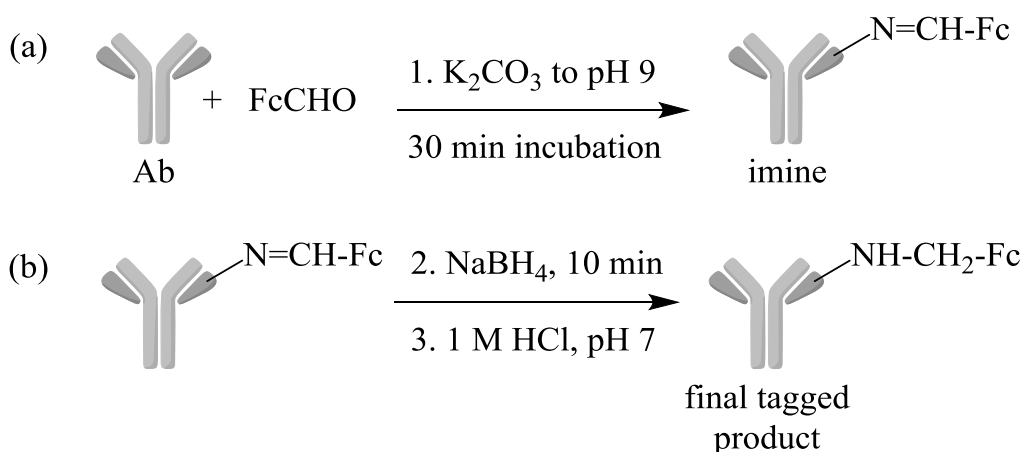


Fig. 44 Illustration depicting the synthesis of the ferrocene tagged antibodies, where step (a) describes the initial attachment of the ferrocene moiety and imine formation; (b) shows the conditions required for the subsequent conversion of the imine to the secondary amine to form the final stable tagged product. This representation shows depicts the attachment of only one ferrocene, in reality this reaction occurs at any available -NH₂ functional group.

3.4.1.4 Immobilisation of Ferrocene Labelled Antibody onto the ITO Surface

The immobilisation of the labelled antibody on the electrode surface was achieved through the coupling of carboxylic acid groups of the antibody to the primary amine groups of the phenylamine-modified ITO electrode surface *via* an amide linkage. This is achieved by using N-(3-Dimethylaminopropyl)-N'-ethylcarbodiimide hydrochloride (EDC) to first form an active ester leaving group (o-Acylisourea ester) *via* reaction with a carboxylate group, in a mechanism similar to that used for N,N-dicyclohexylcarbodiimide (DCC) coupling of amino acids,⁸ followed by fast

transformation into the NHS-ester using N-hydroxysulfosuccinimide sodium salt (sulfo-NHS) (Fig. 46). Briefly, the ferrocene conjugated antibody was mixed with the same volume of activation buffer (containing 2 mM EDC and 5 mM sulfo-NHS in PBS) for 15 min to activate the -COOH group on the antibody (volume dependent on number of electrodes being prepared). Finally, 40 μ L of this solution was applied to each of the -NH₂ functionalized ITO electrode areas and left at 4°C in a fridge for a specific number of hours, typically, unless otherwise specified this was 18 hours.

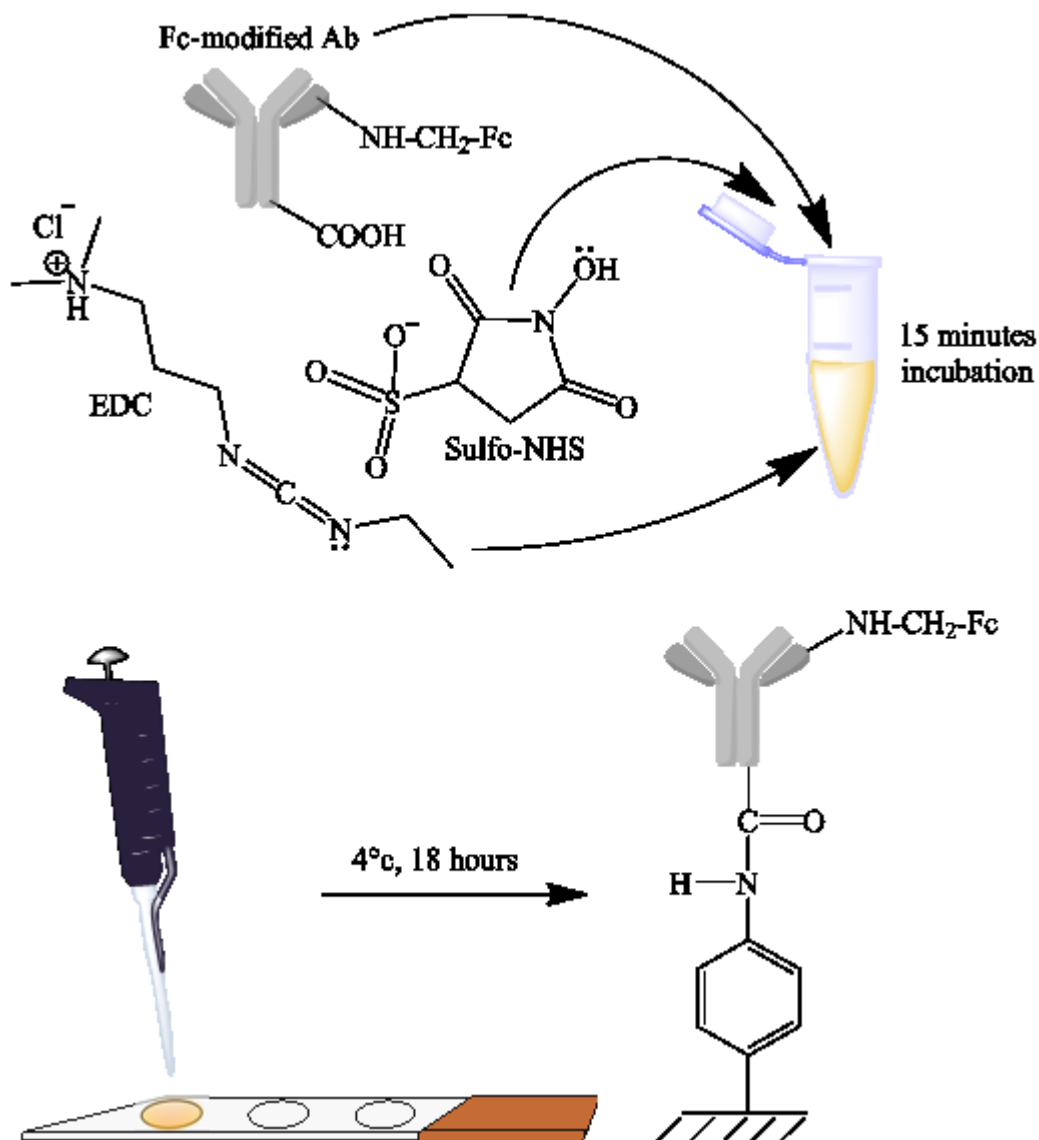


Fig. 45 Illustration of the ferrocene functionalised antibody modified electrode surface procedure, where the carboxy terminal of the antibody is first activated using sulfo-NHS and EDC before application to the electrode surface for subsequent coupling at 4°C over 18 hours.

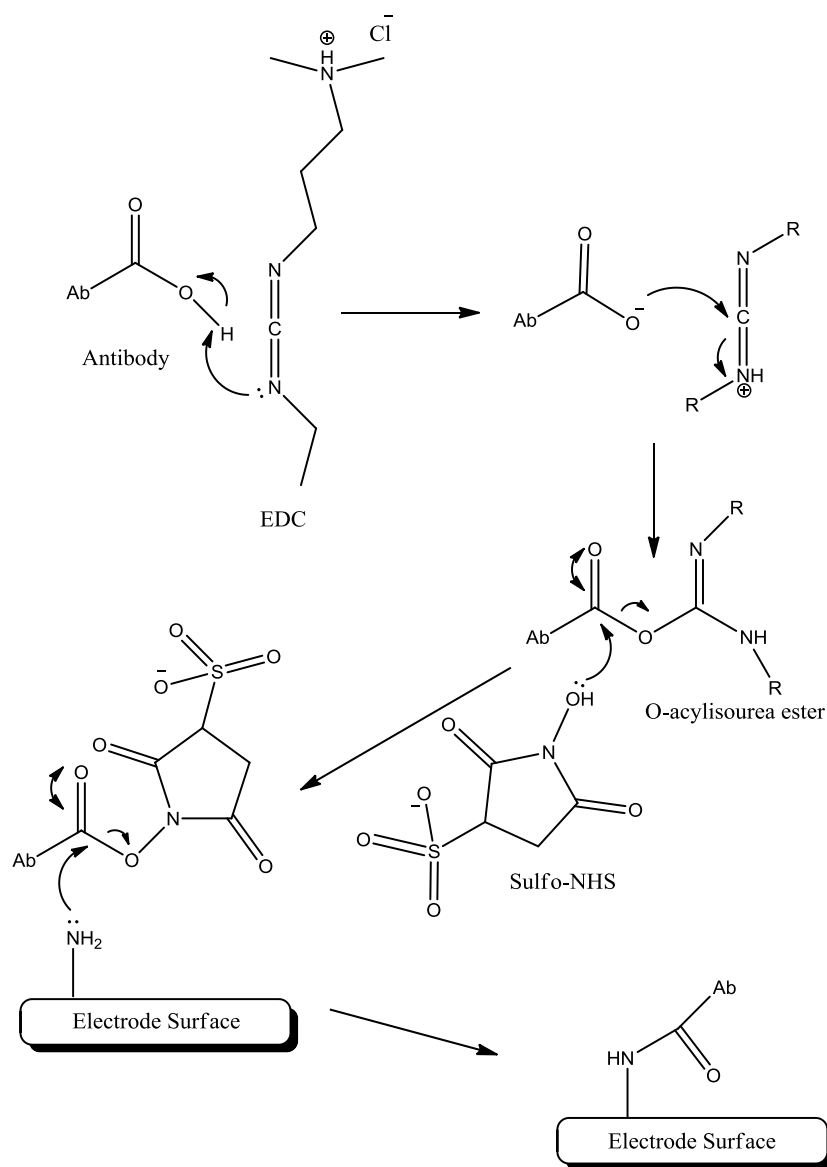


Fig. 46 Mechanism for EDC/Sulfo-NHS activation step and subsequent attachment to the surface bound amine.

3.4.1.5 Finalising Electrode Preparation

Antibody-modified electrodes were first washed with 0.1 vol.% tween 20 in PBS, and the unoccupied ITO surface blocked by applying 30 μ L 1 wt.% BSA-PBS, pH 7.0 for 30 min at room temperature. The BSA step is required to prevent the nonspecific binding of the antibodies in order to prevent interaction of reagents that may foul or interact undesirably with the electrode surface. It is also used because of the lack of reactivity towards many biochemical reactions and its low cost. Other blocking agents include non-fat dry milk and whole serum. Following this, the modified electrodes were washed with both 0.1 vol.% tween 20 in PBS and PBS

successively and dried under a stream of N₂. Finally, all electrodes surfaces were tested in PBS using CV at 0.1 V s⁻¹ over a potential window -0.1 – 0.5 V for the duration of 10 scans; this was to stabilise the ferrocene redox system.

3.5 Detection of hCG and Kinetic Investigation

3.5.1 Detection of hCG in PBS

The freshly prepared antibody-modified electrodes were incubated in known concentrations of hCG antigen in 10 mM PBS for 15 min at room temperature (20 ± 2 °C). Excess and loosely bound antigen was then removed by subsequent washing with tween 20 and PBS buffer solution followed by drying under nitrogen stream. The electrodes were voltammetrically re-examined with cyclic and square wave voltammetry to observe the affects of incubation upon the electrochemical signal. Cyclic voltammetry experiments were carried out between a potential window -0.1 – 0.7 V, $\nu = 0.02 - 1 \text{ V s}^{-1}$ and square wave voltammetry was carried out between -0.1 – 0.7 V, Hz = 25. The data was used for characterisation of the surface and to plot a calibration chart for the change in current response against antigen concentration.

3.5.2 Kinetic Investigation of hCG in PBS

A kinetic investigation was carried out for the whole hCG hormone over incubation times of 15, 30 and 60 minutes. The analysis method was modified, observing a change in oxidation potential (E_p^{ox}) with increasing scan rate, as opposed to Δi_p . This change in E_p^{ox} could be used to determine the 'global fractional antigen coverage, θ ' *via* fitting experimental data to a theoretical simulation. As a result, the heterogeneous electron transfer rate constant, k_s , for the blank and incubated electrodes could be determined and the values compared to determine the surface antigen coverage with respect to incubation time.

3.5.3 Quantitative Detection of hCG in Artificial Urine and Laked Horse Blood

Artificial urine and laked horse blood were investigated as simulated clinical sample matrices to determine the suitability of the sensing protocol. The experiment

involved investigating whether or not a signal response could be obtained in such media, and if so, could the responses be quantified as for preliminary studies.

Artificial urine was prepared as described by Brooks *et al.*,⁹ and various hCG stock solutions were prepared.

Due to the complicated nature of blood as an electrolyte, laked horse blood was first investigated at a diluted concentration, where various hCG stock solutions were prepared to 10 vol.% laked horse blood with 10 mM PBS as the diluent.

Electrochemical investigations were carried out under the same conditions as described in section 3.5.1.

3.5.4 Interference Studies

Under the guidance and instruction of clinical supervision from supervisors professor Steven Atkin and professor Eric Kilpatrick, the electrochemical immunoassay system developed for POC detection of hCG was tested for interference against common constituents of urine and blood. These were glucose in the event of testing patients with diabetes or renal complications such as kidney failure and haemoglobin for conditions such haemoglobinuria, renal complications and for testing in blood samples or blood related mediums.

3.5.4.1 Glucose

Glucose was investigated as an interfering substance due to its natural presence in blood and presence in urine in certain medical conditions, most commonly diabetes from which ~8% of the UK population suffer. Samples of hCG in artificial urine were prepared with the addition of 20 mg mL⁻¹ (111 mM) glucose, exceeding the upper limit found in the urine of diabetic patients. The hCG incubation experiments described in section 3.5.2 were then repeated with the glucose containing samples for a 15 minute incubation period and the data compared with the respective artificial urine data to determine whether or not the glucose presented any interfering issues.

3.5.4.2 Haemoglobin

Haemoglobin was investigated as an interfering substance due to its natural presence in blood and presence in urine in certain medical conditions. Samples of hCG in

artificial urine were prepared with the addition of 1 mg mL^{-1} haemoglobin and the hCG incubation experiments were then repeated with the haemoglobin containing samples. The resulting data was compared with the original artificial urine data to determine whether or not the haemoglobin presented any interfering issues.

3.6 Cardiovascular Disease Detection at the Point of Care

3.6.1 Detection of BNP in PBS

Anti-BNP antibodies were labelled with ferrocene and covalently bound to the ITO surface as described in sections 3.4.1.3 and 3.4.1.4. The freshly prepared antibody-modified electrodes were incubated in known concentrations of BNP antigen in 10 mM PBS for 15 min at room temperature ($20 \pm 2^\circ\text{C}$). Excess and loosely bound antigen was then removed by subsequent washing with tween 20 and PBS buffer solution followed by drying under nitrogen stream. The electrodes were voltammetrically re-examined with cyclic and square wave voltammetry to observe the affects of incubation upon the electrochemical signal. Cyclic voltammetry experiments were carried out between a potential window $-0.2 - 0.7 \text{ V}$, $\nu = 0.02 - 1 \text{ V s}^{-1}$ and square wave voltammetry was carried out between $-0.1 - 0.8 \text{ V}$, $\text{Hz} = 25$. The data was used for characterisation of the surface and to plot a calibration chart for the change in current response against antigen concentration.

3.7 Pregnancy Detection at the Point of Care

3.7.1 Detection of β -hCG in PBS

Anti- β -hCG antibodies were labelled with ferrocene and covalently bound to the ITO surface as described in sections 3.4.1.3 and 3.4.1.4. The freshly prepared antibody-modified electrodes were incubated in known concentrations of β -hCG antigen in 10 mM PBS for 15 min at room temperature ($20 \pm 2^\circ\text{C}$). Excess and loosely bound antigen was then removed by subsequent washing with tween 20 and PBS buffer solution followed by drying under nitrogen stream. The electrodes were voltammetrically re-examined with cyclic and square wave voltammetry to observe the affects of incubation upon the electrochemical signal. Cyclic voltammetry experiments were carried out between a potential window $-0.1 - 0.7 \text{ V}$, $\nu = 0.02 - 1 \text{ V s}^{-1}$ and square wave voltammetry was carried out between $-0.1 - 0.7 \text{ V}$, $\text{Hz} = 25$.

The data was used for characterisation of the surface and to plot a calibration chart for the change in current response against antigen concentration.

3.7.2 Kinetic Investigation of β -hCG in PBS

The aim of this experiment was to further characterise and optimise the sensing platform, to determine at what point the antibody-antigen binding process had reached equilibrium and hence the minimum incubation time possible. The extent of current change (Δi_p) in CV and SWV with incubation time was investigated, where 1 pg mL^{-1} , 1 ng mL^{-1} and $1 \text{ } \mu\text{g mL}^{-1}$ β -hCG was incubated on the ITO electrode surface for 1, 2, 3, 4, 5, 10, 15, 60 minutes up to a maximum of 12 h. The electrodes were washed with tween 20 and PBS before drying under nitrogen and study *via* voltammetric examination.

3.8 Multiplex studies: Chlorpromazine and Ruthenium N-3 Dye as Alternative Redox Tags

Chlorpromazine and cis-bis(isothiocyanato)bis(2,2'-bipyridyl-4,4'-dicarboxylato) ruthenium(II) (N-3 dye) were investigated as alternative labels for signal generation to develop a multiplexed sensing system, capable of multi-analyte detection.

3.8.1 Preparation of Chlorpromazine-labelled Antibody

The chlorpromazine was modified by Mr. Jonathan Knaggs (Hull York Medical School) so as to convert the terminal dimethyl amine moiety to a carboxylic acid functionality. The compound was presented as a gift, without characterisation, and used as received.

Fig. 47 depicts the structural change expected from the modification.

As the functional groups involved ($-\text{COOH}$ and $-\text{NH}_2$) in the conjugation are different to the method presented in section 3.4.1.3 ($-\text{CHO}$ and $-\text{NH}_2$), the label required an alternative method of attachment. Matsunaga *et al.*⁷ suggests the conjugation of these groups is enabled by sulfo-NHS and EDC, in the same way presented in section 3.4.1.4. Figures 47 and 48 depict the conjugation chemistry, however the functional group $-\text{COOH}$ is attached to the electroactive label instead of the antibody and the $-\text{NH}_2$ is attached to the antibody paratope regions as opposed to

the electrode surface, the chemistry remains the same. In this instance, the initial activation incubation of CPZ-COOH is carried out at room temperature for one hour instead of 15 minutes. The addition of Ab is then made for the conjugation step and the mixture stored for two hours at room temperature as opposed to the overnight conditions previously discussed. This process yields Ab-NH-CO-CPZ.

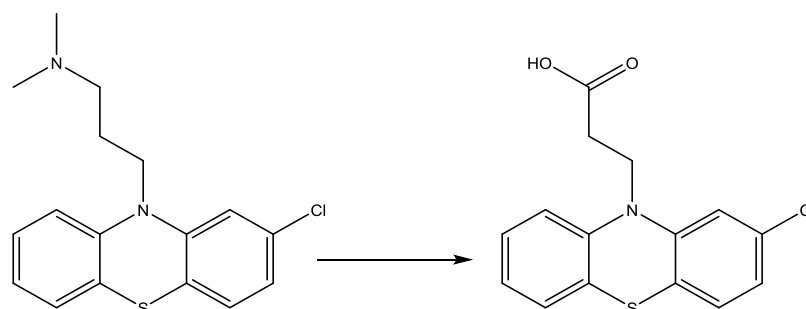


Fig. 47 Conversion of the terminal dimethyl amine to the carboxylic acid functionality required for the labelling procedure.

3.8.2 Detection of BNP with Chlorpromazine Modified Surface

The modified antibodies were subsequently immobilised to the glassy carbon electrode surface as per the procedure set out in section 3.4.1.4 to yield a surface depicted in Fig. 48. The modified surface was investigated voltammetrically by cyclic and square wave methods as carried out in section 3.5.1.

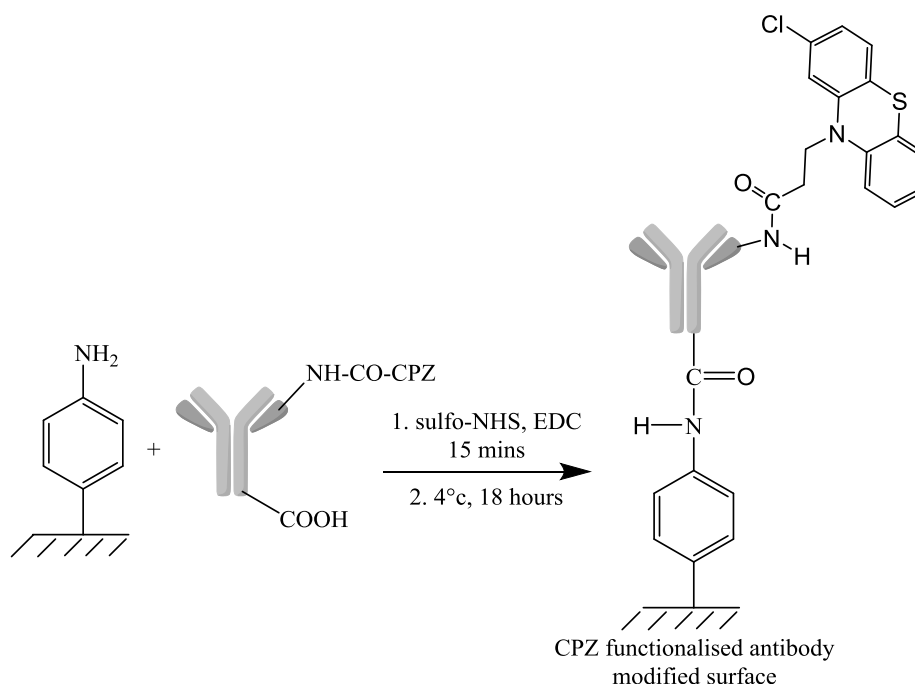


Fig. 48 Schematic breakdown of surface attachment procedure for the CPZ modified antibodies.

3.8.3 Preparation of N-3 Dye labelled Antibody

The N-3 dye was directly conjugated to the anti-BNP antibodies, since it possesses the free $-\text{CO}_2\text{H}$ groups required for the amide linkage reaction. The procedure was carried out as described in section 3.8.1.

3.8.4 Detection of BNP with N-3 Dye Modified Surface

The modified N-3 dye was subsequently immobilised to the glassy carbon electrode surface as per the procedure set out in section 3.4.1.4. The modified surface was investigated voltammetrically by cyclic and square wave methods as carried out in section 3.5.1.

3.8.5 Determination of the Number of Antibody Bound Redox Tags

The aim was to establish the average number of redox tags attached to the antibody following modification and compare this to literature values. This was investigated by two methods: ultraviolet-visible spectroscopy (UV-VIS) and *via* theoretical application of data obtained with CV.

3.8.5.1 Method One: UV-VIS

Ferrocene and ruthenium are both UV-VIS active,^{11, 12} hence employing the UV-VIS technique in conjunction with Beer-Lambert Law analysis

$$A = \epsilon cl \quad (3.1)$$

where A = absorbance, ϵ = extinction coefficient, c is the concentration of the species and l = the path length, it is possible to observe the presence of the label and changes in signal intensity associated with concentration. It is then possible to obtain a calibration graph, from which it may be possible to validate the success of the tagging conjugation process.

To determine the number of ferrocene groups tagged to each antibody, the extinction coefficient of the antibody, ferrocenecarboxaldehyde and the ferrocene-tagged antibody must be known to determine the average number of redox tags bound to each antibody. The extinction coefficient can be determined by plotting a calibration

curve, the gradient of which represents the extinction coefficient analyte. Ferrocene has recorded absorptions at 440, 325 – 322 and 204 nm.^{11, 13} N-3 dye absorbs similarly, at wavelengths ranging 538 – 500, 399 – 375 and ~315 nm.^{12, 14, 15} Proteins such as antibodies also largely absorb at short wavelengths, at ~280 nm,¹⁶⁻¹⁸ therefore the chosen wavelength range was 700 – 200 nm. UV-VIS was carried out using a 200 μL volume quartz cell of 1 cm path length and UV-VIS spectrometer (Perkin Elmer Lambda Bio 10). A set of standards consisting 0.1, 0.3, 0.5, 0.7 and 1 mg mL^{-1} ferrocene in a solution containing DMF and PBS (50:50) to simulate the antibody-conjugate solution.

3.8.5.2 Method Two: Cyclic Voltammetry

The second route to determine the number of tags was through physicochemical analysis of the redox-antibody system. CV was carried out on Fc-Ab modified electrodes in 10 mM PBS as described in section 3.5.1. To calculate the number of tags on each antibody, we must first determine the surface coverage of antibody, Γ . To do this, the peak current data from each scan rate was applied to equation 3.2.

$$\Gamma = \frac{i_p \cdot 4 \cdot RT}{F^2 \cdot S \cdot \nu} \quad (3.2)$$

from this, the number of tags could be derived as follows

$$\text{tags} = \frac{K}{\Gamma} \quad (3.3)$$

3.9 TEMPO Immunoassay

3.9.1 Electrochemical Characterisation

The electrochemical reversibility of 1 mM 2,2,6,6-Tetramethyl-1-piperidinyloxy (TEMPO) was investigated in PBS and 0.1 M TBAP-MeCN *via* CV over variable scan rate conditions (0 – 1.2 V, $\nu = 0.02 - 1 \text{ V s}^{-1}$) at room temperature ($20 \pm 2^\circ\text{C}$).

3.9.2 Antibody Surface Attachment

Currently, antibodies specific to TEMPO are not available, hence Anti-DMPO (5,5-Dimethyl-1-Pyrroline-N-Oxide) antibodies were used due to the specificity to the

nitron moiety present in both DMPO and TEMPO. Anti-DMPO antibodies were covalently bound to the ITO electrode surface as described in section 3.4.1.4.

3.9.3 Calibration of Sensor Response

Stock solutions of 1, 10 and 100 μM TEMPO were prepared in PBS and 40 μL aliquots incubated for one hour on freshly prepared Ab-DMPO modified ITO electrodes. The electrodes were then washed with tween 20 and PBS solutions before drying under N_2 stream. Electrochemical investigation *via* SWV was undertaken over a potential window 0.2 - 1.1 V in degassed 10 mM PBS (N_2 ; 10 min) to determine if a change in signal could be observed as a result of TEMPO incubation. The settings used for SWV were 0.1 V amplitude, 25 Hz frequency, 0.00449 V step potential. A calibration chart of peak current, i_p vs. TEMPO concentration was plotted to determine if the sensor was suitable for quantitative detection of the analyte.

The results of these experiments are discussed in the following chapters.

References

1. A. J. Bard and L. R. Faulkner, *Electrochemical Methods : Fundamentals and Applications*, Wiley, New York, 2nd edn., 2001.
2. BASi Stationary Voltammetry Electrodes, <http://www.basinc.com/products/ec/sve.php>, (accessed 21st May, 2015).
3. BASi Microelectrodes, <http://www.basinc.com/products/ec/micro.php>, (accessed 21st May, 2015).
4. BASi Reference Electrodes, <http://www.basinc.com/products/ec/ref.php>, (accessed 21st May, 2015).
5. F. Berger, J. Delhalle and Z. Mekhalif, *Electrochimica Acta*, 2008, **53**, 2852-2861.
6. A. Laforgue, T. Addou and D. Bélanger, *Langmuir*, 2005, **21**, 6855-6865.
7. M. Okochi, H. Ohta, T. Tanaka and T. Matsunaga, *Biotechnology and Bioengineering*, 2005, **90**, 14-19.
8. J. Jones, *Amino Acid and Peptide Synthesis*, Oxford University Press, Oxford, 1997.
9. T. Brooks and C. W. Keevil, *Letters in Applied Microbiology*, 1997, **24**, 203-206.

10. Y.-H. Dou, S. J. Haswell, J. Greenman and J. Wadhawan, *Electroanalysis*, 2012, **24**, 264-272.
11. D. R. Scott and R. S. Becker, *The Journal of Chemical Physics*, 1961, **35**, 516-531.
12. F. T. Kong, S. Y. Dai and K. J. Wang, *Plasma Science & Technology*, 2006, **8**, 531-534.
13. E. A. Kassab, M. I. Marzouk and M. El-Hashash, *Journal of the Serbian Chemical Society*, 2002, **67**, 593-603.
14. Z. Chen, S. Li and W. Zhang, *International Journal of Photoenergy*, 2011, **2011**, 6.
15. M. Grätzel, *Journal of Photochemistry and Photobiology C: Photochemistry Reviews*, 2003, **4**, 145-153.
16. S. V. Thakkar, K. M. Allegre, S. B. Joshi, D. B. Volkin and C. R. Middaugh, *Journal of Pharmaceutical Sciences*, 2012, **101**, 3051-3061.
17. P. Zhang, H. Lu, J. Chen, H. Han and W. Ma, *Theranostics*, 2014, **4**, 307-315.
18. S. Paul, D. Paul, G. R. Fern and A. K. Ray, *Surface plasmon resonance imaging detection of silver nanoparticle-tagged immunoglobulin*, 2011.
19. A. Radoi, D. Compagnone, M. A. Valcarcel, P. Placidi, S. Materazzi, D. Moscone and G. Palleschi, *Electrochimica Acta*, 2008, **53**, 2161-2169.
20. C. Schoenenberger, J. Jorritsma, J. A. M. Sondag-Huethorst and L. G. J. Fokkink, *The Journal of Physical Chemistry*, 1995, **99**, 3259-3271.
21. O. Zítka, *Acta Chim. Slov.*, 2007, **54**.

Chapter 4

Electrochemical Measurement of Antibody-Antigen Recognition

Biophysics: Thermodynamics, Kinetics and Analytical Detection of Human Chorionic Gonadotropin (hCG) Binding to Redox-Tagged Antibodies in Artificial Urine

This chapter adapts an existing electrochemical immunoassay to understand its mechanism of operation and its ability to be exploited for analytical purposes within a realistic sample matrix.

4.1 Introduction

The ability to monitor health may be exploited to empower patients to manage their own health, based on their own lifestyle and fitness choices. This also provides healthcare services with greater access to technologies which facilitate a healthcare professional to diagnose changes in the day-to-day biochemical functioning of a patient, based on their own biological age, opening out the possibility of early preventative care. The importance of improving health monitoring systems is imperative to making this possibility a reality, as engineering technologies become more economically compelling and technically realistic, the next generation of integrated bioanalytical sensing systems and sensors may afford valuable “big data”,¹

The development of rapid and highly sensitive methods for the sensing of proteins for the diagnosis and management of disease is not without its own intrinsic challenges. The early exploitation of immunoglobulins (antibodies) for antigen detection – the very hallmark of the biochemical adaptive immune response in living systems,² is often considered as versatile route for the detection of disease biomarkers, owing to the versatility of the this technique – antibodies may recognise wide ranges of chemical structures and organisms whilst, provided they are monoclonal, discriminate between closely relative chemical compounds. This is helped by the strong affinity constant ($10^8 \pm 3 \text{ M}^{-1}$) for the antibody-antigen interaction, rendering the association essentially irreversible.^{3,4}

To achieve above, necessitates inexpensive routes for their fabrication, whilst being functionally competent and with rapid assessment quantification over the desired analytical range.

In this work, we examine the development of an inexpensive electroimmunoassay platform that is not only reliable, but is able to afford rapid and quantitative measurement of antigen under “real world” conditions. Through the study of the thermodynamics and the kinetics of the chemoreception biophysics, we empower an analytical sensing strategy that compares very well with those that are currently commercially available. We focus our attention on the pregnancy biomarker human chorionic gonadotropin (hCG).

The determination and monitoring of pregnancy progression, diagnosis of Down’s and Edward’s syndromes and importantly, potential life threatening dangers, most notably ectopic pregnancies is of particular interest as there is no current method used in the clinical environment for the rapid, quantitative detection of early pregnancy at the point of care of a reliable standpoint. A device of this nature is needed for times of rapid decision making in emergency cases where procedures such as X-rays or surgery may affect the health of a recently conceived or otherwise unknown unborn child.

The current healthcare system is deficient of reliable, portable and quantitatively validated point of care (POC) routes for the rapid diagnosis of pregnancy in urine,^{5,6} relying on qualitative, poor accuracy urine 'wand' testing or complicated, labour intensive and lengthy (4 - 6 hour) lab based assay methods unsuitable for point of care testing methodologies, where rapid quantitative data is commonly required.^{7,8}

Human chorionic gonadotropin (hCG) is a 37 kDa glycoprotein secreted by specialist syncytiotrophoblast cells of the developing placenta following implantation of a fertilized egg.^{9, 10} The presence of hCG can be detected in serum and urine in some cases as early as three to four days following implantation, playing an important role in early pregnancy diagnosis.¹¹ However the presence of hCG may indicate other health issues including ectopic pregnancy,¹² choriocarcinoma and hydatidiform moles,¹³⁻¹⁵ offering further clinical utility. The hormone is composed of two dissimilar, non-covalently bound structures: the α and β subunits.¹⁰ The α -subunit is identical to those in the glycoprotein hormone family, such as luteinizing hormone whereas the β -subunit is unique to hCG and determines its immunological properties; providing an ideal target site for specific detection *via* immunoassay techniques.⁹

The majority of hCG immunoassays most commonly utilise enzyme-linked immunosorbent assay (ELISA) and other sandwich assay techniques,⁷ with recent advancements reported in chemiluminescence,^{16, 17} fluorescence¹⁸ and electrochemical immunosensor approaches,¹⁹⁻²¹ in addition to on-disc advancements.²² The diagnostic cut-off for a positive reading is generally 25 milliinternational units per millilitre (mIU mL⁻¹), though this varies significantly from test to test.²³ A hCG level of less than 5 mIU mL⁻¹ generally indicates a negative result.²⁴

The general approach described by Dou *et al.*²⁵ encompasses a proof-of-concept sensing protocol targeted at the detection of the cardiac biomarkers human cytokine interleukin 10 (IL10) and creatine kinase (CK). This involves the electro-deposition of a short molecular wire (0.7 to 3 nm based on the height of a 4-nitrophenyl group at 0.71 nm, up to 4 layers)²⁶ to a gold electrode surface to yield a phenylamine-modified electrode capable of tethering redox-tagged antibodies to the surface *via* the activated carboxylic acid groups of the antibodies. The choice of molecular wire and immobilisation technique used in this method is advantageous in that the distance between the bound Ab and the electrode surface is sufficiently short to provide a fast, direct electrochemical connection to the Ag binding interactions. A longer molecular wire could be used however this incurs additional complexity of the surface modification, potentially greater difficulty in orientational control and most importantly can limit the rate of electron transfer since electron transfer rates are strongly distance-dependent with exponential decay with the distance from the electrode.²⁷ The antibodies are prepared by a general coupling scheme described in section 3.4.1.3.

The detection strategy operates on redox tag conjugation to the amine rich paratope region of the Ab to act as an indicator for Ag binding, where a large electrochemical signal is observed without the presence of antigen. Upon addition of antigen to the immunoassay system, the interaction of antigen binding effectively blocks the ferrocene moieties resulting in a reduced signal intensity. This response can be calibrated to yield the working limitations and limit of detection of the sensing platform.

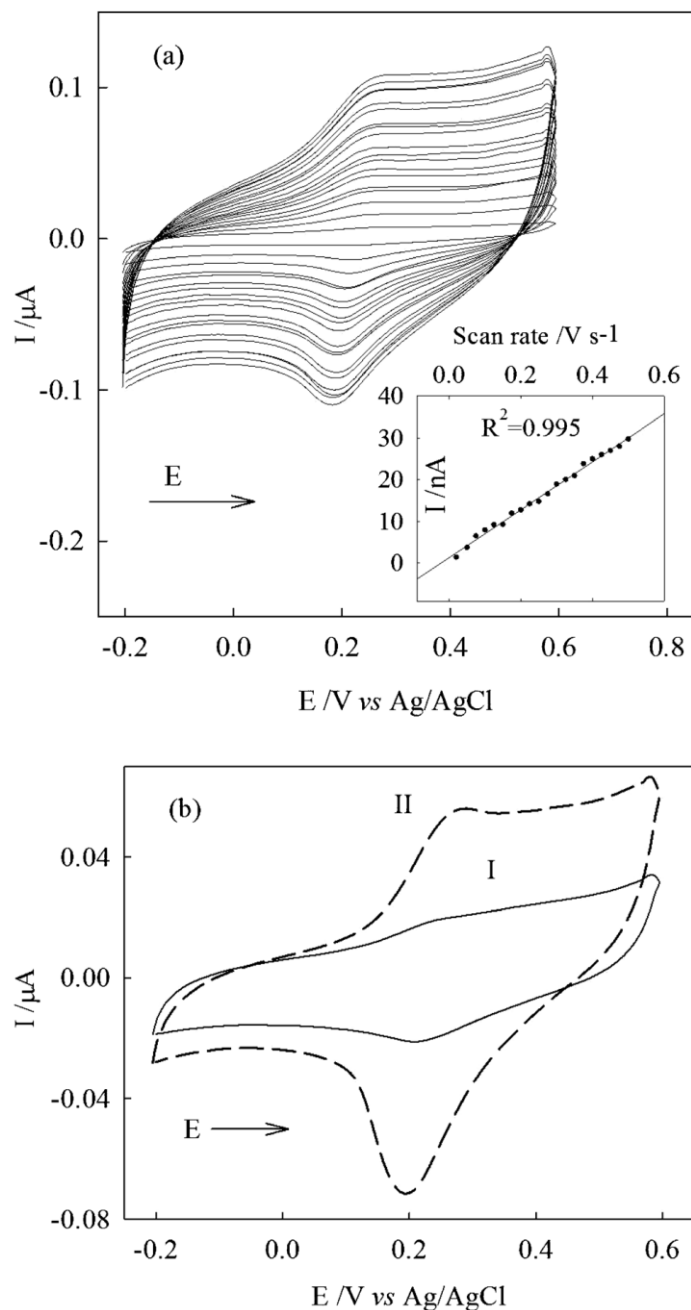


Fig. 49 (a) Cyclic voltammograms of Au/Ab-CK-Fc at scan rates 0.02, 0.05 V s^{-1} and with increments of 0.025 V s^{-1} thereafter up to 0.5 V s^{-1} . Inset a: Variation of CV peak oxidation current with experimental timescale. (b) Cyclic voltammograms on Au/Ab-CD14-FITC-Fc (I) and Au/Ab-IL10-FITC-Fc (II) immunosensors. $\nu = 0.1 \text{ V s}^{-1}$. The concentrations of the antibodies for modification were *ca.* 100 mg mL^{-1} in (a) and 15 mg mL^{-1} in (b). Scans were all in 10 mM PBS-0.1 M NaCl solutions, pH 7.4. Reproduced with permission from Dou *et al.*, 2012.

Electrochemical characterisation of the antibody modified gold surface was undertaken as shown in Fig. 49 where variable scan rate voltammetry clearly results in a single, well-defined pair of oxidation and reduction waves centred around 0.2 V.

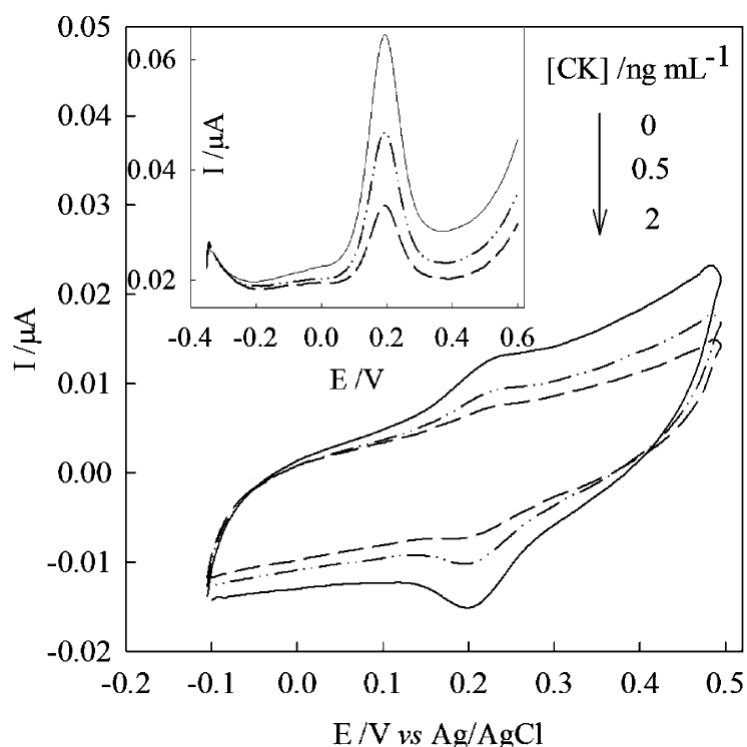


Fig. 50 Cyclic voltammograms of Au/Ab-CK-Fc sensor in biological buffer. After incubation in 0 (solid line), 0.5 (dash-dot) and 2 ng mL⁻¹ CK (dash line) for 15 min. Scan rate, 0.1 Vs⁻¹. Inset: square wave voltammograms corresponding to CV. All potentials are vs. Ag|AgCl (3 M NaCl). Reproduced with permission from Dou *et al.*, 2012.

This corresponds to the oxidation of the antibody tethered ferrocene into the ferricinium cation and subsequent reduction to ferrocene. Furthermore, a proportional relationship for i_p vs. \sqrt{v} confirms the surface bound nature of the attached ferrocene modified antibodies. Fig. 49b illustrated the response of the IL10 and CD14 modified Au electrodes at $v = 0.1 \text{ V s}^{-1}$ where it is clear that the IL10 system provides a greater signal response; a possible explanation for this is there could be a greater availability of modification sites for ferrocene attachment on IL10 than for CD14.

Dou *et al.* state the reduction in current signal occurs due a change in the local environment of the ferrocene labels. It is believed that the radical change in local surroundings as caused by the hydrophobic, electrostatic and van der Waals

interactions and hydrogen bonding associated with antibody-antigen binding, is sufficient to change the formal oxidation potential of the bound ferrocene moieties, such that they can no longer participate in low-potential voltammetry resulting in a lower current.²⁵

The kinetic study (Fig. 51) of CK undertaken in this publication suggests that there is a 70% completion of binding following only 15 minutes of incubation. This gives rise to a rapid assay system where results may be obtained as quickly as *ca.* 20 mins. This coupled with detection limits as low as 0.5 pg mL⁻¹ (Fig. 52) makes the method ideal for use in the clinical setting as a point of care device. The successful demonstration for application to several Abs (published; CK and IL-10, unpublished; progesterone, oestriol and ANP) is attractive and implies the system is theoretically applicable to any Ab. The method has also demonstrated successful operation in physiological buffer, further establishing its potential for clinical applications.

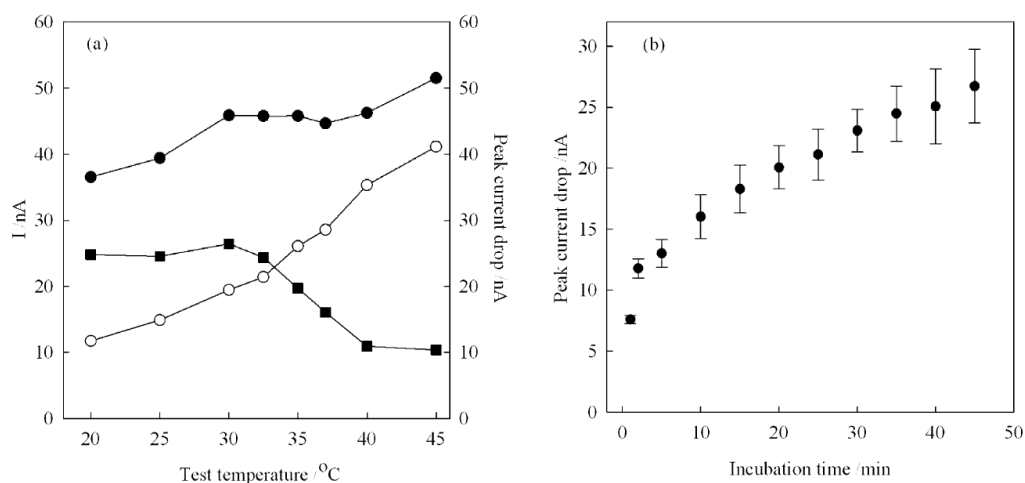


Fig. 51 (a) Peak current variances with test temperature on Au/Ab-CK-Fc (\bullet , i_{pAb}), Au/Ab-CK-Fc-AG (\circ , i_{pAg}) electrodes and the peak current drop Δi_p (\blacksquare). (b) Creatine kinase sensor with incubation time. Error bars represent electrode-to-electrode standard deviation (*SD*) ($n = 3$). In (a), the incubation time with 2 ng mL⁻¹ antigen was 15 min and 1, 2, 5, 10, and up to 45 minutes in (b), respectively. SWV experiments were carried out in pH 7.4, 10 mM PBS-0.1 M NaCl solutions. Reproduced with permission from Dou *et al.*, 2012.

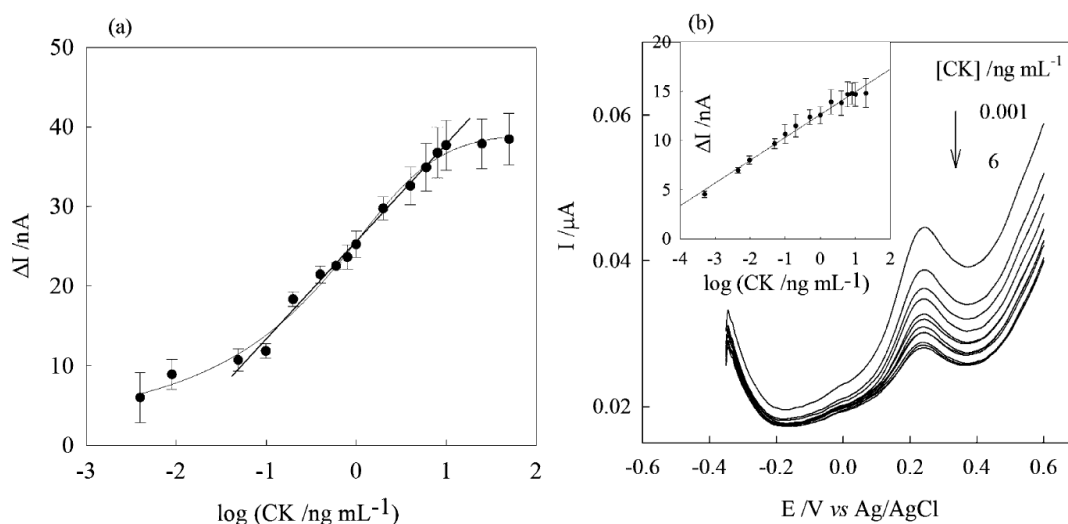


Fig. 52 CK sensor in biological PBS (a) and in MKH perfusion solution (b). Incubation was 15 min at room temperature. Concentration of conjugated Ab-CK-Fc was $\sim 100 \text{ mg mL}^{-1}$ in (a) and $\sim 230 \text{ mg mL}^{-1}$ in (b). The solid line in (a) is drawn to show the linear range. (b) The CK concentrations for the incubation in the SWV were: 0.001, 0.005, 0.01, 0.05, 0.1, 0.2, 0.5, 1, 2, 4, 6 ng mL^{-1} . Inset b: Linear range, 0.005 to 6 ng mL^{-1} . Error bars represent electrode-to-electrode standard deviation ($n=3$) from different batches in (a) and the same batch in (b). Test temperature, 25°C . Note that in both (a) and the Inset b, the abscissa refers to the CK concentration (on a logarithmic scale). Reproduced with permission from Dou *et al.*, 2012.

We begin by first considering the chemical biophysics underpinning the efficacy of our previous electroimmunoassay.²⁵

4.2 Theory

4.2.1 Development of a Global Antigen Coverage Parameter

Our previous work on the development of a versatile platform for electroimmunoassay,²⁵ was exploited as the foundation for the method described herein. In short, a redox-labelled monoclonal antibody was attached to an electrode surface through a covalently bound molecular wire, as schematically illustrated in Fig. 54. The use of diazonium functionality reduction in forming this molecular wire means that a multilayer is present.²⁸ In order to form an amide link with the antibody, the nitro- moieties need to be completely reduced to the amine; there is no easy way in which to coulomb count this, so that we assume the resulting surface is sprinkled with nitro-, nitroso-, hydroxylamine and amine functionalities. This gives rise to an

electrode-wire platform that is chemically non-uniform, and with a unique nanostructure. The antibody is likewise randomly modified with the redox tag – typically this is achieved through the formation of an amide linkage between the free primary amine moieties on the antibody and an aldehyde or acid functional group on the redox compound (such as ferrocenecarboxaldehyde or *cis*-bis(isothiocyanato)bis(2,2'-bipyridyl-4,4'-dicarboxylato)ruthenium(II)).

Characterisation of IgG protein by Tan *et al.*²⁹ demonstrates the abundance of free primary amines at the paratopes of the antibody, however also shows the presence of free lysine groups across the antibody structure, therefore there is a possibility of immobilising the redox functionality all over the antibody on any free lysine residues.

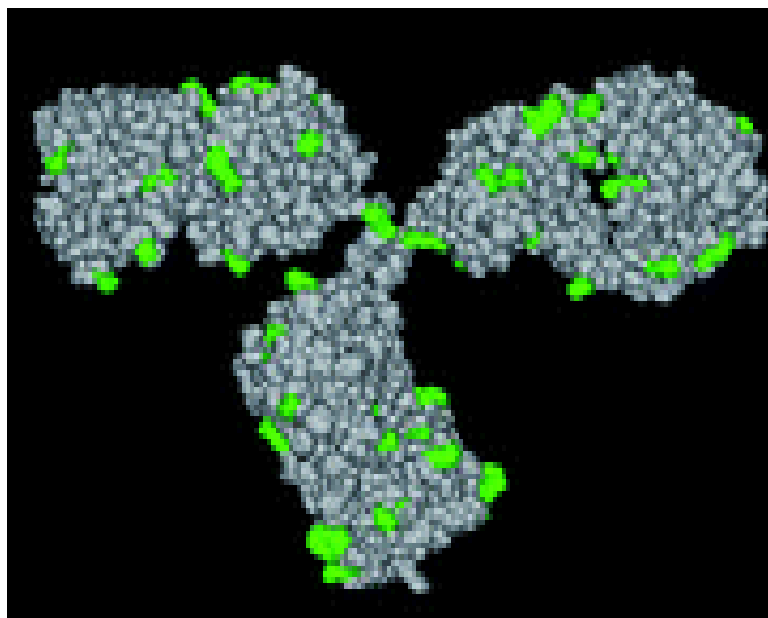


Fig. 53 3D space filling models of immunoglobulin G (IgG) protein structure revealing lysine residues. The lysine (Lys) residues are highlighted in green.²⁹

Furthermore, the known presence of carboxylic acid residues at the C-terminal end of all antibody heavy chains enables the statistical probability that a substantial proportion of the surface bound antibody adopts an “end on” arrangement, rather than “side on”,³⁰ as indicated in Fig. 54. Furthermore, through careful manipulation of the ionic strength of the buffer solution used for the antibody surface conjugation, inter-ionic forces may be less-screened such that the “end on” configuration is more favourable.^{25, 30} It is then the assumption that this method of multilayer formation and modification allows for high coverage of the electrode surface with relatively

controlled orientational positioning of the Ab in the most favourable “end-on” arrangement. However, combining this with the positional and therefore steric variation of the amine groups on the multilayer modified electrode, there is a degree of uncertainty as to whether the antibody is positioned correctly for antigen binding at the paratopes.

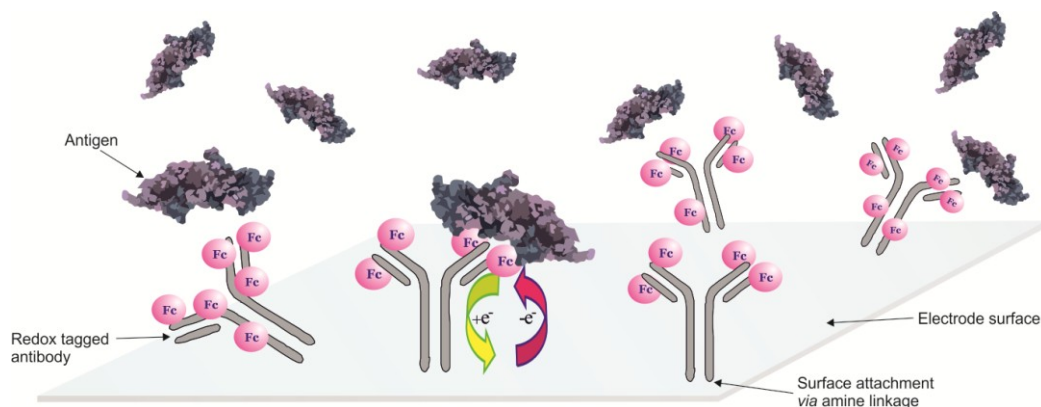


Fig. 54 Schematic illustration of the electroimmunoassay considered

The plethora of possibilities for non-optimal signal generation in this system means that the reliable and accurate sensing of antibody-antigen binding necessitates the use of a comparative approach (before and after exposure to antigen), rather than an absolute approach (where the system chemistry is only surveyed in the presence of a single concentration of antigen). Indeed, in our previous work,²⁵ such antigen binding was inferred through the blocking of the signal due to the ferrocene label, as expected. In this work, we build upon the notions presented in our earlier work: since we have been unable to quantify (1) the number of redox labels per antibody, (2) the yield of the antibody labelling process, and (3) the number of antibodies that are immobilised on the electrode surface and their orientation, we are unable to quantify the avidity of the monoclonal antibodies used, nor enable the predictive optimisation of the electroimmunoassay.

Accordingly, we introduce a global blocking fraction, θ , as a means to parameterise the amount of antigen on the electrode surface ($0 \leq \theta \leq 1$). This is readily inferred from the kinetics of heterogeneous electron transfer in the presence and absence of antigen, as discussed by Saveant,³¹ and Wadhawan and co-workers:³² for an electrode that engages in an electron transfer process in the absence of any degree to

which the redox process is blocked, with standard heterogeneous rate constant (in a Butler-Volmer framework) as k_0 , the rate constant (k_s) is lowered in the presence of a process that impedes this. Such processes include partially blocking the active electrode area for a redox species that relies on transport to the electrode surface,³³ or burying the redox-active group within a self-assembled monolayer so that the electron transfer kinetics are limited by the degree with which the counter ions may move through the structure.²⁷ It is this latter pathway that is believed to be the method through which the electroimmunoassay reported in our earlier work operates. Thus, to a first order approximation, we may write the following for the rate constant for electron transfer when antigen is bound to the antibody paratopes: $k_s = k_0(1 - \theta)$. It thus follows that provided there is a route for the measurement of the heterogeneous electron transfer rate constants, the degree of antigen binding may be quantified through equation (4.1):

$$\theta = 1 - \frac{k_s}{k_0} \quad (4.1)$$

This is a global antigen coverage parameter and is independent of the electrode architecture: it merely depends on the antigen binding thermodynamics and antigen-antibody on/off kinetics. We next consider the affinity of the protein-protein interaction.

4.2.2 Thermodynamics of Antigen-Antibody Recognition

We consider the adsorption reaction between a freely diffusible antigen (AG) and a surface-immobilised receptor, such as a single paratope of an antibody (|-AB):



Equality of the electrochemical potentials ($\bar{\mu}$) of the antigen in both bulk solution and in the adsorbed states occurs at equilibrium,

$$\mu_{AG}^{-ads} = \mu_{AG}^{-bulk} \quad (4.3)$$

Thus, the change in Gibbs energy for the adsorption process, ΔG_{ads}^0 , may be expressed in terms of the activities (a) of the solution and adsorbed antigen:

$$a_{AG}^{ads} = a_{AG}^{bulk} e^{-\frac{\Delta G_{ads}^0}{RT}} = a_{AG}^{bulk} K_{ads} \quad (4.4)$$

where R is the molar gas constant, T is the absolute temperature and K_{ads} is the equilibrium coefficient pertaining to the adsorption process. The adsorbed antigen activity may be expressed through the fraction of the blocked (θ) to unblocked ($1-\theta$) active paratopes on the surface-confined antibody, yielding the familiar Langmuir isotherm, on incorporating solution activity effects into K_{ads} , to afford the Langmuir isotherm constant K^{lang} :

$$\frac{\theta}{1-\theta} = K^{lang} c_{AG}^{bulk} \quad (4.5)$$

in which c_{AG}^{bulk} is the concentration of the antigen in bulk solution.

The Langmuir isotherm neglects, amongst other things, the presence of nearest-neighbour interactions between adsorbed antigen molecules. The occurrence of such attractive or repulsive lateral interactions causes a modification to the enthalpy change (ΔH_{ads}) associated with the adsorption equilibrium, and will depend on the fractional coverage. Thus, Taylor expansion of the standard enthalpy change for adsorption affords to a first-order approximation:

$$\Delta H_{ads} = \Delta H_{ads}^0 (1 - \alpha\theta) = \Delta G_{ads} + T\Delta S_{ads} \quad (4.6)$$

where ΔS_{ads} is the entropy change that takes place on adsorption of the antigen, and α parameterizes the interactions: $\alpha < 0$ corresponds to attractive interactions within the adsorbed layer so that a larger amount of heat is generated through successful adsorption; repulsive interactions are thus manifested through a reduced amount of liberated thermal energy on adsorption as $\alpha > 0$.

Thus, the effect of accounting for lateral interactions is to correct the isotherm constant K^{lang} with:

$$K = K^{lang} e^{A\theta} \quad (4.7)$$

in which,

$$A = \alpha \frac{\Delta H_{ads}^0}{RT} \quad (4.8)$$

giving rise to the Frumkin isotherm, which will be employed within this work:

$$\frac{\theta}{1-\theta} = K^{lang} c_{AG}^{bulk} e^{A\theta} \quad (4.9)$$

It follows that a plot of $\ln \left\{ \frac{\theta}{c_{AG}^{bulk} (1-\theta)} \right\}$ against θ enables the determination of both the affinity constant K^{lang} and the extent of lateral interactions (A). Note that since the adsorption process is exothermic (net bond forming), the constant A is expected to be positive for attractive interactions and negative for repulsive interactions. Moreover, at 298 K, given that the antibody-antigen complex formation is essentially a chemisorption process ($\Delta H_{ads}^0 < -35 \text{ kJ mol}^{-1}$), it is expected that $|A| = 14$ for $|\alpha| = 1$.

We next examine the kinetics of the bio-recognition event.

4.2.3 Rate Laws for the Formation of the Antibody-Antigen Complex from Freely Diffusible Antigen and Surface-Confined Antibody

We consider the adsorption reaction between a freely diffusible antigen (AG) and a surface-immobilised receptor, such as a single paratope of an antibody (|-AB):



The rate at which the surface concentration (Γ) of antibody and antibody-antigen complex changes *via* the heterogeneous adsorption kinetics balances the rate of antigen transport through diffusion-convection:^{34, 35}

$$\frac{d\Gamma_{|-AB:AG}}{dt} = k_f \Gamma_{|-AB} c_{AG}^{surf} - k_b \Gamma_{|-AB:AG} \simeq \frac{D}{\delta} (c_{AG}^{bulk} - c_{AG}^{surf}) \quad (4.11)$$

in which D is the apparent diffusion coefficient of the antigen, with the concentrations of the antigen at the electrode surface and in bulk solution being described through the use of the superscripts *surf* and *bulk*, respectively. Note that although the experiments undertaken within this work (*vide infra*) are over long timescales and in quiescent solution, diffusion is considered here as being the major transport mechanism, since the natural convection that exists over this timescale may be treated in terms of an effective diffusion coefficient.³⁶ Thus, δ is the steady-state diffusion layer thickness.

Mass balance on the electrode requires

$$\Gamma_{TOT} = \Gamma_{|-AB} + \Gamma_{|-AB:AG} \quad (4.12)$$

where Γ_{TOT} is the total surface concentration of the available paratopes. Using this definition, it therefore does not matter that we consider the overall reaction as being first order in antigen concentration, as we are not interested in the number of antigens that bind to each antibody, but rather are interested in the total number of available and active *binding sites*. In this way, we are able to treat the system as tantamount to adsorption to form a monolayer, even though the experimental system consisting of a platform made through diazonium reduction, is more than likely to be multi-layered (*vide supra*). Hence, denoting the fraction of blocked binding sites as

$$\theta = \frac{\Gamma_{|-AB:AG}}{\Gamma_{TOT}} \quad (4.13)$$

and recognising that the surface concentration of antigen is given through

$$c_{AG}^{surf} = \frac{\frac{Dc_{AG}^{bulk}}{\Gamma_{TOT}\delta} + k_b\theta}{k_f(1-\theta) + \frac{D}{\Gamma_{TOT}\delta}} \quad (4.14)$$

we may recast the rate law in the following form.

$$\frac{d\theta}{dt} = \frac{k_f(1-\theta)c_{AG}^{bulk} - k_b\theta}{k_f\left(\frac{\Gamma_{TOT}\delta}{D}\right)(1-\theta)+1} \quad (4.15)$$

We next introduce the following dimensionless variables.

Characteristic diffusion time:

$$q = \frac{\Gamma_{TOT}\delta}{Dc_{AG}^{bulk}} \quad (4.16)$$

Normalised time:

$$\tau = \frac{t}{q} \quad (4.17)$$

Antibody-Antigen Complexation:

$$\kappa = K^{lang}c_{AG}^{bulk} \quad (4.18)$$

Ratio of adsorption to transport rates:

$$\lambda = K^{lang}k_b c_{AG}^{bulk} q \quad (4.19)$$

It thus follows that the ratio of blocked-to-unblocked paratope sites is given by

$$\kappa e^{A\theta} = \frac{\theta}{1-\theta} \quad (4.20)$$

in which A is defined as the parameter of the Frumkin isotherm (*vide supra*), so that the rate constant for the adsorption process is coverage-dependent, whilst the *desorption rate constant may be considered independent of the coverage:*

$$K^{lang}e^{A\theta} = \frac{k_f}{k_b} \quad (4.21)$$

These parameterisations in terms of non-coverage dependent variables enable the rate law to be returned in the following form.

$$\frac{d\theta}{d\tau} = \frac{\lambda e^{A\theta} \left[1 - \left(\frac{e^{-A\theta} + \kappa}{\kappa} \right) \theta \right]}{1 + \lambda e^{A\theta} (1 - \theta)} \quad (4.22)$$

and which requires solution subject to the boundary condition

$$\tau = 0, \theta = 0$$

Note that this form of the rate law recognises that the extent of the lateral interactions within the adsorbed layer changes with time.

We first consider the case of the Langmuir isotherm ($A = 0$), for which no lateral interactions exist.³⁴ Solution of the rate law may then proceed through variable

separation followed by integration through substitution of $1 - \left(\frac{1 + \kappa}{\kappa} \right) \theta$, to yield

$$\lambda \theta - \left(1 + \frac{\lambda}{1 + \kappa} \right) \ln \left(1 - \frac{1 + \kappa}{\kappa} \theta \right) = \lambda \left(\frac{1 + \kappa}{\kappa} \right) \tau \quad (4.23)$$

This integrated rate law is for the general case, where activation and transport both control the bio-recognition process. If this proceeds irreversibly, then, since $\lambda \ll \kappa$, it follows that

$$\frac{\kappa}{1 + \kappa} \theta - \frac{1}{\lambda} \ln \left(1 - \frac{1 + \kappa}{\kappa} \theta \right) = \tau \quad (4.24)$$

There are two limits to this equation. First, for the case when antigen transport to the modified electrode surface limits the adsorption process, $\lambda \rightarrow \infty$, so that

$$\frac{\kappa}{1 + \kappa} \theta = \tau \quad (4.25)$$

Conversely, where the transport is likely dominated by natural convection within the solution, so that the heterogeneous adsorption kinetics are rate-limiting, $\lambda \rightarrow 0$, affording:

$$-\frac{1}{\lambda} \ln \left(1 - \frac{1+\kappa}{\kappa} \theta \right) = \tau \quad (4.26)$$

We are interested in simplifying the rate law for the case that is likely to be most relevant to the experimental work, *viz.* the antibody-antigen binding is irreversible, but with $\kappa < 1$, so that the system is under activation control. Thus,

$$-\ln \left(1 - \frac{1+\kappa}{\kappa} \theta \right) = \lambda \left(\frac{1+\kappa}{\kappa} \right) \tau \quad (4.27)$$

It is relatively facile to test this equation with the experimental data, since the equilibrium coverage of antigen is given by:

$$\theta_{eqm} = \frac{\kappa}{1+\kappa} \quad (4.28)$$

so that the equation may be recast as

$$-\ln \left(1 - \frac{\theta}{\theta_{eqm}} \right) = \frac{\lambda \tau}{\theta_{eqm}} = \frac{1}{\theta_{eqm}} K^{lang} k_b C_{AG}^{bulk} t \quad (4.29)$$

Hence, a plot of $-\ln \left(1 - \frac{\theta}{\theta_{eqm}} \right)$ against time enables the determination of the forward rate constant.

The observation of non-Langmuirian binding of labile antibodies to antigen-modified surfaces has been discussed within the literature.³⁷ For the case of the Frumkin isotherm considered in this work, $A \neq 0$, we have been unable to identify a method for the integration of the general case of the rate law, equation (4.22). Nevertheless, the pragmatic approximation that $\kappa \ll e^{A\theta}$ enables the rate law in equation (4.22) to yield the following tractable form.

$$\frac{d\theta}{dt} = \frac{\lambda e^{A\theta} (1-\theta)}{1 + \lambda e^{A\theta} (1-\theta)} \quad (4.30)$$

Integration proceeds through variable separation and recognition of the validity of the power series expansion of e^x , to afford

$$\lambda\theta + e^{-A} \left[-\ln(1-\theta) + \sum_{i=1}^{\infty} \frac{A^i}{i!i} \left\{ 1 - (1-\theta)^i \right\} \right] = \lambda\tau \quad (4.31)$$

It thus follows that, in the case of irreversible adsorption, $\lambda \rightarrow 0$, encouraging the use of the following expression from which kinetic information may be extracted from experimental data.

$$e^{-A} \left[-\ln(1-\theta) + \sum_{i=1}^{\infty} \frac{A^i}{i!i} \left\{ 1 - (1-\theta)^i \right\} \right] = K^{lang} k_b c_{AG}^{bulk} t \quad (4.32)$$

The sum-to-infinity in the expression on the left-hand side of equation (32) converges rapidly, with $i=200$ being more than sufficient to ensure complete numerical convergence. Accordingly, kinetics information may be extracted directly from experimental data in the light of equation (4.32) through plotting

$e^{-A} \left[-\ln(1-\theta) + \sum_{i=1}^{\infty} \frac{A^i}{i!i} \left\{ 1 - (1-\theta)^i \right\} \right]$ against time.

We next apply these insights to experimental data.

4.2.4 Specific Experimental Conditions

4.2.4.1 Fitting of Experimental Data to Determine the Global Antigen Coverage Parameter

For a one-electron process occurring within a surface monolayer, the current that results from non-interacting redox centres, is the summation of oxidation and reduction processes:

$$i = FS \left(k^{ox} \Gamma^{red} - k^{red} \Gamma^{ox} \right) \quad (4.33)$$

where i is the current, S the electrode area, F the Faraday constant and with rate constants k^j and surface concentrations Γ^j ($j=ox$ or red), with the superscript identifying the particular redox state. When electron transfer occurs from the Fermi

energy of the electrode, and the symmetry factor is close to $\frac{1}{2}$, it has been demonstrated that the Butler-Volmer formulation for electrode kinetics is adequate.²⁷ Here, given that ferrocene redox tags were employed, and given that electrode resistance is the largest source of error, so that only those working areas that held the same resistance could be compared in this manner, the experimental data were treated simplistically, so that values of k_s were extracted from the variation of peak potential with scan rate upon solving equation (4.33) numerically under voltammetric conditions, without considering any Ohmic loss, with:

$$\begin{aligned}
 k^{ox} &= k_s \exp\left\{-\frac{F}{2RT}(E - E^{0'})\right\} \\
 k^{red} &= k_s \exp\left\{\frac{F}{2RT}(E - E^{0'})\right\} \\
 k_s &= k_0(1 - \theta)
 \end{aligned}
 \tag{4.34}$$

This is fully correct, since only those signals, which derived from electrodes with similar resistances, were compared to obtain the results reported herein.

4.3 Results and Discussion

To understand that the modification and subsequent attachment of antibodies to the electrode surface is successful, the voltammetry of the redox label on its own must be first investigated. The literature illustrates a range of oxidation potentials for ferrocene, from ~ 0.2 - ~ 0.6 V depending on the derivative, therefore potentials of this nature should be expected when the modified electrodes are voltammetrically examined.³⁸

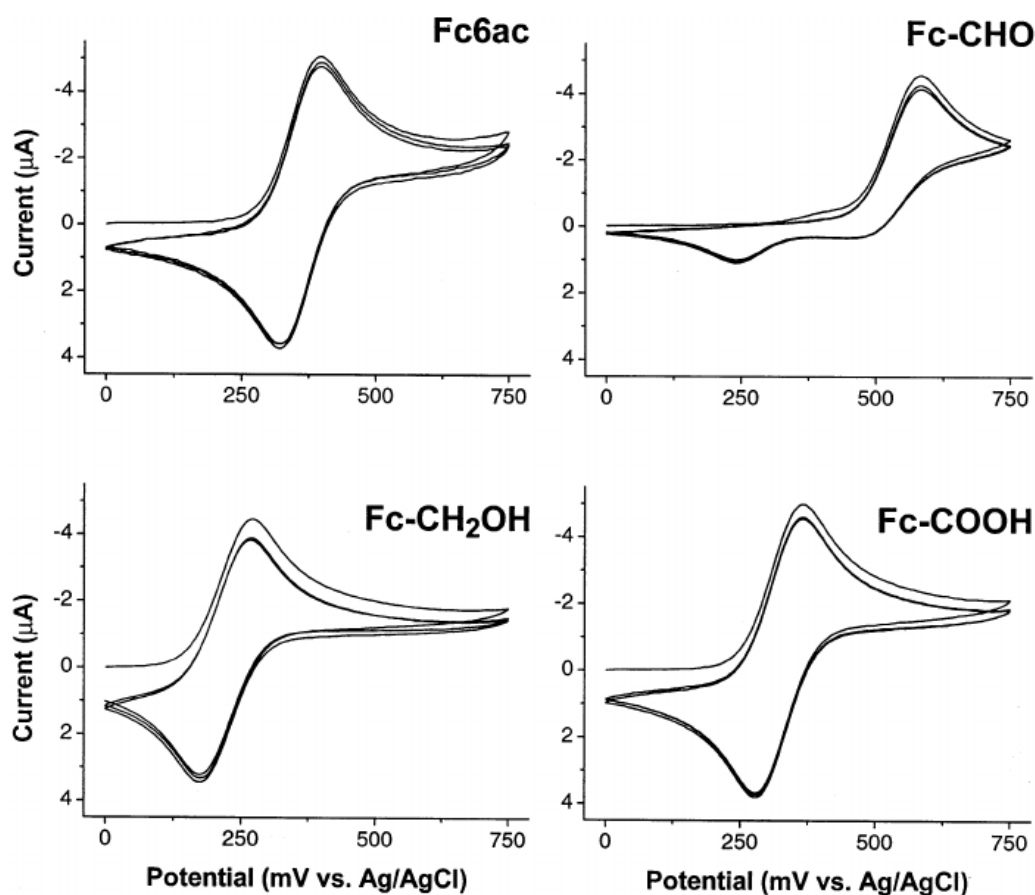


Fig. 55 Cyclic voltammograms of ferrocene derivatives (1 mM in phosphate buffer) using a freshly polished gold electrode. $\nu = 0.1 \text{ V s}^{-1}$.³⁸

Fig. 56 illustrates the voltammetry of anti-hCG antibody-modified electrodes in PBS at a scan rate of 0.1 V s^{-1} . The well-defined waves at $E_{\text{mid}} = \frac{1}{2} (E_{\text{p}}^{\text{ox}} + E_{\text{p}}^{\text{red}}) = 0.22 \text{ V vs. SCE}$ are due to the oxidation and re-reduction of the ferrocene labels covalently bound onto the ITO electrode. The oxidation and reduction waves are stable over the range $-0.1 < E/\text{V vs. SCE} < 0.5$, with the ten cycles enabling an orientation stabilisation of the antibody voltammetry. Increasing the voltammetric scan rate results in an increase in the peak-to-peak potential separation. This is expected, since the rate constant for long-range electron transfer through a peptide chain is³⁹ $0.2 - 0.5 \text{ s}^{-1}$ for peptides comprising 6 - 11 amino acids; in larger nano-objects, such as the antibody proteins, it is expected that electron transfer rate constants would be considerably smaller. Fig. 57 illustrates typical data for the oxidation peak potential. The fitting of the trend in these data with experimental timescale with those anticipated from the Butler-Volmer theory, by finding the minimum in the mean absolute error between experiment and theory enables the determination of the rate constant for the set of data.

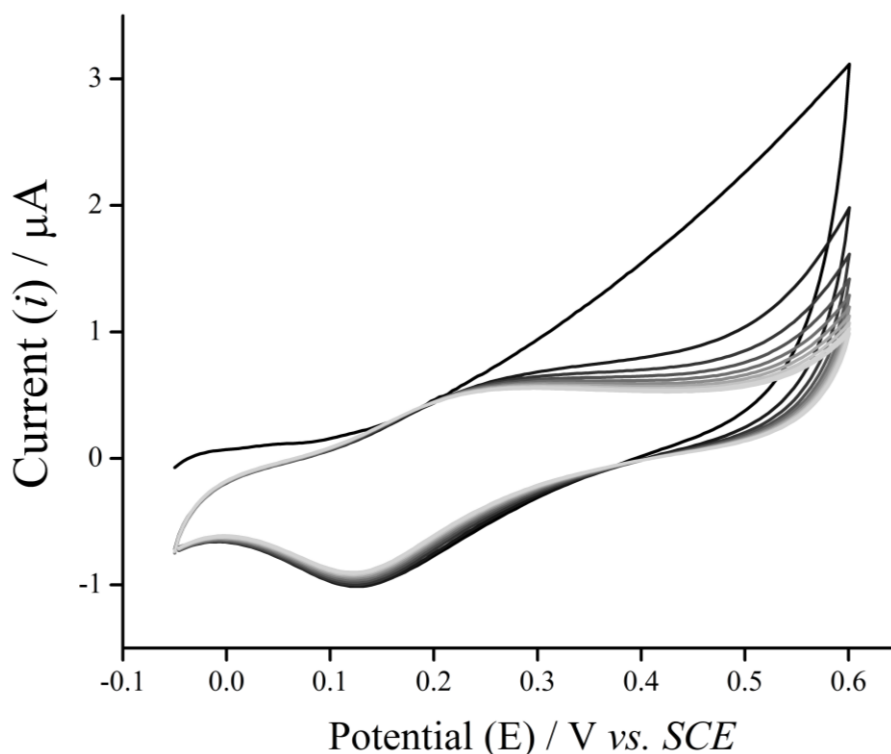


Fig. 56 Voltammograms of the ferrocene-tagged antibody immobilised on an ITO electrode immersed in PBS over 10 scan cycles. See text for details.

In order to determine the global fractional antigen coverage, θ , the heterogeneous electron transfer rate constant, k_s is determined for both the 'blank' electrode (prior to antigen incubation) and post incubation, as required by equation (4.1). By varying the timescale of the antigen incubation period, and by varying the antigen concentration, both the thermodynamics and kinetics of the antibody-antigen binding event may be unravelled. Fig. 58 shows the time-dependence of the blocking of the antibody-modified electrode in the presence of hCG of various concentrations. As expected, as the concentration of antigen increases, the surface coverage also increases until a point of equilibrium, or steady state, is reached. Thus, at equilibrium

($t = 60$ min), a plot of $\ln \left\{ \frac{\theta}{c_{AG}^{bulk}(1-\theta)} \right\}$ against θ , as suggested by equation (4.9), and depicted in Fig. 58, enables the deduction of the affinity constant, $K^{lang} = 2.5 \pm 1.1 \times 10^{11} \text{ M}^{-1}$. This is, in fact, two orders of magnitude larger than that reported for the non-redox tagged antibody,⁴⁰ $2.9 \times 10^9 \text{ M}^{-1}$, suggesting that the presence of the hydrophobic redox tag empowers additional interactions with the antigen, and which augers well for an analytical protocol using this modified antibody.

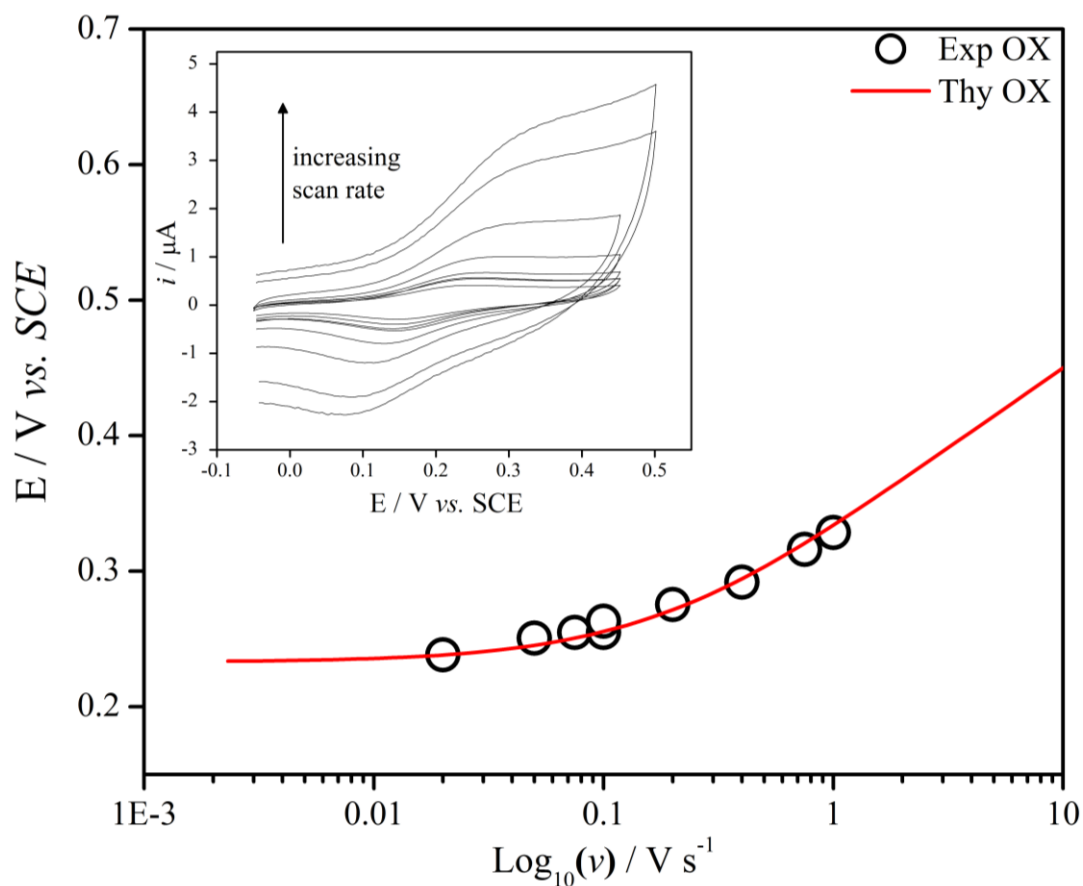


Fig. 57 The simulation fitting profile where peak potential for the oxidation (E_p^{ox}) is plotted against scan rate, ν . Insert shows variable scan rate data for ITO bound Fc-Ab-hCG in 10 mM PBS, pH 7.4.

The gradient of the plot in Fig. 59 enables the deduction of the Frumkin isotherm parameter $A = -13.9 \pm 1.9$. The negative value of this is commensurate with repulsive interactions between chemisorbed antigens, as expected for a surface where steric crowding may occur, affording a value of $\alpha \sim +1$ assuming a standard enthalpy of chemisorption of -35 kJ mol^{-1} .

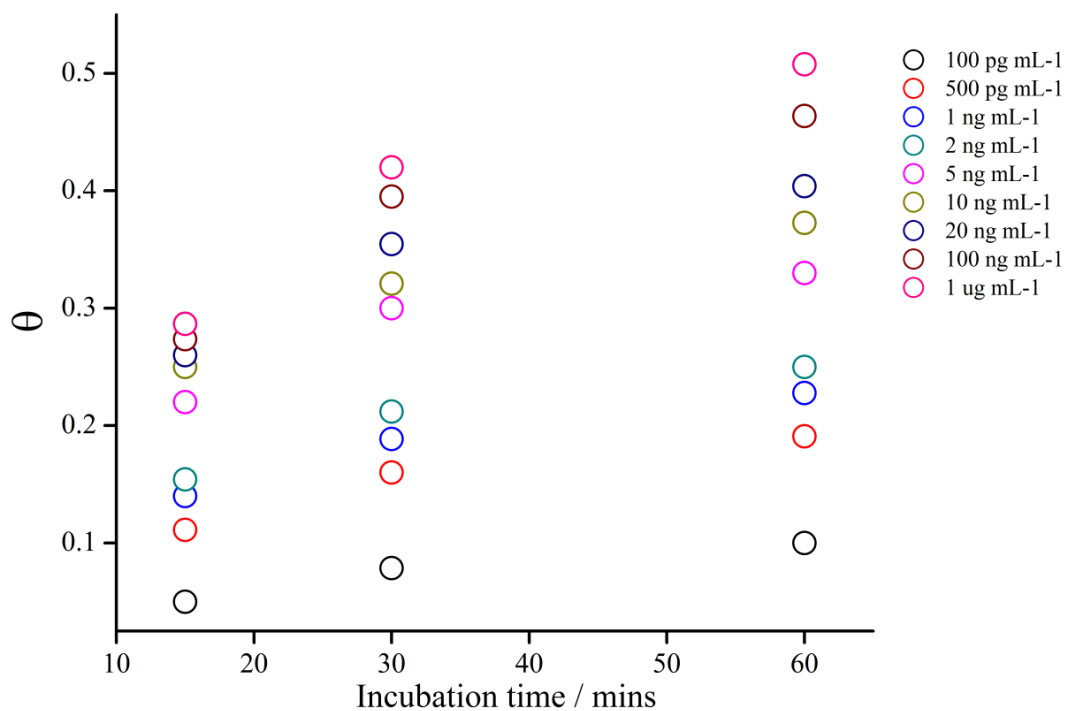


Fig. 58 Fractional surface blocking vs. incubation time for incubations of 15, 30 and 60 minutes with varying concentrations of hCG (100 pg mL⁻¹ to 1 μ g mL⁻¹) in 10 mM PBS buffer at pH 7.

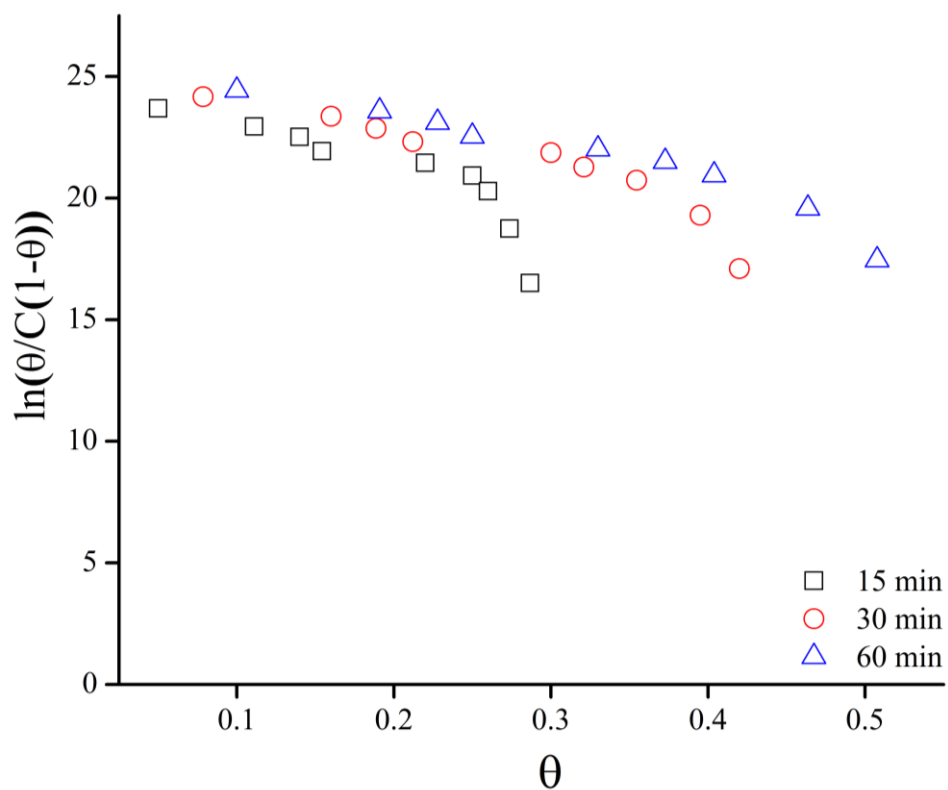


Fig. 59 Frumkin isotherm analysis of the antigen-antibody interaction.

In order to determine the effect of the larger affinity constant on the rate constants for the adsorption and desorption of the antigen, experimental data were treated through the plots suggested by equation (4.32). From the gradients of these plots (not shown), the rate constant for antigen desorption was identified as being essentially independent of the antigen concentration: $k_b = 6.5 \pm 2.7 \times 10^{-5} \text{ s}^{-1}$, enabling the rate constant for antigen adsorption to be determined from equation (4.21): $k_f = 2.2 \pm 0.9 \times 10^7 \exp(-13.9\theta) \text{ M}^{-1} \text{ s}^{-1}$. It is notable that these data are consistent with the increase in favourable binding interactions; the rate constant for adsorption is, at zero coverage, an order of magnitude *larger* than that of the untagged antibody⁴⁰ ($4.0 \times 10^6 \text{ M}^{-1} \text{ s}^{-1}$), whilst that for desorption is an order of magnitude *smaller* than that of the unlabelled antibody⁴⁰ ($1.4 \times 10^{-4} \text{ s}^{-1}$).

In order to examine the closeness of fit between the experimental data and those that may be theoretically observed based on the average kinetic data obtained, equation (4.22) was simulated in Matlab (version R2013a) using the finite difference method. In this case, first the parameter q (equation (4.16)) was identified through a minimum deviation between experiment and theory with its value being varied between 1 and 4000 s, with a convergent data observed for a time node of 10^{-2} s. Typical values of q were on the order of 25 min, suggesting that above this time, antigen transport to the surface may start to dominate the response. Knowledge of the optimised q values enabled the best-fit data to be determined and contrasted with the experimental points, as indicated in Fig. 60, where it is readily seen that whilst the fits are good for lower concentrations of the antigen, the overall fit worsens at higher antigen concentrations. Since rate constants were estimated from activation approximations (equation (4.32)), and the solid lines fits in Fig. 60 determined through simulation of equation (4.22), which includes transport processes, the poorer fit of the experimental transients at higher antigen concentration corresponds to transport-dominated processes at shorter incubation times. This intuitive result nevertheless identifies that the protocols developed may be exploited for bioanalytical measurement of antigen concentration at short incubation times and for low antigen concentrations.

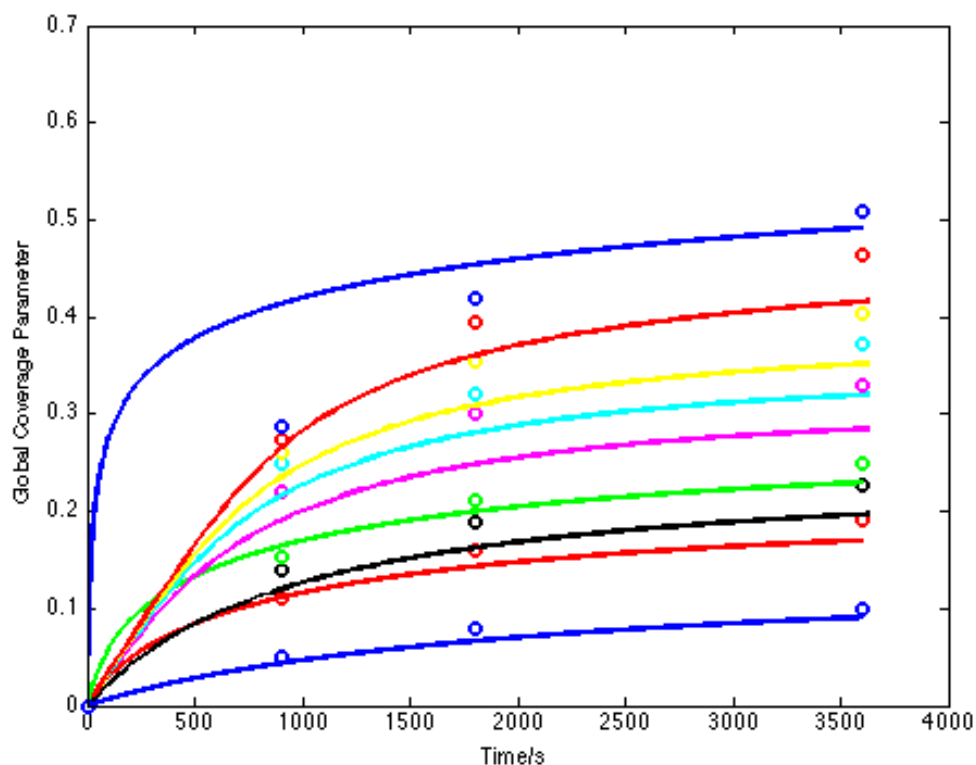


Fig. 60 Comparison of experiment with numerical theory (see text).

Accordingly, in order to develop a quantitative analytical protocol of hCG, working curves for each respective incubation time were obtained for the clinically relevant hCG concentration range within PBS solution. Such curves comprise plots of θ vs. $\lg([\text{hCG}]/\text{ng mL}^{-1})$, and are illustrated in Fig. 61. These curves are linear with R^2 values greater than 0.97 (over three repeats), indicating that even a 15 min incubation time is suitable for rapid and quantitative analysis, with excellent stability and inter-experiment reproducibility. Limits of detection (LOD) were determined (as three times the standard deviation normalised by the calibration graph gradient) to be 20.2, 28.3 and 19.8 mIU mL^{-1} for the 15, 30 and 60 min incubation times, respectively, for hCG concentrations in the range 100 pg mL^{-1} to $1 \mu\text{g mL}^{-1}$. It is notable that the LOD for the 15 min incubation is around the 25 mIU mL^{-1} cut-off considered for pregnancy testing, identifying clinical viability of this protocol.

In order to optimise the analytical measurement protocols in a manner entirely suited for the future clinical deployment of this sensing system for a primary point-of-care environment, the following protocol was envisaged: the manufacturing environment would develop the antibody-modified electrodes (each labelled with a unique identifier) and characterise each electrode through quantification of k_0 in 10 mM

PBS. The electrodes would then be deployed for hCG determination in urine to identify k_s and thus θ , from which, based on known working curves similar to Fig. 61, quantitative hCG estimates may be inferred. To this end, experiments were undertaken with blank calibration scans in 10 mM PBS followed by incubations with hCG concentrations over the range 1 pg mL^{-1} to $1 \text{ } \mu\text{g mL}^{-1}$ (corresponding to $9.3 \times 10^{-3} - 9.3 \times 10^3 \text{ mIU mL}^{-1}$) within artificial urine. Incubations within this latter medium were curtailed at 15 min, so as to afford a good mimic of anticipated point-of-care timescales.

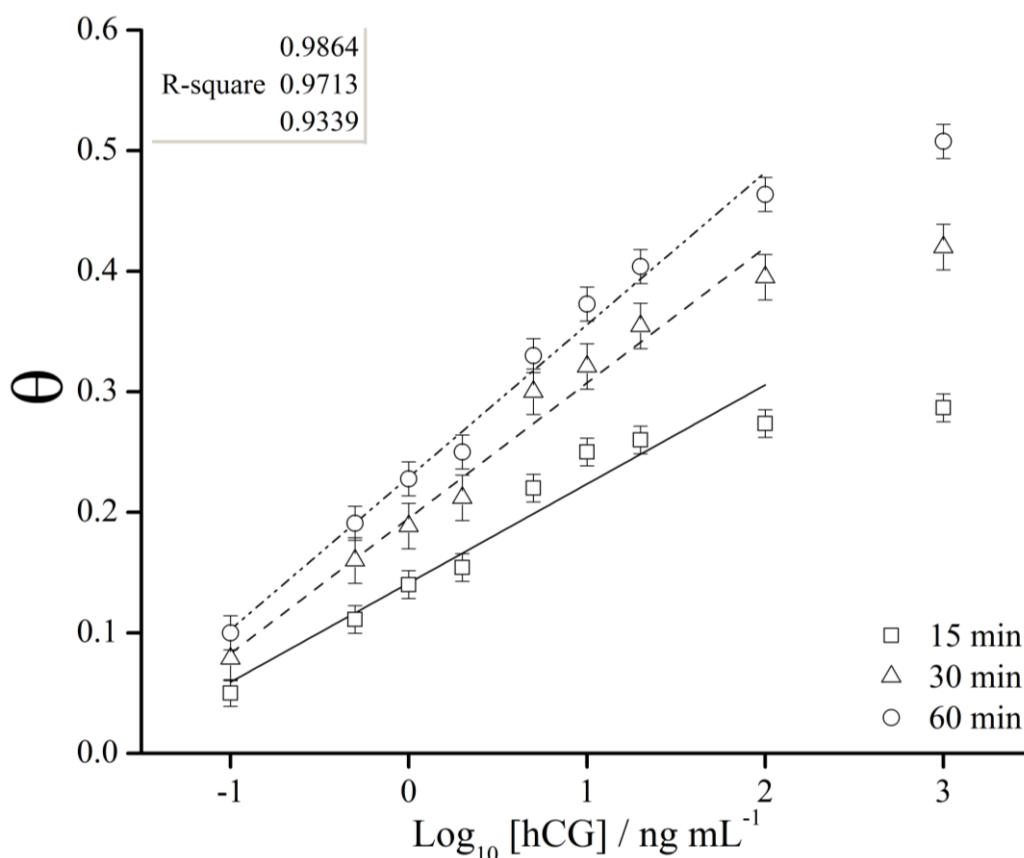


Fig. 61 Calibration chart for the sensor response (fractional antigen coverage, θ) to hCG incubation (100 pg mL^{-1} to $10/100 \text{ ng mL}^{-1}$) at 15, 30 and 60 minute periods in 10 mM PBS at pH 7.

This enabled the data exhibited in Fig. 62 to be generated, and which afford a LOD of 1.9 mIU mL^{-1} , with a t-test confidence of 99% in the measurement accuracy. It is clear that, over the concentration range studies, there is no evidence of an high-dose hook effect at the highest of concentrations studied. A semi blind test of 2 ng mL^{-1} hCG in artificial urine was carried out on the system and positively correlated with the calibration.

It is important to determine whether a species with possible interfering characteristics affects the sensing platforms ability to determine the concentration of antigen correctly. Therefore, the assay system was tested in the presence of two common possible interfering species, glucose and haemoglobin that may be present in a clinical urine sample under various conditions such as diabetes or kidney issues.

The sensing platform was subject to incubation of 1 ng mL^{-1} hCG in artificial urine with the addition of 20 mg mL^{-1} glucose, such that the concentration of glucose was above any level found in the human body or excrements. Fig. 62 shows that glucose has no effect on the analytical signal observed.

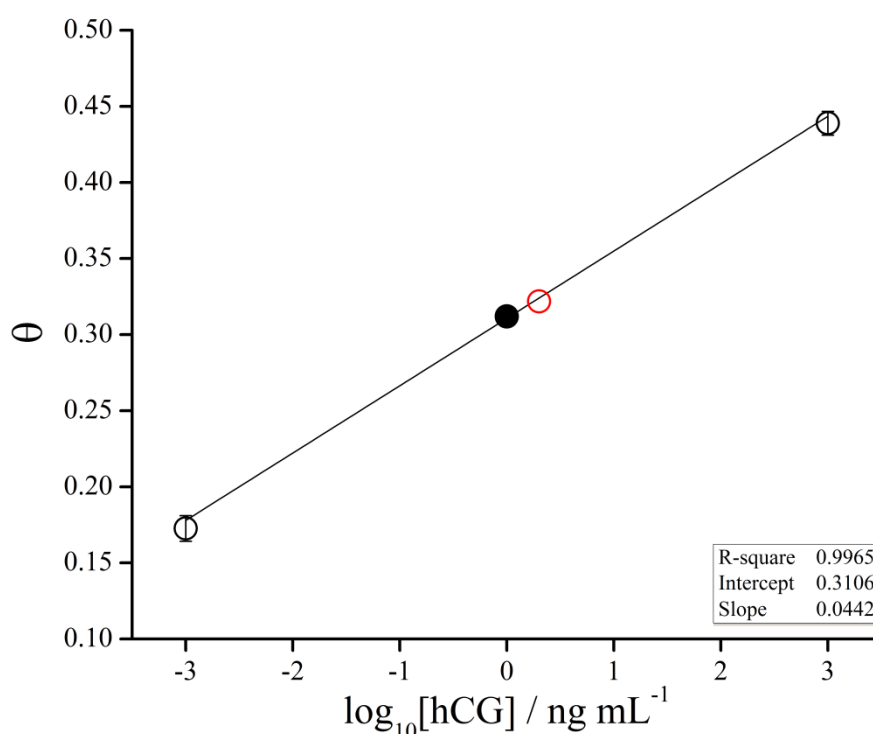


Fig. 62 Interference tests carried out for 15 minute incubations of 1 ng mL^{-1} hCG with 20 mg mL^{-1} glucose (●) (n=2).

The sensing platform was again subject to incubation of 1 ng mL^{-1} hCG in artificial urine though with the addition of 1 mg mL^{-1} haemoglobin, such that the concentration was above levels found in clinical urine samples. Fig. 63 shows that haemoglobin has no effect on the analytical signal observed at the high concentration investigated.

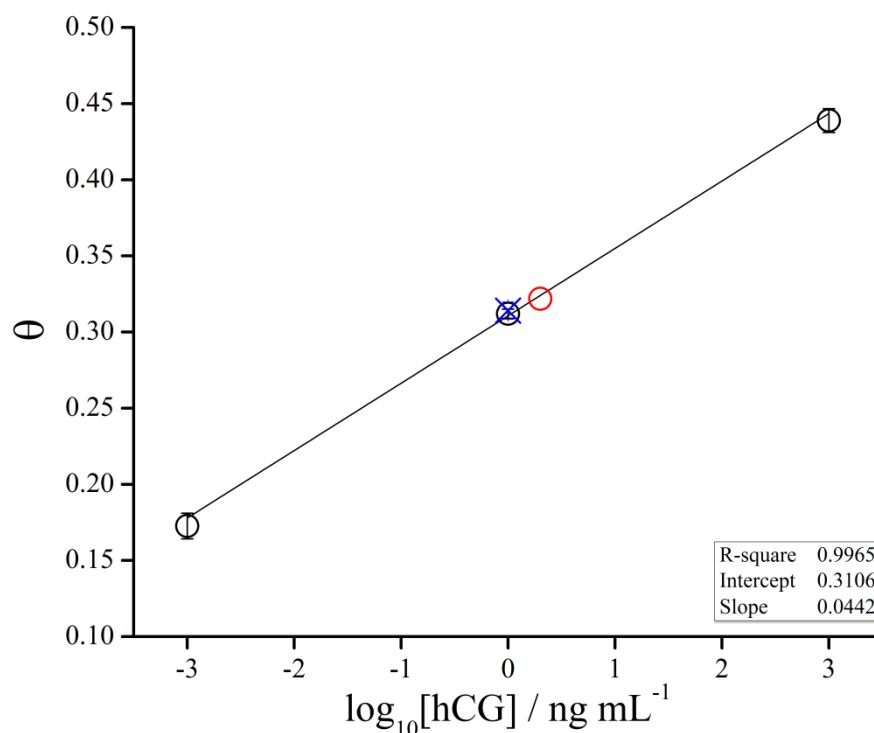


Fig. 63 Interference tests carried out for 15 minute incubations of 1 mg mL^{-1} hCG with 1 mg mL^{-1} haemoglobin (\times) (n=4).

It has been demonstrated that the sensing platform is operable in the presence of glucose and haemoglobin up to at least 20 mg mL^{-1} and 1 mg mL^{-1} respectively, surpassing any levels that may be observed the real world sensing application. Ideally there would have been more interference studies, however do to time constraints with the project this was not possible, though future interference studies could include bilirubin (liver issues), paracetamol and other urine bound metabolites.

4.4 Conclusions

An electrochemical immunoassay has been developed for the detection of hCG by way of direct electrode surface modification to prepare a molecular wire scaffold for the subsequent bio conjugation of electroactive ferrocene labelled anti-hCG antibodies. The sensor demonstrated excellent sensitivity in artificial urine, with a limit of detection of 1.93 mIU mL^{-1} (0.21 ng mL^{-1}) for as little as 15 minute sample incubations showing no observable effects from common interferences. The main advantage of the presented immunosensor is quantitative measurements with short analysis times, that if translated into human samples has promising potential to

provide rapid, accurate hCG level readouts at the point of care to facilitate more informed decision making in the relevant clinical scenarios.

Although this sensing system appears to be versatile, its drawback is that it cannot be used for the combinatorial sensing of multiple biomarkers that make up a disease. The next chapter examines the possibility of achieving this goal.

References

1. E. Siegel, *Predictive Analytics: The Power to Predict Who Will Click, Buy, Lie, or Die*, Wiley Publishing, 2013.
2. D. Male, J. Brostoff, D. B. Roth and I. Roitt, *Immunology*, Elsevier, Philadelphia, 7th edn., 2006.
3. C. Demaille, J. Moiroux, J.-M. Saveant and C. Bourdillon, *Protein Architecture Interfacing Molecular Assemblies and Immobilisation Biotechnology*, Marcel Dekker, New York, 2000.
4. H. C. Berg and E. M. Purcell, *Biophysical Journal*, 1977, **20**, 193-219.
5. P. Berger and C. Sturgeon, *Trends in Endocrinology & Metabolism*.
6. F. L. Cate, C. Moffett, A. M. Gronowski, D. G. Grenache, K. E. Hartmann and A. Woodworth, *Clinica Chimica Acta*, 2013, **421**, 104-108.
7. *Journal*, 2014, 1-2.
8. T. R. J. Holford, F. Davis and S. P. J. Higson, *Biosensors and Bioelectronics*, 2012, **34**, 12-24.
9. L. A. Cole, *Clinica Chimica Acta*, 2012, **413**, 48-65.
10. L. A. Cole, *Clinical Chemistry*, 1997, **43**, 2233-2243.
11. T. Chard, *Human Reproduction*, 1992, **7**, 701-710.
12. C. Chandrasekhar, *Clinical Imaging*, 2008, **32**, 468-473.
13. C. L. Buckner, L. Wilson and C. N. Papadea, *Annals of Clinical & Laboratory Science*, 2007, **37**, 186-191.
14. U.-H. Stenman, A. Tiitinen, H. Alfthan and L. Valmu, *Human Reproduction Update*, 2006, **12**, 769-784.
15. R. S. Berkowitz and D. P. Goldstein, *New England Journal of Medicine*, 1996, **335**, 1740-1748.
16. J. Lei, S. Mei, Y. Zhou and T. Jing, *Journal of the Chinese Chemical Society*, 2014, **61**, 638-642.

17. J. T. Liu, R. P. Liu, M. X. Wang, C. X. Liu, J. P. Luo and X. X. Cai, *Chinese Journal of Analytical Chemistry*, 2009, **37**, 985-988.
18. D. Liu, F. Wu, C. Zhou, H. Shen, H. Yuan, Z. Du, L. Ma and L. S. Li, *Sensors and Actuators B: Chemical*, 2013, **186**, 235-243.
19. R. Li, D. Wu, H. Li, C. Xu, H. Wang, Y. Zhao, Y. Cai, Q. Wei and B. Du, *Analytical Biochemistry*, 2011, **414**, 196-201.
20. N. Xuan Viet, M. Chikae, Y. Ukita, K. Maehashi, K. Matsumoto, E. Tamiya, P. Hung Viet and Y. Takamura, *Biosensors and Bioelectronics*, 2013, **42**, 592-597.
21. S. Teixeira, R. S. Conlan, O. J. Guy and M. G. F. Sales, *Electrochimica Acta*, 2014, **136**, 323-329.
22. X. Li, S. Weng, B. Ge, Z. Yao and H. Z. Yu, *Lab Chip*, 2014, **14**, 1686-1694.
23. S. A. Butler, S. A. Khanlian and L. A. Cole, *Clin Chem*, 2001, **47**, 2131-2136.
24. L. V. Furtado, C. M. Lehman, C. Thompson and D. G. Grenache, *Am J Clin Pathol*, 2012, **137**, 194-202.
25. Y.-H. Dou, S. J. Haswell, J. Greenman and J. Wadhawan, *Electroanalysis*, 2012, **24**, 264-272.
26. J. Pinson and F. Podvorica, *Chemical Society Reviews*, 2005, **34**, 429-439.
27. C. Amatore, E. Maisonhaute, B. Schöllhorn and J. Wadhawan, *ChemPhysChem*, 2007, **8**, 1321-1329.
28. S. Munteanu, J. P. Roger, Y. Fedala, F. Amiot, C. Combellas, G. Tessier and F. Kanoufi, *Faraday Discussions*, 2013, **164**, 241-258.
29. Y. H. Tan, J. R. Schallom, N. V. Ganesh, K. Fujikawa, A. V. Demchenko and K. J. Stine, *Nanoscale*, 2011, **3**, 3395-3407.
30. S. Chen, L. Liu, J. Zhou and S. Jiang, *Langmuir*, 2003, **19**, 2859-2864.
31. C. Amatore, J. M. Savéant and D. Tessier, *Journal of Electroanalytical Chemistry and Interfacial Electrochemistry*, 1983, **147**, 39-51.
32. B. A. Brookes, T. J. Davies, A. C. Fisher, R. G. Evans, S. J. Wilkins, K. Yunus, J. D. Wadhawan and R. G. Compton, *The Journal of Physical Chemistry B*, 2003, **107**, 1616-1627.
33. T. J. Davies, B. A. Brookes, A. C. Fisher, K. Yunus, S. J. Wilkins, P. R. Greene, J. D. Wadhawan and R. G. Compton, *The Journal of Physical Chemistry B*, 2003, **107**, 6431-6444.

34. C. Bourdillon, C. Demaille, J. Moiroux and J.-M. Savéant, *Journal of the American Chemical Society*, 1999, **121**, 2401-2408.
35. I. Bhugun and F. C. Anson, *Journal of Electroanalytical Chemistry*, 1997, **439**, 1-6.
36. C. Amatore, C. Pebay, L. Thouin, A. Wang and J. S. Warkocz, *Analytical Chemistry*, 2010, **82**, 6933-6939.
37. D. B. Hibbert, J. J. Gooding and P. Erokhin, *Langmuir*, 2002, **18**, 1770-1776.
38. C. Padeste, A. Grubelnik and L. Tiefenauer, *Biosensors and Bioelectronics*, 2000, **15**, 431-438.
39. B. R. Chaudhry, J. D. E. T. Wilton-Ely, A. B. Tabor and D. J. Caruana, *Physical Chemistry Chemical Physics*, 2010, **12**, 9996-9998.
40. <http://www.abcam.com>, (accessed 27 June, 2016).

Chapter 5

Voltammetric Investigation of Electrochemical Immunoassays: Towards Combinatorial Sensing of Biomarker Analytes

In this chapter, the electrochemical immunoassay platform is developed further, both in understanding the electrode characteristics (resistance, stability and diversity of analyte), and with respect to identifying the possibility of detecting several biomarkers at the same time.

5.1 Introduction

In the previous work, an ITO electrode was employed. In earlier work, gold electrodes had been used.¹ Due to the polycrystalline, adsorptive nature of gold working electrode surfaces, a fresh surface is required prior to modification. This requires polishing before use with several grades of abrasive paper and in some cases much harsher conditions to dissolve the gold surface in order to remove surface oxides and contaminants to create a fresh surface for modification. The issue with this is that with each polishing of the electrode surface, a new layer of material with potentially differing properties is revealed. Further to this, polishing is a manual process and extremely dependent on user technique and proficiency, it is exceedingly difficult to replicate a flat and smooth surface with increasing polishes hence the effective electrode area and surface properties may change over time due to changes in the microstructure of the electrode material.

To overcome these issues of surface preparation prior to modification, other electrode materials were sought; these were glassy carbon and tin doped indium oxide (ITO).

Glassy carbon is a widely used electrode material that offers low electrical resistance, is highly resistant to chemical attack and doesn't form oxide layers, unlike gold. However this material also requires polishing pre-use in order to prepare a fresh surface for modification thus the surface characteristics and/or area of a glassy carbon electrode may change over time, though may be suitable commercially as a one-use sensor system.

Indium tin oxide is a doped n-type semiconducting oxide material consisting a ternary composition of indium, tin and oxygen in varying proportions, typically 74% In, 18% O₂, and 8% Sn by weight. ITO electrode surfaces were of interest since they are commercially available as thin films deposited onto flat glass slides that require no preparation before use and provide a universally structured surface. The electrodes are supplied in batches with known surface characteristics; this is much more idyllic for the development of an immunoassay protocol since the electrodes are comparable between experiments. Another advantage of this surface is that the working electrode area is not defined, hence is customisable for the application by user modification, allowing for reproducible electrode areas to be prepared and compared between experiments. It is also optically transparent, ideal for potential colorimetric or chemiluminescent/fluorescent detection strategies. However, since ITO is a semiconducting material, it inherently suffers from larger resistances than glassy carbon and gold electrode materials.

The ITO electrode material was chosen for the application of the modification protocol due the commercial availability of flat, ready to use ITO thin film electrodes. The characterisation of these electrodes is discussed as follows

5.2 Results and Discussion

5.2.1 Electrode Characterisation

The electrodes were prepared as described in section 3.4 where three defined electrode areas were prepared with circular adhesives of 6 mm diameter located at 11.9 ± 0.4 , 23.7 ± 0.6 and 35.6 ± 0.4 mm from the connection site respectively. These distances were chosen as to allow spatial resolution between each area and to allow for electrode comparison between individually prepared electrodes.

The electrode resistance of the ITO electrodes was investigated from the point of connection to the centre of these various electrode areas to ascertain whether there was a significant change in resistance with increasing distance since this may incur negative effects on the success of the modification protocol and subsequent measurement signals obtained.

Table 11 Resistance measurements for each individual defined electrode area of the ITO electrode.

	Electrode	1	2	3	4	5	6	Average	SD
Spot 1	R₁ / kΩ	0.81	0.78	0.82	0.91	0.78	0.80	0.82	0.048
	l₁ / m	3.55E-02	3.60E-02	3.55E-02	3.55E-02	3.60E-02	3.50E-02	3.56E-02	3.76E-04
	ρ / Ω m	2.24E-05	2.12E-05	2.26E-05	2.51E-05	2.12E-05	2.24E-05	2.25E-05	1.42E-06
Spot 2	R₂ / kΩ	0.57	0.56	0.57	0.57	0.56	0.57	0.57	0.005
	l₂ / m	2.35E-02	2.30E-02	2.40E-02	2.45E-02	2.40E-02	2.30E-02	2.37E-02	6.06E-04
	ρ / Ω m	2.38E-05	2.39E-05	2.33E-05	2.28E-05	2.29E-05	2.43E-05	2.35E-05	5.93E-07
Spot 3	R₃ / kΩ	0.39	0.36	0.38	0.38	0.36	0.37	0.37	0.012
	l₃ / m	1.20E-02	1.15E-02	1.20E-02	1.20E-02	1.25E-02	1.15E-02	1.19E-02	3.76E-04
	ρ / Ω m	3.19E-05	3.07E-05	3.10E-05	3.10E-05	2.82E-05	3.15E-05	3.07E-05	1.29E-06
	ρ^(3 spot average) / Ω m	2.60E-06	2.53E-06	2.56E-06	2.63E-06	2.41E-06	2.61E-06	2.56E-06	8.04E-08

Table 11 shows the results of this characterisation process, where as expected it was found that there is a clear increase of the electrode resistance in the direction away from the connection site with average values of 0.373 ± 0.012 , 0.567 ± 0.005 and 0.817 ± 0.048 k Ω across the three defined sites. Although the values of R changes across the three electrode areas, one must determine the resistivity of the surface, ρ to investigate if there is an overall change with distance. The resistivity is calculated as shown below

$$\rho = \frac{R}{l} \times A \quad (5.1)$$

where R denotes the resistance in Ω , l is the distance from the connection site measured in meters, ρ is the resistivity in Ω m and A is the cross sectional area of the electrode surface. As shown in Table 11, the values of ρ are not significantly different, hence little to no deviation was expected in measurements made on any of the prepared areas nor on the success of the modification process. Furthermore, this confirms that individually prepared electrodes can be compared by their respective working electrode area since the deviation between each respective prepared area is very small. This generates a method to calibrate these surfaces and obtain repeat data therefore allowing for the determination of ITO viability as a suitable surface.

Having determined that the resistivity does not change between the defined electrode areas, the electrode modification process was characterised. Firstly the electro-deposition of 4-nitrobenzene diazonium salt to the ITO surface was undertaken *via* cyclic voltammetry. This was achieved using four successive scans over a potential range of $+0.7 - (-0.4$ V) vs. SCE with a scan rate of 0.1 V s $^{-1}$. The cyclic voltammogram for this process is shown in Fig. 64 where the first scan illustrates a reduction peak at approximately -0.10 V that corresponds to the formation of nitrobenzene radicals and subsequent attachment to the electrode surface. The electrografting of the phenyl group to the ITO surface occurs through the formation of In-C or In-O-C covalent bonds through oxygen species.²⁻⁴ Successive scans produce a reduction peak current of significantly reduced intensity, attributed to blocking caused by the monolayer attachment and formation of a multilayer

constructed *via* the reaction of electrochemically generated nitrobenzene radicals with surface bound nitrobenzene groups *via* the *ortho* position.⁵

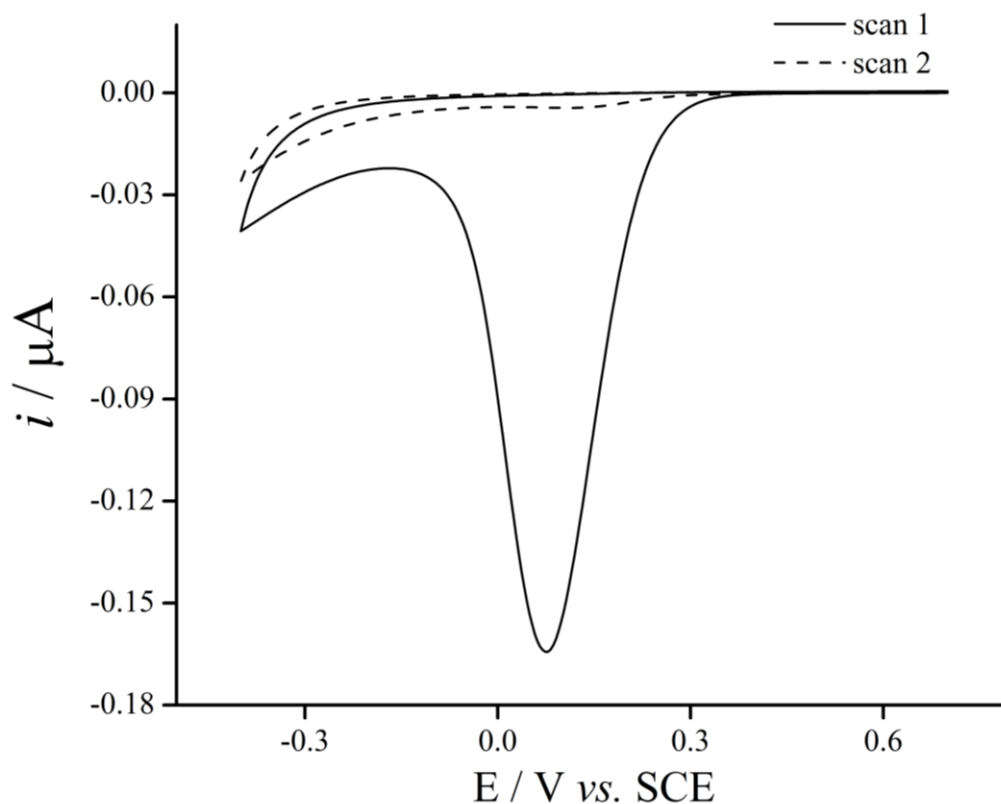


Fig. 64 Cyclic voltammograms obtained for the one electron reduction of nitrobenzene onto the surface of an ITO electrode, $\nu = 0.1 \text{ V s}^{-1}$.

The assumption is made that a monolayer is formed on scan 1, however since the nitrobenzene radical is formed during the monolayer deposition and due its highly reactive nature, it is very difficult to control the secondary attachment that forms the multilayer since the radical seeks to be stabilised as quickly as possible. Therefore it cannot be known for certain if only a monolayer is formed during scan 1. Nevertheless, this is not an issue for the success of the modification or for the subsequent antibody attachment step, where instead of a monolayer coverage, a multi-layered 'nano forest' of nitro groups is constructed with multiple available sites for binding. Pinson and Podvorica⁵ state that multilayers of this nature are likely to form at the *ortho* position to the nitro group due to steric reasons as the sensitivity of the aromatic ring to the donating or withdrawing nature of the substituent is low and the rates of the reaction on the different positions (*ortho* or *meta*) of the aromatic ring are not substantially different.

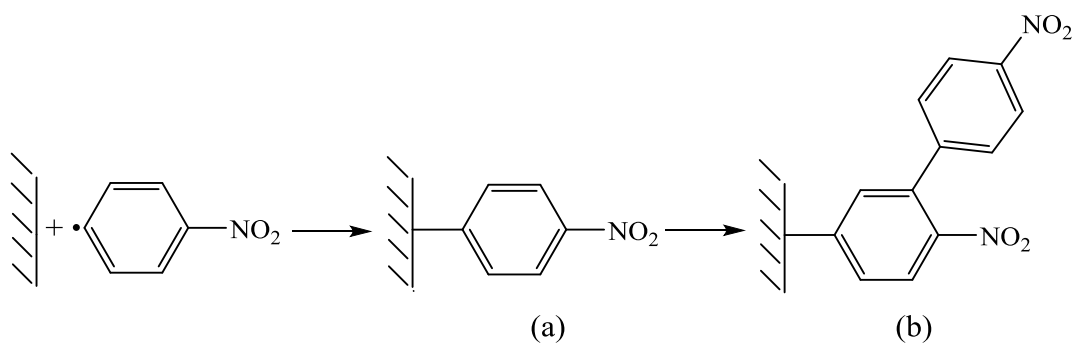


Fig. 65 Schematic illustration of the electro-deposition process where (a) shows the monolayer formation of nitrobenzene as per scan 1 and (b), multilayer formation *via* attachment through the *ortho* position (scan 2).

Following this, the reduction of the nitro group in the *para* position to the amine was undertaken. The reduction of the nitro group to the amine requires six electrons and six protons thus for this reaction to occur, the electrolyte solution must be protic in nature. Consequently ethanol was used in a 10:90 ratio with 0.1 M KCl and cyclic voltammetry was undertaken over four scans of potential range +0.4 – (-1.0) V *vs.* SCE. Fig. 66 illustrates the cyclic voltammograms obtained.

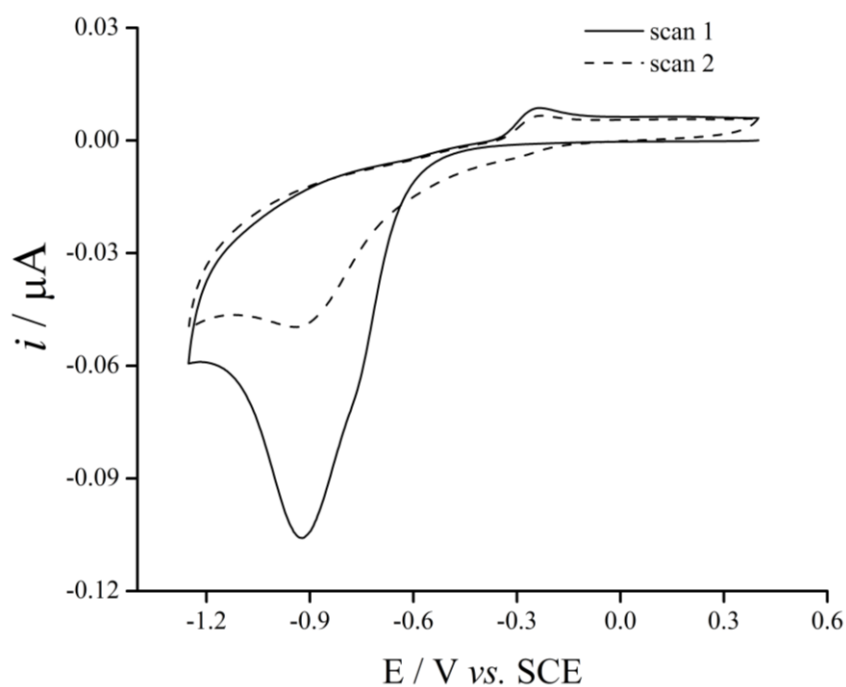


Fig. 66 Cyclic voltammograms obtained for the electrochemical reduction of the nitrophenyl group to the nitro-aniline, $\nu = 0.1 \text{ V s}^{-1}$.

In scan 1 of Fig. 66, we see a redox couple with a reduction peak similar to that of the nitrobenzene reduction in Fig. 64 which confirms the presence of the nitrophenyl

bound layer at the electrode surface. Subsequent scans show a significant decrease in the reductive peak currents and generation of a reversible redox couple, corresponding to the rapid functional group conversion.

To ensure that process does indeed involve 6 electrons, the charge must be determined as per eq. 2.18. To determine the charge, the area under the reduction peak is required; from the voltammogram, the area under the peak is 2.538×10^{-4} . The charge is then calculated by division with the scan rate (0.1 V s^{-1}) to yield $Q = 2.538 \times 10^{-3} \text{ C}$.

To establish the final unknown, the number of moles requires calculation. Given that the reaction employs protons from the ethanol solution, the pH can be determined as $\text{pH} = -\log_{10}[\text{H}^+]$, this was found to be 4.2. Since the pH is known, the concentration of protons can be determined, where $[\text{H}^+] = 6.3 \times 10^{-5} \text{ M}$. Since $70 \mu\text{L}$ of the ethanol solution was applied to the electrode area during voltammetry, the number of moles is therefore calculable as $4.41 \times 10^{-9} \text{ mol}$. Applying this into a rearrangement of eq. 2.18, the number of electrons is $5.95 \approx 6$ which satisfies the expected electron transfer for this reaction.

However it is important to understand that a variety of groups and attachment to alternative sites such as the meta position is highly possible with the nature of this modification strategy, that could substantiate a more complex surface structure such as that in Fig. 67.

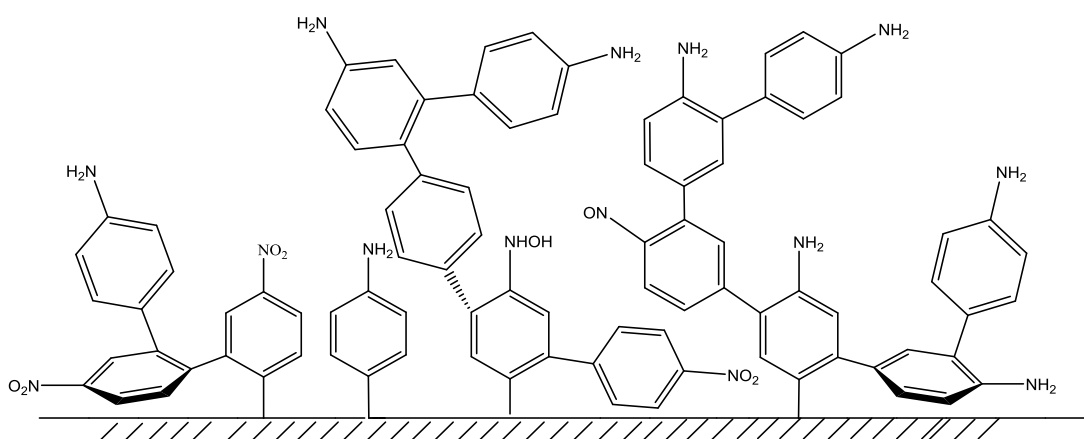


Fig. 67 Possible differences in attachment site and end result functional groups.

5.2.2 Ferrocene Labelled Anti-BNP Antibody Characterisation

Once the multilayer aniline surface had been characterised, the labelling of antibodies as described in section 3.4.1.3 was carried out for anti-BNP antibodies. The resulting labelled antibodies were investigated to determine the success of the labelling protocol and resulting properties of the tagged antibodies.

The ferrocene is attached to the antibody *via* amide linkage as described in section 3.4.1.4. The antibody structure consists two terminal regions, the N-terminal (fab) and C-terminal (fc) that are heavily laden with amine and acid group functionalities respectively. Since there is a high prevalence of free amine groups in the fab region of the antibody, it is expected that the ferrocene moieties attach in this area, which is also the antigen binding site known as the paratope. Through this specific location tagging, it is possible to observe a signal change that is directly related to the interaction of antigen binding at the surface. Because of the signal reliance on the tag location, it is important to characterise the results of the labelling process, in order to determine the approximate number of redox tags per antibody.

Given that ferrocene is observable spectroscopically, UV-visible spectroscopy was undertaken to determine the number of ferrocene tags. To do this, Beer-Lambert Law is applied to determine the extinction coefficients from calibrations of the ferrocene and ferrocene tagged antibodies. Firstly, a scan of the full wavelength spectrum (800 - 250 nm) of ferrocenecarboxaldehyde was carried out to determine the wavelength or wavelengths of light that ferrocene absorbs. It was found that ferrocene absorbs at 454 nm and 319 nm that are attributable to the ferrocene and cyclopentadienyl rings respectively. This coincides with literature values for substituted ferrocenes that are between 440 - 470 nm and 305 - 355 nm depending upon the functionality.⁶

This was followed by the generation of a calibration chart for the ferrocenecarboxaldehyde shown in Fig. 69, where UV-vis spectroscopy was carried out for ferrocenecarboxaldehyde over the concentration range 0.01 – 1 mg mL⁻¹ in DMF. Here we see the data is highly correlated ($R^2 = 0.996$). Beer-Lambert Law defines the extinction coefficient as the gradient of the slope multiplied by the path length. In this experiment the path length was 1 cm, therefore the extinction

coefficient is equivalent to the gradient. Therefore the extinction coefficient, ϵ , for ferrocenecarboxaldehyde was determined as $1.315 \text{ mL mg}^{-1} \text{ cm}^{-1}$.

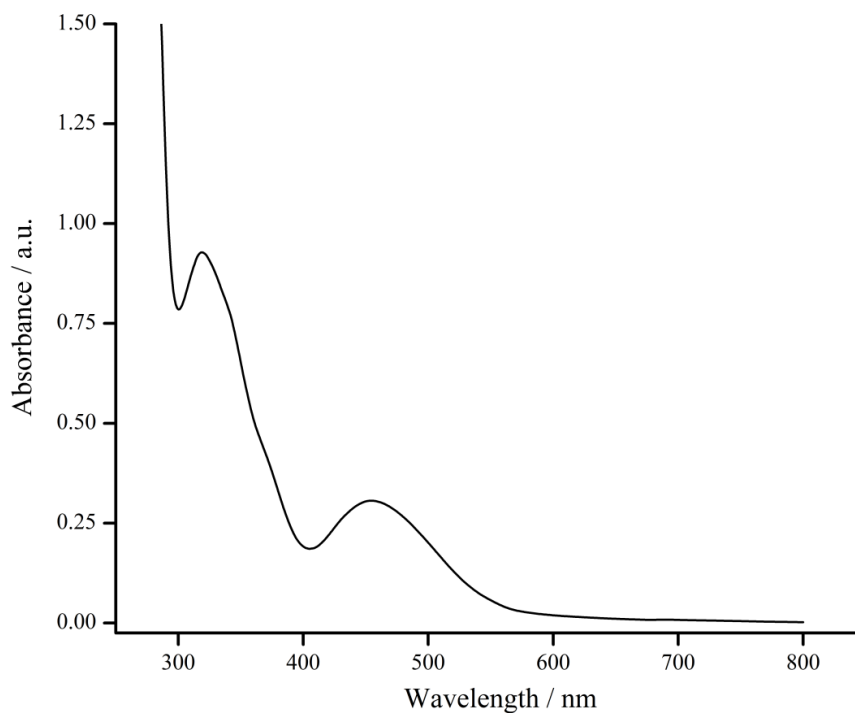


Fig. 68 UV-vis spectrum for ferrocenecarboxaldehyde in DMF.

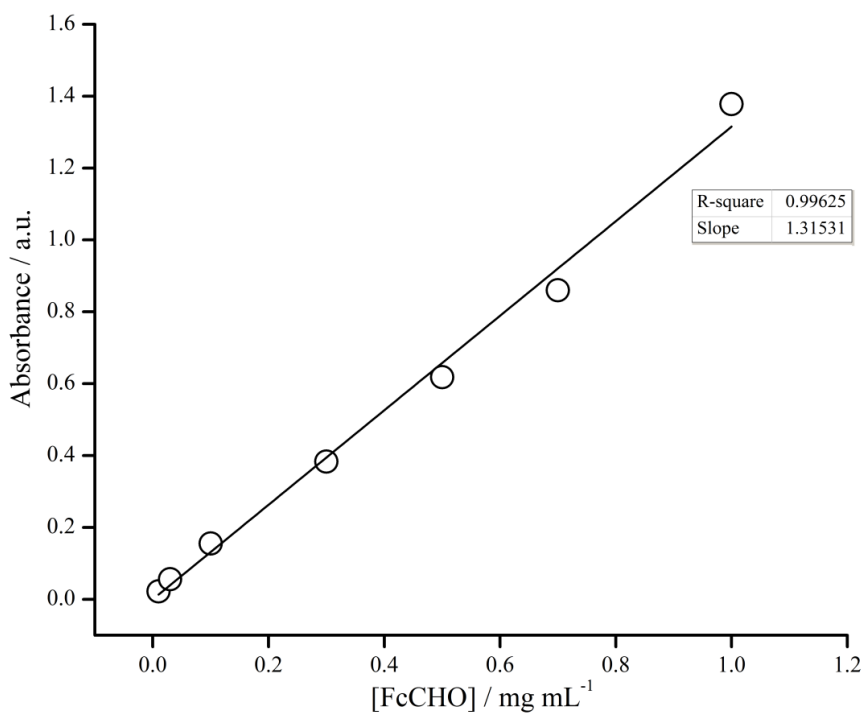


Fig. 69 Calibration of the ferrocenecarboxaldehyde over the concentration range $0.01 - 1 \text{ mg mL}^{-1}$ in DMF.

Next, the ferrocene labelled antibodies were investigated by the same method, the results for which are shown in Fig. 70. Here we see that two similar peaks are observed however the peak originally at 454 nm has shifted to a slightly lower wavelength of 422 nm and the peak at 319 nm shifted higher to 328 nm. This change may be attributed to changes in bonding or structure upon conjugation of the ferrocene to the antibodies. There is also the presence of a much larger, sharp peak at ~280 nm that caps the detector limit; this is caused by the presence of the IgG protein from the antibody conjugates which absorb strongly in the 200-300 nm region.⁷ This is evidence that the ferrocene has been successfully conjugated to the antibody.

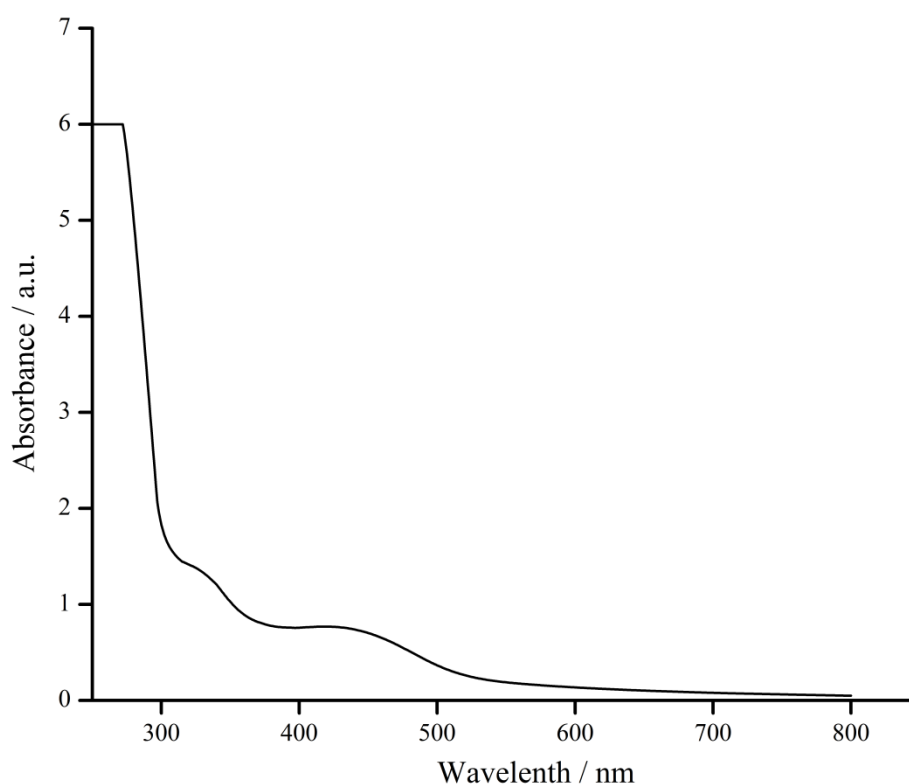


Fig. 70 UV-vis spectra of ferrocene tagged anti-BNP antibodies.

A calibration for the ferrocene labelled antibody was then prepared shown in Fig. 71, with UV-vis spectroscopy carried out over a concentration range $2.83 \times 10^{-2} - 3.53 \times 10^{-3} \text{ mg mL}^{-1}$. Once again the data is highly correlated ($R^2 = 0.994$) with an extinction coefficient of $27.108 \text{ mL mg}^{-1} \text{ cm}^{-1}$.

Since the extinction coefficients for both the ferrocene and labelled antibodies are known, the ratio of the two yields the approximate number of redox tags per antibody, as per eq. (5.2):

$$\begin{aligned} \text{no. Fc tags} &= \frac{\epsilon_{\text{Ab-Fc}}}{\epsilon_{\text{FcCHO}}} & (5.2) \\ &= \frac{27.108}{1.315} = 20.6 \end{aligned}$$

The number of ferrocene tags per antibody was determined as ~ 21 . Work by Okochi *et al.*⁸ has previously determined the number of ferrocene tags bound to IgG antibodies as 8, calculated *via* an atomic absorption spectroscopic route. The larger number of tags observed in this system may be as a result of the significant variation in structure observed in antibodies and their binding sites, hence the number of free amine groups is subject to considerable change. In the case of anti-BNP, there may be more free amine groups available and hence a higher number of sites available for ferrocene conjugation.

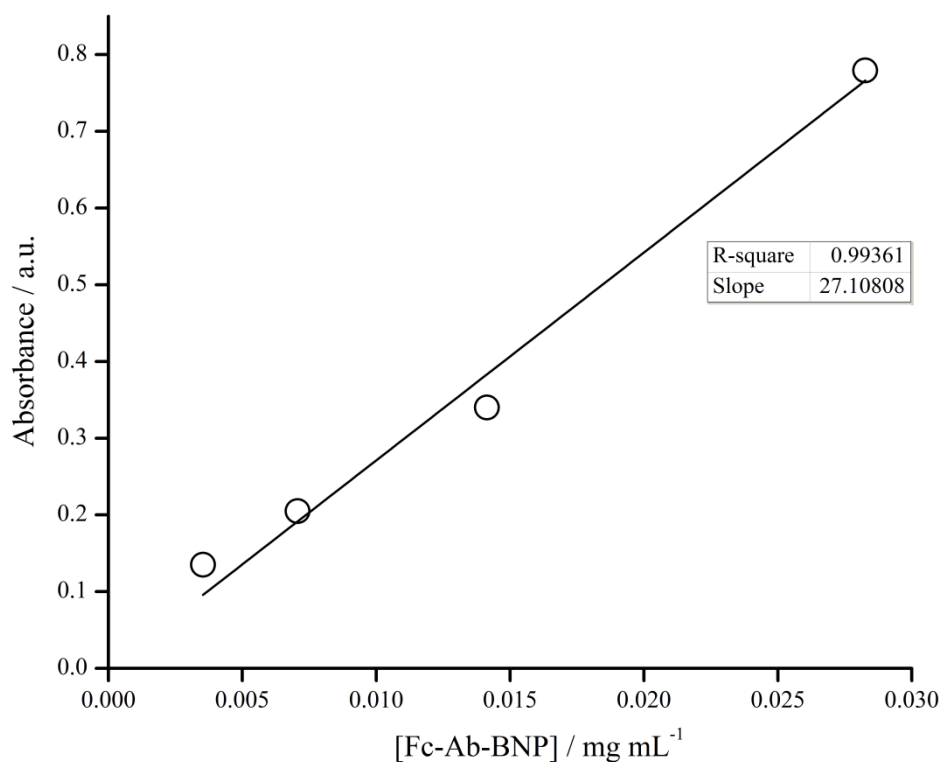


Fig. 71 Calibration of the ferrocene labelled anti-BNP antibodies over the concentration range $2.83 \times 10^{-2} - 3.53 \times 10^{-3} \text{ mg mL}^{-1}$.

5.2.3 Voltammetric Investigation of Fc-Ab-BNP Modified ITO

Following completion of the electrode and ferrocene tagged antibody characterisations, the success of the surface immobilisation required validation. For

the modification to be a success, an electrochemical signal for the ferrocene redox couple should be observed under voltammetric investigation. Therefore the modified ITO electrode was subject to cyclic and square wave voltammetry after sufficient wash steps to remove any unbound antibody.

The results from cyclic voltammetry shown in Fig. 72 clearly illustrate the presence of the ferrocene redox couple with values of E_p^{ox} and E_p^{red} as 0.36 V and 0.12 V respectively, confirming the surface bound nature of the ferrocene. Furthermore, multiple repeat scan cycles show very little deviation between peak position, shape and intensity inferring that the surface bound ferrocene system is stable. The difference observed between the first and following scans is due to the initial stabilisation of the ferrocene modified surface, wherein the surface microstructure is subject to a reorganisation under the influence of potential.

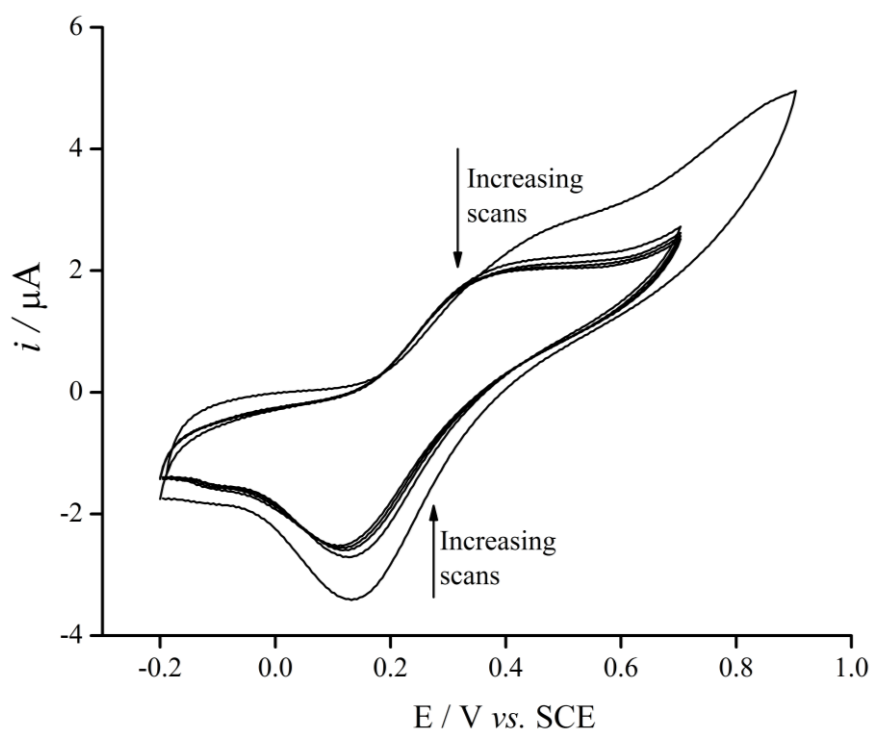


Fig. 72 Cyclic voltammograms of Fc-Ab-BNP modified ITO electrode showing five consecutive scans, $\nu = 0.1 \text{ V s}^{-1}$.

The results of square wave voltammetry, shown in Fig. 73 also show a clear peak assigned to the oxidation of the ferrocene tags. However there is a significant baseline shift following the oxidation process hence a baseline correction is required to normalise the data for analysis in a more suitable format. This was carried out

using the polynomial baseline correction functionality tool in Metrohm Autolab GPES software. Fig. 74 shows that the baseline correction produces a clear peak with little error arising from the procedure, $\sim 0.3 \mu\text{A}$.

Over the four scans undertaken, there is a slight variation in the peak current observed. As seen in Chapter 2, the simple models of the double layer indicate a capacitance present due to an ordering of charge on both the surface of the electrode and the ions present at the electrode|electrolyte interface. The oxidation/reduction of the ferrocene tag causes a developing charge effect. This, coupled with the intrinsic charge already present in the double layer, leads to pseudo-capacitance. The pseudo-capacitance is not described in the models presented thus far but will certainly have an impact on the observed peak current.

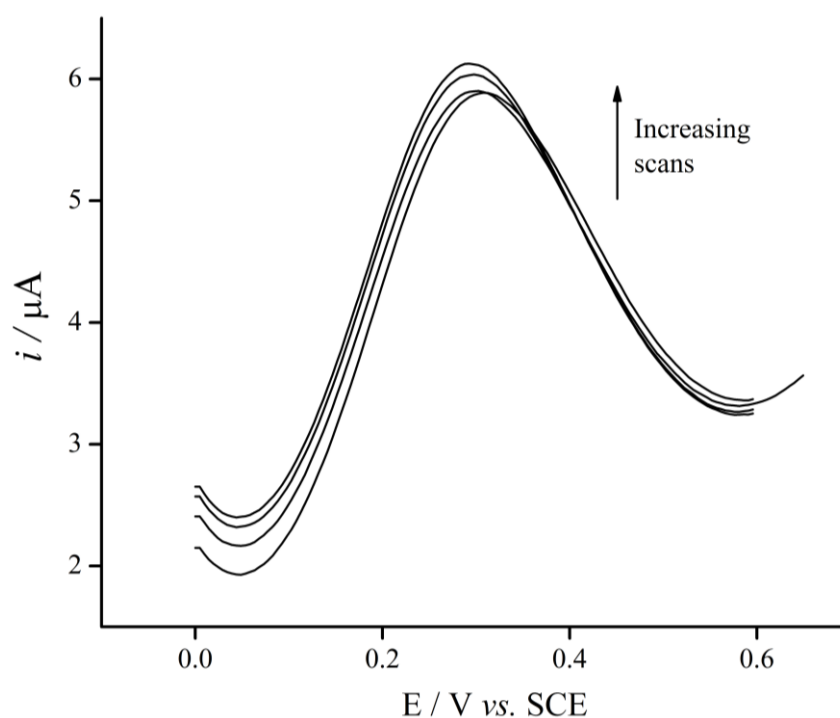


Fig. 73 Square wave voltammograms of Fc-Ab-BNP modified ITO electrode showing four consecutive scans, frequency = 25 Hz, amplitude = 1 mV.

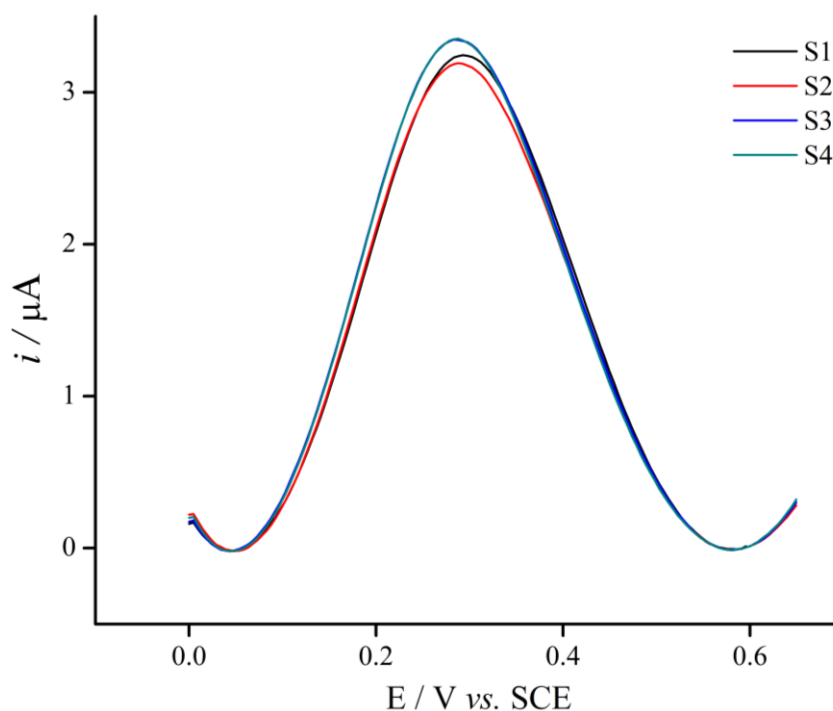


Fig. 74 Baseline corrected square wave voltammograms for the scans shown above in Fig. 73.

5.2.4 Preliminary Electrochemical Immunoassay Viability Investigation

Having characterised the molecular wire modified electrode surface, labelled antibodies and subsequent successful surface immobilisation, the next step was to investigate the viability of the prepared surface as an electrochemical immunoassay platform. From the previous characterisations, it is apparent that both electrochemical methods used are suitable for the electrochemical analysis of the modified surface hence both methods were utilised to investigate the immunological response of antigen incubation.

As stated in section 4.2, it was expected that a reduction in signal intensity would occur as a result of antigen incubation and that this response could be quantified to the concentration of antigen added to the surface. The surface was subject to incubation with BNP over a concentration range of 10 pg mL^{-1} – 1 mg mL^{-1} in one order of magnitude increments to encompass the clinically relevant range where BNP levels in blood can range 20 pg mL^{-1} to $> 2 \text{ ng mL}^{-1}$ in the instance of severe congestive heart failure and the surface investigated by cyclic and square wave voltammetry.

Preliminary results of the cyclic voltammetry method illustrated in Fig. 75 show an electrochemical response with decreasing current for both the oxidation and reduction processes while the antigen concentration increases, as expected. There is a clear increase in ΔE_p with increasing concentration as the oxidative wave shifts more positive to ~ 0.42 V and the reduction process more negative to ~ 0.08 V, a shift of ~ 60 mV and ~ 40 mV over the course of antigen addition. The average $\Delta E_p = 96$ mV ($n=3$). This further evidences the findings of Dou *et al.* where the anticipated change in formal oxidation potential of the bound ferrocene moieties occurs as a result of antigen binding, such that a fraction can no longer participate in low-potential voltammetry coupled with reduced electron transfer kinetics results in a lower current observed.

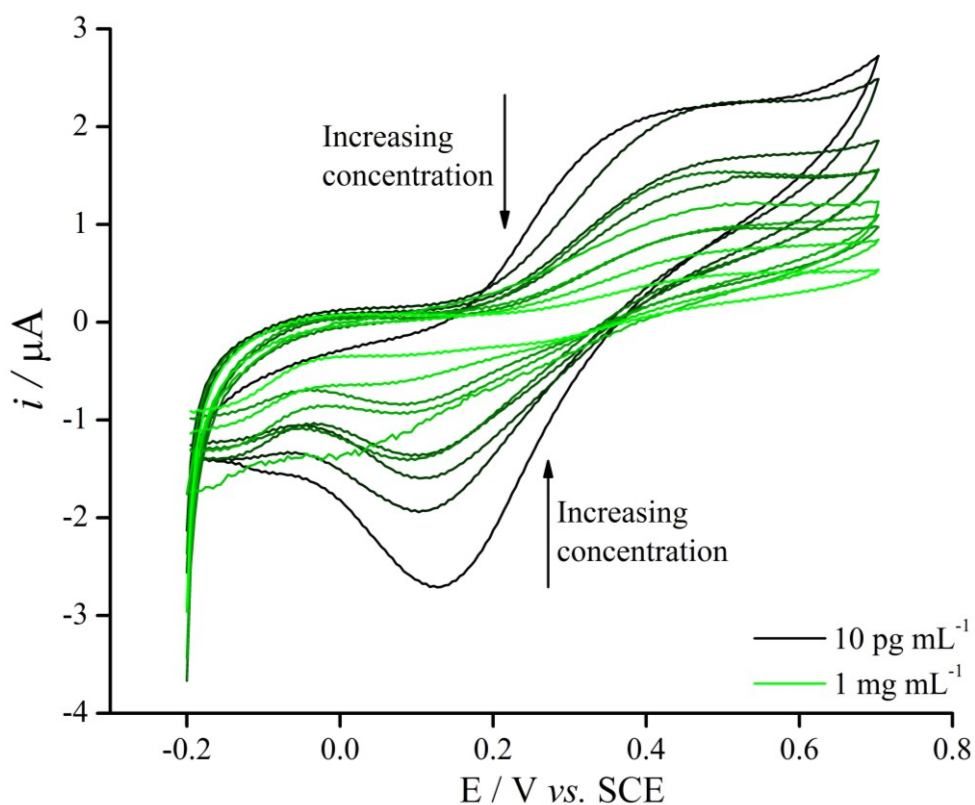


Fig. 75 Cyclic voltammograms for the blank and subsequent 15 minute incubations of increasing concentration of BNP ($10 \text{ pg mL}^{-1} - 1 \text{ mg mL}^{-1}$) to the Fc-Ab-BNP modified ITO.

The current response corresponding to the oxidation of the ferrocene label of the electrode-immobilised anti-BNP is relative to the concentration of BNP analysed, in that the current reduces sequentially with each addition. Hence, the system functionality for use with anti-BNP was confirmed, as expected. To further analyse

the viability of this immunoassay system for the detection of BNP, a calibration of the oxidative current response was prepared. The change in peak current, Δi_p was calculated as $i_p^{\text{blank}} - i_p^{\text{incubation}}$, where i_p^{blank} represents the current response of the modified electrode prior to the antigen addition and $i_p^{\text{incubation}}$ is the current measured after incubation with antigen.

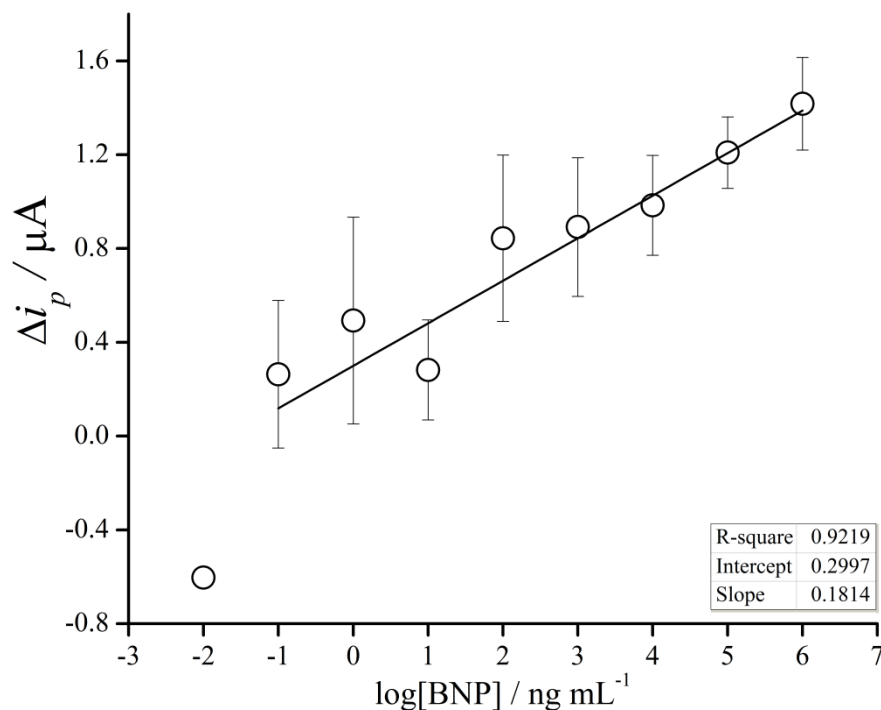


Fig. 76 Calibration obtained for change in baseline corrected peak current with increasing concentration of BNP antigen for the ferrocene labelled anti-BNP modified ITO under cyclic voltammetry investigation. Linear response ranges 100 pg mL^{-1} to 1 mg mL^{-1} BNP ($n=3$).

Fig. 76 shows a large current change from the 10 pg mL^{-1} to the 100 pg mL^{-1} incubation, however current response tends to linearity thereafter up to 1 mg mL^{-1} . This infers that initially there is a fast deposition of antigen to the surface as the surface has the most sites available for binding, leading to the greater difference in current observed with the first additions. As the system tends towards steady state with increasing concentration of antigen, the signal change observed occurs at a more stable rate. The current response is mostly in the desired correlation with $R^2 = 0.9219$ however suffers from considerable error, inferring that the cyclic voltammetry route may not as reliable as required. The limit of detection for this system was determined as $163.39 \text{ ng mL}^{-1}$ which is not as low as expected for this immunoassay protocol

when compared to the pg mL^{-1} LOD obtained by Dou *et al.*¹ This inflation in the LOD may be attributed to the large error observed in the cyclic voltammetry data. If the protocol was carried out with a lower concentration range it may also be possible to reduce the LOD to a suitable value though due to time constraints this was not carried out.

The CV route grants insight into the analytical response to antigen and thus the sensing capability of the immunoassay platform, however concentrations of BNP in patients may only reach in excess of 2 ng mL^{-1} for severe cases, therefore a sensing protocol of greater sensitivity is required for this application.

In light of this, square wave voltammetry was investigated as an alternate electrochemical technique due the potential increased sensitivity this method offers. The preliminary results of the square wave voltammetry investigations are shown in Fig. 77.

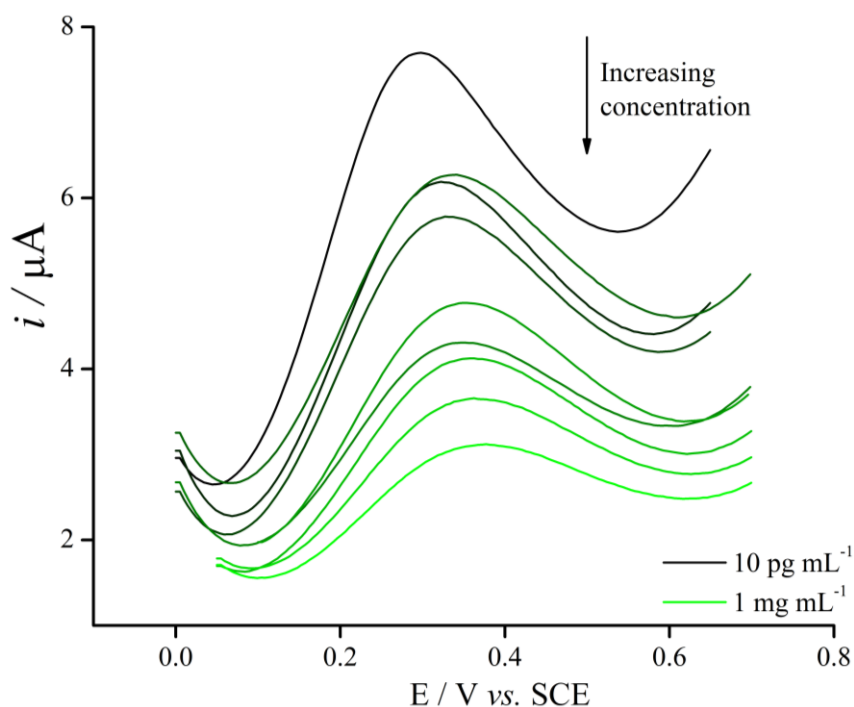


Fig. 77 Square wave voltammograms for the blank (highest current) and subsequent 15 minute incubations of increasing concentration of BNP (10 pg mL^{-1} – 1 mg mL^{-1}) to the Fc-Ab-BNP modified ITO.

The voltammograms observed from square wave voltammetry show a marked improvement in the peak resolution and magnitude enabling greater analysis readability, both visually and numerically and follow the same trend of decreasing

current with increasing antigen concentration. The difference in current measured in this protocol is made without any baseline correction in an effort to determine if a suitable calibration could be obtained with less computational elements involved. A calibration of the current response was plotted to yield a linear response over the full concentration range investigated, though with a lesser degree of correlation within the data ($R^2 = 0.8862$) compared to the CV method. The LOD for this protocol was determined as 833 ng mL^{-1} , over five times less sensitive than the CV method. It is likely that the individually shifting baselines observed in the measurements inflate or deflate the result thereby introducing experimental error, reducing the sensitivity of the immunoassay platform.

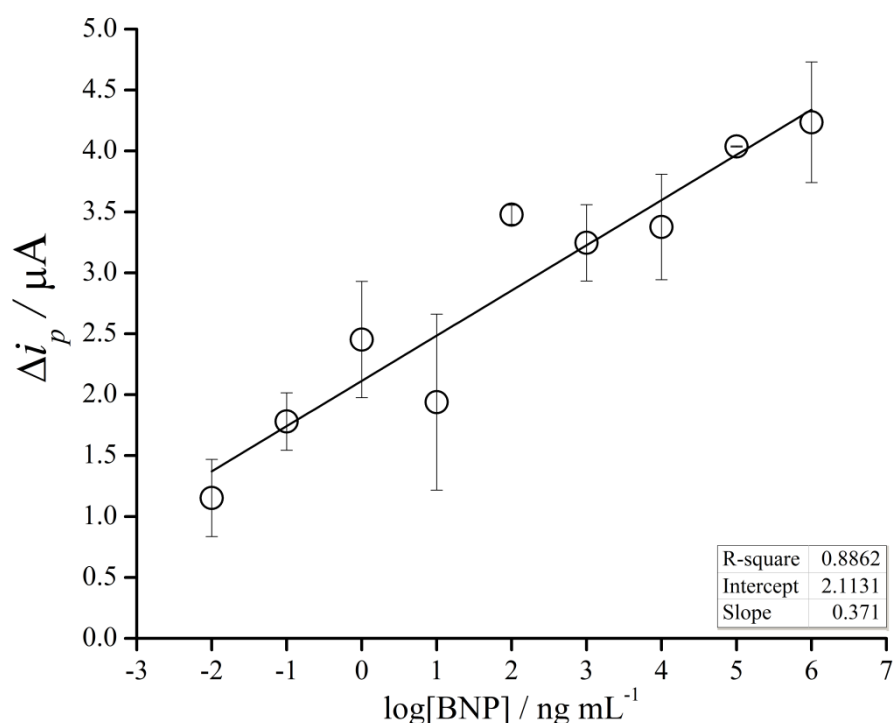


Fig. 78 Calibration obtained for change in peak current with increasing concentration of BNP antigen for the ferrocene labelled anti-BNP modified ITO under square wave voltammetry investigation. Linear response ranges 10 pg mL^{-1} to 1 mg mL^{-1} BNP ($n=3$).

To investigate whether or not a baseline correction normalisation of the square wave data would further improve the sensitivity of the sensing platform, the square wave voltammograms were baseline corrected as shown in Fig. 79. We see that the baseline correction normalises all of the voltammograms to a baseline of zero and produces resolved and clear oxidative peaks.

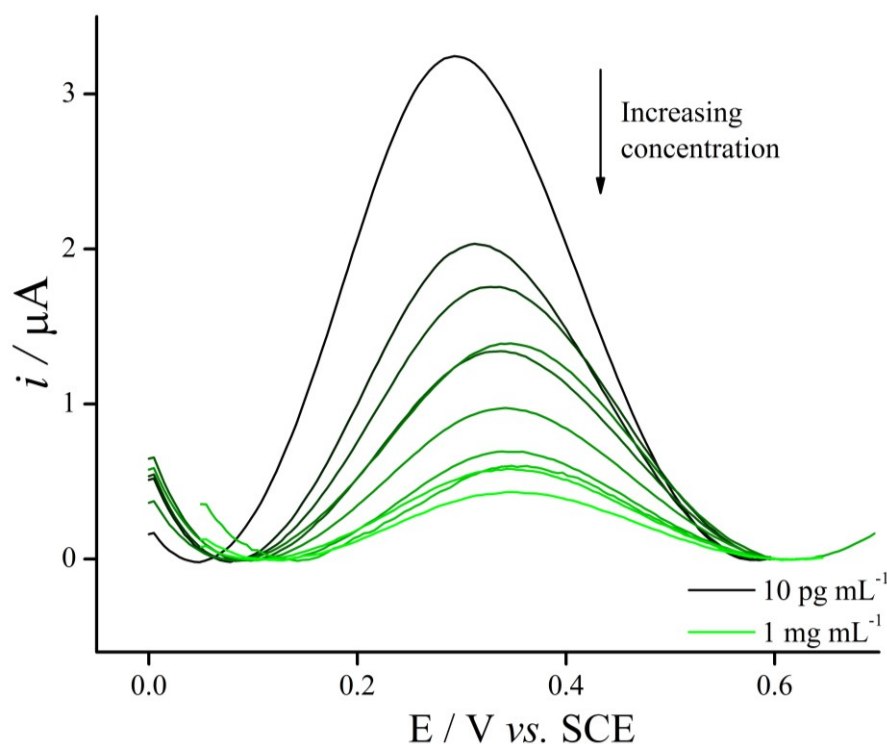


Fig. 79 Baseline corrected square wave voltammograms for the blank (highest current) and subsequent 15 minute incubations of increasing concentration of BNP (10 pg mL^{-1} – 1 mg mL^{-1}) to the Fc-Ab-BNP modified ITO.

The calibration plot was repeated for the baseline corrected data and compared to the un-modified data, where it was found the baseline correction procedure improves the correlation of data ($R^2 = 0.9272$) resulting in an improved LOD of 196 ng mL^{-1} . Though this is an improvement of over four times on the SWV data and is close to the LOD determined for the CV approach, the sensitivity remains not sufficiently high enough for the proposed clinical application.

Further to this, there is a shift in oxidation potential from 0.31 V to 0.37 V , a shift of 60 mVs across the concentration range investigated. the average $\Delta E_p = 66 \text{ mV}$ and 61 mV ($n=3$) for the square wave and baseline corrected square wave voltammetry respectively. This shift in the oxidation potential is smaller than the 96 mV observed for the cyclic voltammetry investigations. However, since there is a peak potential shift in both cases, it was investigated whether or not the shift in oxidation potential could be analysed as an alternative antigen detection strategy to the peak current route. This involved plotting calibrations of the peak potential against concentration of BNP, similarly to the above analysis.

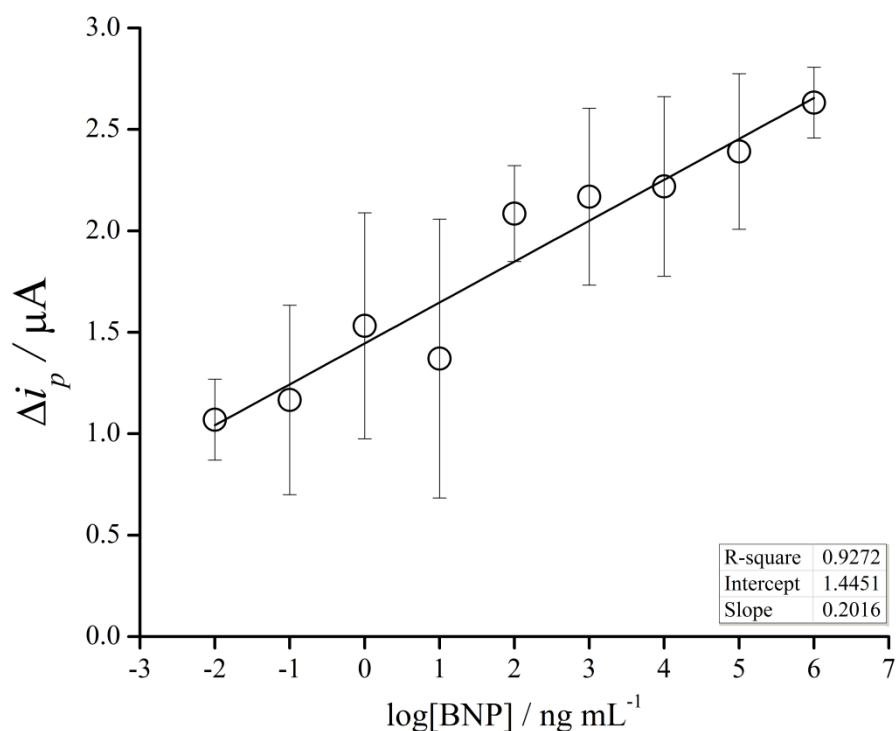


Fig. 80 Calibration obtained for the baseline corrected square wave data shown above. Linear response ranges 10 pg mL^{-1} to 1 mg mL^{-1} BNP ($n=3$).

Firstly the peak potential change in the cyclic voltammetry case was investigated and a calibration plot prepared as shown in Fig. 81. It is clear that the relationship between the peak potential and concentration is not very strong. The reason for such is the lack of peak resolution in the cyclic voltammograms. The flattening effect observed as the peak decreases in magnitude with the increasing antigen concentration increases the difficulty of data analysis to accurately obtain the peak potentials. It was determined that the change in peak potential as observed from cyclic voltammetry was not a suitable technique to quantify the concentration of antigen.

The E_p response observed in square wave voltammetry shown in Fig. 82 illustrates a much improved relationship where $R^2 = 0.9307$. This may be attributed to the greater peak resolution observed in the square wave voltammograms, retaining clear peak shapes at the higher concentrations allowing for accurate data analysis. As a result the LOD was found to be much lower at 106 ng mL^{-1} , a significant improvement on the i_p detection strategy.

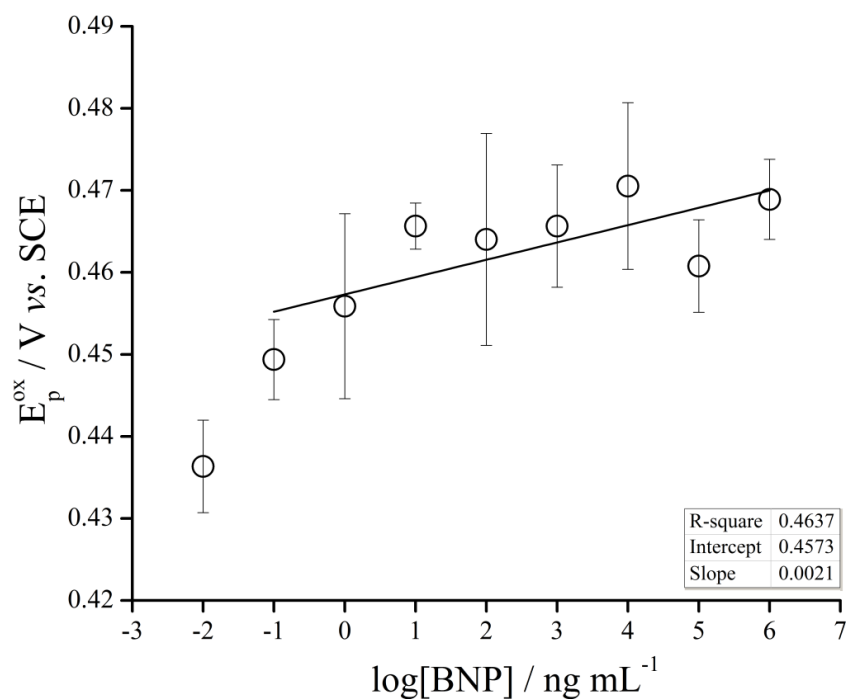


Fig. 81 Calibration of oxidative peak potential shift with increasing antigen concentration during cyclic voltammetry.

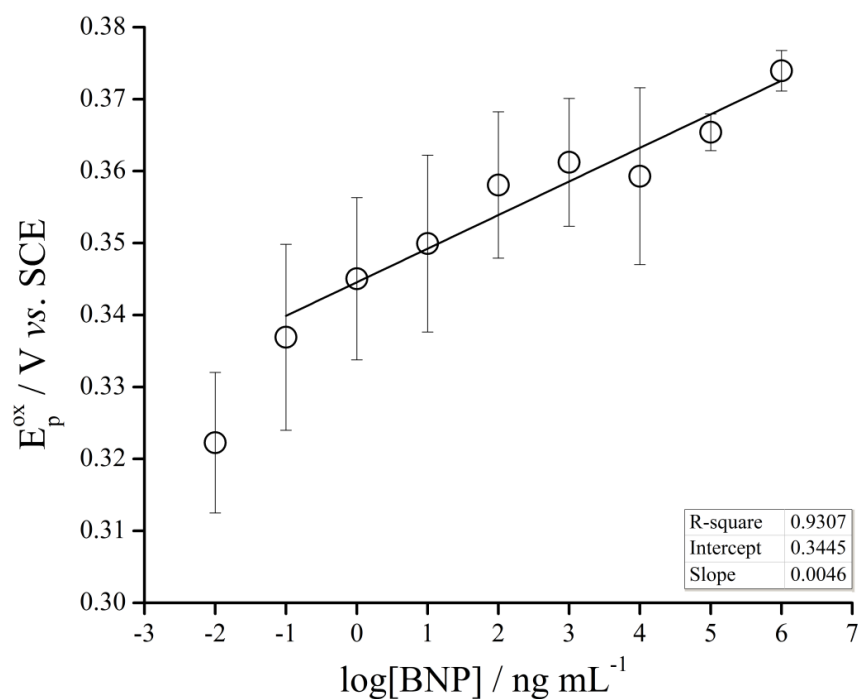


Fig. 82 Calibration of oxidative peak potential shift with increasing antigen concentration during square wave voltammetry.

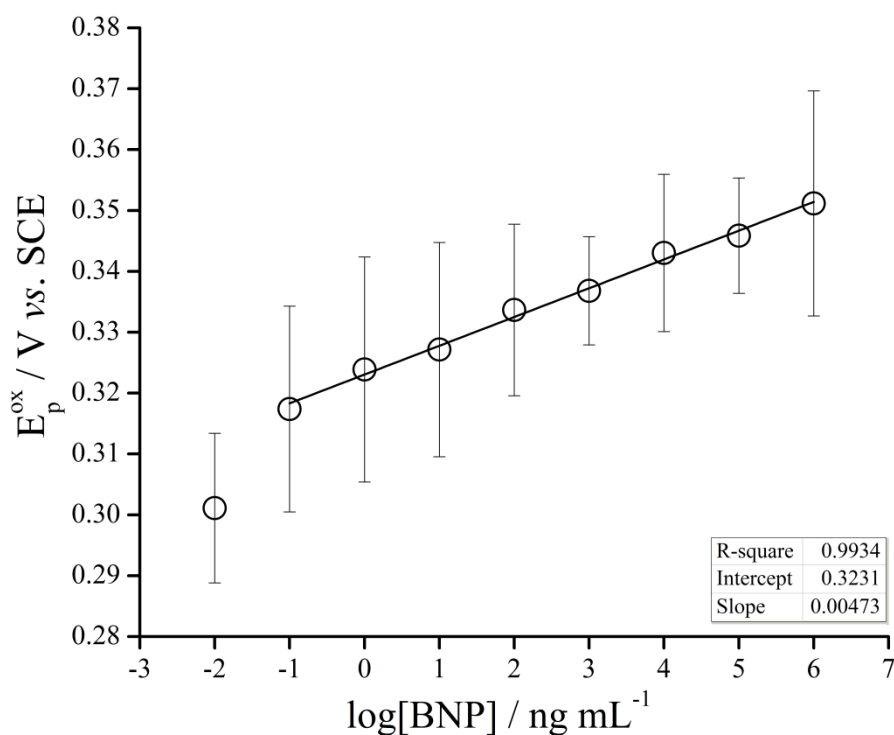


Fig. 83 Calibration of oxidative peak potential shift with increasing antigen concentration for the baseline corrected square wave voltammetry data.

Finally, taking the baseline corrected square wave data into account, in Fig. 83 we see a vastly improved calibration of linear response from 100 pg mL⁻¹ to 1 mg mL⁻¹ with $R^2 = 0.9934$. The LOD was determined as 3.98 ng mL⁻¹, which is a substantial two order of magnitude improvement on the concurrent i_p detection strategy.

It is important to note that even though the LOD is not sufficiently low in this case, this could potentially be improved if the concentration range investigated was increased as to include lower concentrations of antigen. Since lower concentrations were not investigated, the immunoassay platform does not perform to the sensitivity required for clinical application in either the current or potential detection routes discussed, though if revisited, holds the potential to operate at the intended concentration requirements.

Another issue with this system is that the comparison of experimental data is made between the prepared electrode areas of one electrode i.e. between electrode areas one, two and three. This means that there is likely to be a difference between the readings observed from electrode are one to three as the distance increases from the point of connection, as a result of resistance effects. This is in fact observable

between the three data sets and is the source of the relatively large error. This in turns reduces the sensitivity, increasing the LOD. If the error was much smaller between the data sets, the LOD would be largely reduced and the sensing platform may be operable in the desired concentration range.

We next explore the possibility of undertaking electroimmunoassay for the β sub-unit of hCG so as to emphasise that this voltammetric approach is sufficiently versatile as an electroimmunoassay.

5.3 Voltammetric Determination of the Pregnancy Biomarker β -hCG

For this method, the procedure carried out for the anti-BNP tagging with ferrocene and subsequent conjugation to an ITO electrode surface was chosen as the most ideal sensing platform for device development as the results showed excellent promise for reducing experimental turnaround time couple with ease of data analysis. Therefore the method for labelling the anti-BNP was repeated for anti- β -hCG antibodies and three independent electrode areas on one ITO slide were prepared. The electrodes voltammetrically investigated and subject to variable scan rates to determine the success of the label conjugation and surface modification protocols and characterise the electrochemical system.

As shown in Fig. 84(a), the electrochemical system stabilises to yield reproducible redox waves for the surface bound ferrocene, comparable to the behaviour of the Fc-Ab-BNP sensing surfaces previously discussed. Variable scan rate CV from scan rates 0.02 V s^{-1} to 1 V s^{-1} as shown in Fig. 84(b), illustrates two clear redox waves sequentially increasing in peak current with increasing scan rate, where E_p^{ox} and E_p^{red} were found to be 0.234 V and 0.143 V vs. SCE respectively at 0.1 V s^{-1} scan rate. Furthermore, there is an increase in peak separation with increasing scan rate, inferring a quasi reversible system with a total average increase in peak separation of 82 mV from lowest to highest scan rate.

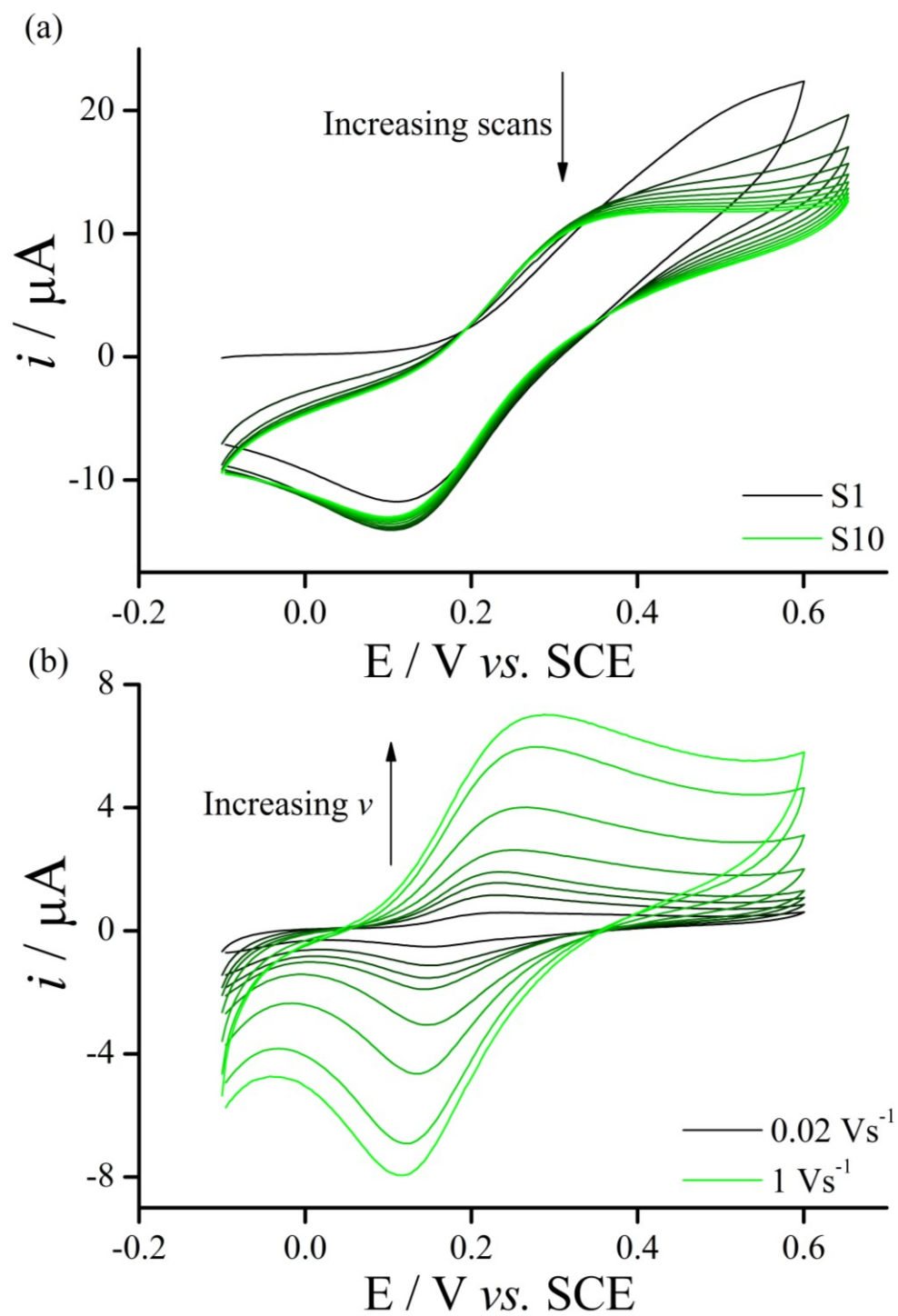


Fig. 84 (a) Cyclic voltammetry of the Fc-Ab β -hCG modified ITO electrode over ten scan cycles. (b) Variable scan rate of the system where $\nu = 0.02 - 1 \text{ V s}^{-1}$ from bottom to top.

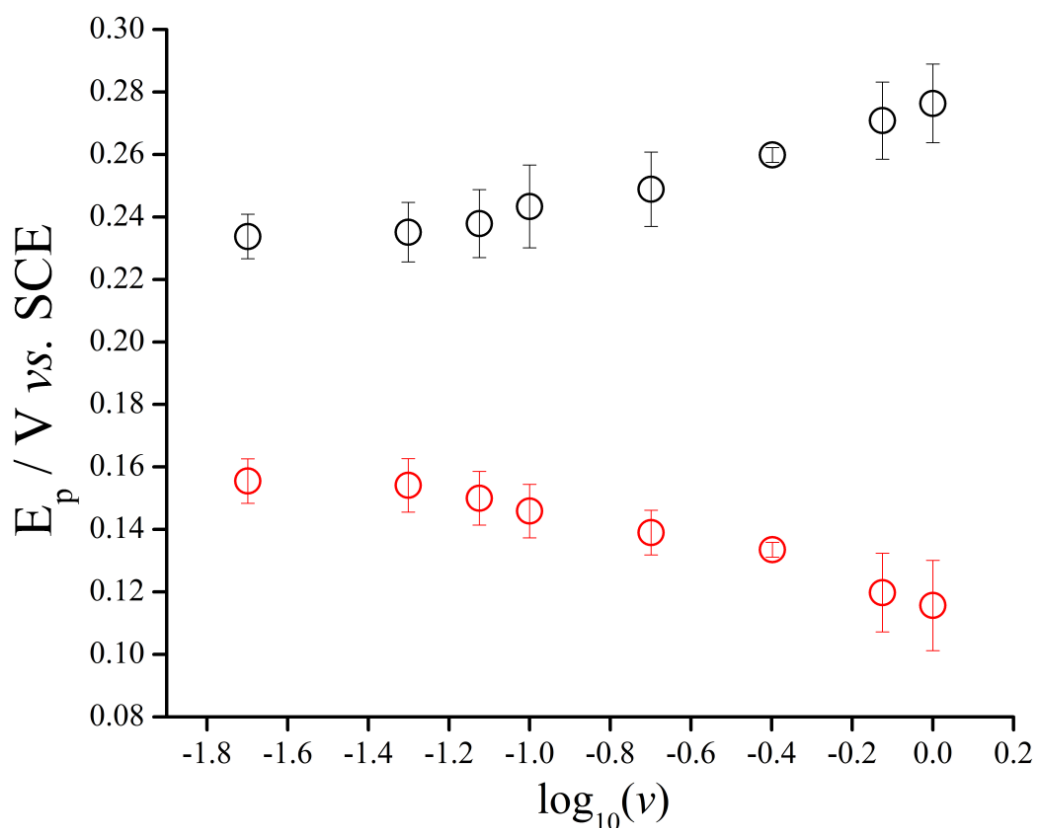


Fig. 85 Plot of E_p vs. $\log(v)$ illustrating the peak splitting with increasing scan rate. (●) denotes E_p^{ox} and (●) denotes E_p^{red} .

To confirm the surface confined nature of the redox species, a plot of peak current versus scan rate was constructed where it was found that the electron transfer process is mass transport controlled as opposed to by electron transfer, which is strange for this system. The peaks observed under cyclic voltammetry were stable and reproducible after several potential cycles electrode washings, thus confirming that the electrochemical process originates from the surface-confined redox species. One would expect for this case, that the peak current should increase linearly with scan rate as theoretically predicted by Laviron *et al.*⁹ Fig. 86(a) shows that this does in fact occur for scan rates 0.02 - 0.1 V s^{-1} however from 0.2 - 1 V s^{-1} the peak current tails off from the expected trend.

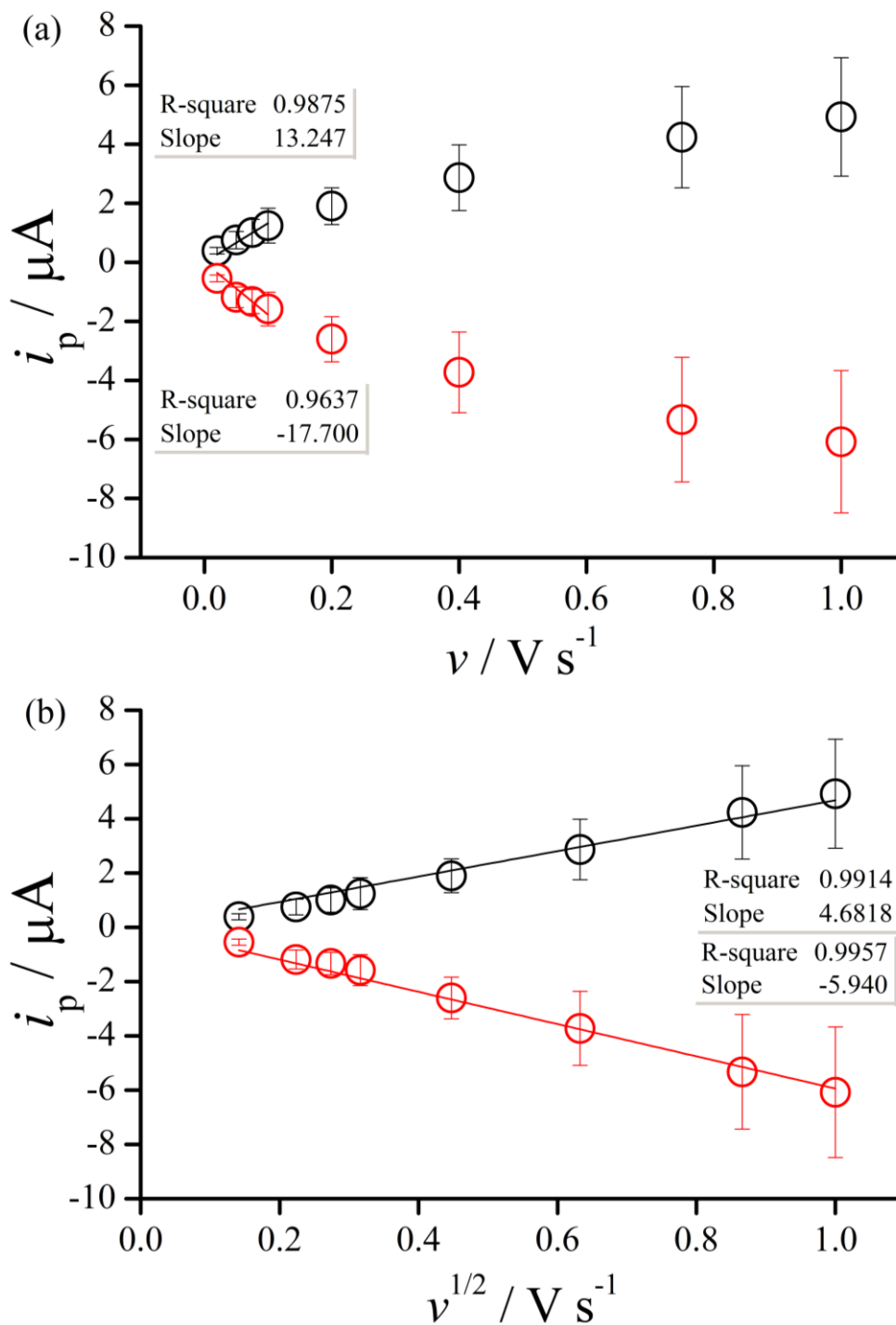


Fig. 86 Plots of peak current versus scan rate and square root scan rate for variable scan rate investigations of the Fc-Ab- β -hCG modified ITO electrode (n=3) where (a) illustrates a plot of peak current data versus the scan rate as for surface confined systems and (b) shows plot of peak current data versus square root of the scan rate as for mass transport controlled systems. Here (O) and (●) denote i_p^{ox} and i_p^{red} respectively.

When the current data is plotted versus the square root of the scan rate as shown in Fig. 86(b), a more favourable correlation with proportionality between peak current and square root of scan rate is observed, as predicted for mass transport dependent electrochemical processes by the Randles-Sevcik equation. This may be rationalised *via* the higher resistive nature of the ITO material compared to other electrodes such as gold or glassy carbon, hence at low ν the current responds proportionally with ν as expected however at higher ν , the resistance begins to interfere thus reducing the observed current to yield the tailing effect seen in Fig. 86(a).

For proof of concept detection, the electrodes were incubated with increasing concentrations of β -hCG over the range $100 \text{ pg mL}^{-1} - 10 \text{ }\mu\text{g mL}^{-1}$, adequately covering the clinical range requirements for β -hCG sensing as previously described followed by voltammetric investigation with CV and SWV. The results reported herein are for a singular experiment as a preliminary study, no repeats were undertaken.

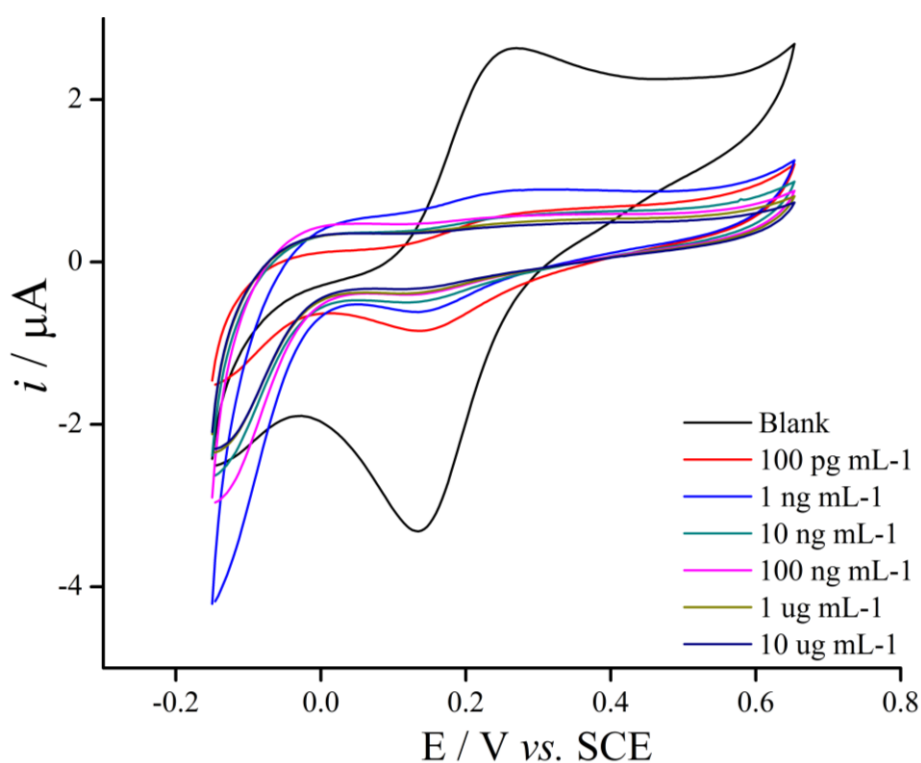


Fig. 87 Voltammograms for CV response of the Fc-Ab- β -hCG modified ITO to increasing concentration of β -hCG at 15 minute incubation time.

As can be seen in Fig. 88, cyclic voltammetry yields a linear response between 1 ng mL^{-1} to $10 \text{ }\mu\text{g mL}^{-1}$. The 100 ng mL^{-1} incubation appears to be an outlier that

without produces a very high R-square correlation, however after carrying out a Dixons Q-test, it was found that this was not the case. This "outlier" result may be caused by the pseudo-capacitance of the ITO surface as discussed previously. There may also be an element of sample loss during washing steps that could cause the variation seen in this incubation result.

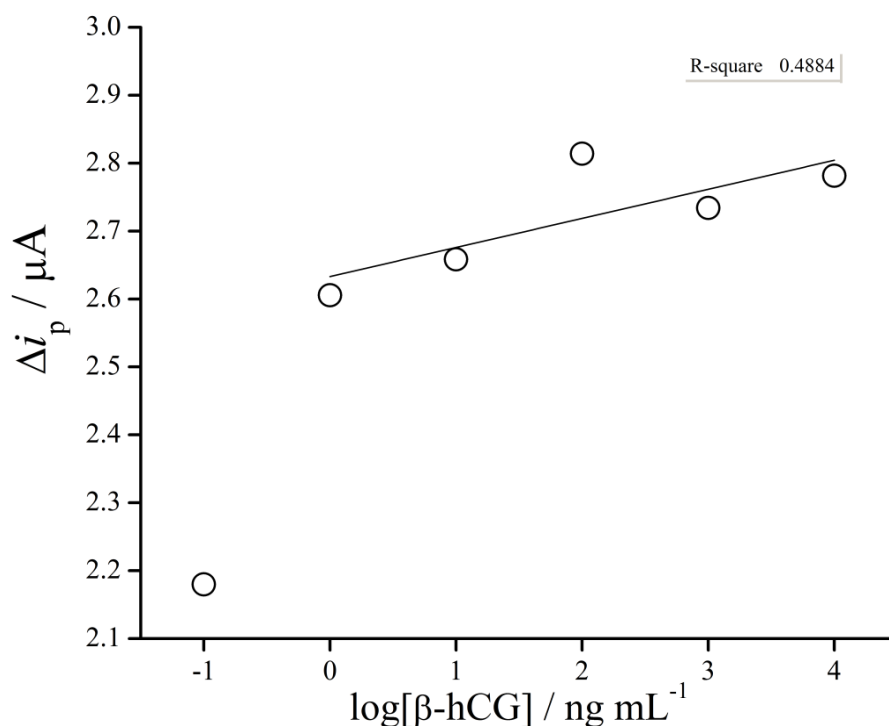


Fig. 88 Calibration plot of CV oxidative current response to β -hCG incubation.

The peak potential shift was also investigated as an alternative method for antigen detection. The identification of accurate peak potential data is subject to considerable ambiguity since the peak resolution decreases with increasing antigen concentration. To best identify the peak potential, a chart of each individual scan was manually inspected alongside the CV data. The approximate correct peak potential was identified in each case at the point after where the current rises to oxidation such that the gradient of the current plateaus before falling off, indicative of the 'tip' of the peak. From the calibration shown in Fig. 89, a stronger overall correlation is observed.

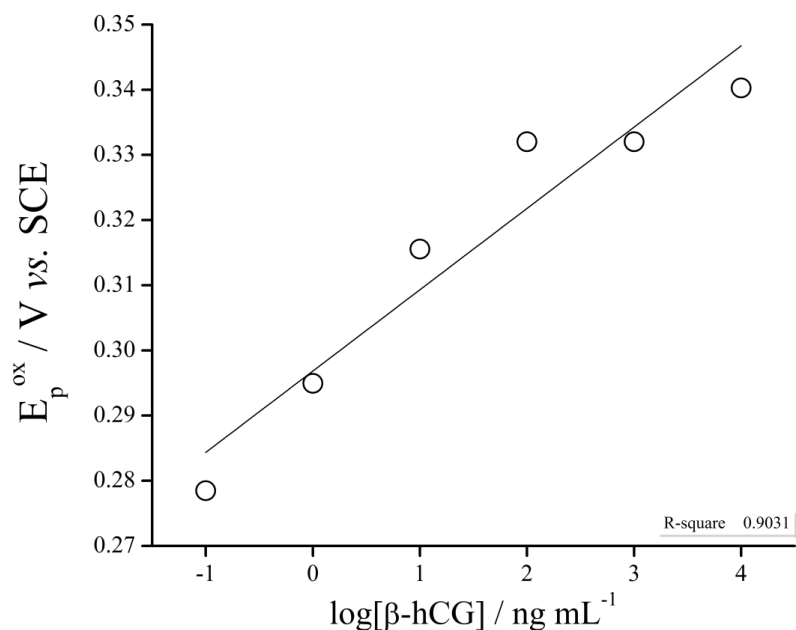


Fig. 89 Calibration plot of CV oxidative peak potential response to β -hCG incubation.

The SWV response, shown in Fig. 90 is much clearer than that of the CV response in Fig. 87, allowing for greater ease of analysis. The current response is in chronological order of addition, therefore the resulting calibrations for the current and peak potential shift responses are significantly improved as a result of this technique.

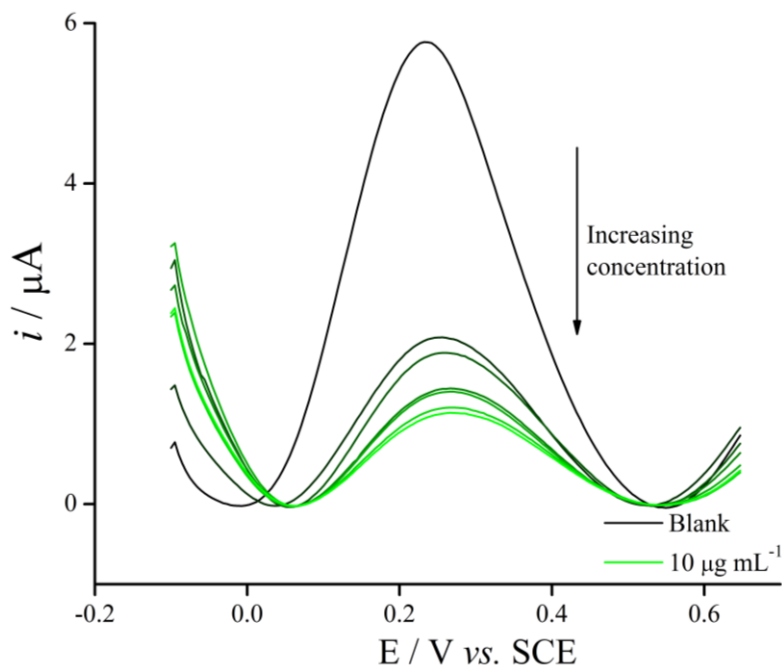


Fig. 90 Baseline corrected SWV response of a Fc-Ab- β -hCG modified ITO electrode to β -hCG incubations (100 pg mL^{-1} to $10 \text{ } \mu\text{g mL}^{-1}$) of 15 minutes.

In particular, the peak potential shift (Fig. 91) gives excellent results up until $10 \mu\text{g mL}^{-1}$, where the peak potential remains steady, giving a linear range of 100 pg mL^{-1} to $1 \mu\text{g mL}^{-1}$. It must, however, be noted that these results are for a physiological buffer which does not recreate the conditions of a real sample. The inherent presence of other electroactive substances or interfering agents could affect this technique where the peak may be obscured or caused to shift, potentially reducing the accuracy or ability to use this method in real world applications.

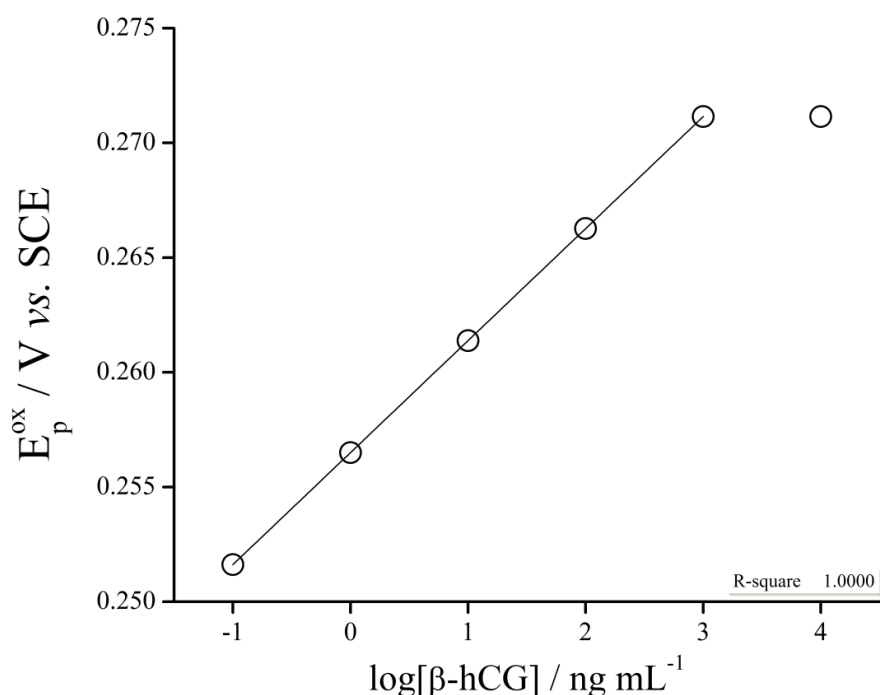


Fig. 91 Calibration plot of SWV oxidative peak potential response to β -hCG incubation.

The peak current results for SWV in Fig. 92 are a significant improvement over those observed from the CV approach in Fig. 88, however there are still some slight erroneous results, that may be attribute to possible dilution errors.

Having thus determined that the developed sensing platform is robust and sensitive to at least two antibodies individually in physiological buffer, we next turn to investigating the exploitation of our system for combinatorial detection of analytes.

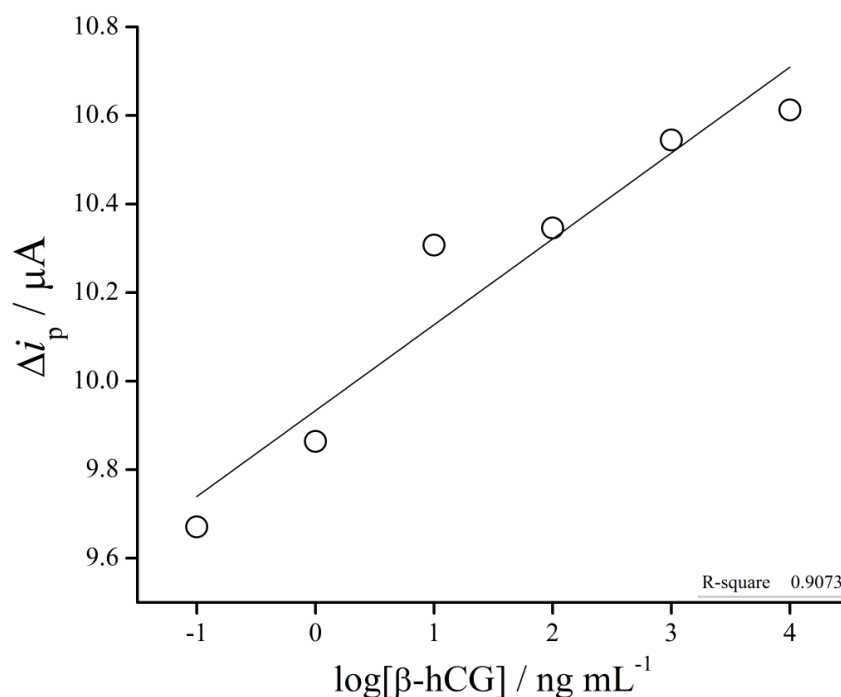


Fig. 92 Calibration plot of SWV oxidative current response to β -hCG incubation (100 pg mL^{-1} to $1 \text{ } \mu\text{g mL}^{-1}$).

5.4 Investigation into Immunoassay Multiplexing

Multiplexing of the immunoassay protocol was of interest to make possible the simultaneous detection of two or more analytes in one sample. Multiplexing is made possible where two redox mediators are identifiable by each respective oxidation potential. This is highly desirable as multiple targets can be identified with one assay system, in which the change in electrochemical response of each redox mediator is specific to the presence of a target molecule. Multiplexing is particularly useful in the clinical detection of cardiovascular disease since specific biomarkers present themselves in the event of certain conditions offering vastly improved clinical utility where rapid sample analysis, biomarker detection and the subsequent relevant treatment decisions can be reduced to one device.

The multiplexing was attempted with both a ruthenium (N-3 Gratzel) dye and chlorpromazine such that the antibodies are labelled similarly to the ferrocene route discussed previously. These two compounds were chosen due to their significantly different redox potentials such that the oxidation and reduction of these compounds is easily identified, as well as their possession of various functionalities for successful conjugation. The results of both prospective labels are discussed below.

5.4.1 Chlorpromazine as an Alternative Redox Tag

Chlorpromazine (CPZ) is a well known anti-psychotic drug that is also redox active and highly electrochemically reversible in nature. Since CPZ and ferrocene oxidise at approximately 0.6 V and 0.35 V respectively, the peaks will be easily identifiable.

Work by McCreery and co-workers^{10, 11} has shown that the electrochemistry of CPZ is known to proceed through two one-electron processes; firstly formation of a cation radical at the ring contained nitrogen *via* one electron oxidation followed by a second electron transfer event to form a another cation radical on the ring bound sulphur atom that subsequently forms the sulfoxide in order to stabilise the compound. The mechanism of oxidation has two possible routes; (i) the cation radical is attacked directly by a nucleophile such as buffer constituents then the adduct is oxidized to CPZ sulfoxide and the nucleophile regenerated or (ii) the disproportionation of the cation to a dication intermediate and subsequent stabilisation as the sulfoxide product.

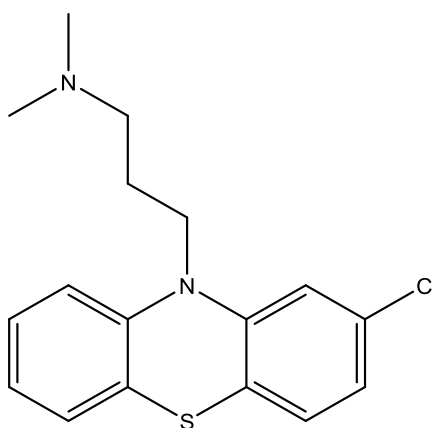


Fig. 93 Structure of chlorpromazine.

To provide the electroactive sensing surface required for antigen sensing *via* the same antibody labelling method used for ferrocene, the CPZ required modification as to contain the suitable -COOH functional group for conjugation to the free amine groups of the antibodies. This was carried out by Mr. Jonathan Knaggs and was presented as a gift, without characterisation, and used as received.

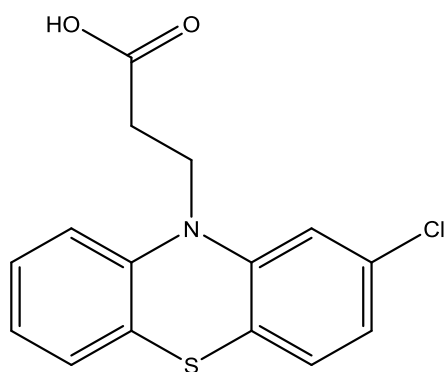


Fig. 94 Converted CPZ used for the labelling procedure.

The labelling procedure was carried out as per section 3.8.1, though the electrode material used was glassy carbon. The electrodes were electrochemically investigated in 10 mM PBS with CV and SWV techniques to determine the success of the conjugation protocol. The expected result of the surface modification is shown in Fig. 95.

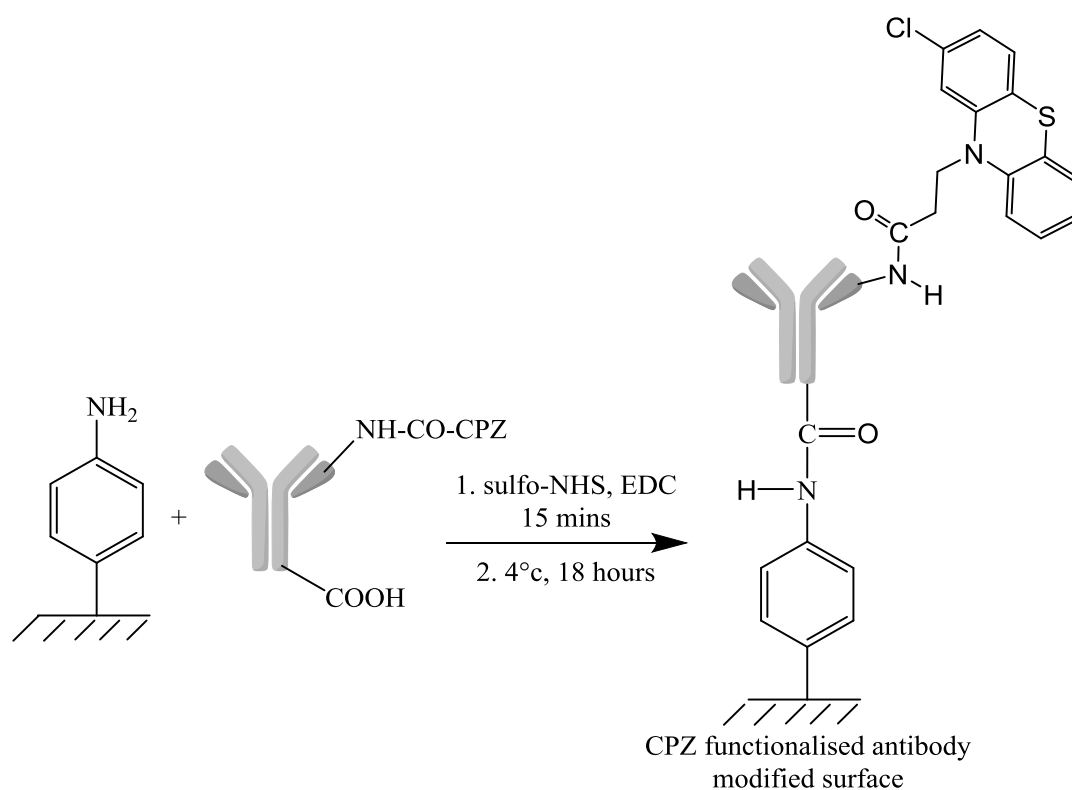


Fig. 95 Schematic breakdown of surface attachment procedure for the CPZ modified antibodies.

In the previous characterisation work, both Ab- β -hCG and Ab-BNP were comparable in performance. The antibody used for this preliminary study into the use of multiple

redox tags was anti-BNP (Ab-BNP) as the cardiovascular sensing application was of immediate clinical interest.

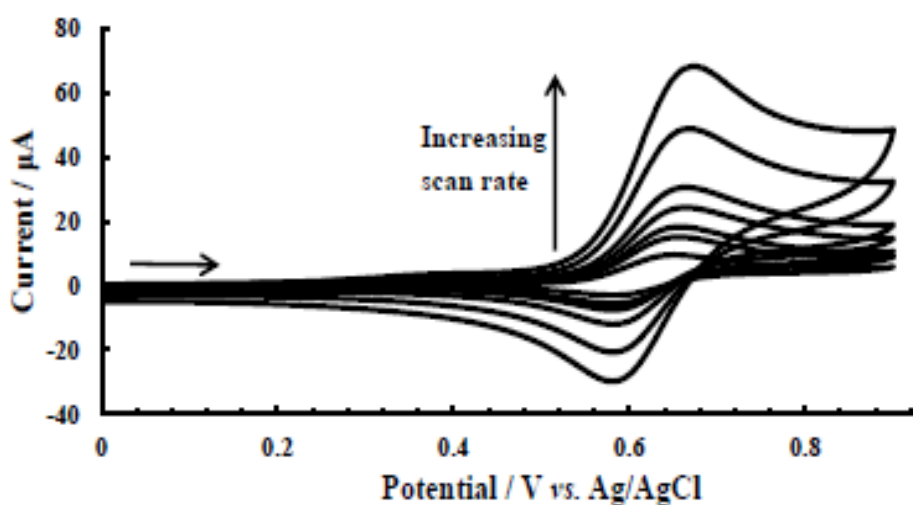


Fig. 96 Cyclic voltammetry of CPZ in 0.1 M KCl at scan rates 0.02 V s^{-1} to 1 V s^{-1} .¹⁴

The voltammetry of CPZ on its own in 0.1 M KCl at a glassy carbon electrode is shown above with an $E_p^{\text{ox}} = 0.65 \text{ V}$ at 0.1 V s^{-1} .¹⁴ The results for CV investigations of the immobilised CPZ show a visible oxidation at $\sim 0.58 \text{ V}$ that roughly coincides with the oxidation potential of CPZ therefore confirming the surface confined nature or the redox mediator. The peak shift may be attributable to the change in electrolyte medium and the surface bound nature of the electroactive compound compared to free in solution. In the immobilised system, the peak shape is less resolved than desired and the peak current magnitude drastically diminishes on subsequent scans. The reason for this may be that the system has not been subject to a sufficiently negative potential to completely reduce the CPZ back to its original state such that upon re-oxidation there is less starting material available. Other explanations may include possible instability of the CPZ on the surface and stripping from the surface upon oxidation.

Even though the initial voltammetry is poor, antigen addition was carried out as for the ferrocene system, where 15 minute incubations of increasing concentration of antigen were made to a freshly prepared CPZ-Ab-BNP modified surface and subsequent CV and SWV investigations to determine if a working response could be obtained.

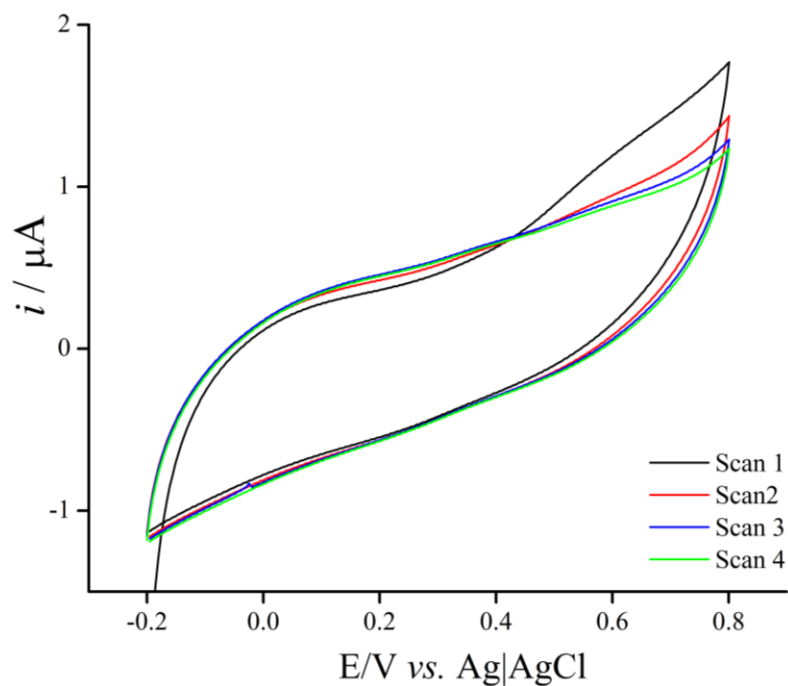


Fig. 97 Cyclic voltammograms for CPZ-Ab-BNP modified glassy carbon surface over a four scan cycle.

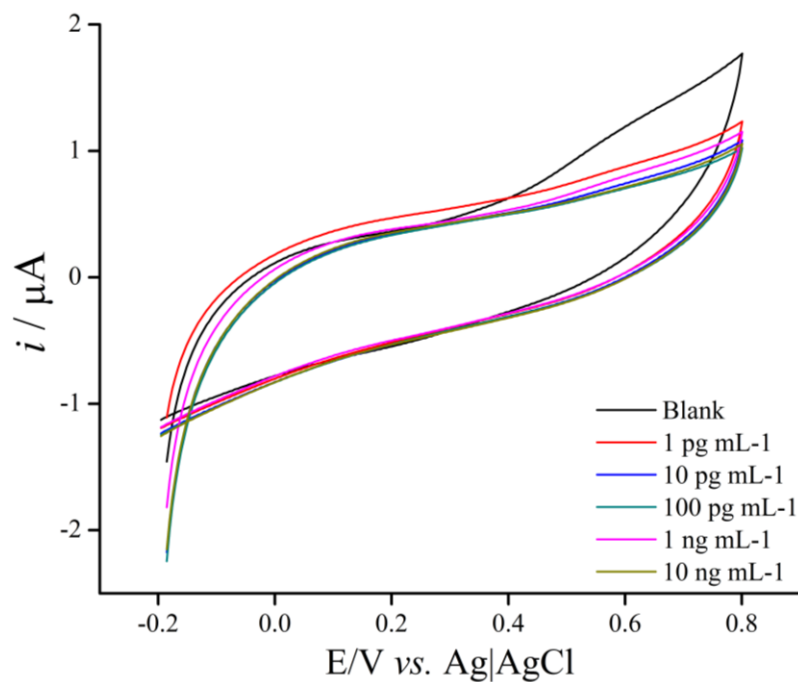


Fig. 98 CV data for incubations of increasing concentration of BNP (1 pg mL^{-1} to 10 ng mL^{-1}) to a CPZ-Ab-BNP modified glassy carbon electrode surface in 10 mM PBS.

In the CV experiments, as expected the current response decreases as the antigen concentration increases though the readings become increasingly difficult to analyse

with increasing concentration as a result of the poor peak resolution observed. For calibration, the electrode was subject to three scan cycles and the data averaged.

Note that this is comparison of scans 1 - 3 and not 3 separate electrodes, successful repeats of this work were not carried out because of issues with the unknown purity of the CPZ product used.

The LOD was found to be $0.98 \mu\text{g mL}^{-1}$ that is far too high for the desired sensing application. There was again significant error between scans 1-3, inferring that the cyclic voltammetry method has low reliability. Given the loss of signal with repetitive scans highlighted in Fig. 97, an average of 3 subsequent scans is likely to introduce significant error as seen above. Furthermore, it is also exceptionally difficult to determine whether or not the reduction in signal is absolutely attributable to the presence of antigen or if this is an artefact of the irreversibility or instability discussed above.

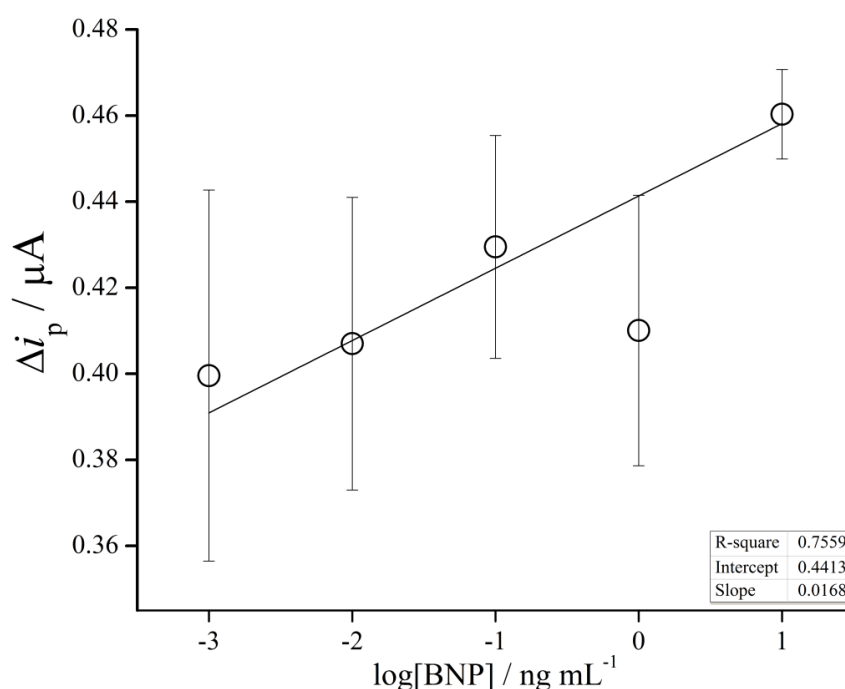


Fig. 99 Calibration for the baseline corrected cyclic voltammetry data. Data averaged over 3 sequential scans following incubation. Linear response ranges 1 pg mL^{-1} to 10 ng mL^{-1} BNP.

However, the results for SWV are more promising, where a significantly clearer oxidation wave is observed at $E_p^{\text{ox}} = 0.62 \text{ V}$.

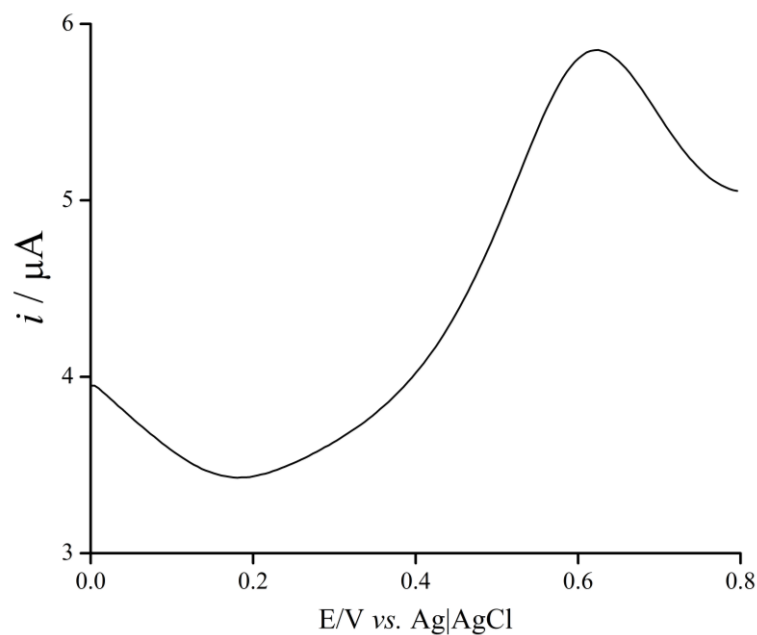


Fig. 100 SWV for CPZ-Ab-BNP modified glassy carbon surface in 10 mM PBS, scan 1 only.

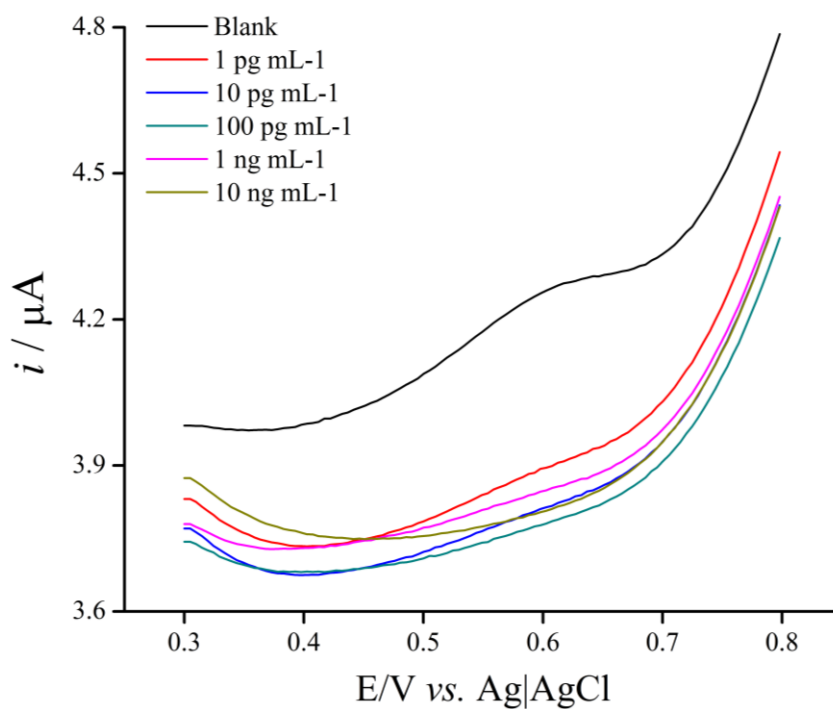


Fig. 101 SWV data for incubations of increasing concentration of BNP (1 pg mL^{-1} to 10 ng mL^{-1}) to a CPZ-Ab-BNP modified glassy carbon electrode surface in 10 mM PBS.

On incubation testing (Fig. 101), SWV produced clearer peaks compared to cyclic voltammetry although it can be seen that the SWV response is not ideal, where each

sample scan has a different baseline. It is difficult to determine a reliable analytical response with the data in this form, therefore baseline correction is required to normalise the data for analysis in a more suitable format. This was carried out using the polynomial baseline correction functionality tool in Metrohm Autolab GPES software.

The calibration plot shown below for the baseline corrected square wave voltammetry data (Fig. 103) shows that the electrochemical response to antigen averaged over three scans with this system is not particularly accurate or reliable. The LOD was determined as $11.55 \mu\text{g mL}^{-1}$ which is particularly poor compared to the ferrocene system. There is also a shift in peak potential observed, however there is no clear trend where some of the potentials shift positively and others negatively thus rendering this method of analysis useless in this case.

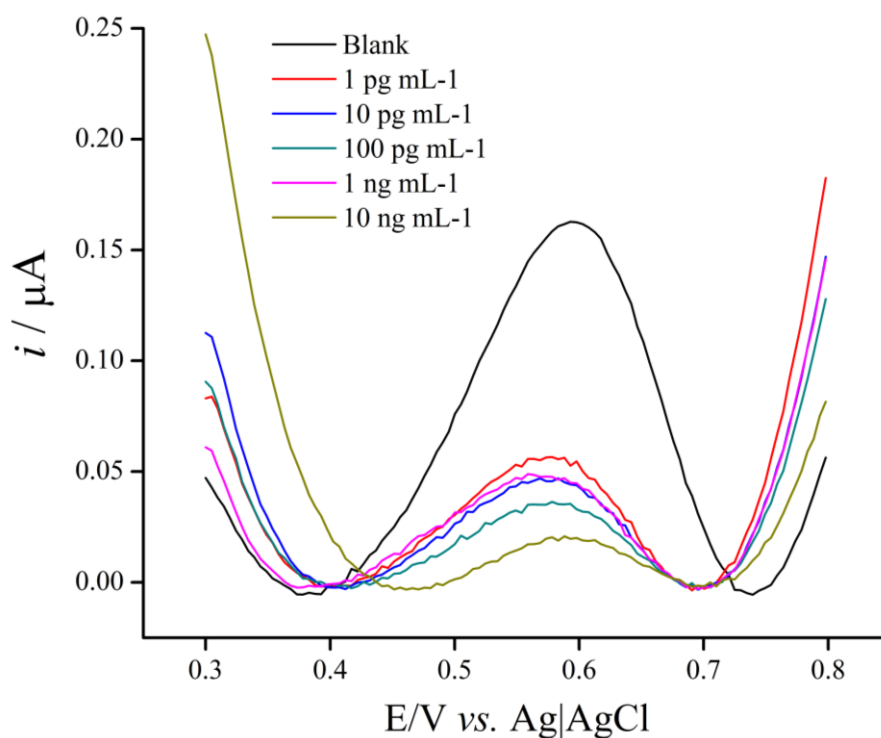


Fig. 102 Baseline corrected SWV data for incubations of increasing concentration of BNP to a CPZ-Ab-BNP modified glassy carbon electrode surface.

Overall, these attempts to synthesise a pure chlorpromazine derivative and successfully conjugate it to antibodies and an electrode surface proved largely unsuccessful. In the event of successful surface modification, the observed peak

currents were small where analysis protocols became particularly difficult as a result. In these preliminary investigations without optimisation, the initial CV and SWV results are very poor, making the method of further reducing signal with antigen addition difficult to implement. This coupled with long synthesis times and difficulty in determining the purity of the electrochemical tag precursor; no further investigations into optimisation were carried out.

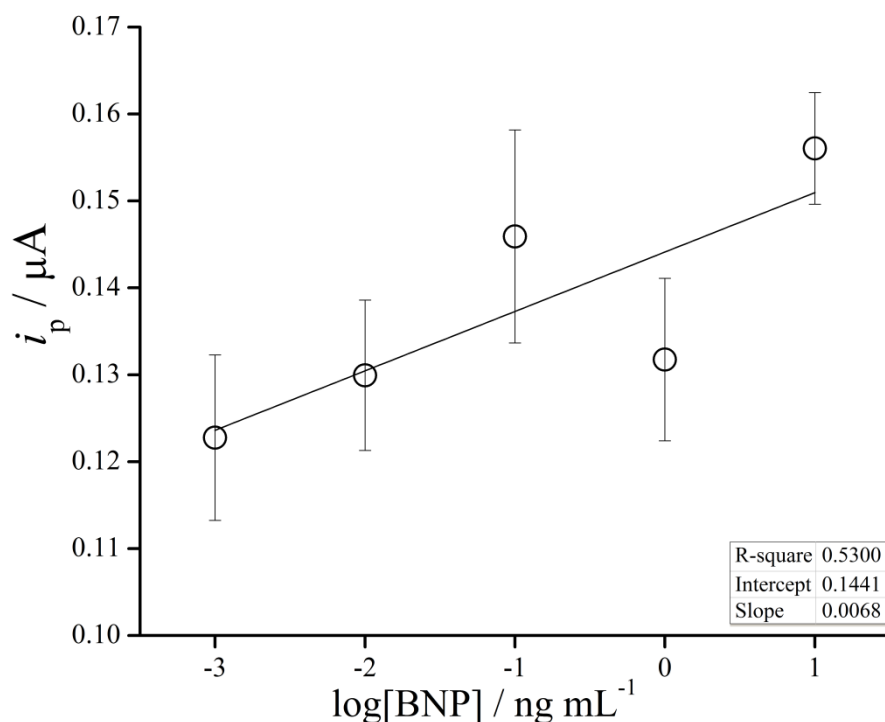


Fig. 103 Calibration for the baseline corrected square wave voltammetry data. Data averaged over 3 sequential scans following incubation.

5.4.2 Ruthenium Dye as an Alternative Redox Tag

Ruthenium (Ru) dyes are well known redox active species, in particular the Gratzel dye, *cis*-bis(isothiocyanato)bis(2,2'-bipyridyl-4,4'-dicarboxylato)ruthenium(II) (N-3 dye) was of ideal choice for use a redox tag in this system, owing to the unhindered external carboxylic acid groups required for bio-conjugation step to the Abs.

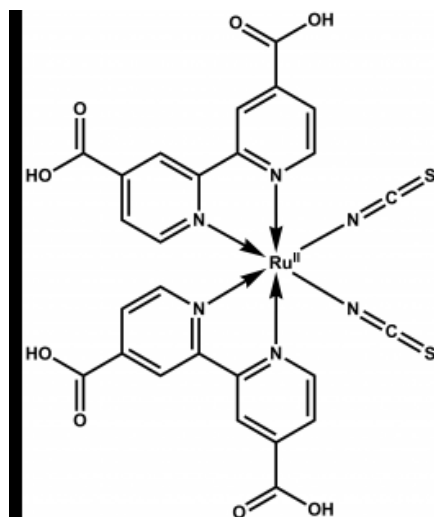


Fig. 104 Structure of N-3 dye

The labelling procedure was carried out as per section 3.8.1 in the same way as for CPZ. In order to confirm the presence and the utility of the ruthenium redox centre at the electrode surface, the electrode was characterised using cyclic voltammetry over potential range +0.2 – -0.4V vs. SCE. This was carried out first in PBS solution to record a blank scan, and following successive and increasing concentrations of BNP antigen; the solution was not de-gassed as the effect of dissolved oxygen on ITO electrode systems involving ruthenium compounds occurs at more negative potentials than those imposed in this method (~ -0.35 V to -0.5 V).¹²

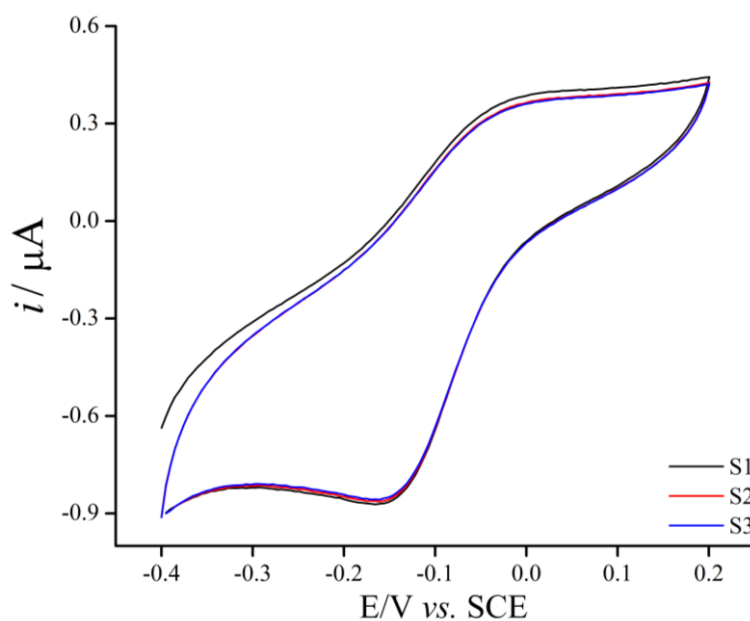


Fig. 105 Baseline cyclic voltammogram for electrode #1 in PBS with 0 [BNP] antigen added.

The voltammogram obtained is characteristic of a redox system, with an oxidation peak at approximately -0.0295 V vs. SCE and a reduction peak at -0.146 V vs. SCE. In the literature, the redox behaviour of ruthenium dyes is described with values of approximately 0.7 V for oxidation and 0.55 V for reduction in acetonitrile solvent,¹⁵ much different to that above. This may be rationalised by the solvent selection, which can have significant effect upon the peak potential value depending on its composition and pH. In this case, the change to aqueous PBS from acetonitrile would be expected to cause a shift in redox potentials due to a change in solvent reorganisation energy.¹⁶ These changes may also be linked to specific interactions between the oxidized or reduced species and the solvent which may alter the thermodynamic driving force and thus the equilibrium constant of electrochemical reactions; in this medium, the presence of chloride in PBS as a counter-ion is known to cause potential shift behaviours.¹⁷

After the initial characterisation of the electrode, successive additions of BNP antigen were added to each modified electrode surface of increasing concentrations by one order of magnitude from 1 fg mL⁻¹ to 1 mg mL⁻¹ at 15 minute incubation periods.

Following each addition, the electrode washed successively with Tween 20/PBS solution and then PBS and dried under N₂ stream. Each electrode was examined by cyclic voltammetry after each addition. Fig. 106 below illustrates the successive cyclic voltammograms obtained for a Ru-Ab-BNP modified electrode.

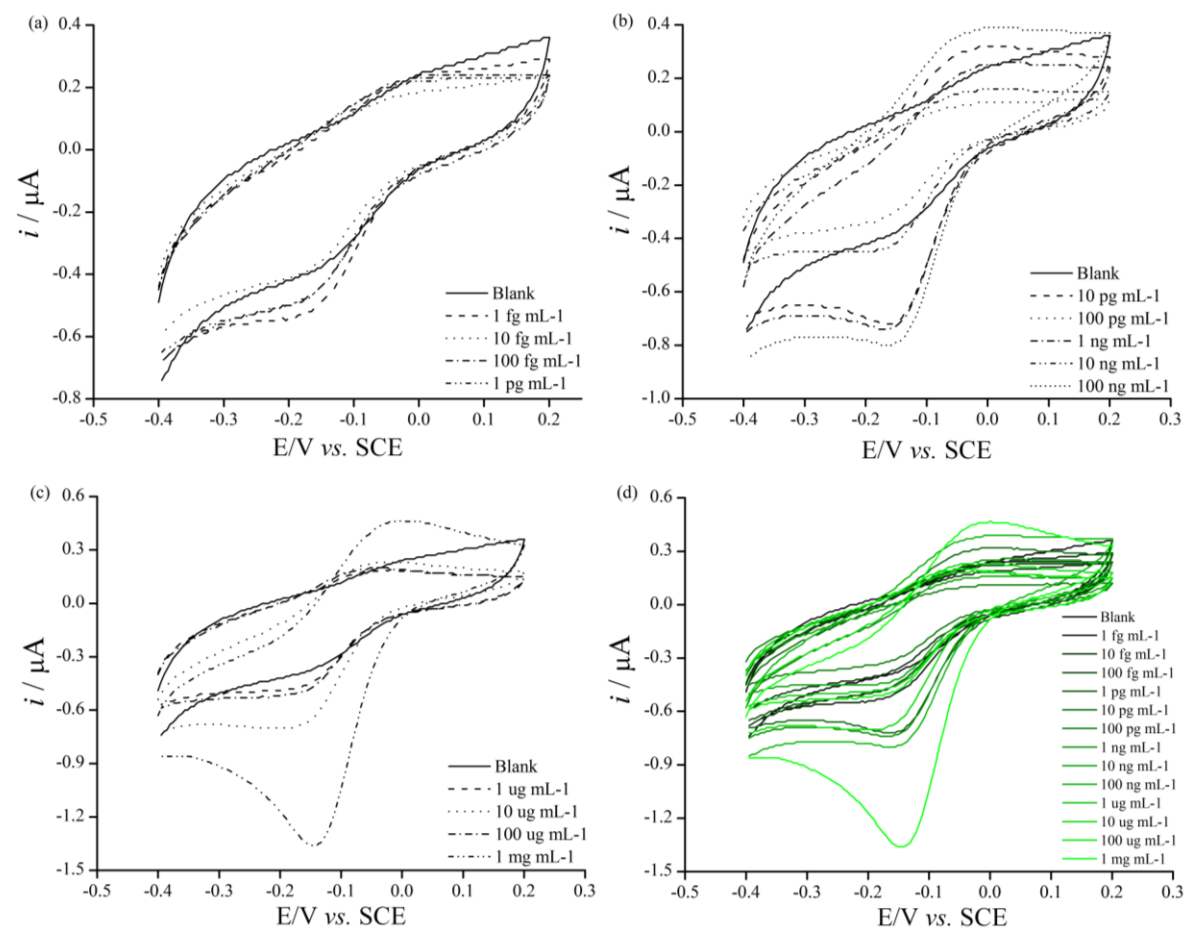


Fig. 106 Cyclic voltammograms of electrode response to BNP additions (1 fg mL^{-1} to 1 mg mL^{-1}) for electrode 1. For clarity these are split into three charts to more clearly define the differences between each incubation scan. (a) illustrates the sensor response 1 fg mL^{-1} to 1 pg mL^{-1} incubation concentrations, (b) shows 10 pg mL^{-1} to 100 ng mL^{-1} , (c) 1 μg mL^{-1} to 1 mg mL^{-1} and (d) all scans overlaid.

The procedure indicated a decrease in the oxidation current observed as the modified surface was blocked with increasing concentration of antigen. A similar increase in the reduction current was also observed. However as the addition of antigen to the modified surface was continued, the electrochemical response became random, even beginning to increase the observed current as opposed to the expected reduction. This is reflected in the calibration plot shown in Fig. 107, where the averaged response of three individually prepared electrode surfaces demonstrates that the immunoassay system does not respond to antigen addition in the desired manner, with significant variances observed in many of the responses. These results therefore indicate that the ruthenium label is not suitable for application as an alternative redox label under cyclic voltammetry conditions.

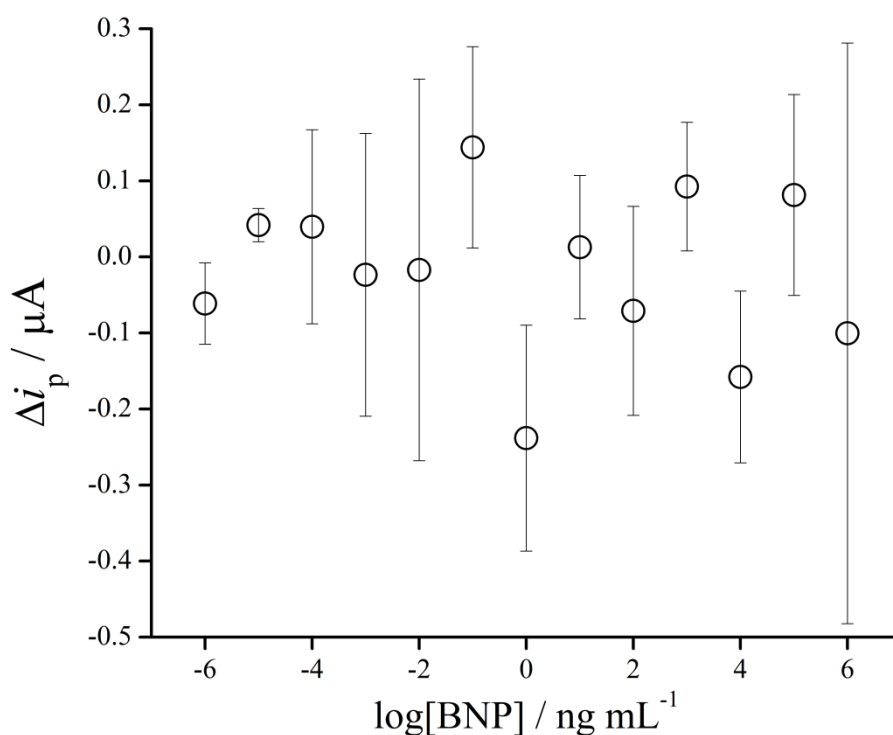


Fig. 107 Calibration of the CV response across 1 fg mL^{-1} to 1 mg mL^{-1} BNP incubations (n=3).

The peak potential shift with increasing antigen concentration was also investigated producing significantly superior results as shown in Fig. 108. Although there is some significant error, a general linear response is observed over the range 1 fg mL^{-1} to $100 \text{ } \mu\text{g mL}^{-1}$ and a total ΔE_p shift of 13 mV. Although the peak current response for the cyclic voltammetry route is poor, the change in peak potential allows for the possibility to multiplex the system wherein one electrochemically active label is

identified through changes in peak current and another that is identified through a change in peak potential. This work demonstrates potential for the development of a novel multiplexed assay of this nature where ferrocene could act as the current based label and ruthenium as the potential based label.

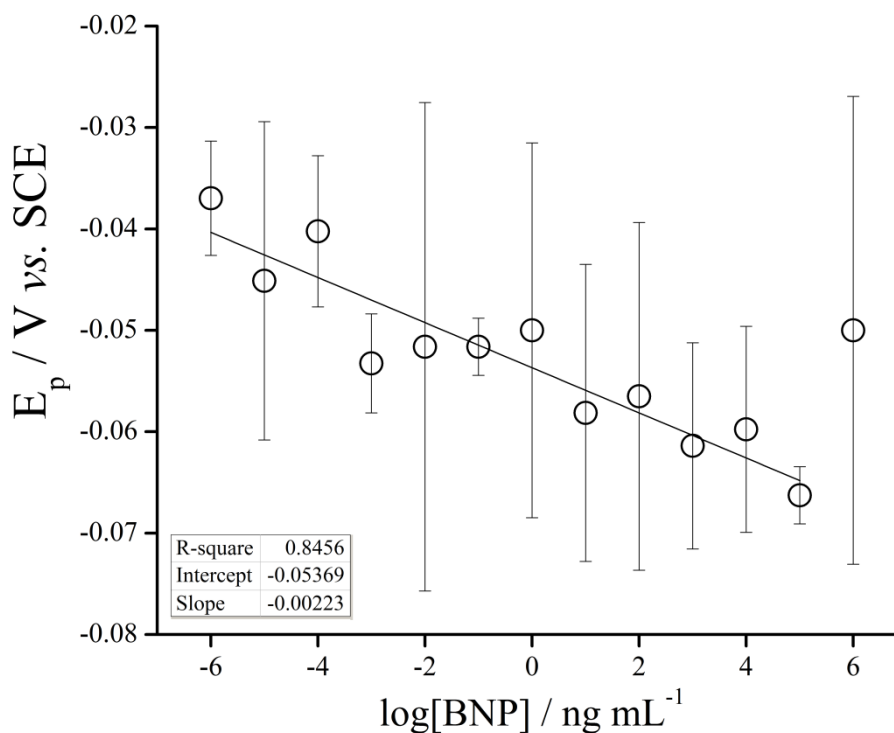


Fig. 108 Calibration of the peak potential shift in response to incubation of BNP over the range 1 fg mL^{-1} to 1 mg mL^{-1} BNP incubations ($n=3$).

The electrodes were also subjected to examination with square wave voltammetry in order to determine whether a more suitable response could be obtained. Fig. 109 below illustrates the baseline corrected square wave data obtained. There is a general decrease in the peak current signal with corresponding addition of antigen however there are several anomalies where the observed response does not continue as expected. These anomalies in the decrease in current observed with increasing concentrations of antigen can again be attributed to pseudo-capacitance at the surface of the aniline mono/multilayer.

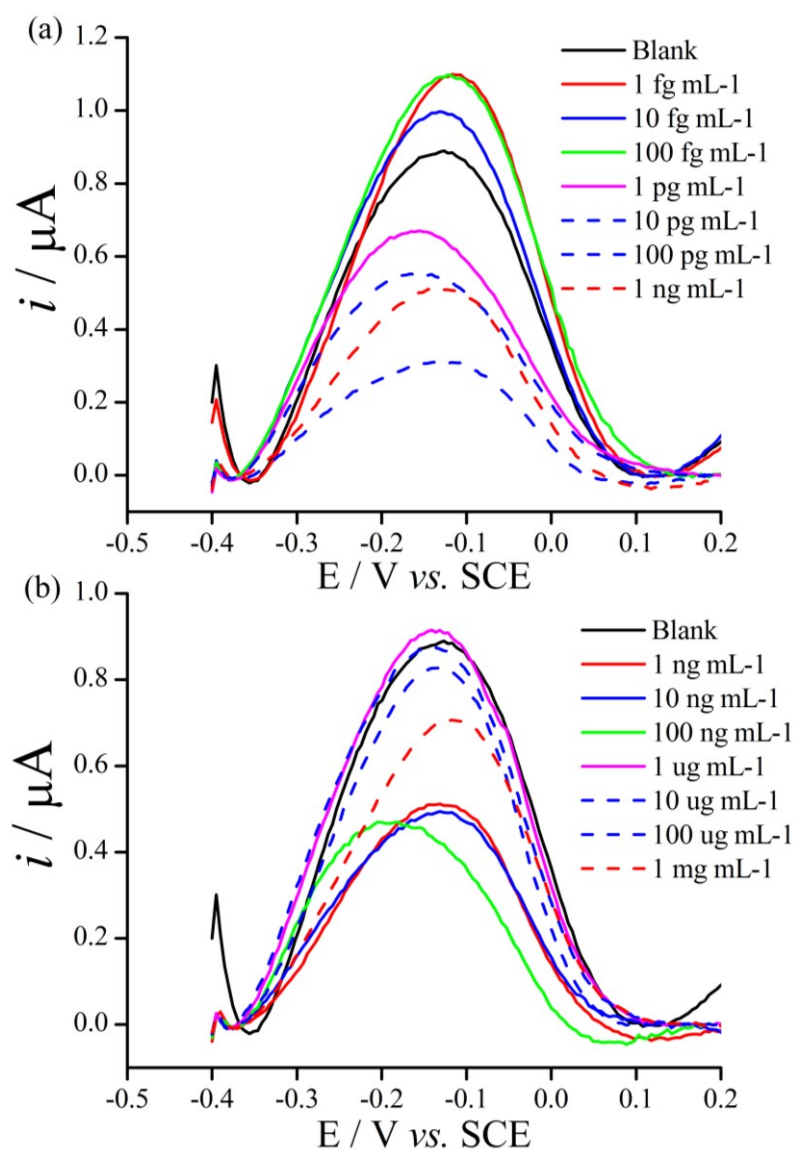


Fig. 109 Baseline corrected square wave voltammograms for electrode 1 for (a) the concentration range of antigen incubation: 1 fg mL⁻¹ to 1 ng mL⁻¹ and (b) 1 ng mL⁻¹ to 1 mg mL⁻¹.

A plot of peak current against concentration was prepared for averaged data of three electrode systems to determine the viability of square wave voltammetry as a suitable electrochemical technique for the ruthenium labelled system. As shown in Fig. 110, the baseline corrected SWV response, Δi_p as determined from $i_p^{\text{blank}} - i_p^{\text{incubation}}$ illustrates a lack of order and significant error observed between the three electrodes tested. Since the non-covalent interaction between the Ab and Ag is highly specific, these interactions, including hydrogen bonding, ionic bonding, hydrophobic interactions, and van der Waals forces are cumulative and form the basis for the

binding interaction between the Ab and Ag. Therefore an especially high degree of specificity between the Ab and the Ag is required for the non-covalent interactions to form since they activate over short distances.¹³ The behaviour observed here is believed to be as a result of the much larger redox label interfering with this local chemistry of the paratope to a degree such that the strength of the binding interaction at the paratope is weakened causing a shift from equilibrium control to kinetic control where antigen leaves the surface faster than it is bound.

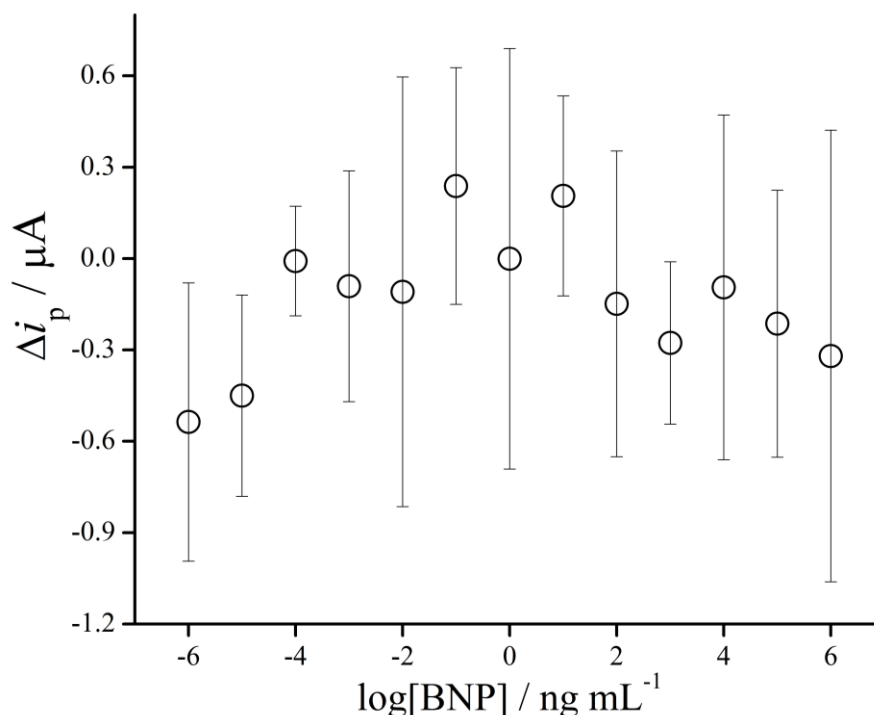


Fig. 110 Calibration of the baseline corrected SWV response across 1 fg mL⁻¹ to 1 mg mL⁻¹ BNP incubations (n=3).

The shift in peak potential was also investigated as for the CV case, where a calibration plot was prepared, shown in Fig. 111. It is clear that in this case there is no trend at all for the peak potential shift with increasing antigen concentration, confirming that the SWV technique does not operate as desired for the ruthenium label.

Overall, only the CV technique produced viable results where the shift in peak potential with increasing antigen concentration produced a clear correlation. This lends the hypothesis that a novel combinatorial multi-analyte sensing platform could be developed with at least two redox-labelled antibodies and two detection strategies;

one label for current based detection and another label for potential based detection. This is conceptually possible with the ferrocene label previously discussed and the ruthenium label since the peak potentials are significantly different and therefore easily identifiable in a combined system. Unfortunately the research did not extend to continue this work into a combinatorial sensing device of this nature, however, these results show great promise for the future development of such a device.

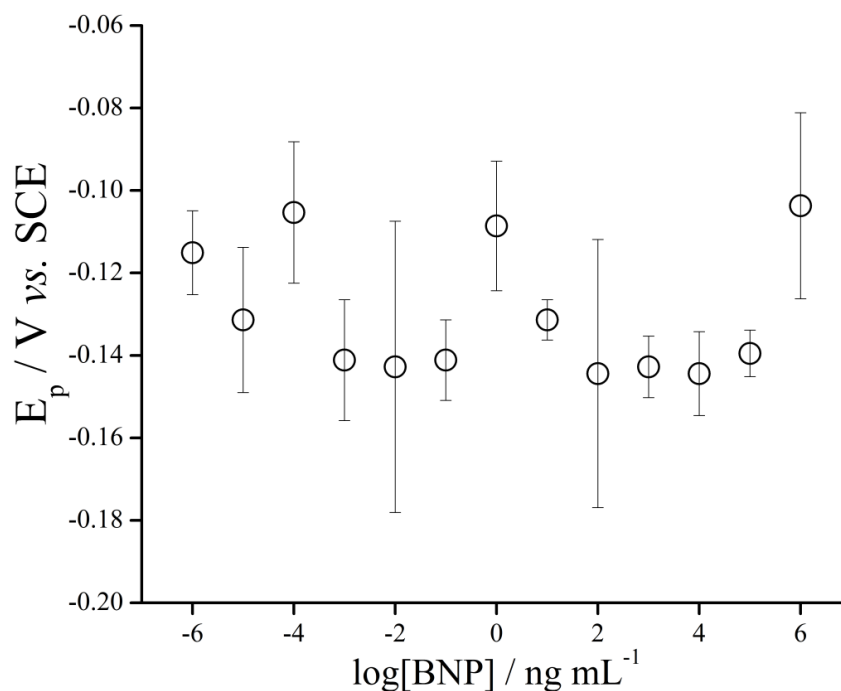


Fig. 111 Calibration plot for the shift in SWV peak potential with increasing antigen concentration (n=3).

5.5 Conclusions

This chapter has illustrated that the platform from Chapter 4 works well with SWV and CV methods, where SWV performed best. We have seen how the sensing platform is capable of managing a diverse range of antibodies and antigens with multiple redox tags as electrochemically responsive labels. Of those investigated (CPZ, ruthenium N-3 dye and ferrocene), ferrocene tags have been demonstrated to be the most promising in terms of stability, reproducibility and measurement performance.

The possibility of using separate tags for dual sensing has not really been established using the chemistries developed. However, in order to undertake multiplexing, it

could be envisaged that using different antibodies on different and individually addressable electrodes each with same Fc tag would be a route forward.

Having thoroughly examined the response of this sensing methodology for stable analytes, the next chapter develops an alternative and proof-of-concept electroimmunoassay specifically for the detection of the transient, unstable biomarkers that exist during the process of aging in which oxidative damage of proteins occurs.

References

1. Y.-H. Dou, S. J. Haswell, J. Greenman and J. Wadhawan, *Electroanalysis*, 2012, **24**, 264-272.
2. P. Allongue, C. Henry de Villeneuve, G. Cherouvrier, R. Cortès and M. C. Bernard, *Journal of Electroanalytical Chemistry*, 2003, **550–551**, 161-174.
3. B. L. Hurley and R. L. McCreery, *Journal of The Electrochemical Society*, 2004, **151**, B252-B259.
4. S. Maldonado, T. J. Smith, R. D. Williams, S. Morin, E. Barton and K. J. Stevenson, *Langmuir*, 2006, **22**, 2884-2891.
5. J. Pinson and F. Podvorica, *Chemical Society Reviews*, 2005, **34**, 429-439.
6. E. A. Kassab, M. I. Marzouk and M. El-Hashash, *Journal of the Serbian Chemical Society*, 2002, **67**, 593-603.
7. P. Zhang, H. Lu, J. Chen, H. Han and W. Ma, *Theranostics*, 2014, **4**, 307-315.
8. M. Okochi, H. Ohta, T. Tanaka and T. Matsunaga, *Biotechnology and Bioengineering*, 2005, **90**, 14-19.
9. E. Laviron, L. Roullier and C. Degrand, *Journal of Electroanalytical Chemistry and Interfacial Electrochemistry*, 1980, **112**, 11-23.
10. R. L. McCreery, *J Pharm Sci*, 1977, **66**, 357-361.
11. H. Y. Cheng, P. H. Sackett and R. L. McCreery, *Journal of the American Chemical Society*, 1978, **100**, 962-967.
12. A. J. Gross and F. Marken, *Electroanalysis*, 2015, **27**, 1035-1042.
13. N. J. Ronkainen, H. B. Halsall and W. R. Heineman, *Chemical Society Reviews*, 2010, **39**, 1747-1763.
14. Y. Zhou, *PhD Thesis: Molecular Electrochemistry*, 2012, 72-76.

15. A. Fattori, L. M. Peter, S. R. Belding, R. G. Compton and F. Marken, *Journal of Analytical Chemistry*, 2010, **640**, 61-67.
16. R. A. Ransdell, "Solvent and Substituent Effects on the Redox Potentials of Several Substituted Tetraphenylporphyrins", 1991, Dissertations and Theses. Paper 1230.
17. N. Priyantha and S. Malavipathirana, *Journal of the National Science Foundation of Sri Lanka*, 1996, **24**, 237-246.

Chapter 6

Electroimmunoassay of TEMPO for Biomarker Detection *via* Spin Trap Adducts

In the previous chapters we explored a route through which biomolecules are detected through their direct recognition with immunoglobulin proteins (IgG). It has been observed that this affords a rapid and highly sensitive sensing pathway when the protein is immobilised through a molecular wire on an ITO surface. The downfall of this analytical system is, however, the requirement that the species to be detected (analyte) is temporally stable. This chapter develops a route to overcome this issue in the very first electrochemical system for radical biomarkers.

6.1 Introduction

Oxidative damage to biomolecules such as proteins and DNA has been shown to generate biomolecule-centred radicals. Free radicals are molecules, ions or atoms that have a lone unpaired electron in an outer orbital, incurring extremely reactive and unstable characteristics. Under normal circumstances, these bio-radicals have as little as microsecond lifetimes,¹ however they can be stabilised in the presence of a spin trap molecule, increasing radical lifetimes and allowing the direct analysis of their presence.¹⁻³

The interaction of the reactive radical species ($R\bullet$) with a spin trap, forms much more stable products in the form of radical adducts. 2,2,6,6-tetramethyl-1-piperidinyloxy (TEMPO) is a chemical compound able to form such stable free radical nitroxide adducts with protein and DNA structures.⁴ Furthermore, TEMPO is electrochemically active with highly reversible characteristics thus exhibiting potential viability for a new, novel electrochemical immunoassay method.⁵ There are two detection routes possible for such a system; (1) surface modification with a TEMPO specific antibody to bind TEMPO that is bound to target proteins and (2) surface modification with target protein specific antibody to bind spin trapped biomarker of interest. The covalently bound TEMPO molecules provide signal generation in both cases; both routes are thus label free. The two routes are schematically illustrated in Fig. 112.

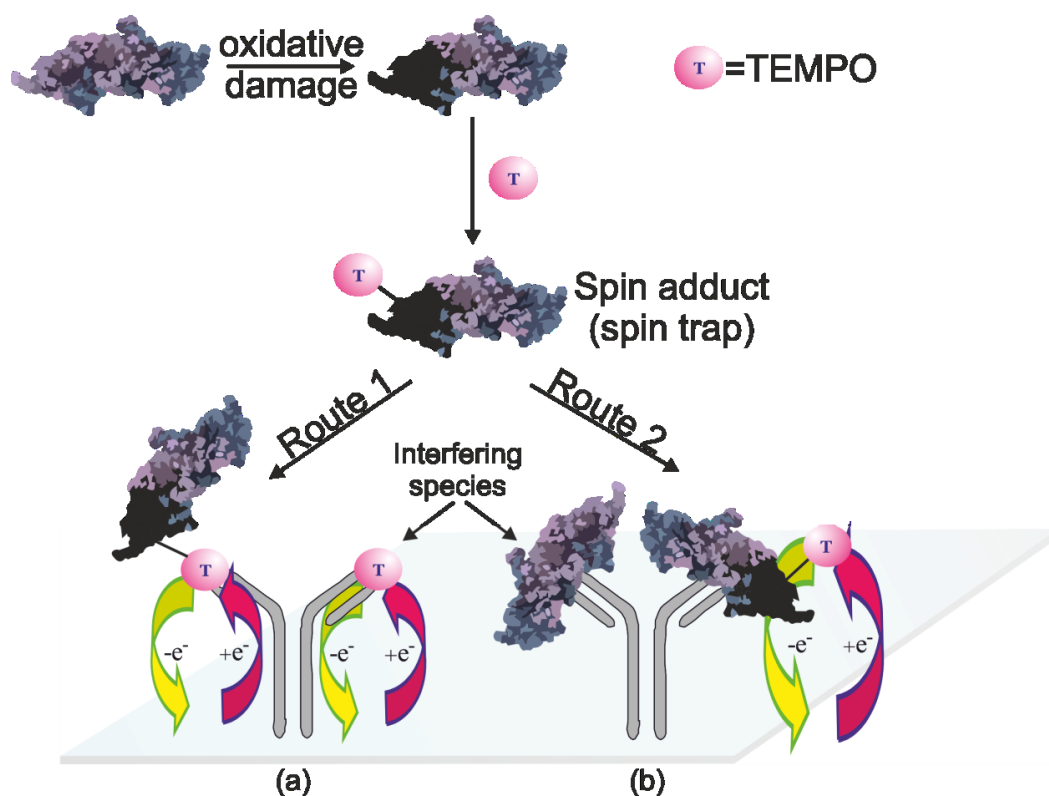


Fig. 112 Schematic illustration of the proposed routes for the detection of TEMPO. (a) demonstrates the case for route (1) wherein antibodies specific to the spin trap molecule TEMPO are immobilised to the surface and (b) antibodies specific to the target biomarker are immobilised to the surface.

6.2 Route 1 - TEMPO Specific

To yield a selective surface for the TEMPO molecule, a suitable antibody is required. Currently, antibodies specific to TEMPO are not available, hence Anti-DMPO (5,5-Dimethyl-1-Pyrroline-N-Oxide) antibodies were used due to the specificity to the nitron moiety present in both DMPO and TEMPO. The attachment of anti-DMPO antibodies to the electrode surface is achieved *via* the same molecular wire approach as in previous works (chapters 4 and 5). The Ab-DMPO remains selective to the TEMPO molecule due to the highly antigenic nature of the nitron moiety.¹

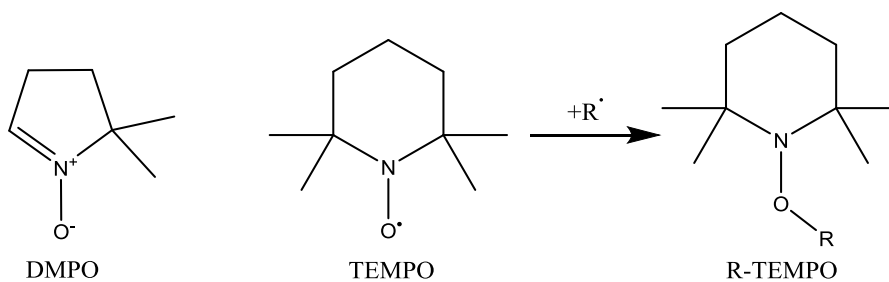


Fig. 113 Structures of DMPO, TEMPO and the TEMPO-biomolecule adduct

The protein radical adducts are formed by introducing a radical initiator into the sample and subsequent stabilisation by the spin trap molecule. Once the stable radical adducts have formed i.e. the TEMPO is bound to the protein of interest, the sample is incubated with the sensor for a set period of time before washing and voltammetric examination. The signal observed may be directly attributed to the concentration of TEMPO-stabilised protein bound to the surface. The benefit of this approach is that no external tagging method is required to provide a signal such as that in the ferrocene tagged antibody surfaces in previous work; here the TEMPO is the signal generator. Because the spin trap is not selective in which radicals are trapped, the immunoanalyses of TEMPO-target nitroxide adducts require separation from free TEMPO and TEMPO-small molecule-centred radicals. On the other hand, it is a largely significant benefit that the prospect of false positives from the sample is avoided, because the nitroxide group does not exist in nature.⁶ Inasmuch as virginal TEMPO will interfere with TEMPO spin adducts, it has been demonstrated in chapters 4 and 5 that the larger, more slowly diffusing protein-TEMPO complex is more likely to dominate over a longer period of time so that provided there is knowledge of the global fraction of the antigen binding sites, it should be possible to determine the spin adduct selectively.

6.3 Route 2 - Biomarker Specific

The concept involves the attachment of an antibody specific to the biomarker of interest to the electrode surface *via* the same molecular wire approach as in previous works; this yields a selective surface for the biomarker molecule. In this case, the biomarker of interest is hCG, hence anti-hCG antibodies are most suited. Once the stable radical adducts have formed i.e. the TEMPO is bound to the protein of interest, the sample is incubated with the sensor for a set period of time before washing and voltammetric examination. The change in signal observed may be directly attributed to the concentration of TEMPO-stabilised protein bound to the surface. Once again, the benefit of this approach is that no complicated tagging method is required to provide a signal and no sample separation steps are required as in assay route A.

However, the problem with this route is that over a longer time frame the larger concentration of undamaged protein will interfere with the detection process.

Accordingly, for proof of concept detection of the TEMPO molecule by anti-DMPO antibodies, route (1) was investigated.

6.4 Special Experimental Conditions

The electrochemical reversibility of 1 mM 2,2,6,6-Tetramethyl-1-piperidinyloxy (TEMPO) was investigated in PBS and 0.1 M TBAP-MeCN *via* CV over variable scan rate conditions (0 – 1.2 V, $\nu = 0.02 - 1 \text{ V s}^{-1}$) at room temperature ($20 \pm 2^\circ\text{C}$). The anti-DMPO antibodies were covalently bound to the ITO electrode surface as described for Ab-hCG. Stock solutions of 1, 10 and 100 μM TEMPO were prepared in PBS and 40 μL aliquots incubated for 1h on freshly prepared Ab-DMPO modified ITO electrodes and voltammetry undertaken to determine if a change in signal could be observed as a result of TEMPO incubation.

6.5 Experimental Results and Discussion

The TEMPO compound was first investigated in aqueous and organic medium to determine any significant difference between the electrochemical reversibility in either environment.

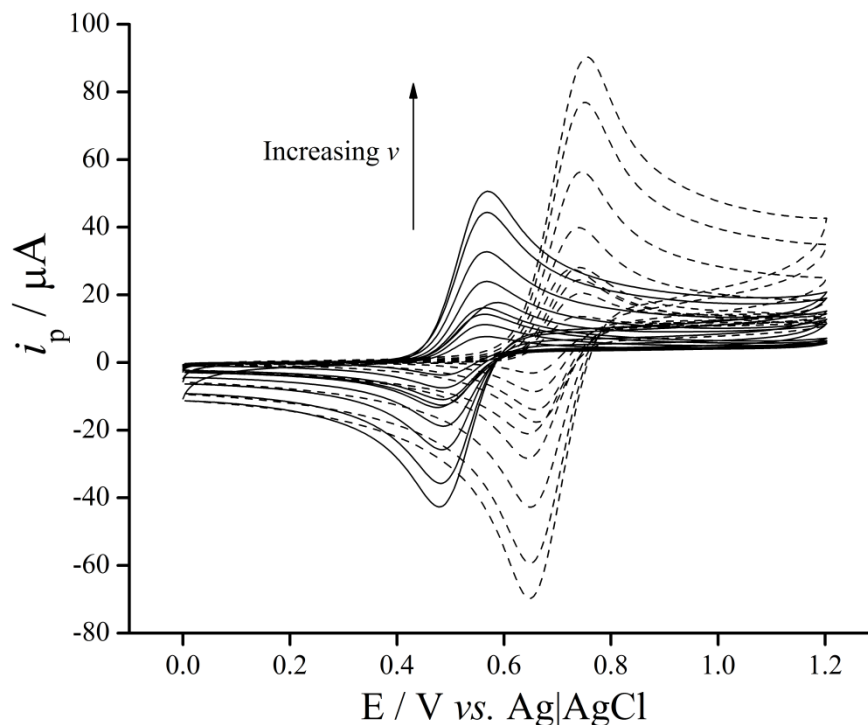


Fig. 114 Voltammetric comparison of 1 mM TEMPO in 10 mM PBS (-) and 0.1 M TBAP in MeCN (- -) at scan rates 0.02, 0.05, 0.075, 0.1, 0.2, 0.4, 0.75 and 1 V s^{-1} .

It can be seen from Fig. 114, that there is a reasonably significant change observed in both the peak currents and peak potentials however a Randles-Sevcik plot shown in Fig. 115 illustrates that both the oxidised and reduced forms of TEMPO are stable in both solutions across the scan rate range investigated. Furthermore, the ratio of peak currents yields a value of one across the entire scan rate range for both cases, inferring that TEMPO is very electrochemically reversible. That the electrochemical reversibility of TEMPO remains unchanged across both environments, except for a small potential shift and a corresponding change in the diffusion coefficient and thus peak current observed, augers very well for the utilisation of a TEMPO signal for bioanalysis.

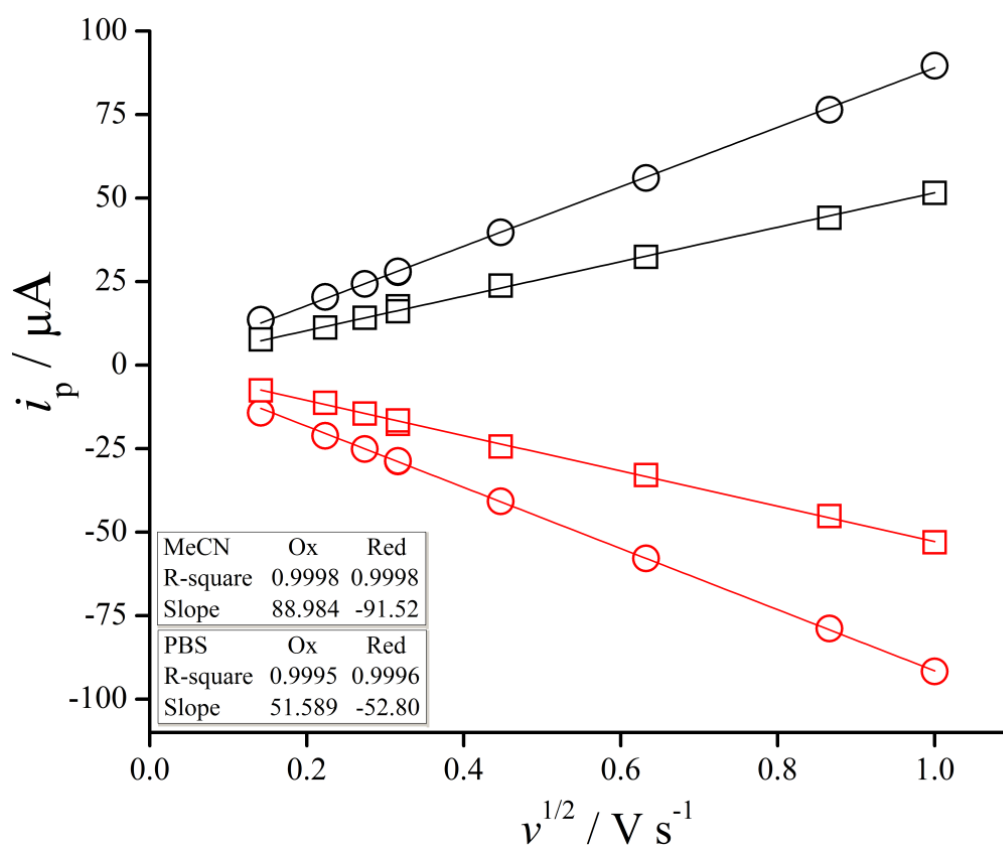


Fig. 115 Randles-Sevcik plot showing i_p vs. $\sqrt{v} / \text{V s}^{-1}$ for the oxidation and reduction processes of 1 mM TEMPO in MeCN (O) and PBS (\square).

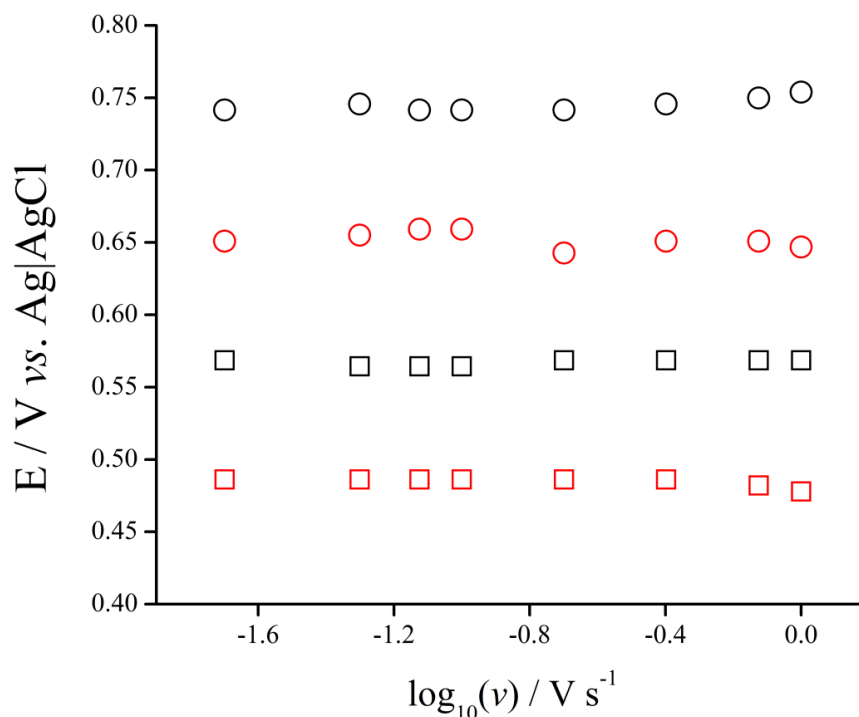


Fig. 116 Graph showing E_p vs $\log(v / \text{V s}^{-1})$ to assess the electrochemical reversibility of TEMPO (O) denotes MeCN and (□) denotes PBS.

The results of the peak potential separation with increasing scan rates are shown in Fig. 116, that show ideal behaviour, where little to no shift occurs demonstrating reversible characteristics. The E_p^{ox} and E_p^{red} values for 1 mM TEMPO in MeCN are 0.742 V and 0.651 V respectively and 0.569 V and 0.486 V for PBS with $\Delta E_p = 90.6$ mV and 82.4 mV respectively. This shows that the TEMPO is not a purely reversible system, at an ~ 30 mV differential from the ideal case, though overall the TEMPO shows strong promise for use an electrochemical signalling agent.

We next examine the electrochemical detection of TEMPO using DMPO antibodies. As can be seen in Fig. 117 and Fig. 118, preliminary cyclic and square wave voltammetry experiments show the observation of a successful signal generation following one hour incubation, this is not present before incubation.

Fig. 118 shows a reduction in peak current with each subsequent square wave scan; this may be attributable to the bound fraction of TEMPO desorbing from the surface to a region of lower concentration (bulk solution) over time, in accordance to antibody-antigen kinetic binding laws, hence a reduction in signal is observed.

Further work to be undertaken is the calibration of signal response to incubation time to identify the lowest incubation possible whilst retaining the relevant sensitivity required for real sample application.

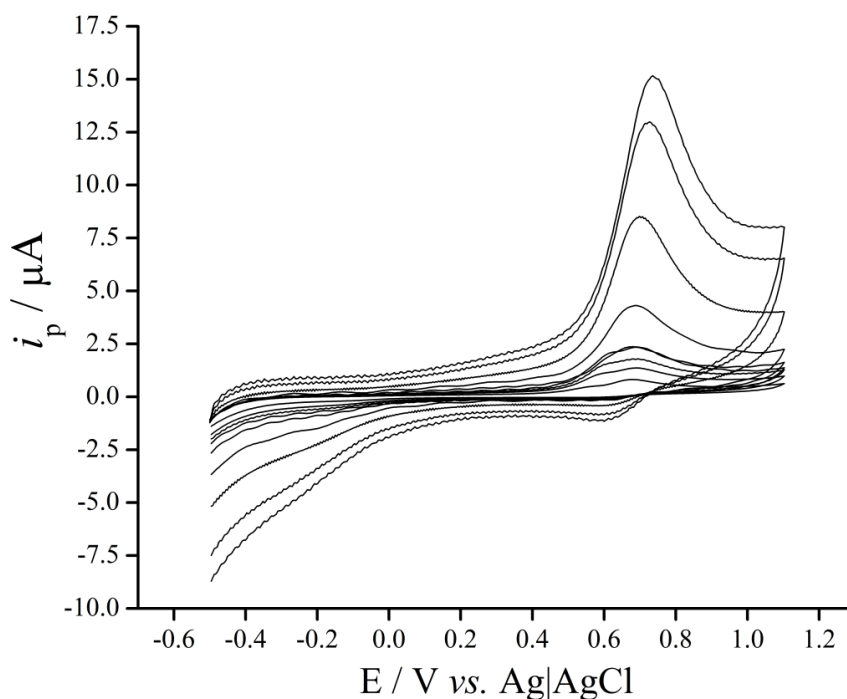


Fig. 117 Variable scan rate scans via cyclic voltammetry for an anti-DMPO modified ITO surface incubated with 1 mM TEMPO in PBS for one hour, $\nu = 0.02 - 1 \text{ V s}^{-1}$.

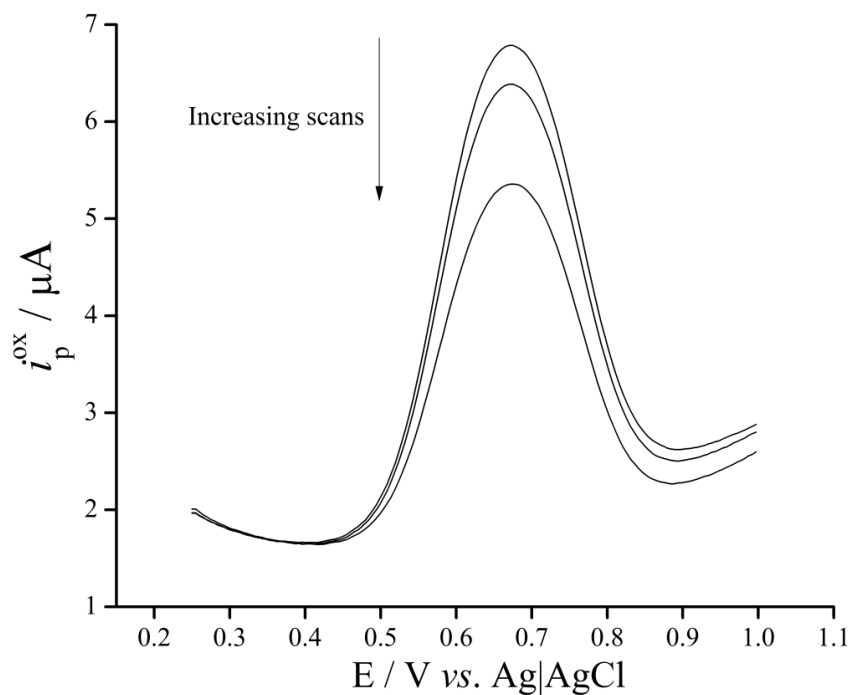


Fig. 118 Square wave voltammetry following 1 hour incubation with 1 mM TEMPO in PBS over three scans.

Fig. 119 shows the Randles-Sevcik and peak potential shift plots for the modified surface following 1h incubation with 1 mM TEMPO, where a clear proportional response of i_p^{ox} to ν is observed up to $\nu = 0.75 \text{ V s}^{-1}$, where the trend is lost. As discussed for other ITO based sensing platforms developed in this thesis, the semiconductor characteristics of ITO impose a higher resistance than other electrode materials, in turn causing these short falls in peak current at high ν .

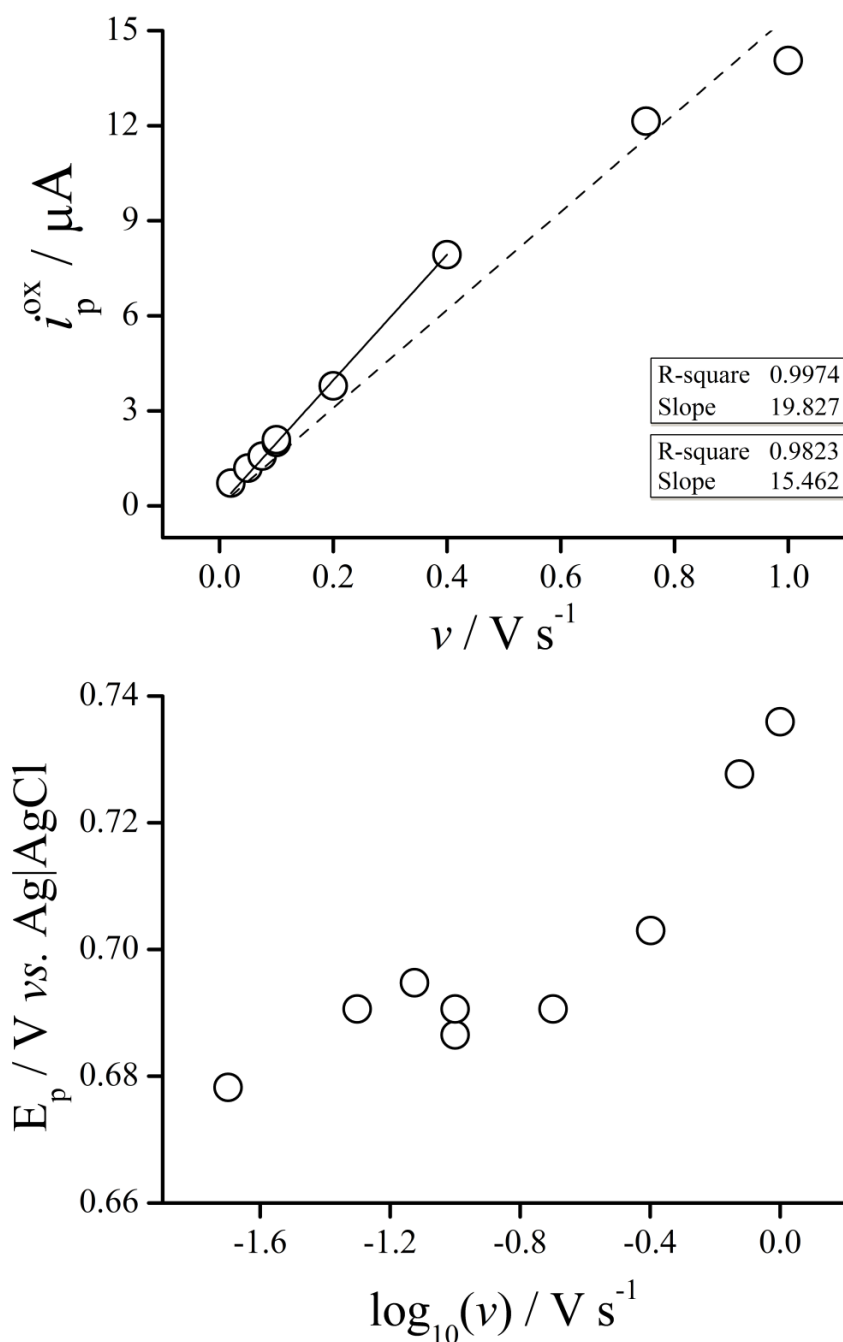


Fig. 119 Randles-Sevcik and peak potential shift plots for the anti-DMPO modified surface response to 1h incubation with 1 mM TEMPO in PBS

The peak potential shift does not behave in the same way as when free in solution. Instead we see a vast change from the clear electrochemical reversibility at all scan rates in PBS to irreversibility when confined to the electrode surface by the anti-DMPO, with a $\Delta E_p = \sim 60$ mV. This may be rationalised by a change in the local environment of the TEMPO molecules, that when bound to the surface are easily oxidised however become unfavourable to reduce. Perhaps this may be attributed to conformational changes or unavailability of the electrochemical centre upon binding of TEMPO, becoming difficult to reduce in the process.

6.5.1 Calibration of the Sensor Response

Following the success of the preliminary investigations, the response of the sensing protocol to 1 h incubations (40 μ L aliquots) of 1, 10 and 100 μ M TEMPO on freshly prepared Ab-DMPO modified ITO electrodes was carried out *via* SWV to determine if a repeatable response was possible. Fig. 120 reveals a linear response across these three concentrations ($R^2 = 0.9988$), demonstrating proof of concept detection of TEMPO on Ab-DMPO modified ITO electrodes.

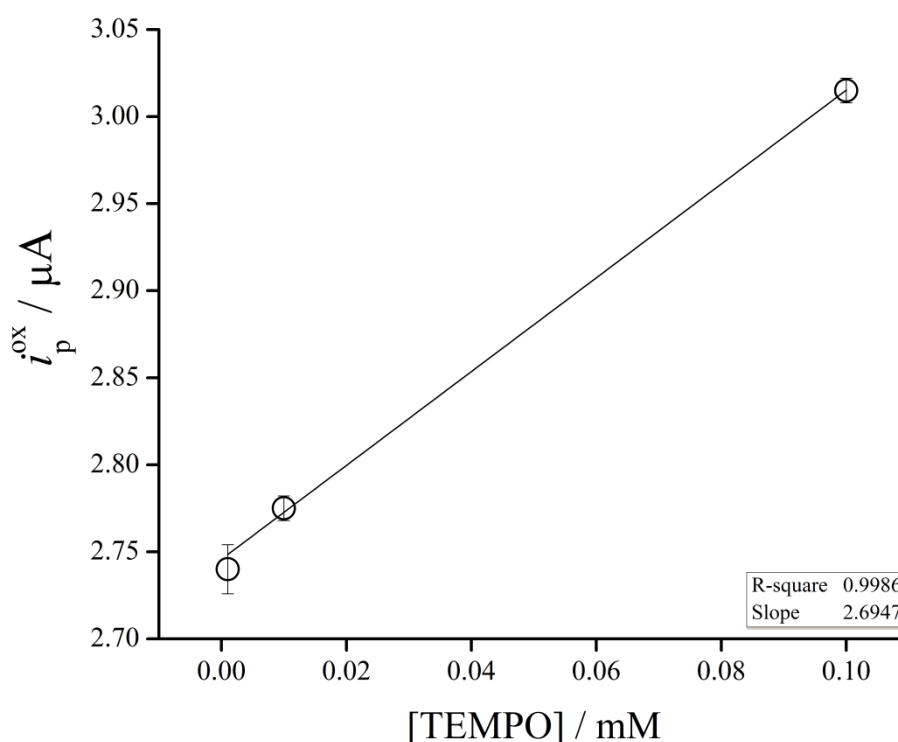


Fig. 120 Average baseline corrected SWV response for 1, 10 and 100 μ M TEMPO 1h incubation to Ab-DMPO modified ITO, (n=2).

6.6 Conclusions

In this chapter, the development of a proof of concept electrochemical immunoassay platform for the quantitative detection of the spin trap 2,2,6,6-tetramethyl-1-piperidinyloxy (TEMPO) has been demonstrated. In PBS (10 mM), the sensor response was linear for sample incubations of 1 - 100 μ M TEMPO over a 60 minute incubation period, verifying the capability of the platform to detect the target analyte.

The use of the longer incubation time in this work (60 minutes) compared with that in chapters 4 and 5 (15 minutes) is required for the small TEMPO molecule. Although experiments were not undertaken with a protein-TEMPO spin adduct, the results presented in chapters 4 and 5 identify that reducing the detection (incubation) time to 15 minutes would enable the preferential detection of the spin adduct. Accordingly, the method shows clear promise for future development in applications for the detection of protein radicals.

References

1. S. E. Gomez-Mejiba, Z. Zhai, H. Akram, L. J. Deterding, K. Hensley, N. Smith, R. A. Towner, K. B. Tomer, R. P. Mason and D. C. Ramirez, *Free radical biology & medicine*, 2009, **46**, 853-865.
2. E. G. Janzen, in *Free Radicals in Biology*, ed. W. A. Pryor, Academic Press, 1980, pp. 115-154.
3. C. Mottley and R. Mason, in *Spin Labeling*, eds. L. Berliner and J. Reuben, Springer US, 1989, vol. 8, ch. 10, pp. 489-546.
4. P. J. Wright and A. M. English, *Journal of the American Chemical Society*, 2003, **125**, 8655-8665.
5. L. Marx and B. Schollhorn, *New Journal of Chemistry*, 2006, **30**, 430-434.
6. in *Laboratory Techniques in Biochemistry and Molecular Biology*, ed. M. S. Catherine Rice-Evans, Elsevier, 1991, vol. Volume 22, ch. 1: Introduction to Free Radicals, 15-16.

Chapter 7

Overall Conclusions

Hitherto, three alternative methodologies have been considered for an electrochemical immunoassay that exploits a molecular wire platform. In Chapter 4 the development of an electrochemical immunoassay for the detection of hCG is presented, whereby direct electrode surface modification yields a molecular wire scaffold to enable the subsequent bio-conjugation of anti-hCG antibodies labelled with electroactive ferrocene. The fundamental kinetics of the sensing platform were investigated intensively, in order to develop bespoke theory and a successful unique analytical method for the detection of antigen in terms of a 'fractional antigen coverage' of the electrode sensor surface. The sensor demonstrated excellent sensitivity to hCG in artificial urine, with a limit of detection of 1.93 mIU mL^{-1} (0.21 ng mL^{-1}) for as little as 15 minute sample incubations showing no observable effects from common interferences glucose and haemoglobin. Therefore it was demonstrated that the immunosensor is capable of quantitative measurements with short analysis times, well within the clinical range required for pregnancy applications. In spite of this, the weakness is that it cannot be used for the combinatorial sensing of multiple biomarkers or antigens simultaneously.

This was addressed in Chapter 5, where the platform from Chapter 4 was investigated and characterised with square wave (SWV) and cyclic voltammetry (CV) methods, where it was found SWV performed best. The ability of the sensing platform to manage a range of antibodies and antigens (BNP for cardiovascular applications and β -hCG for pregnancy) with multiple redox tags as electrochemically responsive labels (chlorpromazine, ruthenium N-3 dye and ferrocene) was explored. Of the labels investigated, ferrocene tags were demonstrated to be the most promising in terms of stability, reproducibility and measurement performance on both antibodies. The investigation of using separate labels for dual sensing was unsuccessful using the chemistries developed. However, future work could be undertaken to enable multiplexing by using different antibodies on an array of individually addressable electrodes each with same Fc label chemistry, though tested independently of each other.

Chapter 6 explored a new application entirely; detection of proteins with oxidative damage. Radicals that are formed during the process of oxidative damage may be stabilised in the presence of a spin trap molecule. The manipulation of an electro-active spin trap molecule 2,2,6,6-tetramethyl-1-piperidinyloxy (TEMPO) was investigated for the development of a proof of concept electrochemical immunoassay platform capable of quantitative detection of spin trap molecule stabilised analyte. This preliminary study demonstrated the successful detection of the TEMPO molecule after 1 hour incubation in PBS, however the addition of protein and initiation of radicals to investigate the detection of the stabilised analyte was not possible within the timescale of study.

Overall, a robust, well characterised electrochemical immunoassay platform on ITO has been developed and demonstrated to operate well for Ab-hCG, Ab- β -hCG and Ab-BNP antibodies. Of particular success, detection of the pregnancy hormone hCG in artificial urine samples was achieved at timescales of 15 minutes and without interference. If taken further and translated into human samples, the sensing platform has promising potential to provide rapid, accurate quantitative readouts at the point of care to facilitate more informed decision making in the relevant clinical scenarios.

Definitions

Ab	Antibody
Ag	Antigen
Ag AgCl	Silver Silver Chloride Reference Electrode
Au	Gold
BNP	Brain Natriuretic Peptide
CHF	Congestive Heart Failure
CPZ	Chlorpromazine
CV	Cyclic Voltammetry
CVD	Cardiovascular Disease
e ⁻	Electron
EDC	N-(3-dimethylaminopropyl)-N'-ethylcarbodiimide
ELISA	Enzyme-Linked Immunosorbent Assay
Fc	Ferrocene
GC	Glassy Carbon
GOx	Glucose Oxidase
hCG	Human Chorionic Gonadotropin
HRP	Horseradish Peroxidase
IgG	Immunoglobulin
ITO	Tin-doped Indium Oxide
LOD	Limit of Detection
PBS	Phosphate Buffered Saline
POC	Point-of-Care
R	Molar Gas Constant (8.314 J mol ⁻¹ K ⁻¹)
Ru	Ruthenium
SCE	Saturated Calomel Electrode
Sulfo-NHS	N-Hydroxysulfosuccinimide
SWV	Square Wave Voltammogram
T	Absolute Temperature (K)
TEMPO	2,2,6,6-Tetramethyl-1-piperidinyloxy
TnT	Troponin T
β-hCG	Beta sub-unit Human Chorionic Gonadotropin